NUMERICAL SIMULATION OF DIESEL SPRAY PROCESSES

by

Cedomir Kralj

B.Sc. (Mech. Eng.)

Thesis submitted for the degree of

Doctor of Philosophy of University of London

and for

the Diploma of Imperial College

Mechanical Engineering Department

Imperial College

London, SW7

October 1995

Abstract

This study deals with a mathematical model and numerical procedure for simulation of diesel spray processes, excluding ignition and combustion, on unstructured moving meshes. Two important aspects to achieve plausible predictions are the quality of mathematical modelling of all relevant physical phenomena, and the strategy used for solving the governing equations. The former includes the modelling of two-phase turbulent flow, spray processes, and inter-phase transport, and the latter is determined by the accuracy of the numerical approximations and solution procedure.

The study is restricted to the simulation of single-component diesel sprays. The gas flow is described by a set of mutually coupled, density-weighted ensemble-averaged conservation (transport) equations in which, as a result of the gas-spray interactions, additional coupling source terms appear. The turbulence phenomena are modelled via the k-ϵ turbulence model.

The diesel spray, which in reality comprises a large number of droplets, is not represented directly, but modelled by a changing Monte-Carlo population of sample droplets. This allows each droplet's behaviour to be described separately by a set of ordinary differential equations for the conservation of mass, energy and momentum. The following detailed spray processes are modelled: atomisation, turbulence dispersion and modulation, drop breakup and collision, spray-wall interactions, and inter-phase transfer of mass, momentum and energy.

The solution strategy for the continuous phase is based on the finite volume method. Unstructured meshes of the finite-element type are used, together with a collocated variable arrangement. The governing integro-differential equations are discretised into sets of simultaneous algebraic equations, which after linearisation and decoupling by the PISO predictor-corrector sequence, are solved by the conjugate gradient methods. The spray equations are completely embedded in the PISO predictor-corrector solution procedure, and are solved in an Eulerian implicit fashion by a temporal subcycling technique.

The overall method is assessed by reference to experimental data for sprays injected into a quiescent pressure chamber and for two forms of DI diesel engine. Sensitivity studies on mesh density, droplet drag and breakup correlations, and turbulence modulation are performed. A novel model for spray-wall interaction is implemented, and the predictions of two recently developed atomisation models are compared against the experimental results. The results are found to be very sensitive to the mesh density, breakup correlations and turbulence modulation modelling, and are less sensitive to the drag coefficient correlations. Both atomisation models show acceptable agreement for the spray penetration prediction, and less satisfactory agreement in the prediction of the fuel vapour concentration.

Acknowledgements

I would like to express my sincere gratitude to my supervisor Prof. A. D. Gosman for his guidance and sharp but constructive criticism throughout the course of this project.

Thanks are due to Prof. I. Demirdzic for his suggestions and instructive remarks on the material covered in Chapters 2-5.

I have benefited from occasional discussions with members of Fluid Section who are too numerous to list here.

My wife Jadranka and son Igor and my parent have encouraged me throughout this long and time-consuming work; for their patience and understanding I will always be grateful.

My thanks also go to Ms. N. Scott-Night for the arrangement of many administrative matters.

Finally, I take the opportunity to acknowledge the financial support provided by the Joint Research Committee of European Engine Manufacturers and Science and Engineering Research Council.

Nomenclature

Latin characters

A	area
$\mathcal{A}$	matrix coefficient
B	bore diameter; mass transfer number
$\mathbf{b}$	source term of vector equation
b	source term of scalar equation
$\mathcal{C}$	convective flux
C	coefficient
c	specific heat capacity; coefficient
D	diameter; diffusion flux
$\mathbf{d}$	diffusion flux vector
$\mathcal{D}$	mass diffusivity, diffusion flux coefficient
$\mathbf{D}$	rate-of-strain tensor
d	differential
E	collision efficiency
e	internal energy
$\mathbf{e}$	unit vector
F	function; wall function
f	cell face; local direction in cell; correction function
$\mathbf{I}$	tensor unit
j	imaginary unit
k	kinetic energy of turbulence
L	injector hole length; length scale
$\mathbf{N}$	discretised ∇ operator
p	thermodynamic pressure
$\mathbf{q}$	heat flux vector
r	normalised residual
$\mathbf{r}$	position vector
R	residual
S	boundary of control volume

$\mathcal{S}$	surface vector
s	specific source term; per unit volume or unit mass and time
T	absolute temperature
$\mathbf{T}$	stress tensor
t	time
U	injection velocity
$\mathbf{u}$	velocity vector
V	volume
w	weighting factor
$\mathbf{x}$	spatial coordinate; x, y, z
Y	mass fraction; random number

Greek characters

α	gas component; angle
β	azimuthal angle
Γ	diffusivity coefficient
γ	ratio of specific heats, c_p/c_v
δ	Dirak function
ϵ	turbulence dissipation rate
ϑ	void fraction
κ	von Karman constant; wavenumber
Λ	integral length scale
λ	interpolation factor
μ	dynamic viscosity
ν	kinematic viscosity; collision frequency
π	Ludolf's number
ρ	density
ϕ	general fluid field
σ	Prandtl/Schmidt number; surface tension coefficient
τ	time scale; relaxation time
ω	complex wave celarity

Subscripts

a	average
b	boundary
cyl	bulk cylinder value
d	droplet
eff	effective
f	local direction; cell face; value at the cell face
ft	total fuel
h	injection hole
l	liquid
m	molecular
N	neighbouring cell
n	nozzle
$norm$	normalisation factor
P	central cell
$\mathcal{P}$	SP-part of source term
p	computational parcel; piston
r	relative
ref	reference
t	turbulence
$\mathcal{U}$	SU-part of source term
v	fuel vapour; valve
W	wall
w	wave

Superscripts

a	available value
c	cross-diffusion (non-orthogonal) part
d	drop; spray

i	subcycling step
j	algebraic corrector step
k	corrector step
nor	direct (orthogonal) part
o	old-time value
P	related to cell P
$'$	fluctuation about Reynolds mean value; relative pressure; intermediate value
$''$	fluctuation about density-weighted (Favre) mean value

Symbols

∂	partial derivative
$\bar{}$	Reynolds mean value; average; normalised
$\hat{}$	instantaneous value
$\tilde{}$	density-weighted (Favre) mean value
∇	gradient operator
$\cdot$	scalar product

Abbreviations

$ATDC$	after top dead center
BCG	bi-conjugate gradient
BDC	bottom dead center; also used as subscript
CFD	computational fluid dynamics
Co	droplet Courant number
CG	conjugate gradient
DI	direct injection
DIO	duration of injection
EOI	time at end of injection; also used as subscript
FEM	finite element method
IV	inlet valve

LHS	left hand side
MPI	Max Planck Institute
Nu	Nusselt number
OV	Outlet valve
On	Ohnesorge number
Pe	Peclet number
Re	Reynolds number
RHS	right hand side
rms	root mean square
Sc	Schmidt number
Sh	Sherwood number
SOI	time at start of injection; also used as subscript
TDC	top dead center; used as subscript too
We	Weber number

Contents

List of Tables

List of Figures

Chapter 1

Introduction

1.1 Background

Internal combustion (IC) engines date back to the late 19^{th} century when the first spark-ignition and compression-ignition (diesel) engines were developed. Since then, they have experienced a rapid development which has ensured their dominant role in the transportation (land, sea, air) of the 20^{th} century. Throughout this period, the design, performance and efficiency of the engines have been improved mainly as a result of continuous research driven by the competition between manufacturers. Especially rapid progress took place after World War II, when the new materials and technologies were invented, and when the passenger car became accessible in the developed countries to 'ordinary' people.

As is the case with many of man's activities, the wide-spread usage of IC engines in transportation creates negative effects. The first well-known one was the air pollution problem in the 1940s in Los Angeles, resulted from reactions of the nitrogen oxides and hydrocarbon compounds from the automobile exhaust gases [100]. It has been realised since then that automobiles in urban areas are a major cause of high concentrations of nitrogen oxides, hydrocarbons, carbon monoxide and soot. Taking into account that these compounds can cause a variety of health problems to the population, many countries have decided to introduce stringent emission standards for automobiles. A similar response has developed towards noise pollution, since IC engines are important noise sources in towns. While this practice of legislative restrictions on the pollutant and noise emission levels was limited at the early stage to the developed countries, it seems the same path will be followed by others. Moreover, there is a persistent pressure from different 'green' movements for the further reduction of permissible emission levels. Due to this development, the engine manufacturers are faced with problems of building the engines which fulfill these demands.

A later blow to the automobile manufacturers was the oil crisis in the 1970s, when the oil prices become so high that the development of low-fuel-consumption engines was seen by companies as the way to survive. The oil crisis not only emphasized the importance of engine efficiency, but also caused the extensive utilisation of diesel engines in passenger cars, due to their known beneficial fuel consumption efficiency. This trend has been much more visible in Europe than in the USA, since Europe has traditionally higher fuel prices, and is more sensitive to the fuel costs. Fig. 1.1 (taken from [144]), where the percentage of diesel registrations in the EEC countries vs. years is shown, illustrates the trend. Also, port-injection spark-ignition engines have become much more common.

The oil crisis also initiated consideration that fossil fuels are non-regenerative energy sources, and that their exploitation need more rational management. This is the background for demands on engines to be able to use fuels of different ignition qualities, which again was in favour of diesel engines.

All the aforementioned developments, together with the similar demands on gas turbines, intensified research on sprays and mathematical models thereof[1], because spray behaviour has a key role in mixing and combustion processes in diesel engines, port-injection, spark-ignition engines and gas turbine combusters. It became clear that the old design tools used in automobile industry, mainly consisting of empirical correlations of the engine processes based on measurement, sometimes used in conjunction with zero-dimensional analysis were not sufficient. New approaches, both experimental and computational, required to be developed, which could offer detailed insight into the in-cylinder phenomena, to enable designers proper assessment and selection between different variants of engine. Hence, new experimental meth-

[1] Sprays have many other applications, but they are beyond the scope of this work.

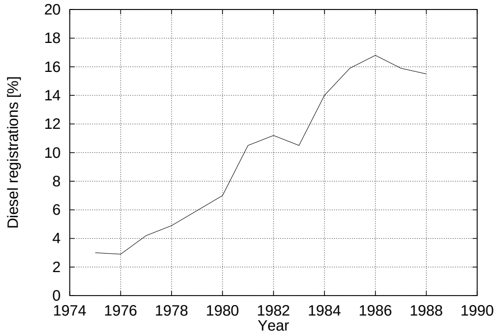

Figure 1.1: Diesel registrations in EEC countries.

ods and numerical simulation approaches have been and are still being developed. They are complementary and benefit each other.

In the following two sections, (1.1.1) and (1.1.2), general computational and experimental methods for engine analysis will be briefly described. In section (1.2), the overall processes in diesel engines are described, followed by the review of approaches to the spray modelling. Efforts made in this thesis to build a consistent mathematical model of spray-gas behaviour and computational procedure for its solving, and to investigate effects of various spray submodels, empirical correlations and numerical procedures, are summarised in §(1.3). §(1.4) deals with the outline of the thesis.

1.1.1 Computational methods

The starting step of all computational methods is a mathematical model of the physical/chemical processes to be predicted or simulated. However, this mathematical description necessarily neglects some less important or less influential phenomena in order to reduce the complexity of the final mathematical model. Generally, such models can be categorised into phenomenological and multi-dimensional categories (MDMs), [78]. The former consists of zero-dimensional and one-dimensional models. The zero-dimensional models ignore spatial variations of flow parameters, and are capable of predicting only their temporal variations. In the one-dimensional approach, the full three-dimensional forms of the governing equations are reduced to one-dimensional by ignoring or making assumptions about variations in two other spatial directions. The MDMs are much more complex, but they offer prediction of the spatial and temporal distribution of flow parameters. In this sense, the mathematical model can be seen as an approximation of the real processes to the required or acceptable level of accuracy, generally given as a set of coupled differential equations.

The second step comprises a solution procedure of this set of equations, which can be analytical or numerical. Unfortunately, only few problems, usually very simple and of a minor practical interest, have analytical solutions. Therefore, various numerical methods have been developed and used. In general, these methods consist of discretisation of the solution domain into a finite number of subdomains, and approximation of the original equations by a system of simultaneous algebraic equations, linking the variables in these subdomains. Solution of this system by a solution algorithm provides a set of numerical values at these subdomains, which represents the approximate solution. Intuitively, one expects better accuracy if a large number of subdomains is used, but then corresponding large number of simultaneous equations must be solved. This has became practically possible by the appearance of digital computers.

The appearance of the first digital computers in the 1940's, and their rapid development since then, as well as a rapid improvement and development of a various numerical methods, especially in the last 15 to 20 years, have boosted wide application of, firstly, codes based on the finite element method (FEM) in the fields of structural analysis, and then various FEM or finite volume (FV) CFD codes in analysing complex fluid flows, in all types of application.

The FEM originated from the field of structural analysis by the pioneering works of Argyris and Kelsey [15], Turner et al. [214], and Clough [45], and found its successful application in the continuous field problems by works of Zienkiewicz and Cheung, [229] and others. For fluid flow problems, the general approach by the FEM was developed by Chung [42], and recently by Baker [19] and Hirsch [103].

The FV method has its roots in the field of fluid mechanics. The first works date back in the late 1960's and early 1970's; Gosman et al. [87], MacDonald [133] and others. From then on a number of general and special-purpose CFD codes were developed, including: TEACH-T [81], the two-dimensional 'CONCHAS' code [37] and its improved three-dimensional counterparts 'KIVA' [11], 'STAR-CD' [194], 'SPEED' [88], [86] and others; see also the review in [161].

However, it is difficult to generally assess the potential possibilities of all these codes in predicting complex flows because, in contrast to the well-developed and accurate mathematical models available in the field of structural analysis (at least for practical engineering calculations), in fluid mechanics there are still a number of incomplete or non-universal mathematical models. The main problem is in the modelling of turbulence; the existing simpler models fail in some circumstances, while the application of the more complex models of turbulence in engineering problems are beyond the acceptable financial and/or computational resources. There are also a number of other processes in fluid mechanics which are incompletely understood and which do not have satisfactory models, including for example sprays, as will be pointed out in this study. It must also not be forgotten that the numerical method introduces additional potential errors, mentioned above, and that only solutions on different mesh densities enable these to be evaluated.

All the aforementioned give reasons for the cautious conclusion that CFD can in principle, offer a powerful tool in predicting flows if used in a proper manner and by experienced users. This is one of the reasons why the CFD became so attractive. The second reason is the greater ease and lower cost of investigating the effects of variations in engine geometry and/or flow parameters than the experimental approach can offer. In these cases the CFD gives quicker and more detailed answers to designers of the trends of solution - the information of real importance. However, it would be wrong to claim that the stage where the engine designing can rely only on the CFD methods has yet been reached.

The efforts made in this thesis should be seen in a light of further assessment of proposed models of spray processes, and investigation of their particular affects on the overall gas-spray behaviour.

1.1.2 Experimental methods

There is a large number of experimental methods used for flow measurement. They can be classified as a local, global and visualisation. The latter involves photographing of flow with or without seeding (tracing) particles. The global methods give only overall information on flow. The methods of real interest for providing detailed flow parameters at different sites in the flow are the local methods. They will be briefly reviewed here.

Classical measuring techniques for velocity measurements are hot-wire and laser-Doppler anemometry (LDV). The former is older and despite its limitations (problems with calibration, restricted application due to limitations on the diameters of wire, etc.) is still used and capable of providing useful information, [102].

The LDV technique dates back to the early 1970's, and from then on its applications have seen a rapid increase. It requires optical access to the measuring sites (expensive modifications and reconstruction of apparatus are often unavoidable), and usually seeding of the flow. Although laser measurement equipment is expensive and demands expertise, this technique today represents the main research and development tool in flow measurements.

Various laser-based techniques have been developed for measuring scalar parameters of the flow; concentration can be measured by laser-induced fluorescence, Rayleigh and Raman scattering techniques, and temperature by the coherent anti-Stokes Raman scattering (CARS) method.

Particle velocities in dispersed two-phase flows can also be measured by LDV. Phase-Doppler anemometry (PDA), another laser-based technique, is used for particle size measurements. These techniques have important applications in spray measurements, providing data for better understanding of spray processes and their modelling. However, they can be used only in regions of low droplet number density (dilute regions), at the periphery of spray and far from the injector, because the dense-spray region is non-transparent to the laser beams.

Reviews of the measuring methods can be found in Arcoumanis and Whitelaw [14] and in a recent book by Taylor [201].

1.2 Previous and related studies

1.2.1 Processes in diesel engines

Internal combustion engines can be grouped, with respect to ignition, into two categories, namely, spark-ignition (SI) or Otto, and compression-ignition (CI) or diesel engines, and with respect to the number of strokes, into two-stroke and four-stroke engines. There are two main types of diesel engines; direct-injection type (DI), where the injection of fuel takes place in a chamber directly above the piston or in the bowl-in-piston chamber, and indirect-injection type (IDI) where the injection occurs in a separate chamber connected to the main chamber by a nozzle-type passage, Fig. 1.2. Diesels can be further classified into two groups; naturally aspirated engines, where atmospheric air is induced into the cylinders, and charged engines where the inlet air is compressed, either by an exhaust-driven compressors (turbocharged engines), or by the mechanically driven blower (supercharged engines), [100].

Although there are substantial differences between processes in SI and CI engines (preparation of the fuel-air mixture, ignition and combustion processes), their in-cylinder flows share the following common features:

- it is three-dimensional and unsteady with a rapid velocity changes,
- it is turbulent at all engine speeds, with a time-varying range of length scales, from the smallest dictated by the gas viscosity, to the largest limited by the cylinder dimension, and
- it is compressible, due to the time-varying cylinder volume.

In four-stroke engines, the engine cycle starts with the induction stroke in which a premixed charge, in the case of SI engines[2], or air, in the CI engines, is sucked into the cylinder. On its the fluid goes through the intake system consisting of the air filter, inlet manifold, intake ports and inlet valve openings (valve curtains). The main role of the inlet manifold is to uniformly distribute the flow to the intake

[2]In the case of port-injection SI engines, the intake air at the cylinder entrance, contains liquid fuel in the form of a spray.

ports with minimum pressure losses. The intake port's task is to distribute the fluid at the valve curtain, or in the case of swirl-producing ports (pre-valve swirl generation), to form a flow pattern at the valve curtain which has a substantial net angular momentum about the cylinder axis. The inlet valve opens and closes the inlet passage, and in the post-valve swirl generation designs, the inlet valve is specially shaped to discharge the flow tangentially toward the cylinder wall where it is deflected sideway forming a swirl motion. The valve cross section area and discharge coefficient vary with the valve movement. The swirl motion is used, in SI engines, to speed up the combustion process, and in diesels to promote mixing between the air and injected fuel. (In two-stroke engines it is alos used to improve scavenging). For a review of the various designs of intake ports and intake valves see for instance Heywood [100], and Arcoumanis and Whitelaw [14].

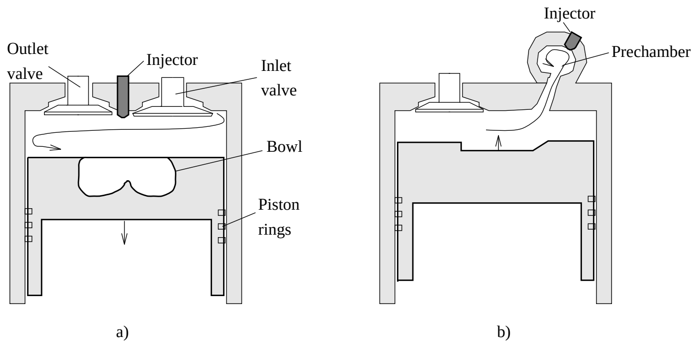

Figure 1.2: Types of diesel engines; a) Direct-injection, b) Indirect-injection

In order to maximise the engine volumetric efficiency (defined as the intake volume flow rate of the fluid divided by the rate at which volume is displaced by the piston, [100]), special care is paid to the design of manifold and intake ports to avoid any unnecessary restrictions to the flow and flow separations.

The following stage of the engine cycle is the compression stroke, during which the piston moves up, reducing the cylinder volume, and increasing gas density and temperature. The in-cylinder flow is subjected to substantial changes. In DI engines, the tangential (swirl) component of velocity in the bowl increases (according to the

law of conservation of angular momentum, since more gas mass is concentrated in the bowl, closer to the cylinder axis), and in IDI engines, a swirl in the prechamber starts, induced by the flow through a narrow connecting passage, Fig. 1.2b.

At some instant, usually a few CA degrees BTDC, injection of fuel takes place. The liquid fuel, usually injected at high velocity through one (IDI engines) or more injector holes (DI engines), interacts with the surrounding, high-pressure and high-temperature air and penetrates into the combustion chamber. The fuel vapourises and mixes with the air, and after a few crank angle degrees ignition delay, the fuel-air mixture spontaneously ignites and starts burning. The heat released by combustion increases the pressure and temperature in the cylinder, which pushes the piston toward the BDC producing a mechanical work (expansion stroke). Before the piston reaches BDC, the outlet valves starts opening. Burned gases exit the cylinder, firstly, due to the higher pressure in the cylinder than in the outlet port, and then by the piston displacement towards the TDC (exhaust stroke). With the exhaust stroke, the engine cycle is completed.

Even from this simplified description of the engine cycle, it can be seen that the diesel-engine processes are extremely complex; they are dependent on the cylinder geometry, in-cylinder gas parameters, injection system and fuel characteristics. The flow which begins as single-phase, but after the start of injection becomes two-phase, with a heterogeneous chemical composition, due to the local fuel evaporation, and steep gradients of all flow properties as a result of combustion. On addition, there is heat transfer between the in-cylinder gases and the chamber walls, as well as losses of the gas mass between the piston rings and cylinder liner.

Since this thesis deals with the multi-dimensional diesel spray predictions, in this section, only works related to the multi-dimensional engine calculations will be considered[3]. In the following section, a detailed review of approaches to the spray -gas modelling will be given.

The first multi-dimensional prediction method was developed by Watkins [217] who calculated laminar flow in an axisymmetric engine without valves. It was fol-

[3]A review of the phenomenological models can be found in Blumberg et al. [30], Watkins [217] and Heywood [100].

lowed by the works of Diwakar et al. [56], which made numerical predictions of the two-dimensional inviscid flow and temperature fields in engine with intake and outlet ports. Later Watkins [217] performed calculation of three-dimensional turbulent flow, and the group at the Los Alamos National Laboratory, [37] and [11], included a combustion calculations for the first time. Significant contributions to the modelling of turbulence in engines were made by El Tahry [60]. A number of further studies have been made; no attempt will be made to report them here since they are comprehensively reviewed in the works of Ahmadi-Befrui [6], Gosman [78] and Begleris [24]. However, reference will be to research at Imperial College; by Ahmadi-Befrui [6], Begleris [24] and Tsui [210], as well as that of Theodoropoulos [204], who deals with methodology employing unstructured meshes. The last mentioned is particularly relevant because in the present thesis the same numerical basis has been used and extended.

1.2.2 Approaches to the spray modelling

The gas-spray interactions comprise a number of processes such as atomisation, drop breakup, droplet collision and transfer of mass, momentum and energy between phases. Also, there are other phenomena which do not involve direct interaction with the gas phase, but influence or are affected by these interactions. The flow in injector nozzles and spray-wall interactions are examples of these. All of these processes have to be included in a complete model to properly simulate sprays in diesel engine chambers. This is achieved by assembling a number of submodels which describe particular processes. In this section, a summary of general approaches to the gas-spray modelling will be given. Detailed reviews of approaches to each particular phenomenon will be given in the introductory part of its description in the following chapters.

There are several theoretical methods of treating sprays and several ways to group these methods. One of the divisions, extracted from Faeth [68] and [69], applied to general dispersed flows (spray, particles and bubbles) is shown in Fig. 1.3. According to this, approaches to the multiphase flow description can be grouped into two main categories depending on the manner of treatment of the phases. The first

is the locally homogeneous treatment (LH) in which the multiphase flow is treated as a variable-property single phase flow. The LH treatment implies local kinematic and thermodynamic equilibrium (and this requires infinite interphase transfer rates) with density variations due to the variation of dispersed phase concentration. This approach was introduced by Thring and Newby, [205] and Newman and Brzustowski, [149]; the following later works made contributions: Shearer and Faeth [187], Khalil and Whitelaw [117], and Mao et al. [134]. This approach is limited to sprays with very small droplets, since only in this case the interphase transport rates are very high and almost assure the local kinematic and thermodynamic equilibrium. When applied to practical spray flows, the results obtained show significant discrepancies with measurements.

The second category comprises separated-flow methods, which model the phases separately and take into account the finite interphase transfer rates. The carrier phase is treated as a continuum, while the dispersed phase is described by either discrete or continuum formulations, Fig. 1.3. The continuum formulations can be further sub-divided into two branches depending on how the dispersed phase is treated. In one group the dispersed phase is treated as a second, co-existing, interpenetrating continuum (Harlow and Amsden [90], Bracco [33], Travis et al. [208] and others); and in the other, the dispersed phase is described by a multi-dimensional distribution function, Williams [223]. In the latter, a transport equation of the spray distribution function must be solved, which, since the distribution function is defined in a multi-dimensional space[4], requires large computer storage space and computational time (Haselman and Westbrook [93]).

The discrete formulations, often called discrete droplet methods (DDM) in the spray literature, are most widely used for the calculation of liquid sprays in diesel engines. The approach dates back to the mid-1950s in the aerospace industry (see Crowe [49] and Crowe et al. [51]), but the real breakthrough in its application was made in the early 1980s by the works of Dukowicz [58] and O'Rourke [162].

In discrete formulations, the spray is represented by a finite number of computa-

[4]The Williams statistical spray model, [223], defines a general spray distribution function in eight-dimensional space of droplet size, location, velocity and time. In [11] the domain is extended by the droplet temperature and fluctuating gas velocity.

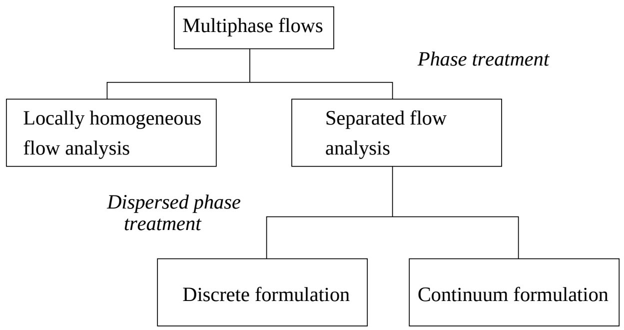

Figure 1.3: Approaches to multiphase flow modelling (from Faeth [68])

tional samples, each containing droplets possessing the same characteristics such as size, velocity, temperature etc. The motion and interactions of the sampled droplets with the surrounding gas are governed by ordinary differential equations using a Lagrangian formulation. The interphase transfer rates of mass, momentum and energy, which play major roles in these equations, are based on empirical correlations, so their accuracy affects the accuracy of the complete spray model. Therefore, special attention is paid to these correlations, in both theoretical and experimental investigations.

An important aspect of any spray model is the manner of its representation of turbulence effects on the droplet behaviour (turbulent diffusion of particles). In many early studies this effect was completely ignored (Gosman et al. [84]), or introduced in a deterministic way (Abbas et al. [1]). Later a more appropriate stochastic approach was proposed by Yuu et al. [226] and Dukowicz [58], and further developed by O'Rourke and Bracco [163], Amsden et al. [11], Gosman and Ioannides [83] and others. These methods require an estimate of the mean and turbulent properties of the continuous phase, and relevant length and time scales for particle trajectory calculations.

In the past 15 years substantial progress has been made in the development of models of other spray phenomena. Of particular note are the model of droplet collision by O'Rourke and Bracco [163], the model of droplet breakup by Reitz and Diwakar [178] and [179], of turbulence modulation by Mostafa and Mongia [146],

and Chen and Wood [40], and of spray-wall interactions by Naber and Reitz [148] and Watkins and Wang [218].

There are continual discussions among researchers regarding the advantages and disadvantages of the continuum and discrete formulations of spray. Comparisons of the performances of the two approaches are reviewed and discussed by many authors: Crowe [50], Gosman and Ioannides [83], Beshay et al. [28], Mostafa and Mongia [145] and others. Their conclusions can be summarised as follows. The disadvantages of the continuum approach are that it requires very fine spatial discretisation in the near-injector zone to resolve steep gradients of the spray properties and to avoid numerical diffusion, and that the spray equations must be solved in the whole solution domain. Numerical diffusion causes unrealistic distributions of the fuel vapour concentration and gas temperature which, in combustion simulations may lead to the wrong ignition location with consequences on the prediction of all other fields. These methods demand also large computer storage space. The discrete droplet formulation does not suffer from numerical diffusion and its calculation of the turbulent dispersion is more accurate ([50]). This is offset by the expensive tracing (in computational terms) of the large number of computational parcels needed to represent the spray. Nevertheless, the discrete droplet method is regarded as the most accurate for diesel spray calculations and is adopted in this study.

1.3 Present contributions

This study is concerned with the simulation of gas-spray behaviour in diesel engine conditions, excluding the ignition and combustion processes. It presents the author's contribution, which is only a part of the efforts made by a group of researchers at Imperial College during past decade to develop a comprehensive computational tool for the prediction of flow, spray-gas behaviour and combustion in diesel engines. It is also a continuation of a work done my predecessors et Imperial College in the spray area, Beshay, [27], Tabrizi, [200] and Zhang, [228]. Their contributions mainly relate to spray calculations on structured meshes; Tabrizi, [200] and Zhang, [228] have embedded spray calculation methodology in the EPISO solution procedure,

[24] and have introduced spray temporal subcycling procedure, while Zhang has developed the first version of a spray methodology for unstructured meshes.

The following specific contributions to diesel spray simulation have been made in this study:

- Application of two recently developed atomisation models, namely Huh's model [108], and a model developed at the Max Planck Institut in Göttingen (MPI), [158]. The first model assumes that the initial perturbations on the surface of liquid jet issuing from a nozzle have their origin in nozzle turbulence, and that their subsequent growth is caused by the aerodynamic forces at the gas-liquid interface. The second model combines the detailed representation of the nozzle flow and detachment of drops from the liquid jet emerging from the nozzle by aerodynamic forces, and collision between the large structures in the liquid core caused by differences in their velocities.

- Inclusion of a spray-wall interaction model developed at the Max Planck Institut, [156]. This model, based on a number of measurements, simulates three possible outcomes of droplet collision with a wall: drop sticking on the wall, drop breakup, and drop reflection from the wall.

- Simulation of turbulence modulation phenomena by inclusion of additional previously-devoid source terms in the k-ϵ turbulence model, extension of the predictor-corrector solution procedure to allow for these terms, and examination of the effects of modulation on spray and gas behaviour.

- Investigation of effects of different correlations proposed for the drop drag coefficient and coefficients in the drop breakup submodel.

- Restructuring of the EPISO solution procedure to incorporate the energy and fuel vapour continuity equations, and rearrangement of the solution sequence for its application to combustion calculations.

- Assessment of the overall method by reference to experimental data for spray injected into a quiescent pressure chamber and for two forms of DI diesel engine, and investigation of effects of mesh density on the predictions.

1.4 Thesis outline

In Chapter 2, the mathematical model of the gas phase is assembled, taking into account the presence of the dispersed phase (i.e. droplets). The derivation starts from the instantaneous transport equation for a general conserved property in coordinate-free integral form, for an arbitrary moving control volume. Then, this equation is density-weighted (Favre) ensemble-averaged, and the resulting additional terms are modelled via the k-ϵ turbulence model. Finally, the complete set of governing equations for gas are summarised, together with boundary and initial conditions.

In Chapter 3, a model of the discrete phase, i.e. the spray is presented. The discrete-droplet approach is used, in which each computational droplet represents a parcel of droplets of the same properties. The model comprises conservation Lagrangian equations in ordinary differential form for drop mass, momentum and energy, and submodels for atomisation, drop breakup, collision, and spray-wall interactions. Finally, the coupling source terms arising from the interactions between the droplets and gas are assembled.

Chapter 4 deals with the discretisation of the governing equations. It starts with a description of the basis of finite volume method employed for the discretisation of the gas transport equations, on general unstructured meshes and with a collocated variable arrangement, §(4.2). The discretised form of the general transport equation is given in §(4.3), and the full set of discretised gas governing equations is assembled in §(4.4). The Lagrangian spray equations are discretised in the first-order Euler-implicit fashion in §(4.5). As a result of this discretisation sets of simultaneous non-linear algebraic equations are obtained.

In Chapter 5, the solution procedure for solving the sets of discretised equations for the gas and spray is described. The solution procedure is split into two stages, the average thermodynamics calculation and the predictor-corrector calculation. The equations, apart from the turbulence model set, are temporarily decoupled by the EPISO algorithm, enabling sequential solution The equations are then linearised and solved by conjugate gradient methods. The turbulence equations are solved in their own predictor-corrector sequence, after the other flow equations.

Chapter 6 deals with the assessment of applied models and calculation procedure. The calculated results are compared against experiments for three situations: axisymmetric sprays injected into a pressure chamber and injection two types of DI optical engine. A comparison of the performance of the two atomisation models is given, and the effects of turbulence modulation and spray-wall interactions are examined.

Finally, in Chapter 7, the findings and conclusions are summarised, and suggestions for future research are given.

Chapter 2

Model of the gas phase

2.1 Introduction

The aim of this chapter is to set out a mathematical description of the in-cylinder behaviour of the gas phase in diesel engines, and provide a framework suitable for numerical solution. The mathematical description is based on the assumption that the fluid is a continuum, despite the presence of a liquid phase in the form of droplets, so that all the well-developed equations arising from the fundamental principles of conservation of mass, momentum and energy can be applied, Truesdell [209] and Bird et al. [29]. These equations are presented in an Eulerian frame, where the characteristic fluid properties are considered as continuous functions of space and time in an absolute frame of reference. An alternative description is provided by the Lagrangian formulation, in which the dependent variables are the characteristic properties of material particles that are followed in their motion; this description will be later used for the dispersed phase. Further assumptions are that the fluid obeys the Newtonian law of viscosity, Fourier law of conductivity, Fick law of diffusivity and an equation of state.

The mathematical model of the gas phase takes into account the following features of in-cylinder diesel processes:

- presence of liquid phase,
- momentum, heat and mass transfer between phases and at walls,

- multi-component composition of gas mixture, and
- time changing boundary of the solution domain.

All of these processes take place in a turbulent environment, where the field variables fluctuate about some average values with a wide range of length and time scales. To obtain a solution in these circumstances, the spatial and temporal discretisation of domain should be finer then the smallest scales[1]. This would result in an enormous number of discretised equations, whose solution would require computational and storage performances which exceed the limits of existing computers. The application of these methods is therefore restricted to provide new insight in turbulence, and data for development of turbulence models. A summary of these methods can be found in Reynolds [181].

In this study an alternative, widely-used statistical approach will be used, where the field variables are resolved into mean (average) and fluctuating components. The governing equations are then averaged in order to filter out small scale fluctuations and to obtain equations which describe behaviour of the mean field variables. The averaging procedure corresponds to the typical laboratory situation, in which measurements are taken at fixed locations in a statistically steady flow field, from which some mean, representative values are then extracted. However, because the overall features of in-cylinder flows repeat during each engine cycle, the only appropriate averaging technique is ensemble or phase averaging, defined as an average of a number of identically performed experiments; see Hinze [102] and Heywood [100]. Since the original equations are non-linear, the averaging of their non-linear terms generates additional (non-zero) statistical correlations, which have the form of the average of products of the fluctuating components of dependent variables. However, there is no direct way of knowing their magnitudes, therefore they must be modelled in terms of known quantities, or additional (transport) equations for these terms must

[1]The smallest length and time scales of a turbulent flow are the Kolmogoroff scales, η and η_t, respectively, Hinze [102]. Gosman [78] has shown that in an engine environment, their order of magnitudes are $\eta = O(10^{-4}D_b)$ and $\eta_t = O(10^{-4}\tau_C)$; D_b and τ_C stand for the bore diameter and engine cycle period, respectively. See also measurements of turbulence scales by Fraser and Bracco, [73] and [74] .

be derived. In the latter approach, because of the inherited non-linearity of these new equations, higher order correlations will appear, which again need modelling or further equations. This problem of providing additional turbulence parameter equations, which when solved with the averaged flow equations simulates the flow behaviour, is known in the literature as a closure problem, [122].

Generally, the closure problem can be approached by:

- models based on the Boussinesq hypothesis, [32], often referred to as or 'eddy' viscosity models, and
- Reynolds stress models (RSM).

The methods of the first group range from algebraic models to different variations of two-equation differential models; see Launder and Spalding [122]. These models have been widely used in the calculation of turbulent flows. The models of the second group are of much higher complexity. They require solution of seven or more differential equations, and have been less frequently used in engineering calculations.

In the present study, the two-equation k-ϵ turbulence model is applied. With these additional 'turbulence' equations the total number of equations is equal to the number of unknowns, and with the given initial and boundary conditions, the system is completely determined.

Because all the equations of conservation (transport) of mass, momentum, energy and chemical species are of similar form, the presentation in the following section begins with a general transport equation for a general variable ϕ, for single-phase flow. This equation will be given in an integral form, for an arbitrary moving control volume. Then, the presence of liquid phase will be taken into account, and averaging will be performed, yielding the final form of the general transport equation. This will provide basis for all averaged equations needed for the flow description. In section §(2.3) these equations, along with the required constitutive relations, will be assembled.

The initial and boundary conditions are considered in §(2.4). Four types of boundary conditions are examined: inflow/outflow boundaries, symmetry planes, cyclic boundaries, and walls. Since the presence of walls causes steep gradients in the nearby flow properties, special treatment is needed at these boundaries. In this study, the 'wall function' approach (Jones and Launder [115]) is used, in which the flow conditions at the walls are linked with those in the interior of the solution domain via algebraic expressions.

Transfers of mass, momentum and energy between the gas and spray are represented in transport equations by additional source terms. Their complete expressions will be given in the following chapter.

2.2 General transport equation

2.2.1 Instantaneous transport equation

In an Eulerian description of a single-phase flow, the conservation of a transferable property ϕ, defined per unit mass, in an arbitrary moving spatial region of volume V bounded by a closed surface S, Fig.2.1 reads, [209],:

$$\underbrace{\frac{d}{dt}\int_V \hat{\rho}_m \hat{\phi}\, dV}_{I} + \underbrace{\int_S d\mathcal{S}\cdot \hat{\rho}_m(\hat{\mathbf{u}}-\mathbf{u}_b)\hat{\phi}}_{II} = \underbrace{-\int_S d\mathcal{S}\cdot \hat{\rho}_m \hat{\mathbf{q}}_m^{\phi}}_{III} + \underbrace{\int_V \hat{s}_\phi\, dV}_{IV} \tag{2.1}$$

where ρ_m represents the microscopic fluid density, $\mathbf{u}$ is the fluid velocity, $\mathbf{u}_b$ is the velocity of the boundary of the volume V; $\hat{\mathbf{q}}_m^{\phi}$ is the molecular diffusivity flux vector (or if ϕ is a vector, $\hat{\mathbf{q}}_m^{\phi}$ stands for a second-order tensor, a case which will be addressed later on), and s_ϕ stands for the volumetric source of the property ϕ, per unit time. The hat sign, $\hat{}$, over symbols denotes the instantaneous values of these quantities. The four terms in this equation are the transient term (I), the convection term (II), the diffusion term (III), and the source term (IV), respectively.

To simplify notation, from now on, the relative velocity $\hat{\mathbf{u}}_r$ defined as:

$$\hat{\mathbf{u}}_r = \hat{\mathbf{u}} - \mathbf{u}_b \tag{2.2}$$

will be introduced. It is important to note that the considered control volume must obey the so-called 'space conservation law', Demirdzic [55], which reads:

$$\frac{d}{dt}\int_V dV = \int_S d\mathcal{S}\cdot \mathbf{u}_b \tag{2.3}$$

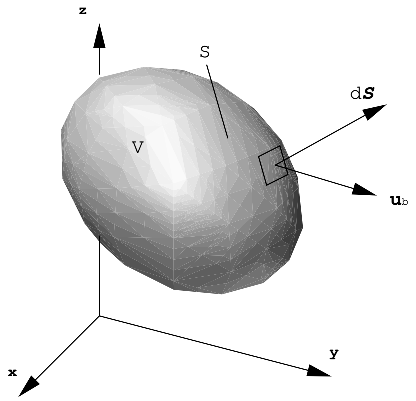

Figure 2.1: Control volume.

Eqs.(2.1) and (2.3) represent the general conservation law of a property ϕ in an arbitrary moving control volume. In Eq.(2.1), ϕ can stand for a tensor quantity of an arbitrary order. In that case, s_ϕ is the tensor of the same order as ϕ. It has to be emphasized again that above equations are strictly valid only for single-phase flow. With further assumptions, and by introducing a new field variable, their application can be extended to the two-phase flows. This is the subject of the following section.

2.2.2 Effects of the dispersed phase

The presence of a dispersed liquid phase affects the gas phase in two primary ways. The first is the transfer of property ϕ between the phases; this could be the transfer of mass, momentum or energy. This contribution to the gas phase will be represented by an additional source term, s_ϕ^d in Eq.(2.1), which represents the rate of exchange of property ϕ between phases per unit volume. The second effect is the reduction of space available to the gas phase due to the presence of spray. In other words, the liquid phase occupies space which would otherwise be occupied by the gas, thus displacing it. This phenomenon is handled by the introduction of the void fraction ϑ, Travis et al. [208], defined as:

$$\vartheta(\mathbf{x},t) = \lim_{\delta V \to \delta V^*} \frac{\delta V(\mathbf{x},t) - \delta V_l(\mathbf{x},t)}{\delta V(\mathbf{x},t)} \tag{2.4}$$

where $\delta V(\mathbf{x},t)$ is the volume enclosing a point $\mathbf{x}$ at time t, $\delta V_l(\mathbf{x},t)$ is the volume of liquid phase inside δV and δV^* represents the smallest volume for which the ratio, Eq.(2.4), approaches a definite limit asymptotically. When this concept is applied to the general transport equation, Eq.(2.1), it takes the following form, Soo [191]:

$$\frac{d}{dt}\int_V \hat{\rho}\hat{\phi}\, dV + \int_S d\mathcal{S}\cdot \hat{\rho}\hat{\mathbf{u}}_r\hat{\phi} = -\int_S d\mathcal{S}\cdot \hat{\rho}\hat{\mathbf{q}}_m^{\phi} + \int_V (\hat{s}_\phi + \hat{s}_\phi^d)\, dV \tag{2.5}$$

in which $\hat{\rho}$, usually called the apparent or macroscopic density, is defined by:

$$\hat{\rho} = \hat{\rho}_m\hat{\vartheta} \tag{2.6}$$

In the next section, the averaging of Eq.(2.5) will be considered.

2.2.3 Ensemble averaging

The selection of averaging methods depends on the characteristics of turbulent flow, and according to Hinze [102], the following three averaging method can be distinguished:

1. Time averaging for a stationary turbulence,
2. Space averaging for a homogeneous turbulence,
3. Ensemble averaging for a series of identical experiments.

All these methods can appear in two versions, unweighted (Reynolds) and weighted. (Conditional averaging, [130] and [57], can be considered as the special case of weighted averaging). Among the latter methods, the density-weighted averaging suggested by Favre, [71], and later on named after him, has some features which favour its application to compressible flows and flows with combustion, i.e.:

- It keeps the number of additional terms to a minimum in the way that all first-order correlations between the Favre fluctuating components and instantaneous density are equal to zero; and
- The physical interpretation of particular terms in averaged transport equations is clearer and the resulting (final) form of the equations is similar to the original form.

As was mentioned in the introduction, the only appropriate averaging technique for transforming instantaneous equations into the averaged ones, in the context of unsteady sprays, is ensemble-averaging. Taking into account the aforementioned features of the density-weighted averaging, in this study, density-weighted ensemble-averaging technique is used.

However, the density-weighted averaging technique presents a problem in the extraction of unweighted quantities from the weighted predictions or measurements, when corresponding unweighted data are available for comparison (for instance, velocities measured with LDA are regarded as the Reynolds averages, as opposed to those measured by a hot-wire technique, [102]). In these cases, the unweighted values are calculated from Eqs.(A.5)[2], and, as can be seen from these relations, an additional correlation has to be known.

As originally proposed, the Reynolds and Favre ensemble-averaging techniques operate as follows. Let $\hat{\rho}_m(\mathbf{x},t)$ and $\hat{\phi}(\mathbf{x},t)$ represent the instantaneous values of microscopic density and any other variable at the location $\mathbf{x}$ and time t, respectively. Then $\hat{\phi}(\mathbf{x},t)$ can be decomposed into two components:

for **Reynolds** averaging by:

$$\hat{\phi}(\mathbf{x},t) \;=\; \overline{\phi}(\mathbf{x},t) \;+\; \phi'(\mathbf{x},t) \tag{2.7}$$

and for **Favre** averaging by:

$$\hat{\phi}(\mathbf{x},t) \;=\; \widetilde{\phi}(\mathbf{x},t) \;+\; \phi''(\mathbf{x},t) \tag{2.8}$$

Here, $\phi'(\mathbf{x},t)$ and $\phi''(\mathbf{x},t)$ denote the fluctuations about the Reynolds, $\overline{\phi}(\mathbf{x},t)$, and Favre, $\widetilde{\phi}(\mathbf{x},t)$ mean values, defined as:

$$\overline{\phi}(\mathbf{x},t) \;=\; \lim_{N\to\infty}\frac{1}{N}\sum_{i=1}^{N}\hat{\phi}(\mathbf{x},t+i\tau_C) \tag{2.9}$$

$$\widetilde{\phi}(\mathbf{x},t) \;=\; \frac{1}{\overline{\rho}_m(\mathbf{x},t)}\lim_{N\to\infty}\frac{1}{N}\sum_{i=1}^{N}\hat{\rho}_m(\mathbf{x},t+i\tau_C)\,\hat{\phi}(\mathbf{x},t+i\tau_C) \tag{2.10}$$

[2] Given in Appendix A.1

The last equation can be expressed, via Eq.(2.9), by:

$$\tilde{\phi}(\mathbf{x},t) = \frac{1}{\overline{\rho}_m(\mathbf{x},t)}\,\overline{\hat{\rho}_m(\mathbf{x},t)\hat{\phi}(\mathbf{x},t)} \tag{2.11}$$

In Eqs.(2.9) and (2.11) τ_C is the time period of an engine cycle, $\overline{\rho}_m(\mathbf{x},t)$ is the Reynolds mean of density, and N is the number of identically performed experiments (equivalent, in the engine case, to the number of engine cycles). The above formula can be applied directly to the equations which describe single-phase flow, see for example Begleris [24].

In gas-spray flows, the situation is more complex since both microscopic density and void fraction fluctuate about their mean values. Therefore, it is necessary to consider how to accommodate this during averaging procedure. This can either be done by treating $\hat{\vartheta}$ as any other field variable, i.e. by calculating its Favre mean $\tilde{\vartheta} = (\overline{\hat{\rho}_m\hat{\vartheta}})/\overline{\rho}_m$, or by taking the previously introduced apparent density, $\hat{\rho} = \hat{\rho}_m\hat{\vartheta}$, as a new weighting quantity. The latter is our present choice, because it gives simpler averaged equations, and, apart from few terms, ϑ does not (explicitly) appear in these equations. However, this requires redefinition of the Favre mean value, as follows:

$$\tilde{\phi} = \frac{1}{\overline{\rho}}\,\overline{\hat{\rho}\,\hat{\phi}} \tag{2.12}$$

where

$$\overline{\rho} = \overline{\hat{\rho}_m\hat{\vartheta}} \tag{2.13}$$

In Eqs.(2.12) and (2.13), the symbols $\mathbf{x}$ and t are omitted. Other useful relations which link Reynolds and Favre averaged quantities can be found in Appendix A.1.

During averaging of the transport equations, there will be terms where the void fraction multiplies some field variable (for instance a term $\hat{\vartheta}\nabla\hat{p}$ in the instantaneous gas momentum conservation equation). In these cases, averaging will produce new unknown correlations like $\overline{\vartheta'\nabla p'}$, involving fluctuating components of the void fraction and this variable. These correlations need to be expressed in terms of known quantities, so further modelling would be required. Since there is no general approach to the modelling of these terms, at least to the knowledge of this author, and following the practice in [200], these correlations will be omitted.

2.2.4 Favre-averaged transport equation

When the instantaneous equation, Eq.(2.5), is subjected to density-weighted ensemble averaging, the result is:

$$\begin{aligned} \frac{d}{dt}\int_V \overline{\rho}\tilde{\phi}\,dV + \int_S d\mathcal{S}\cdot\overline{\rho}\tilde{\mathbf{u}}_r\tilde{\phi} &= -\int_S d\mathcal{S}\cdot(\overline{\rho}\,\tilde{\mathbf{q}}^{\phi}_m + \overline{\hat{\rho}\phi''\mathbf{u}''}) + \\ &+ \int_V (\overline{s}_\phi + \overline{s}^d_\phi)\,dV \end{aligned} \tag{2.14}$$

As is the case with all non-linear terms, their averaging produces additional unknown correlations, in this case $\overline{\hat{\rho}\phi''\mathbf{u}''}$. This term represents the turbulent diffusion flux of ϕ, and must be known in order to close the set of equations.

At this point a distinction will be made depending on the scalar/vector nature of ϕ, because the diffusion terms $\overline{\rho}\tilde{\mathbf{q}}^{\phi}_m$ and $\overline{\hat{\rho}\phi''\mathbf{u}''}$ then have essentially different forms. Firstly, the case when ϕ is a scalar will be considered.

2.2.5 Scalar transport equation

In this case, with respect to our assumption mentioned in §2.1 that the fluid obeys Fourier/Fick's law of diffusivity, the instantaneous diffusion term can be expressed as, [29]:

$$\hat{\rho}\hat{\mathbf{q}}^{\phi}_m = -\hat{\rho}\hat{\Gamma}_\phi\nabla\hat{\phi} \tag{2.15}$$

where $\hat{\Gamma}_\phi$ is the coefficient of molecular (kinematic) diffusivity. After averaging, and neglecting fluctuations of $\hat{\Gamma}_\phi$, which is justifiable on the ground that the fluctuations of $\hat{\Gamma}_\phi$ for non-reacting flows are small, [220], this term reads:

$$\overline{\hat{\rho}\hat{\mathbf{q}}^{\phi}_m} = -\overline{\rho}\Gamma_\phi\nabla\tilde{\phi} \tag{2.16}$$

The term which represents the turbulent diffusion, is modelled by assuming an analogy between molecular and turbulent motion (the Boussinesq turbulent viscosity hypothesis,[32]), as:

$$-\overline{\hat{\rho}\phi''\mathbf{u}''} = \overline{\rho}\Gamma_{\phi,t}\nabla\tilde{\phi} \tag{2.17}$$

where $\Gamma_{\phi,t}$ is the turbulence or eddy (kinematic) diffusion coefficient which, in contrast to the molecular coefficient, is not a fluid property but depends on the local state of turbulence.

The sum of these two diffusion fluxes yields:

$$\overline{\hat{\rho}\hat{\mathbf{q}}_m^{\phi}} + \overline{\hat{\rho}\phi''\mathbf{u}''} = -\overline{\rho}\Gamma_{\phi,eff}\nabla\tilde{\phi} \tag{2.18}$$

where

$$\Gamma_{\phi,eff} = \Gamma_{\phi} + \Gamma_{\phi,t} \tag{2.19}$$

Here, $\Gamma_{\phi,eff}$ stands for the effective diffusivity, which allows for the combined molecular and turbulence transport of property ϕ.

By substituting Eq.(2.17) into Eq.(2.14) the averaged general transport equation reads:

$$\frac{d}{dt}\int_V \overline{\rho}\tilde{\phi}\, dV + \int_S d\mathcal{S}\cdot\overline{\rho}\tilde{\mathbf{u}}_r\tilde{\phi} = \int_S d\mathcal{S}\cdot\overline{\rho}\;\Gamma_{\phi,eff}\nabla\tilde{\phi} + \int_V (\overline{s}_\phi + \overline{s}_\phi^d)\, dV \tag{2.20}$$

The diffusivity coefficient $\Gamma_{\phi,eff}$ is usually expressed in terms of the effective viscosity (see §(2.2.6)) and Prandtl/Schmidt number (regarded as constant), determined from experiments. Values of Prandtl/Sdhmidt numbers for all the scalar variables are given in Table 2.1, [24].

For convenience, the symbols ¯ and ˜ in Eq.(2.20) will be omitted from now on, so its final form reads:

$$\frac{d}{dt}\int_V \rho\phi\, dV + \int_S d\mathcal{S}\cdot\rho\mathbf{u}_r\phi = \int_S d\mathcal{S}\cdot\rho\;\Gamma_{\phi,eff}\nabla\phi + \int_V (s_\phi + s_\phi^d)\, dV \tag{2.21}$$

$\Gamma_{\phi,eff} = \frac{\nu_{eff}}{\sigma_\phi}$				
ϕ	Y_{ft}	e	k	ϵ
σ_ϕ	0.9	0.64	1.0	1.2

Table 2.1: Prandtl-Schmidt numbers

2.2.6 Vector transport equation

In the present mathematical model of the continuous phase, only one conservation equation of a vector variable will be considered, namely the momentum conservation

equation. Then ϕ stands for the velocity field, $\mathbf{u}$, and $\hat{\rho}\hat{\mathbf{q}}_m^{\mathbf{u}}$, in Eq.(2.5) (or its averaged counterpart in Eq.(2.14), $\overline{\rho}\;\tilde{\mathbf{q}}_m^{\mathbf{u}}$) represents the molecular stress tensor.

For Newtonian (single-phase) fluids the instantaneous molecular stress tensor is defined as, [29]:

$$\hat{\rho}_m\hat{\mathbf{q}}_m^{\mathbf{u}} = -\hat{p}\,\mathbf{I} + \hat{\mathbf{T}}_m \tag{2.22}$$

where p is the thermodynamic pressure, $\mathbf{I}$ is the tensor unit, and $\mathbf{T}_m$ is the molecular shear stress tensor given by:

$$\hat{\mathbf{T}}_m = \hat{\rho}_m\;(\;2\hat{\nu}_m\hat{\mathbf{D}} - \frac{2}{3}\,\hat{\nu}_m\nabla\cdot\hat{\mathbf{u}}\,\mathbf{I}\;) \tag{2.23}$$

In this equation ν_m is the molecular kinematic viscosity, and $\mathbf{D}$ is the rate-of-strain (deformation) tensor:

$$\hat{\mathbf{D}} = \frac{1}{2}\,[\,\nabla\hat{\mathbf{u}} + (\nabla\hat{\mathbf{u}})^T\,] \tag{2.24}$$

In the presence of the second phase, the void fraction multiplies the stress tensor (Eq.(2.5)), so the complete force exerted on a fluid in the control volume due to the stress tensor, obtained by the integration over the entire control volume and by applying the Gauss divergence theorem on the pressure term, becomes:

$$\int_S d\mathcal{S}\cdot\hat{\vartheta}(-\hat{p}\,\mathbf{I} + \hat{\mathbf{T}}_m) = -\int_V \nabla(\hat{\vartheta}\,\hat{p})\, dV + \int_S d\mathcal{S}\cdot\hat{\vartheta}\;\hat{\mathbf{T}}_m \tag{2.25}$$

The integrand of the first term on the RHS of Eq.(2.25), $\nabla(\hat{\vartheta}\,\hat{p})$ can be resolved as:

$$\nabla(\hat{\vartheta}\,\hat{p}) = \hat{\vartheta}\nabla\hat{p} + \hat{p}\nabla\hat{\vartheta} \tag{2.26}$$

and the last term in the above equation is discarded on a reasoning that its presence would violate equilibrium for an inhomogeneous droplet distribution in the absence of gravity, see Harlow and Amsden [90][3].

Substituting Eqs.(2.23) and (2.24) into Eq.(2.25), taking into account the above, and its averaging, the following final form is obtained:

$$\int_S d\mathcal{S}\cdot\overline{\hat{\vartheta}(-\hat{p}\,\mathbf{I} + \hat{\mathbf{T}}_m)} = -\int_V \overline{\vartheta}\nabla\overline{p}\, dV + \int_S d\mathcal{S}\cdot\tilde{\mathbf{T}}_m \tag{2.27}$$

[3] This is well-known problem of transforming a surface or volume integrals over a single phase to integrals over the entire control volume. In the cited paper (and in the paper by Travis et al. [208]) the authors, by employing a statistical distribution function for the dispersed phase, argue that the term $p\nabla\vartheta$ does not exist if the dimensions of particles are small compared to the scale of pressure variations in the continuous phase.

where $\widetilde{\mathbf{T}}_m$ is defined as:

$$\widetilde{\mathbf{T}}_m = \overline{\rho}\,(\,2\nu_m\widetilde{\mathbf{D}} - \frac{2}{3}\,\nu_m\nabla\cdot\tilde{\mathbf{u}}\,\mathbf{I}\,) \tag{2.28}$$

$$\widetilde{\mathbf{D}} = \frac{1}{2}\,[\,\nabla\tilde{\mathbf{u}} + (\nabla\tilde{\mathbf{u}})^T\,] \tag{2.29}$$

In the above expressions, the fluctuation of ν_m is neglected on the same grounds as was neglected fluctuation of the scalar diffusivity in the previous section.

The turbulent diffusion term, $\overline{\hat{\rho}\mathbf{u}''\mathbf{u}''}$ (the momentum counterpart to $\overline{\hat{\rho}\phi''\mathbf{u}''}$, which appears as a result of the averaging of instantaneous convective term, see Appendix A.2.2), is a tensor, usually called the Reynolds stress tensor. In analogy with the molecular stress tensor, this tensor, which now includes the normal and shear components, is modelled according to:

$$\mathbf{T}_t = \overline{\rho}\,(\,2\nu_t\widetilde{\mathbf{D}} - \frac{2}{3}\nu_t\nabla\cdot\tilde{\mathbf{u}}\,\mathbf{I}\,) - \frac{2}{3}\overline{\rho}\,\tilde{k}\,\mathbf{I} \tag{2.30}$$

Here ν_t is the turbulent or eddy (kinematic) viscosity, which will be given in §(2.3.4) by Eq.(2.46), while k denotes the kinetic energy of turbulence, defined as:

$$\tilde{k} = \frac{1}{2}\,\widetilde{\mathbf{u}''\cdot\mathbf{u}''} \tag{2.31}$$

The sum of the molecular shear stresses and Reynolds stresses yields:

$$\widetilde{\mathbf{T}}_m + \mathbf{T}_t = \overline{\rho}\left[\,\nu_{eff}\,(2\widetilde{\mathbf{D}} - \frac{2}{3}\nabla\cdot\tilde{\mathbf{u}}\,\mathbf{I}) - \frac{2}{3}\,\tilde{k}\,\mathbf{I}\,\right] \tag{2.32}$$

where ν_{eff} is the effective viscosity, which combines molecular and turbulence transport, defined as:

$$\nu_{eff} = \nu_m\ +\ \nu_t \tag{2.33}$$

The momentum transport equation, i.e. the case when $\phi = \mathbf{u}$, will be given in §(2.3.2).

2.2.7 Favre-averaged constitutive relations

The working fluid is assumed to behave as an ideal gas, thus the gas state parameters - pressure, density and temperature (p, ρ_m, and T) obey the ideal gas law:

$$\hat{p} = \hat{\rho}_m\hat{R}\hat{T} \tag{2.34}$$

where R is the individual gas constant which depends on the gas composition. Assuming that the gas constant fluctuations due to the fluctuating gas composition are small and can be neglected, favre-ensemble averaging of the above equation yields:

$$\overline{p} = \overline{\rho}_m\overline{R}\,\tilde{T} \tag{2.35}$$

The caloric equation links the gas internal energy with the gas temperature via the specific heat capacity c_v. In the present case c_v depends on the gas temperature and composition, represented by the mass fractions (Y_α) of the α gas components Y_α, i.e. $c_v = c_v(Y_\alpha, T)$, so the instantaneous gas internal energy is as follows:

$$\hat{e} = \hat{c}_v\,(\hat{T} - T_{ref}) \tag{2.36}$$

where $\hat{c}_v = c_v(\hat{Y}_\alpha, \hat{T})$, and T_{ref} is the reference temperature. Favre-ensemble averaging of Eq.(2.36) gives:

$$\tilde{e} = \tilde{c}_v\,(\tilde{T} - T_{ref}) \tag{2.37}$$

where:

$$\tilde{c}_v = c_v\,(\tilde{Y}_\alpha, \tilde{T}) \tag{2.38}$$

In Eq.(2.37), it is taken that the correlation $\overline{\hat{\rho}\,c_v''\,T''}$ is small and can be neglected.

The other constitutive relations - Fourier's law of heat conduction, Fick's law of diffusion, and Newton's law of viscosity, were described in the previous section (§(2.2.5) and §(2.2.5)) and will not be repeated here.

2.3 Governing equations

2.3.1 Mass conservation equation

The gas phase in diesel engines is a mixture of various components. Since the total mass of gas in the cylinder, despite chemical reactions, can not be created or destroyed, it can only be changed by some external source or sink. In the present case, the vapourisation (or condensation) of the fuel, represents this 'source'. Thus, the mass conservation equation of the mixture is given by:

$$\frac{d}{dt}\int_V \rho\,dV + \int_S d\mathcal{S}\cdot\rho\mathbf{u}_r = \int_V s^d\,dV \tag{2.39}$$

where s^d is the rate of change in vapour mass by evaporation (or condensation) per unit control volume.

Since the evaporation and chemical reactions change the composition of mixture, the mass conservation equations of individual components must also be considered. Generally, the mass-conservation equation of the component α, where s_{Y_α} stands for its mass consumption/production rate per unit volume, reads ([224] and [191]):

$$\frac{d}{dt}\int_V \rho Y_\alpha \, dV + \int_S d\mathcal{S}\cdot \rho \mathbf{u}_r Y_\alpha = \int_S d\mathcal{S}\cdot \rho \Gamma_{Y_\alpha,eff} \nabla Y_\alpha + \int_V s_{Y_\alpha} \, dV \tag{2.40}$$

Here Y_α is the mass fraction of α defined as the ratio of the mass of that component per unit mass of mixture, i.e. :

$$Y_\alpha = \frac{\rho_\alpha}{\rho} \tag{2.41}$$

where ρ_α is the partial density of considered component.

In describing the composition of a non-reacting mixture, composed of air and a single-component fuel, just one additional field variable is required, here taken as the fuel vapour mass fraction, Y_{ft}. Its conservation equation is:

$$\frac{d}{dt}\int_V \rho Y_{ft} \, dV + \int_S d\mathcal{S}\cdot \rho \mathbf{u}_r Y_{ft} = \int_S d\mathcal{S}\cdot \rho \Gamma_{Y_{ft},eff} \nabla Y_{ft} + \int_V s_{Y_{ft}} \, dV \tag{2.42}$$

where $s_{Y_{ft}} = s^d$ is the spray evaporation rate per unit volume.

2.3.2 Momentum conservation equation

Following from Eqs.(2.14), (2.27) and (2.30), the momentum conservation equation can be expressed as follows, [208] and [90]:

$$\begin{aligned} \frac{d}{dt}\int_V \rho \mathbf{u} \, dV + \int_S d\mathcal{S}\cdot \rho \mathbf{u}_r \mathbf{u} \;&=\; -\int_V \vartheta \nabla p \, dV + \\ &+ \int_S d\mathcal{S}\cdot (\mathbf{T}_m + \mathbf{T}_t) + \\ &+ \int_V \mathbf{s}^d_{\mathbf{u}} \, dV \end{aligned} \tag{2.43}$$

In this equation $\mathbf{s}^d_{\mathbf{u}}$ is the rate of momentum exchange between the droplets and the gas phase per unit volume, while p, $\mathbf{T}_m$ and $\mathbf{T}_t$ have already been defined in §(2.2.4). Note here that gravity is neglected, since its effect is negligible compared to inertia and viscous forces, White [220].

The molecular shear stress and Reynolds stress tensors were defined in §(2.2.4) by Eqs.(2.28) and (2.30). With these relations, Eq.(2.43) can be recast into:

$$\begin{aligned} \frac{d}{dt}\int_V \rho \mathbf{u} \, dV + \int_S d\mathcal{S}\cdot \rho \mathbf{u}_r \mathbf{u} \;&=\; -\int_V \vartheta \nabla p \, dV + \\ &+ \int_S d\mathcal{S}\cdot \rho \left[\nu_{eff} \left(2\mathbf{D} - \frac{2}{3}\nabla\cdot\mathbf{u}\,\mathbf{I}\right) - \frac{2}{3} k\,\mathbf{I} \right] + \\ &+ \int_V \mathbf{s}^d_{\mathbf{u}} \, dV \end{aligned} \tag{2.44}$$

2.3.3 Energy conservation equation

The energy conservation equation is given here in term of the internal specific energy, e. In the absence of body forces it reads, [191]:

$$\begin{aligned} \frac{d}{dt}\int_V \rho e \, dV + \int_S d\mathcal{S}\cdot \rho \mathbf{u}_r e &= \int_S d\mathcal{S}\cdot \rho \Gamma_{e,eff} \nabla e \\ &+ \int_V \left(-\vartheta p \nabla\cdot\mathbf{u} + s_e + s^d_e\right) \, dV \end{aligned} \tag{2.45}$$

Here, the term $\vartheta p \nabla\cdot\mathbf{u}$ represents the rate of work done on gas by pressure forces per unit volume; s_e is the rate of heat generation by chemical reactions, and s^d_e is the rate of heat exchange between the gas and spray. Both quantities are expressed per unit volume.

In the above equation terms representing molecular shear work and the work of Reynolds stresses are neglected due to their small contribution to the overall energy balance, see Appendix A.2.3. Also, the heat transferred by radiation is neglected on the ground that the droplets are very small and, in the cases where combustion is not present (the only cases which will be considered here, i.e. $s_e = 0$), the temperature differences between the droplets and surrounding air are not so high as in the case with combustion. Even then, i.e. in combustion case, according to [25] and [67], radiation can be neglected since gaseous spectral radiation bands are generally not coincident with absorption bands of most liquid fuels[4].

[4] There are cases when the radiation must be considered; when some absorbing particles are present in the fuel, or when the soot is present in the flow, [67].

2.3.4 Turbulence model

The main classes of turbulence modelling approaches were mentioned in §(2.1), where it was concluded that k-ϵ model still provides the optimum solution for practical engineering calculations. Some 'arbitrariness' in disregarding particular terms in the k-ϵ equations, and different values of model coefficients, result in a number of 'versions' of the model; see Ahmadi-Befrui [7]. The model was first used in predictions of in-cylinder flows by Watkins [217], and from then on by a number of researchers; Syed and Bracco [199], Moler and Mansour [143], El Tahry [60], Ahmadi-Befrui [6], and others.

The model adopted in this study is a Favre-averaged version of that presented by Ahmadi-Befrui [6] (which takes into account effects of compression reported by El Tahry [60]) extended to two-phase flows. Also, the model is expanded with additional source terms to allow for turbulence modulation, i.e. for so-called direct effects the spray creates on turbulence properties of the gas, [69]. The turbulence modulation excludes effects created by the spray modifying the mean gas velocity (often called an 'indirect' effect) with consequences on the processes of generation and dissipation in turbulence, comprising phenomena such as turbulence in a wake of drops and modified local shear stresses in the gas by the interaction between drops and turbulent eddies [101]. Although current understanding of these phenomena is incomplete, they are included in the turbulence model to investigate their effects on the total gas-spray behaviour.

This section is divided into four parts. The first part deals with the basis of the k-ϵ model. In the second part, a review of efforts to understand processes involved in the turbulence modulation and to include them in turbulence models is presented; it is concluded with a discussion of how these works relate to diesel sprays. The last two parts comprise the transport equations for turbulence kinetic energy and its dissipation, extended with additional spray-related terms which accounts for the turbulence modulation; the derivation is given in Appendix A.2.4.

Basis of the k-ϵ model

A form of k-ϵ model was first proposed by Harlow and Nakayama [91], and later versions were proposed by Jones and Launder ([114], [115]), and Hanjalić [89] among others. The present 'standard' form was given by Launder and Spalding [123], and the particular version employed here is that of El Tahry [60] and Ahmadi-Befrui [6].

The model is based on the Boussinesq turbulent viscosity hypothesis (see §(2.2.5) and (2.2.6)), which assumes that the turbulent scalar fluxes and turbulent stresses can be expressed by Eqs.(2.17) and (2.30), where $\Gamma_{\phi,t}$ is the turbulent diffusivity and ν_t is the kinematic eddy viscosity. The latter is evaluated from:

$$\nu_t = C_\mu \frac{k^2}{\epsilon} \tag{2.46}$$

where k stands for the turbulence kinetic energy (defined by Eq.(2.31)), and ϵ represents its dissipation rate, defined as:

$$\epsilon = \frac{1}{\rho} \overline{\mathbf{T}'_m : \nabla \mathbf{u}''} \tag{2.47}$$

where $\mathbf{T}'_m$ stands for the fluctuating component of molecular shear stress tensor, Eq.(2.23). The values of k and ϵ are calculated from their own transport equations which will be given at the end of this section.

A turbulent diffusivity $\Gamma_{\phi,t}$ is expressed in terms of the turbulent Prandtl/Schmidt number, $\sigma_{\phi,t}$ and eddy viscosity as:

$$\Gamma_{\phi,t} = \frac{\nu_t}{\sigma_{\phi,t}} \tag{2.48}$$

The Prandtl/Schmidt numbers are determined from experiments and assumed constant (see §(2.2.5)); their values for all the scalar variables used in this study can be found in Table 2.1.

Spray contributions to turbulence

The nature of interactions between the continuous phase and the dispersed phase are rather complex and not well understood at present. It is well known that even relatively small amounts of dispersed particles can cause a significant change in the turbulence structure of the continuous phase; Goldschmidt and Eskinazi [75], Hestroni and Sokolov [99], Tsuji and Morikawa [211], Tsuji et al. [212]. A number of reasons, as will be summerised below, have been postulated for this behaviour. They are: the inability of the particles to follow the fluid motion due to their inertia; the resistance of particles to continuos deformation experienced by the surrounding fluid; and the effects of different initial velocity between phases so the additional shear forces appear with the impact on the turbulence structure. Some experiments have shown a reduction in turbulence intensity with increased dispersed phase fraction; others enhancement or even negligible effects; see Faeth [69]. These changes of gas turbulence intensity can be explained by considering whether the dispersed phase is moving faster or slower than the continuous phase, and whether the ratio of a particle size to a characteristic turbulent length scale is smaller or greater than some critical value; details will be provided below.

Firstly, studies which investigate modifications in turbulence spectrum, and those which search for correlations from experimental data caused by turbulence modulations, are given. This is followed by a review of works which deal with mathematical models of these phenomena and their implementation in a complete description of turbulence.

Hinze [101] proposes the following mechanisms to explain phenomena of turbulence modulation: (1) effect due to the locally increased shear rates at the phase interfaces; this affects the turbulent energy-spectrum of continuous phase in the wave number range corresponding to the distances between the particles (the latter are linked to the particle number density), (2) effect due to the vortex shedding and flow in the wakes downstream of the particles; here, the turbulent energy spectrum in the wave number range corresponding to the size of particles is affected.

The analysis of Al Tawell and Landau [9] considers the response of an isolated spherical particle to sinusoidal oscillations of its surrounding fluid. Applying Kolmogorov's concepts of spectral energy transfer and taking into account the additional energy dissipation arising from the inability of the dispersed particles to completely follow turbulent eddy fluctuations due to their inertia, they have found relations for the amplitude ratio and phase lag of a particle as a function of the dimensionless frequency of oscillation. The comparison with the experiments for the oil drop-laden jet of Hestroni and Sokolov [99] was reasonably good. They concluded that the presence of dispersed phase attenuates the turbulence intensity and results in additional dissipation of turbulence energy. The study has several severe limitations with respect to the practical flows; the most important of them is a restriction to the linear Stokes regime (very small particle Reynolds number).

The analysis by Gore and Crowe [76] of the available experimental data on the turbulence modulation in particle-laden jet and pipe flows shows that there is a critical parameter, namely, the ratio of particle diameter to the integral turbulent length scale, D_d/l_e (l_e is the integral length scale of the most energetic eddy in the corresponding particle-free flow). They argue that the ratio $D_d/l_e \approx 0.1$ is the level determining whether the turbulence intensity of the gas will be increased or decreased by the presence of the dispersed phase. Their conclusion was that those particles for which $D_d/l_e < 0.1$ will follow the eddy flow for a part of eddy's lifetime, during which the energy of the eddy will be transferred to the particles through the drag force. This causes a reduction of the gas turbulence intensity. In the case when $D_d/l_e > 0.1$ and if the particle Reynolds number is large enough, the particles cause vortex shedding, producing the turbulence in their wakes and increasing the turbulence kinetic energy of the flow; here the energy of the mean flow is transferred to the turbulence energy. In their later work [77], the authors tried to correlate the changes in turbulence intensity to the particle Reynolds number and velocity scale ratio, but got unsatisfactory results. Also, they noticed that the results for the particle-laden pipe flows become less correlated for the D_d/l_e ratio in the near-wall region due to the increased anisotropy of turbulence there (i.e. rapid change of the turbulence length scale l_e as the pipe wall is approached).

Hestroni [98] proposed two parameters to characterise the effects of turbulence modulation on the gas turbulence. The first is a redefined particle Reynolds number which accounts for a difference in the densities between the particles and gas, and the second is the ratio of the particle momentum relaxation time (see Eq.(3.71)) to the characteristic time of eddies. He analysed some experimental measurements of particle-laden flows for which the data on both gas and particle velocity were known (such data are sparse), and proposed that particles with a low particle Reynolds number (less than 400) tend to suppress the turbulence intensity of the carrier fluid, while the particles with a Reynolds number larger than 400 enhance the turbulence. This limiting value 400 for the particle Reynolds number corresponds to the value when the vortex shedding from a sphere commences, [3].

Elghobashi and Truesdell [64] studied turbulence modulation in the homogeneous grid turbulence using direct numerical simulation to solve the flow equations which include all the forces exerted by the solid particles on the fluid; the particle diameters are less than the Kolmogorov length scale. They found that the presence of the dispersed phase causes an increase of turbulence kinetic energy at high wave numbers (small length scales), accompanied by an increase of its dissipation rate. This results in the enhanced transfer of turbulence kinetic energy from larger length scales toward these small scales, reducing the overall level of turbulence intensity compared to the particle-free flow.

The majority of the present turbulence models which attempt to account for turbulence modulation are based on an Eulerian approach for both phases. They are restricted to well-dispersed (dilute) steady flows where particle-particle interaction is negligible, with small mean relative velocities between the phases. Also, they usually assume isothermal, non-reacting flows with no vapourisation. Below, a brief review of the most important works are given.

Two-equation k-ϵ turbulence models are used by Elghobashi and Abou-Arab [62], Elghobashi et al. [63], and Chen and Wood [40] for gas-particle flow calculations. Their studies are limited to the small relative velocities between phases (Stoke's regime) for both mean and fluctuating velocities. In [62], the exact derivation of the turbulence kinetic energy and its dissipation rate equations is given. Fourth-order correlations, together with the diffusion terms due to pressure fluctuation, were neglected, and the remaining terms were modelled. The turbulence modulation terms were modelled based on the linearised Lagrangian equation of motion of a spherical particle in a turbulent flow, [38]. This model is then used in [63] for the prediction of axisymmetric gas-particle jet. The results obtained match the experimental results well.

Chen and Wood [40] simplified the governing flow equations used in [63] by

completely neglecting displacement effects, (see §(2.2.2)), thereby limiting their application to the dilute flows. The correlations between particle and carrier phase fluctuating velocity components were modelled as an exponential dependence on the ratio of the particle momentum relaxation time and eddy lifetime, and the mean velocities of the gas and dispersed phase were assumed equal, restricting the application of model to particles much smaller than the Taylor microscale, [102]. This model was applied to the axisymmetric, isothermal, mono-dispersed particle-laden jet, and gave good predictions of the jet spreading and velocity decay rates as compared with experiments.

A k-ϵ model based on an Eulerian approach for the gas and a stochastic (Lagrangian) approach for the dispersed phase, has been successfully used to predict a turbulent round gaseous jet laden with solid particles by Mostafa and Mongia [146]. They modelled turbulence modulation contribution terms to the k-ϵ equations based on the linearised Lagrangian equation of motion of a spherical particle in a homogeneous turbulent flow. These terms depend on the carrier phase Lagrangian time scale and particle momentum relaxation time, and a coefficient of the additional term in the ϵ equation was tuned to fix experimental data.

Reitz and Diwakar [179], in their predictions of dense high-pressure sprays, included extra terms which represent the turbulence modulation effects in the k and ϵ equations in the KIVA code, [11]. They used a different value of the coefficient which multiplies the turbulence modulation term in the ϵ equation than in [146], reasoning that 'the turbulence length scale should be uneffected by an interaction with drops'. They used the stochastic Lagrangian approach for the spray description, and the overall model of the spray also accounts for the processes of atomisation, drop breakup and inter-drop collision. They compared the predictions of gas centerline velocity, with and without these extra terms, with measurements, and found that their inclusion produce a significant increase in gas velocity in the near-injector region close to the spray/injector axis. Effects on the prediction of Sauter mean diameter were negligible.

Berlemont et al. [26] investigated effects of evaporation on the gas mean properties in a round jet laden with liquid droplets. They used a Lagrangian approach for the liquid phase (excluding the droplet breakup and collision processes), and they included the turbulence modulation terms in the k-ϵ model of turbulence. They found significant differences in the gas axial mean velocity and turbulence intensity between the droplet-free and droplet-laden flows. However, they did not investigate the particular effect of the inclusion of the turbulence modulation terms, so their influence could not be separated from the effects of droplet evaporation.

We have seen from the above summary that several proposals have been made to include turbulence modulation in turbulence models, but unfortunately, the uncertainties of present experimental data on the one hand, and a lack of knowledge of real droplet-turbulence interaction processes, on the other hand, prevent definitive assessment of the quality of these approaches. All of the proposals, apart from [179] and [26], consider dilute (which means that possible inter-particle collision is neglected), mono-dispersed, isothermal, particle-laden flows where the relative velocities, both mean and fluctuating, between particles and gas are small.

The situation in the case of diesel sprays is much more complex and in many aspects it deviates from the aforementioned assumptions. Here, the droplets have large initial velocities relative to the gas, and they undergo through a number of processes mostly not included in the above models; droplet breakup, inter-droplet collision and coalescence, and droplet vapourisation (see §(3)). These processes give, as a result, a wide ranges of droplet sizes (from the order of $1\mu m$ to hundreds of μm), and relative velocities (from the order of $1m/s$ for the very small droplets, up to the order of $100m/s$ for the largest droplets). Also, two distinct regions in diesel sprays with respect to the droplet number density can be distinguished; one close to the injector exit and spray axis (up to the order of hundred nozzle diameters downstream) where the spray comprises irregularly-shaped liquid elements and a large number of droplets, and another beyond this region or/and at the spray periphery where the droplet number density is low. This droplet size distribution is linked (via the vapourisation rate which depends on the droplet size, droplet and local gas temperature and the gas chemical composition) to the inhomogeneous gas temperature and gas composition distributions, again in contrast to the assumptions made in the above models. However, despite these differences, turbulence modulation modelling

has been included in the present turbulence model in order to investigate its effects on the gas-spray behaviour.

The present approach mainly follows those of Mostafa and Mongia [146], and Reitz and Diwakar [179]. An additional source term is included in the k equation, arising from the presence of dispersed phase, which is calculated directly from the instantaneous droplet and gas velocities, available from the applied random walk technique (see [83] and §(3.3)). An additional term in the ϵ equation representing turbulence modulation is modelled in the same way as in [146].

Turbulence energy equation

The conservation equation of turbulence kinetic energy reads (the full derivation is given in Appendix A.2.4):

$$\frac{d}{dt}\int_V \rho k \, dV + \int_S d\mathcal{S}\cdot\rho\mathbf{u}_r k = \int_S d\mathcal{S}\cdot\rho\Gamma_{k,eff}\nabla k + \int_V \left(G - \rho\epsilon + s_k^d\right) dV \qquad (2.49)$$

where G is the production rate (generation) of turbulence energy, s_k^d represents the spray contribution, and $\Gamma_{k,eff}$ is the diffusivity of the turbulence energy alternatively expressed by the Prandtl/Schmidt number as: $\Gamma_{k,eff} = \nu_{eff}/\sigma_k$, see table 2.2. The generation term represents the rate of transfer of kinetic energy from the mean to the turbulent motion[5], defined as:

$$G = \mathbf{T}_t : \nabla\mathbf{u} \qquad (2.50)$$

One way of obtaining Eq.(2.49) is by contraction of the transport equation for the Reynolds stresses and then averaging. If this procedure is performed keeping track of the spray contribution term in the gas momentum conservation equation, Eq.(2.43), one can get the following expression for s_k^d (see Appendix A.2.4):

$$s_k^d = \overline{\mathbf{u}''\cdot\hat{\mathbf{s}}_{\mathbf{u}}^d} - \overline{\mathbf{u}''\cdot\hat{\mathbf{u}}\;\hat{s}^d} + \frac{1}{2}\overline{\mathbf{u}''\cdot\mathbf{u}''\;\hat{s}^d} \qquad (2.51)$$

where $\hat{\mathbf{s}}_{\mathbf{u}}^d$ is the instantaneous rate of momentum transfer from the spray to the gas phase, $\hat{s}^d$ is the local evaporation rate, and $\mathbf{u}''$ is the fluctuating velocity component (see §§(3.4) and (3.5), and Appendix B.1).

[5] It is worth mentioning here that this term (which is always positive) appears in the kinetic energy conservation equation of the mean motion with opposite sign as a sink term.

In the above expression the first term on the RHS represents the rate of exchange of kinetic energy between the droplets and eddies due to the droplet drag forces (see §(3.4)). The remaining two terms on the RHS allow for the effects on k of the mass transfer between the droplets and surrounding eddies due to evaporation (see §(C3-mass-section)). In diesel sprays, in the early stage of injection when the temperature of droplets, and therefore evaporation are low, the contributions of these terms to k are small. In isothermal (non-evaporating) sprays their contributions completely disappear.

Turbulence energy dissipation equation

The transport equation of the turbulence dissipation rate ϵ is as follows (the derivation is given in Appendix A.2.4):

$$\frac{d}{dt}\int_V \rho\epsilon \, dV + \int_S d\mathcal{S}\cdot \rho \mathbf{u}_r \epsilon = \int_S d\mathcal{S}\cdot \rho\Gamma_{\epsilon,eff}\nabla\epsilon + \int_V \left(C_{\epsilon 1} G\frac{\epsilon}{k} - C_{\epsilon 2}\rho\frac{\epsilon^2}{k} + C_{\epsilon 3}\rho\epsilon\nabla\cdot\mathbf{u} + s_\epsilon^d \right) dV \tag{2.52}$$

where $\Gamma_{\epsilon,eff} = \nu_{eff}/\sigma_\epsilon$ stands for the diffusivity of ϵ, and $C_{\epsilon 1}, C_{\epsilon 2}$ and $C_{\epsilon 3}$ are the model coefficients; see Table 2.2.

The spray contribution term, s_ϵ^d is modelled according to [146] as:

$$s_\epsilon^d = C_{\epsilon 4}\, s_k^d\, \frac{\epsilon}{k} \tag{2.53}$$

where $C_{\epsilon 4}$ is the coefficient given in Table 2.2, and s_k^d stands for the spray contribution to the turbulence kinetic energy (previous section). The value of this coefficient was chosen by Mostafa and Mongia [146] to match the experimental data of Shuen et al. [189], and is close to that reported in [62] and [63].

σ_k	σ_ϵ	C_μ	$C_{\epsilon 1}$	$C_{\epsilon 2}$	$C_{\epsilon 3}$	$C_{\epsilon 4}$
1.0	1.2	0.09	1.44	1.92	-0.373	1.0

Table 2.2: The coefficients in the k-ϵ model

2.4 Boundary and initial conditions

The mathematical description of the gas flow is completed by specification of the initial and boundary conditions. They must be provided for all dependent variables. One can distinguish the following types of boundaries:

- walls,
- inflow and outflow surfaces,
- planes of symmetry, and
- cyclic (periodic) boundaries.

They will now be explained in turn.

2.4.1 Wall boundaries

The near-wall region has important features that distinguish flow in this region from other parts. The presence of the wall causes steep gradients in the flow properties, due to the no-slip condition and the damping of the turbulence. These effects can be allowed for by employing a 'low Reynolds number' k-ϵ model, see eg. Jones and Launder [115]. However, such calculations require a very fine grid near the walls, and consequently very large computer storage and time. So, this approach can be only used when it is feasible, which is not the case in the present study.

An alternative approach, called the 'wall function method' avoids the above problems by employing submodels of the boundary layers, see Launder and Spalding [123]. The wall functions link the wall shear stress and heat flux to the conditions at or beyond the edge of boundary layer. This requires the near-wall grid points to be sufficiently remote from the wall.

Strictly speaking, the conventionally-employed wall functions are only valid for the steady, one-dimensional turbulent Couette flow; see Hinze [102] and Tennekes and Lumley [203]. But, because of the simplicity and economy of computation they offer, they are widely used in practical calculations. Following the successful application of wall functions for engine calculations by Ahmadi-Befrui [6] , Begleris

[24] and Tsui [210], they are adopted in the present study. Similar functions, using the '1/7 -law', are used by Amsden et al. [11] in the well-known KIVA code.

Basis of the wall functions

The wall functions are derived from the analysis of the turbulent Couette flow under the following assumptions:

1. The flow is steady state and one dimensional.
2. The three-layer model of a turbulent boundary layer, (a viscous layer, a buffer zone, and an inertial layer, see [102] and [203]),is replaced by a two-layer model. In this, the viscous and inertial sublayers are extended at the expense of the buffer zone.
3. The shear stress and heat flux are taken to be constant in the boundary layer.
4. The production and dissipation of the turbulence kinetic energy in the inertial layer are assumed to be in equilibrium.
5. The turbulence length scale in the inertial sublayer is taken to be proportional to the distance from the wall.

More details can be found in Spalding and Patankar [168], Gosman and Ideriah [82] and Begleris [24].

Shear stress and heat flux

The velocity boundary condition is no slip, while the temperature boundary conditions can be adiabatic wall (no heat transfer) or fixed temperature at the wall. All these types of boundary conditions are treated by the wall functions. Here, the latter are expressed in terms of dimensionless distance, y^+, velocity, u^+, and temperature, T^+, defined as:

$$\begin{aligned} y^+ &= \frac{\rho\, u^* y}{\mu_m} \\ u^+ &= \frac{u'_P}{u^*} \\ T^+ &= \frac{c_v\, \rho\, u^*(T_W - T_P)}{q_W} \end{aligned} \tag{2.54}$$

where y, T_P, T_W, c_v, q_W, and u^* are respectively the normal distance of a point P in the fluid from the wall W, the temperatures of the fluid at the point P and W, the specific heat capacity, the heat flux to the wall, and the friction velocity; see Fig.2.2.

The symbol u'_P stands for the tangential velocity of the fluid at the point P relative to the wall, calculated from:

$$u'_P = |\mathbf{u}'_P| \tag{2.55}$$

$$\mathbf{u}'_P = \mathbf{u}_P - \mathbf{u}_W - [\,(\mathbf{u}_P - \mathbf{u}_W)\cdot\mathbf{n}\,]\,\mathbf{n} \tag{2.56}$$

where $\mathbf{n}$ is the normal unit vector to the wall, and $\mathbf{u}_P$ and $\mathbf{u}_W$ are the gas and wall velocities, respectively (Fig.2.2).

The friction velocity is defined as:

$$u^* = \sqrt{\frac{\tau_W}{\rho}} \tag{2.57}$$

where τ_W is the wall shear stress.

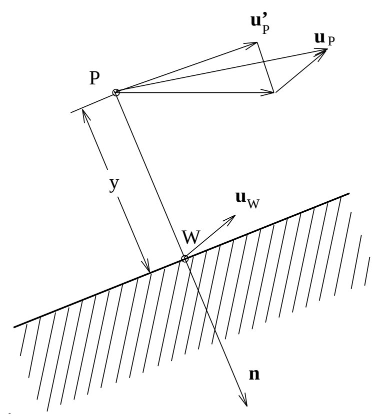

Figure 2.2: Wall boundary

The expressions for non-dimensional velocity and temperature profiles are:

1. Viscous sublayer

$$y^+ \leq y_c^+ \;\Rightarrow \begin{cases} u^+ &= y^+ \\ \\ T^+ &= \sigma_e u^+ \end{cases} \tag{2.58}$$

2. Inertial sublayer

$$y^+ > y_c^+ \;\Rightarrow \begin{cases} u^+ = \frac{1}{\kappa} \ln\left(E\, y^+\right) \\ \\ T^+ = \sigma_{e,t}\, [u^+ + P(\frac{\sigma_e}{\sigma_{e,t}})] \end{cases} \tag{2.59}$$

where y_c^+ is the critical value of y^+ and represents the interface of the two layers, κ is the von Karman constant, E is an empirical constant that depends on a wall roughness, $P(\frac{\sigma_e}{\sigma_{e,t}})$ is the viscous sublayer resistance factor expressing the resistance of the laminar sublayer to the momentum and heat transfer, and σ_e and $\sigma_{e,t}$ are the laminar and turbulent Prandtl numbers; see Table 2.3. The function $P(\frac{\sigma_e}{\sigma_{e,t}})$ used in this study follows Jayatillaka [112]s:

$$P(\frac{\sigma_e}{\sigma_{e,t}}) = 9\,(\frac{\sigma_e}{\sigma_{e,t}} - 1)(\frac{\sigma_e}{\sigma_{e,t}})^{-1/4} \tag{2.60}$$

From the above formulae the wall shear stress and the wall heat flux can be explicitly expressed in terms of the velocity and temperature (internal energy) at the point P as follows:

$$\tau_W = F_w^{\mathbf{u}}\, u_P' \tag{2.61}$$

$$q_W = F_w^e\, c_v\, (T_P - T_W) = F_w^e\, (e_P - e_W) \tag{2.62}$$

where $F_w^{\mathbf{u}}$ and F_w^e are the wall functions defined, in the viscous sublayer, by:

$$y^+ \leq y_c^+ \;\Rightarrow \begin{cases} F_w^{\mathbf{u}} = -\,\frac{\mu_m}{y} \\ \\ F_w^e = -\frac{\mu_m}{\sigma_e\, y} \end{cases} \tag{2.63}$$

and in the inertial sublayer by:

$$y^+ > y_c^+ \;\Rightarrow \begin{cases} F_w^{\mathbf{u}} = -\frac{\rho\, C_\mu^{1/4}\, k^{1/2}\, \kappa}{\ln(E\, y^+)} \\ \\ F_w^e = -\frac{\mu_m}{\sigma_{e,t}\, y} \frac{y^+}{\frac{1}{\kappa}\ln(E\, y^+) + P(\frac{\sigma_e}{\sigma_{e,t}})} \end{cases} \tag{2.64}$$

where y^+ is calculated from:

$$y^+ = \frac{\rho\, C_\mu^{1/4}\, k^{1/2}\, y}{\mu_m} \tag{2.65}$$

κ	E	y_c^+	σ_e	$\sigma_{e,t}$
0.4187	9.793	11.63	0.7	0.9

Table 2.3: Coefficients of the wall functions

In the above formulae, q_W and τ_W represent components of the heat flux density vector in a direction normal to the wall, and component of the shear stress tensor in the direction of the projection of $\mathbf{u}_P'$ on the wall, $\mathbf{t}$, see Fig.2.3. The vector expressions of Eqs.(2.61) and (2.62) read:

$$\tau_W\, \mathbf{t} = (\mathbf{n} \cdot \mathbf{T})_W = F_w^{\mathbf{u}}\, \mathbf{u}_P' \tag{2.66}$$

$$\mathbf{q}_W = \mathbf{n}\, F_w^e\, (e_W - e_P) \tag{2.67}$$

where $\mathbf{T}$ is the shear stress tensor. In expanded form $\tau_W\, \mathbf{t}$ becomes (see Eg.(2.56)):

$$\tau_W\, \mathbf{t} = F_w^{\mathbf{u}}\, [\mathbf{u}_P - \mathbf{u}_W - (\mathbf{u}_P - \mathbf{u}_W) \cdot \mathbf{n}\, \mathbf{n}] \tag{2.68}$$

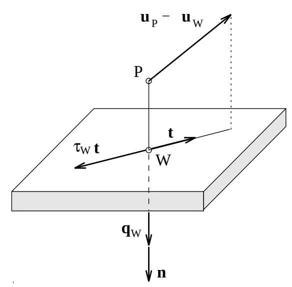

Figure 2.3: Heat flux and shear force vectors at the wall boundary

Turbulence energy and its dissipation

In the near-wall region, the production and dissipation terms in the k and ϵ equations must be appropriately modified in order to account for their assumed local equilibrium there.

In the k equation, this is done by setting the zero-diffusion condition at the wall and using the local, spatially-averaged generation and dissipation rates. (It will be show in §(4.4.4) that the former is accomplished by setting the corresponding coefficient in a discretised equation to zero, and the latter by modifying the source term).

In the ϵ equation, this modification is done by forcing the near-wall value of ϵ to its local equilibrium value:

$$\epsilon = C_\mu^{3/4} \frac{k^{3/2}}{\kappa y} \tag{2.69}$$

More details about this practice can be found in Jones and Launder [114], Launder and Spalding [123] and Launder [121].

2.4.2 Inflows and outflows

During the engine cycle, the gas flow to and from cylinder is controlled by the inlet and outlet valves which periodically open and close flow passages, Fig.2.4, determining in this way amount of gas in the cylinder and influencing all other gas parameters. Since these quantities (flow rate, gas pressure, temperature, velocities and turbulence parameters) represent initial and boundary conditions for our mathematical model, knowledge of their values is of a crucial importance for a good prediction.

For this purpose, one has to select regions on the control surface of the computational domain which will represent inlet/outlet boundaries. Any of a number of flow cross-section surfaces can be chosen if all necessary flow parameters to characterise the flow are available there. However, selection of, for example, a surface S_1 in the inlet port, demands also the modelling of the inlet port geometry between the cylinder and S_1, which entail additional computing overheads which it was decided to avoid in the present study.

The control surfaces chosen here, are the so-called valve curtains $S_{v,1}$ and $S_{v,2}$

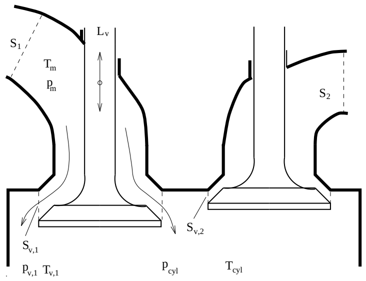

Figure 2.4: Sketch of valve flow

shown in Fig.2.4. The necessary input data for the complete specification of the valve flow are:

- valve-lift profile, L_v, vs. time (crank angle), see (Fig.2.5),
- gas pressure, temperature, and turbulence parameters (k and ϵ) at the valve curtains,
- mass flow rate vs. time, or the valve discharge coefficient vs. the valve-lift and the pressures in the inlet and outlet manifolds and in the cylinder,
- directions of the velocities at the valve curtains vs. time.

These quantities are usually given in terms of experimental data, or in the absence of these, as is often the case with the turbulence parameters, they are based on physical reasoning, see Begleris [24].

More details about the valve flows can be found in the works by Heywood [100], Watkins [217], Begleris [24], and Theodoropoulos [204].

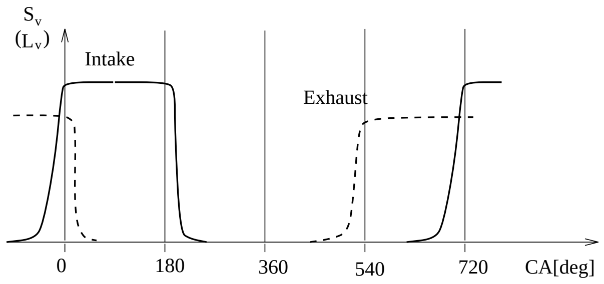

Figure 2.5: Valve-lift profile for an 4-stroke engine

2.4.3 Symmetry plane

When a problem is symmetric with respect to a plane, as is the case in some engine geometries, it is possible to exploit this symmetry to reduce the size of the computational domain by employing the symmetry boundary condition. At symmetry planes the normal velocity component and the normal component of the gradient of all other variables are equal to zero.

2.4.4 Cyclic boundaries

This type of boundary condition can be used when the solution domain has pair of geometrically identical boundaries at which flow repeats itself. In this case, the magnitude of fluxes and the scalar quantities at the corresponding locations of cyclic boundaries are equal, provided the vectors are rotated to ensure the same relative orientation to the boundary. This property is exploited, similar to the symmetry boundary condition, to reduce the size of the computational domain.

A simple example of a cyclic boundary pair, with the ϕ-profiles at the boundaries and the velocities at two corresponding points at the boundaries, is the axisymmetric geometry shown in Fig.2.6. The convective fluxes of a general scalar property ϕ at two opposite elementary surfaces $d\mathcal{S}_1$ and $d\mathcal{S}_2$ are respectively: $d\mathcal{S}_1 \cdot (\rho\ \phi\mathbf{u})_{P_1}$ and $d\mathcal{S}_2 \cdot (\rho\ \phi\mathbf{u})_{P_2}$. Since

$$
\begin{aligned}
(\rho\ \phi)_{P_1} &= (\rho\ \phi)_{P_2} \\
\mathbf{u}_{P_2} &= \mathbf{R}^\alpha \cdot \mathbf{u}_{P_1} \qquad (2.70)
\end{aligned}
$$

$$
d\mathcal{S}_2 = -\,\mathbf{R}^\alpha \cdot d\mathcal{S}_1
$$

where $\mathbf{R}^\alpha$ is a rotation matrix which rotates vectors for an angle α around the axis, the sum of the convective fluxes of ϕ through $d\mathcal{S}_1$ and $d\mathcal{S}_2$ is zero, i.e.:

$$
d\mathcal{S}_1 \cdot (\rho\ \phi\mathbf{u})_{P_1} + d\mathcal{S}_2 \cdot (\rho\ \phi\mathbf{u})_{P_2} = 0 \qquad (2.71)
$$

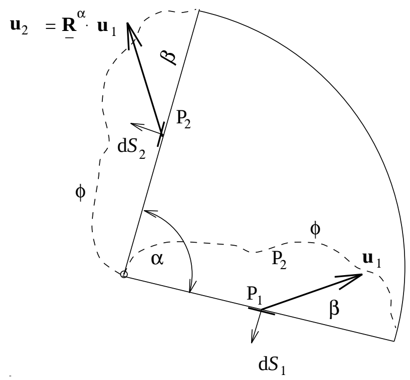

Figure 2.6: Cyclic boundaries

The same is valid for the diffusive fluxes at P_1 and P_2, represented here by their flux vectors $(\Gamma_\phi \nabla\phi)_{P_1}$ and $(\Gamma_\phi \nabla\phi)_{P_2}$, respectively, i.e.:

$$
(\Gamma_\phi \nabla\phi)_{P_1} \cdot d\mathcal{S}_1 + (\Gamma_\phi \nabla\phi)_{P_2} \cdot d\mathcal{S}_2 = 0 \qquad (2.72)
$$

2.4.5 Initial conditions

In an unsteady problem, due to the parabolic nature of governing equations with respect to time, the initial conditions for all dependent variables in a solution domain must be known. They are usually based on experimental data, physical reasoning and experience. Attention must be payed that the initial conditions are physicaly consistent.

2.5 Closure

In this chapter the mathematical model of the gas phase has been provided. In §(2.2.1), the conservation equation of an instantaneous general property in a single-phase flow, in an arbitrary moving control volume, has been described. Then, in §(2.2.2) the effects of a dispersed phase have been allowed for via introduction of the void fraction and additional spray source terms.

In §(2.2.3), the available averaging techniques have been briefly described, and the modified definition, needed because of the spray presence, of the chosen density-weighted (Favre) ensemble averaging has been given. Then, the Favre-averaged general transport equation has been developed in §(2.2.4), and the nature of the resulting additional turbulence diffusion terms for the scalar and vector quantities, has been described in §(2.2.5) and §(2.2.6), respectively. The Favre-averaged constitutive relations have been given in §(2.2.7).

The averaged conservation equations of mass, momentum and energy have been given respectively in §§(2.3.1), (2.3.2) and (2.3.3). Turbulence has been modelled with the engine-version of k-ϵ model which takes into account the compressibility of flow during the compression and expansion strokes, §(2.3.4). The turbulence modulation, i.e., the direct effects of the spray presence in the flow on the gas turbulence, has been introduced through additional source terms in the k and ϵ equations.

Finally, in §(2.4), the boundary and initial conditions have been given. Wall functions have been employed for the wall boundary conditions, §(2.4.1). The other boundary conditions have been explained: inflows and outflows in §(2.4.2), and symmetry planes and cyclic boundaries in §(2.4.3) and §(2.4.4), respectively. The initial conditions have been given in §(2.4.5).

With the last section (the boundary and initial conditions), the description of the gas phase behaviour, apart from the spray source terms, has been completed. It comprises a set of mutually coupled, non-linear integro-differential equations. In the following chapter, the mathematical model of spray and expressions for the coupling spray source terms will be given.

Chapter 3

Model of dispersed phase

3.1 Introduction

The primary problem in analysing and modelling the spray behaviour lies in the incomplete understanding of all the important physical processes and the lack of relevant experimental data. These processes comprise cavitation in the nozzle, atomisation, drop breakup, inter-droplet collision and coalescence, interphase transfer of mass, momentum and energy, and spray interaction with the chamber and/or piston walls. Experimental measurement of these phenomena, which is based mainly on laser techniques, is difficult since the spray is optically dense, except near its edge. In addition such experiments, especially in the real diesel engine conditions, require expensive modifications to provide optical access and also substantial time and effort. For these reasons a limited number of engine measurements of gas-spray characteristics are available. These are the reasons why early spray modelling was founded on measurements at atmospheric conditions or in quiescent pressure chambers. A comprehensive review of the available spray measurements can be found in Tabrizi [200], and no attempt will be made to repeat them here. Details of the experimental data used in the present study for validation purposes are given in §(6).

On the modelling side, two closely-related approaches are currently employed, namely, the Williams statistical model [223] and the 'discrete droplet' model, as noted in §(1).

The discrete droplet model employed in this study has been used by Crowe [49], Gosman and Johns [85], Dukowicz [58] and others; for more information see §(1.2). It represents spray by a number of 'computational parcels', each of which represents a large number of droplets of the particular size, velocity and temperature. The motion, mass and temperature changes of each parcel are computed by solving the ordinary differential equations governing the momentum, mass and energy conservation for a representative member of the parcel. The effects on and by the gas phase are simulated with the aid of calculations of the local exchange rates of mass, momentum and energy, which appear in the gas conservation equations as 'source' terms.

All the spray processes mentioned above have their own submodels whose descriptions, accompanyed by a brief literature review, are described in the following sections. The following general assumptions are adopted:

- single-component fuel,
- the droplets are spherical with infinitely fast mixing within them, such that the interior temperature and density are always uniform,
- the interphase transport of mass, momentum and energy are quasisteady, i.e. their rates are equal to the steady-state rates under the same boundary conditions,
- the transfer coefficients for mass, momentum and energy to and from the droplets are independent of the proximity of neighbouring droplets, and can be represented by empirical correlations.

It has to be noted that these assumptions represent significant idealisation of real diesel spray processes, made in order to simplify the mathematical modelling and enable affordable numerical treatments. Diesel fuels are always mixture of different hydrocarbon compounds, accompanied also by a number of other desirable or undesirable additives (see [100]), which have strong impact on all the fuel properties, and to some degree the droplet history. Moreover, the calculation of evaporation, taking into account the multicomponent features of real diesel fuel, demands calculation of

the unsteady diffusion processes inside droplets, the selective vapourisation due to the different volatility of the fuel components, and solution of additional mass conservation equations for each of the fuel components. Also, there is one phenomenon which is only present in multicomponent droplets, namely, microexplosion due to the trapped vapour bubbles of the most volatile component, [124] and [4]. The surface tension coefficient is especially sensitive to even very small amounts of impurities and this affects drop breakup because the surface tension forces are important in breakup. There have however been studies which analysed the evaporation of a single multicomponent droplet, considering the finite diffusion and transient effects in the liquid phase (see for instance [137] and [4]). The numerical effort required to allow for these effects in the whole spray, i.e. to solve for governing equations for all representative parcels is very large, and therefore they are not included in this study. Fortunately, experiments performed for spray model validations usually use single-component fuels. The other assumptions adopted in particular submodels are noted when they are described.

In section §(3.2.2) two atomisation models are presented, namely, Huh's model in §(3.2.1) and the 'MPI' model developed in the Max Planck Institut in §(3.2.2). Section §(3.3) deals with the droplet trajectory calculation (including the inclusion of turbulence effects by the random walk approach). Then sections §(3.4), §(3.5), §(3.6) respectively present the droplet conservation equations for momentum, mass and energy. The introductory parts of these sections contain brief literature reviews on empirical correlations for the corresponding droplet transfer coefficients and conclude with expressions for the source terms in the gas transport equations (ensemble-averaging of the general spray source term is given in Appendix B.1). In section §(3.7) two droplet breakup models are given; the Reitz-Diwakar model in §(3.7.1), and the Pilch-Erdman version in §(3.7.2). The O'Rourke collision model is described in §(3.8), and the model of spray-wall impingement developed in the Max Planck Institut is presented in §(3.9). Finally, the spray initial conditions and the closure of this chapter are given respectively in §(3.10) and §(3.11).

3.2 Atomization models

The basic task of diesel injectors is to atomise and disperse the liquid fuel to achieve high rates of mixing and evaporation. This enables the desired ignition delay and completion of combustion in the crank angle range close to the TDC to be achieved. Also, rapid mixing of the injected fuel and air reduces or prevents formation of various pollutants which usually accompany diesel combustion.

One of the main difficulties in spray modelling is the specification of the droplet initial conditions as they are produced at or near the nozzle. This has been the subject of research over many years, centered on the idea that the liquid issues from the nozzle as a jet, which subsequentially breaks up. An understanding of controlling processes for the breakup of low-speed jets has been well developed; see review of McCarty [136]. However, for the high-speed jets characteristic of diesel injection, a number of conflicting theories have been proposed, ascribing the jet breakup to aerodynamic effects, liquid turbulence, jet velocity rearrangement effects and cavitation phenomena in the nozzle; Reitz and Bracco [177], Sirignano [190], Bracco [34] and [35], Faeth [68], Lefebvre [125], [126] and [127], Clift [44], Reitz [176]. None of these theories alone can explain the jet breakup characteristics and their dependence on the nozzle geometry, injection velocity and ambient gas density.

Several breakup regimes have been identified (Faeth [70]), namely - in order of increasing flow rate (injection velocity): Rayleigh breakup, first and second wind-induced breakup, and atomisation breakup. In the Rayleigh breakup regime, [174], the surface tension forces induce the instability of the axisymmetrical jet surface perturbations whose wavelengths are greater than the jet perimeter (the smaller wavelengths are damped). The amplitudes of these unstable perturbations grow, resulting, many nozzle diameters downstream from the nozzle exit, in the jet breakup. The average size of the drops formed is nearly twice the diameter of the nozzle.

The first wind-induced breakup is induced by the still-dominant surface tension forces, accompanied and augmented by the effects of aerodynamic forces due to the relative motion between the jet and surrounding air. This produces a liquid twisting motion and unstable wave growth at the jet surface. The perturbations with a smaller wavelengths than in the Reyleigh regime become unstable, yielding the jet breakup into drops with diameters comparable to the injector hole diameter.

In the second wind-induced breakup regime, the importance of the forces due to the relative motion between the jet and gas becomes higher, causing surface perturbations with the yet smaller wavelengths than in the previous regime to be the most unstable. The surface tension forces in this regime oppose the growth of these perturbations, which are supported by the aerodynamic forces. This results, at some distance downstream from the injector exit, in detachment of parts of the jet surface, producing droplets in a wide range of sizes. The average drop diameter is now less than the nozzle diameter.

In all the above regimes, the breakup starts at some finite distance from the nozzle exit. With a further increase of a flow rate (injection velocity), the start of breakup is believed to take place very close to or immediately at the nozzle exit, although the evidence is not conclusive. This regime is usually referred to as the atomisation regime. The average drop diameter is much less than the nozzle diameter.

The above description of the breakup regimes is a simplified picture of the complex processes which lead to jet breakup. There are other influential parameters which affect breakup, namely, the liquid and gas viscosity, characteristics of turbulence in the jet and surrounding air, as well as the conditions of flow in the nozzle (pressure pulsations, velocity distribution and occurrence of cavitation). Some of these will be discussed in what follows.

At the present there is no model of the jet breakup which gives satisfactory predictions in diesel circumstances. The reasons lie, on the one hand, partly in the incomplete theoretical understanding of all the processes involved, and on the other in the lack (impossibility) of measurement of relevant quantities for the validation of models. Therefore, modellers rely on a combination of theoretical hypothesis, outcomes of order of magnitude and dimensional analyses, and tuning of unknown model coefficients to match the experimental data. However, this restricts the generality of models to the limited number of cases.

To date, the most successful theoretical models are based on the unstable wave growth mechanism (also called the Kelvin-Helmholtz instability theory). According to this, initial perturbations at the jet surface results in unstable wave growth due to pressure variations provoked by the relative motion with the surrounding gas; the droplets are formed by the detachment of these waves.

In the present study, two recently-developed atomisation models for round-hole diesel injectors are employed: Huh's atomisation model, [108], and the model developed at the Max Planck Institute (MPI model) by Obermeier and Chaves, [160]. They can be briefly described as follows. The former assumes two atomisation phenomena: the development of turbulence in the nozzle causes initial perturbations on the jet surface, and the growth of these perturbations and their detachment from the jet surface occurs by the action of aerodynamic forces. The later MPI model allows for the cavitation in the injector nozzle, stripping of drops from the jet surface (by the aerodynamic forces), and collision between large lumps of liquid and their further disintegration. More detailed descriptions of these models are given in the following sections.

3.2.1 Huh's model

This model couples effects of two phenomena relevant in spray atomisation, namely, the turbulent fluctuations in the liquid jet, and the unstable wave growth at the jet surface by aerodynamic effects between the jet and surrounding gas at their interface. The conceptual picture of the atomisation process takes it to proceed in two stages:

1. Turbulence developed in the nozzle hole induces initial perturbations on the jet surface when it leaves the hole,

2. Once the perturbations have reached a certain level, they grow by the action of aerodynamic forces until they become detached from the jet surface as droplets; these droplets will, from now on, be called secondary droplets.

In the model, firstly the length and time scales of atomisation are identified, and then they are used to determine the breakup rate, droplet size distribution and spray cone angle.

An one-dimensional analysis of the single-phase flow in the nozzle (the cavitation phenomenon is at this stage neglected) gives the initial values of turbulence length and time scales in the jet at the nozzle exit. However, both scales are subjected to changes since the jet turbulence decays with time as the jet travels downstream. This is because there are no mechanisms in the jet which can generate turbulence once it has left a nozzle. (In the nozzle hole, due to the no-slip condition at the hole wall, the liquid experiences tangential stresses from the wall, leading to turbulence generation.)

It is postulated that the turbulence causes perturbations at the jet surface with wavelengths proportional to the turbulence length scales. Under the action of surrounding gas, i.e. its normal (pressure) stresses at the jet surface, the amplitude of these perturbations starts to rise. The rate of this amplitude amplification is characterised by a corresponding time scale, called a wave growth time. This time scale, together with the aforementioned turbulence time scale, determine the atomisation time scale. Both atomisation scales, time and length, together with the average injection velocity, are used to estimate a spray cone angle.

The sizes of secondary droplets are determined by a random choice from an assumed probability distribution function (pdf). It is taken that the pdf for the droplet sizes is proportional to the spectrum of the turbulence kinetic energy in the jet, and inversely proportional to the atomisation time scale. The initial velocities of secondary droplets are taken to be equal to their parent drops.

Under normal diesel conditions cavitation usually occurs within the nozzle, invalidating the assumed single-phase flow assumption. In order to allow for this effect to some extent, simple overall mass, momentum and energy balances are used to estimate the exit jet characteristics. Also, the determination of a number of model coefficients by reference to measurements for the real diesel conditions, implicitly accounts for cavitation.

Nozzle turbulence and its decay

The relations which link characteristics of turbulence in the nozzle hole to the nozzle geometry and flow conditions are given below. The pressure drop Δp_h in the nozzle hole between section i and o, Fig.3.1, obtained from the Bernoulli equation, is:

$$\Delta p_h = \frac{\rho_d U^2}{2} \left[\frac{1}{c_d^2} - K_c - (1 - s^2) \right] \tag{3.1}$$

where ρ_d is the liquid density, and K_c, c_d and s are the form loss coefficient, the discharge coefficient and the inlet:outlet area ratio, respectively; see Fig.3.1. The average injection velocity, U, is calculated from:

$$U = \frac{4\pi}{D^2} \int_{t_1}^{t_2} \dot{Q}(t)\, dt \tag{3.2}$$

where t_1 and t_2 denote the times at the start and the end of injection, $\dot{Q}$ is the volumetric flow rate, and D is the nozzle hole diameter.

The force balance for the liquid in the nozzle hole yields for fully-developed flow:

$$\pi DL\, \tau_{wall} = \frac{\pi D^2}{4} \Delta p_h \tag{3.3}$$

where τ_{wall} is the average tangential stress at the hole wall, and L is the hole length. Combination of Eqs.(3.1) and (3.3) gives:

$$\tau_{wall} = \frac{\rho_d U^2}{8\frac{L}{D}} \left[\frac{1}{c_d^2} - K_c - (1 - s^2) \right] \tag{3.4}$$

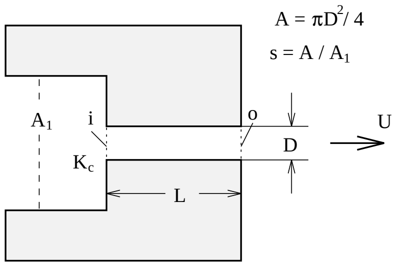

Figure 3.1: Nozzle geometry

The average turbulence kinetic energy, k_a and its dissipation rate, ϵ_a are estimated from one-dimensional force and energy balances in the nozzle hole between cross-sections i and o, giving, when combined with Eq.(3.4), the following relations:

$$k_a = \frac{U^2}{8\frac{L}{D}} \left[\frac{1}{c_d^2} - K_c - (1 - s^2) \right] \tag{3.5}$$

$$\epsilon_a = \frac{K_\epsilon U^3}{2L} \left[\frac{1}{c_d^2} - K_c - (1 - s^2) \right] \tag{3.6}$$

The coefficient K_ϵ is tuned to 0.5 from the comparison of the one-dimensional model with multidimensional flow field calculations, [80]. The turbulence length and time scales at the nozzle exit are linked to k_a and ϵ_a by:

$$L_t^o = C_\mu^{3/4} \frac{k_a^{3/2}}{\epsilon_a} \tag{3.7}$$

$$\tau_t^o = C_\mu^{3/4} \frac{k_a}{\epsilon_a} \tag{3.8}$$

where C_μ is a coefficient of the $k - \epsilon$ model (see §(2.3.4)).

Once the liquid leaves the nozzle, the jet velocity is assumed to become uniform, since the gas can not retard the liquid surface as effectively as the nozzle walls. This suppresses turbulence production in the liquid, causing the turbulence to decay with time. The following relations describe this time dependence:

$$L_t(t) = L_t^o\,(1 + C_{a1}\frac{t}{\tau_t^o})^{C_{a2}} \tag{3.9}$$

$$\tau_t(t) = \tau_t^o(1 + C_{a1}\frac{t}{\tau_t^o}) \tag{3.10}$$

where C_{a1} and C_{a2} are the empirical coefficients given in Table 3.1.

Surface wave growth

The second stage of atomisation process is the interaction between the liquid jet - with these initial perturbations on its surface - and surrounding gas field. The interaction results in increasing of the amplitudes of the perturbations, until they become detached from the jet surface as droplets. This amplification of the perturbations obeys the dispersion equation, Taylor [202]. Detailed derivation of this equation can be found in Reitz [177], and will not be given here.

The dispersion equation relates the grow rate of amplitudes of surface waves to its wavelength, and reads:

$$(\omega + 2\nu_d\kappa^2)^2 + \frac{\sigma\kappa^3}{\rho_d} - 4\nu_d^2\kappa^3(\kappa^2 + \frac{\omega}{\nu_d})^{\frac{1}{2}} + (\omega + jU\kappa)^2\frac{\rho_m}{\rho_d} = 0 \tag{3.11}$$

In this equation the symbols denote: σ - coefficient of surface tension, ν_d - liquid kinematic viscosity, κ - wavenumber, $\kappa = 2\pi/L_w$; L_w is the wavelength of perturbation, ρ_m - gas density, j - imaginary unit, ω - complex wave celerity; reciprocal values of its real part is the wave growth time, τ_w.

C_μ	K_c	K_ϵ	C_{a1}	C_{a2}	C_1	C_2	C_3	C_4
0.09	0.45	0.5	0.92	0.4565	2.0	0.5	1.0	1.5

Table 3.1: Coefficients of Huh's atomization model

Atomization scales

The atomisation scales are estimated based on the following two hypothesis:

- The dominant length scale of atomisation, L_A, is proportional to the turbulent length scale, L_t, i.e.:

$$L_A = C_1 \, L_t \tag{3.12}$$

  where C_1 is an empirical coefficient. The corresponding wavelength of perturbations, L_w, is:

$$L_w = \frac{L_A}{C_2} \tag{3.13}$$

  where C_2 is the another empirical coefficient.

- The time scale of atomisation, τ_A is taken to be a linear combination of the turbulent time scale, τ_t and the wave growth time scale, τ_w, i.e.:

$$\tau_A = C_3 \, \tau_t + C_4 \, \tau_w \tag{3.14}$$

  Here, C_3 and C_4 are further empirical coefficients. The above form of the atomisation time scale guarantees the limiting behaviour of τ_A, i.e. that the atomisation does not occur in vacuum ($\tau_w \rightarrow \infty$), or with the laminar flow in the jet ($\tau_t \rightarrow \infty$).

The values of coefficients $C_1, \ldots C_4$ are chosen based on the following reasoning. The value of C_1 is set to 2.0 on the assumption that an atomisation length scale L_A is equal to the eddy diameter which is twice the turbulence length scale L_t. The value of C_2 is chosen to be 0.5, from the conceptual picture that the half of the jet surface wave, when detached from the jet, forms the secondary droplet. The remaining two coefficients, C_3 and C_4, are chosen to match experimental data reported in [108]. The values of all the coefficients are given in Table 3.1.

When these two atomisation scales are known, the spray semi-cone angle is calculated from:

$$tan \frac{\Theta}{2} = \frac{L_A/\tau_A}{U} \tag{3.15}$$

Droplet size

It is assumed that when the jet issues from the nozzle, it immediately breaks up into large drops, called parent drops, with the initial diameter equal to the nozzle hole diameter, D, and that these subsequently break up at a rate governed by:

$$\frac{dD_d}{dt} = -2 \, \frac{L_A}{\tau_A} \tag{3.16}$$

It is taken that during its breakup the parent drop maintains its injection velocity.

The probability density function (pdf) of the sizes of the secondary droplets is based on the assumption of isotropic turbulence in the liquid phase and the following four hypotheses:

- the number of droplets of size x is inversely proportional to the atomisation time scale τ_A,
- the number of droplets of size x is proportional to the jet-droplet surface area ratio, D^2/x^2,
- the number of droplets with size x is proportional to the turbulence energy spectrum $\Phi(x)$, and
- the number of droplets in the range $(x, x + dx)$ is proportional to the unit size interval, dx/x.

The pdf is defined as the volume fraction of the droplets with size x per interval dx, per total volume of secondary droplets,V_d, i.e.:

$$p(x) = \frac{1}{V_d} \frac{dV_d}{dx} \tag{3.17}$$

and its value is evaluated from:

$$p(x) = C \frac{\Phi(x)}{\tau_A(x)} \tag{3.18}$$

where C and Φ are a normalisation constant and the dimensionless turbulence energy spectrum, respectively. The latter is estimated according to [102] by:

$$\Phi(x) = \frac{[\kappa(x)/\kappa_e]^2}{[1 + (\kappa(x)/\kappa_e)^2]^{11/6}} \tag{3.19}$$

where the peak wavenumber $\kappa_e = 2\pi/L_e$, and $L_e = L_t/0.75$. The length scale L_e can be interpreted as the average size of the energy-containing eddies.

The cumulative distribution function, $F(x)$, is calculated from:

$$F(x) = \int_{x_{min}}^{x} p(x)dx \tag{3.20}$$

The integration of the above starts from the minimum droplet size, x_{min} , calculated from the Kelvin-Helmholtz instability theory by the expression:

$$x_{min} = 2\pi \frac{(\rho_d + \rho_m)\,\sigma}{\rho_d\,\rho_m\,U^2} \tag{3.21}$$

The sizes of the secondary droplets, x_{sec}, and their number, N_s, are determined from the distribution function F and a randomly chosen value, Y_r in the range $(0, 1)$, and the mass balance of liquid. The following expressions are used:

$$x_{sec} = F^{-1}(Y_r) \tag{3.22}$$

$$N_s = \frac{(D_d)^3 - (D_d^n)^3}{x_{sec}^3}\,, \tag{3.23}$$

where a superscript n denotes the condition after breakup.

Droplet velocity

The initial velocity of parent droplets is determined based on the injection rate history and the spray cone angle as will be described in §(3.10). The secondary droplets at the time of their creation inherit the velocity of their parent drops.

3.2.2 MPI model

This atomisation model was developed at the Max Planck Institut (MPI) by Obermeier and Chaves, [160]. It comprises two submodels; one deals with the flow in the injector nozzle, and the other considers disintegration processes of the liquid jet.

The main task of the nozzle flow model is to predict the liquid exit velocity from the nozzle, because this is one of the most important parameters for spray atomisation. The model takes into account the geometry of injector nozzle (the nozzle hole diameter, its length, and the roughness of the hole wall), pressures in the nozzle and engine chamber and the fuel flow rate. Also, one empirical or assumed coefficient which characterises the flow contraction at the entrance of the nozzle hole must be known (the entrance area contraction ratio). The model considers the nozzle flow as axi-symmetrical, and calculates the thickness of the boundary layer and the onset and extent of the cavitation region along the nozzle. Based on these data, it determines the exit area contraction ratio and liquid exit velocity.

The model of atomisation processes considers the jet breakup into a number of large structures (primary drops) and their further disintegration into smaller secondary droplets by the stripping action of the aerodynamic forces, and by collision between the primary drops. The liquid exit velocity from the nozzle is the input to this model. It also requires input data about the nozzle hole diameter, spray cone angle, gas density and fuel properties. The model determines the sizes of droplets and their initial conditions.

Details of the derivation of mathematical models for nozzle flow and atomisation processes can be found in [159] and [158], respectively, while here, only summaries will be given. We will start with the nozzle flow model.

Nozzle flow model

The model arises as a result of observations of the flow in a transparent injector in the Max Planck Institut. The experiments were performed with water and diesel fuels in stationary and unstationary flow conditions, under atmospheric and high ambient pressure. The results, reported in [140], [141], [139], and [151], show the appearance of a irregular cavitation region which starts at the entrance of nozzle (plane i in Fig.3.2) and propagates downstream. Depending on the supply pressure in the nozzle and the flow rate, this cavitation region either collapses inside the nozzle or reaches the exit. It shows inherent instability, i.e., parts of the cavitation region break off from the rest and are convected downstream, during which they further break up into smaller cavities (bubbles) or collapse, [157]. Cavitation causes the reduction of the available cross section area for a liquid flow, affecting the liquid velocity profile in the nozzle and at its exit. It was also noticed that the presence of cavitation in the flow improves spray atomisation, especially when the cavitation region reaches the nozzle exit. Then, the creation and collapsing of the cavitation bubbles cause strong perturbations at the exit jet surface, which are then stripped away by the aerodynamic forces provoked in the the surrounding gas (details of this process will be presented in the following section). According to these measurements, the liquid exit velocity is in general not equal to its 'effective' value u_{eff}, given by the volume flow rate divided by the cross section area of the nozzle hole. This difference in velocities is attributed to cavitation, and the nozzle model attempts to account for this.

The model simplifies the picture of in-nozzle flow, assuming quasi-steady axisymmetric flow and formation of two characteristic regions; one at the entrance portion of the nozzle hole, called separation/cavitation 'bubble', b in Fig.3.2, and the other downstream of this bubble, l, where the turbulent boundary layer and cavitation region develop. The length of the entry bubble is taken to be equal to the hole diameter ($x_o = D$), and its height (i.e., the site of the maximum flow area contraction) is linked to the entrance area contraction ratio, explained later.

The following additional assumptions are made:

1. The cross-section of the flow between c and x_o is constant and with no frictional losses, Fig.3.2.

2. The turbulent boundary layer starts at x_o, and the velocity profile obeys a '1/7 power law'; outside the layer a 'plug' velocity profile is assumed,Fig.3.3.

3. The cavitation region is approximated by a quasi-cylindrical cavity of variable cross section, located along the nozzle axis. It starts from x_o with a thickness determined from the continuity equation.

4. The pressure inside the cavitation cavity is equal to the saturation fuel vapour pressure for a known temperature of fuel.

5. At the nozzle exit, the flow is subjected to a pressure jump from the pressure inside the nozzle to the chamber pressure (the authors called this 'a Carnot shock'). The mass and momentum of the flow across the pressure jump are conserved, and based on these balances, the exit injection velocity and exit contraction area ratio are determined.

There are two cross-sectional areas available to the liquid which are considered in the model; one at the entrance part of the nozzle hole at the site of maximum area contraction, c in Fig.3.2, characterised by the entrance area contraction coefficient C_c, defined at the figure, and the other at the nozzle hole exit, characterised by an another contraction ratio, called the exit area contraction ratio C_{ch}, defined as:

$$C_{ch} = \frac{A_{ch}}{A} \tag{3.24}$$

where A_{ch} is the available exit cross-sectional area for the liquid, and A is the geometrical section area; see Fig.3.2. Depending on the pressure in the chamber

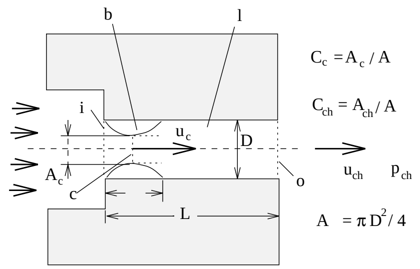

Figure 3.2: Nozzle geometry

(cylinder), p_{ch} and the length of the cavitation region, the model distinguishes three flow regimes:

1. Non-cavitating flow, $p_{ch} > p_{ch,crit}$;
   $C_{ch} = 1$,

2. Cavitating flow, $p_{ch} \leq p_{ch,crit}$;
   cavitation region reaches the nozzle exit, $C_{ch} < 1$,

3. Cavitating flow, $p_{ch} \leq p_{ch,crit}$;
   cavitation region collapses inside the nozzle, $C_{ch} = 1$.

The critical pressure, $p_{ch,crit}$ at which cavitation occurs is derived from simplified, one-dimensional mass and momentum conservation equations between cross-sections A_c and A_{ch}. It is evaluated with $C_{ch} = 1$, which represents the threshold value of C_{ch} when the cavitation region reaches the nozzle exit, by the following expression:

$$p_{ch,crit} = \rho_d \left\{ C_c u_c^2 - \left[C_{ch} + \frac{1}{2}\lambda(\frac{L}{D} - 2) \right] u_{eff}^2 \right\} \tag{3.25}$$

where C_c is the assumed (or known from experiment) entrance area contraction ratio (its value is in the range 0.6-0.8), u_c is the velocity at the site of maximum contraction (i.e. site c in Fig.3.3, u_{eff} the effective velocity, and λ is the friction factor.

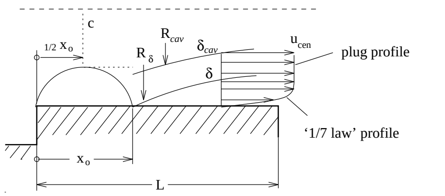

Figure 3.3: Boundary layer and cavitation region in the nozzle

The velocities u_c and u_{eff} at time t are calculated from the specified volumetric flow rate $\dot{Q} = \dot{Q}(t)$ by:

$$u_{eff} = \frac{\dot{Q}}{A} \tag{3.26}$$

$$u_c = \frac{u_{eff}}{C_c} \tag{3.27}$$

The friction factor, which depends on the nozzle hole wall roughness, k_r and a nozzle Reynolds number, Re_n, is determined from the following formula:

$$\frac{1}{\sqrt{\lambda}} = -2\ log \left[\frac{2.51}{Re_n\sqrt{\lambda}} + \frac{k_r}{3.71D} \right] \tag{3.28}$$

where

$$Re_n = \frac{\rho_d\ u_{eff} D}{\mu_d} \tag{3.29}$$

If cavitation takes place, i.e. $p_{ch} < p_{ch,crit}$, the development of the boundary layer along the nozzle hole wall, the cavitation region around the nozzle axis and the velocity u_{cen}, Fig.3.3, are calculated from the following governing ordinary differential equations:

- $\overline{R}_\delta > \overline{R}_{cav}$:

$$\frac{\overline{R}_\delta}{d\overline{x}} = -\ c_f \frac{1}{\frac{7}{90} + \frac{7}{60}\overline{R}_\delta} \tag{3.30}$$

$$\overline{R}_{cav} = \sqrt{\frac{49}{60} + \frac{7}{60}\overline{R}_\delta + \frac{1}{15}\overline{R}_\delta^2 - C_c} \tag{3.31}$$

$$u_{cen} = u_c \tag{3.32}$$

- $\overline{R}_\delta = \overline{R}_{cav}$:

$$\frac{\overline{R}_\delta}{d\overline{x}} = -c_f \frac{\frac{49}{240} + \frac{7}{240}\overline{R}_\delta - \frac{7}{30}\overline{R}_\delta^2}{\frac{49}{180}\overline{R}_\delta + \frac{49}{360}\overline{R}_\delta^2 - \frac{49}{120}\overline{R}_\delta^3} \tag{3.33}$$

$$u_{cen} = \frac{u_c C_c}{\frac{49}{60} + \frac{7}{60}\overline{R}_\delta - \frac{14}{15}\overline{R}_\delta^2} \tag{3.34}$$

In these formulae, $\overline{R}_\delta$, $\overline{R}_{cav}$ and $\overline{x}$ are the distances of the boundary and cavitation regions from the nozzle axis and coordinate along the axis, respectively, all normalised by the nozzle radius; c_f is the skin friction coefficient defined as:

$$c_f = \frac{1}{4}\left(\frac{u_{eff}}{u_{cen}}\right)^2 \lambda \tag{3.35}$$

where λ is calculated from Eqs.(3.29) if $\overline{R}_\delta = 0$ (fully developed turbulent flow) or, when $\overline{R}_\delta > 0$ from the following relations:

$$\begin{aligned} \frac{1}{\sqrt{\lambda}} &= -2\ log \left[\frac{2.51}{Re_n\sqrt{\lambda}} + \frac{k_r}{7.42\delta} \right] \\ Re_n &= \frac{1.633\ \rho_d\ u_{cen}\delta}{\mu_d} \end{aligned} \tag{3.36}$$

$$\delta = \frac{D}{2}(1 - \overline{R}_\delta) \tag{3.37}$$

The initial value of boundary layer thickness is taken to be $\delta = 0$ at $x_o = D$, while the initial thickness of the cavitation region, δ_{cav} at $x_o = D$ is calculated from the continuity equation, assuming a 'plug' velocity profile. Integration of Eqs.(3.30) and (3.33) give the thickness of boundary layer along the nozzle, and Eqs.(3.31) and (3.34) determine the thickness of the cavitation region, when $\overline{R}_\delta > \overline{R}_{cav}$, or a velocity u_{cen} when $\overline{R}_\delta = \overline{R}_{cav}$, respectively.

The exit area contraction ratio is obtained from the combined mass and momentum conservation equations at the nozzle exit as (see item 5 at the beginning of the section):

$$C_{ch} = \frac{u_c^2 C_c^2}{u_c^2(L)\left[\frac{49}{72} + \frac{7}{36}\overline{R}_\delta(L) + \frac{1}{8}\overline{R}_\delta^2(L) - \overline{R}_{cav}^2(L)\right] - \frac{p_{ch}}{\rho_d}} \tag{3.38}$$

If $C_{ch} \geq 1$, cavitation region does not reach the nozzle exit, and the actual exit velocity is equal to the effective velocity, ($u_{ch} = u_{eff}$). Otherwise, the actual velocity is obtained from:

$$u_{ch} = \frac{\dot{Q}}{C_{ch} A} \tag{3.39}$$

This velocity is taken to be the magnitude of initial velocity of drop/parcel injected at considered time period.

Model of atomisation processes

The model of atomisation processes assumes the following phenomena:

- The jet breaks up into a number of large structures (primary drops) forming the so-called liquid core.
- Further atomisation occurs via two mechanisms: (i) stripping of droplets from the liquid core by aerodynamic forces provoked in the surrounding gas, and (ii) collision between the primary drops in the liquid core due to their different velocities.

Essential to the model is the assumed presence of a high shear-rate region in the gas in the vicinity of a highly perturbed liquid core surface caused by cavitation [157], Fig.3.4. The stripping of these perturbations from the liquid surface in a form of secondary droplets, is attributed to the overcoming by a Saffman lifting forces over adhesive surface tension forces. The balance between these forces determines the size of secondary droplets.

The further assumptions made in the model are, [157]:

1. The diameter of the primary drops changes along their path and is equal to the diameter of the liquid core.
2. The diameter of the tip of liquid core is equal to the size of secondary droplets formed there.
3. The ejection angle of secondary droplets randomly varies between 0 and α_{max}; α_{max} is the input value to the model, and must be know from experiment.
4. The collision between the primary drops due to their different velocities, leads to the creation of secondary droplets; the size of these droplets is one-tenth of their initial size.

The liquid core is represented by a chain of primary (parent) drops which leave the nozzle with velocity u_{ch}, and whose initial diameter is taken to be equal to the nozzle diameter, D; see Fig.3.4. The exit nozzle velocity, u_{ch} is calculated from the previously described nozzle model. On its way, the primary drop loses a part of its mass by the stripping action mentioned above. It is assumed that the change of primary drop diameter along the core is given by:

$$D_d = \sqrt{(D_c^2 - D^2)\frac{x}{L_c} + D^2} \tag{3.40}$$

where D_c is the diameter at the tip of the core (set equal to the diameter of the secondary droplet formed at the tip of the core, see assumption 2), and x is the current position of the drop along the core. The steady core length L_c is calculated according to the empirical expression of Cheroudi, [41]:

$$L_c = 7.0\ D\sqrt{\frac{\rho_d}{\rho_m}} \tag{3.41}$$

The diameter of the secondary drops, D_s, is calculated from an assumed equilibrium between a disruptive lift force, F_α, provoked in the gas due to a velocity gradient in the near-core region, and a opposing surface tension force, F_σ. The former is described by the following relations; see Mei [138] and Dandy [52]:

$$F_\alpha = \begin{cases} \left[(1 - 0.3314\ \alpha^{1/2})e^{(-Re_n/10)} + 0.3314\ \alpha^{1/2}\right]\ F_S & ; Re_n \leq 40 \\ \\ 0.0524\ (\alpha Re_n)^{1/2}\ F_S & ; Re_n > 40 \end{cases} \tag{3.42}$$

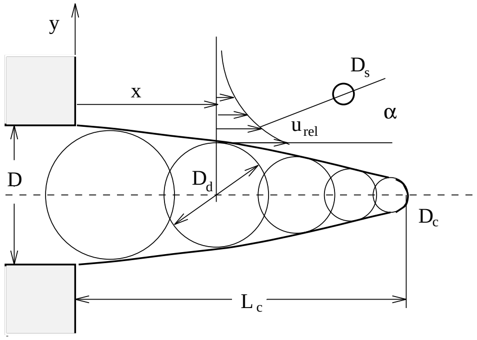

Figure 3.4: Stripping mechanism of atomisation

where α is the droplet ejection angle, Fig.3.4, and F_S is the Saffman force

$$F_S = 1.62\,\rho_m\,u_{rel}\,(\frac{\mu_d}{\rho_d}\frac{du}{dy})^{1/2}\,D_s^2 \tag{3.43}$$

The surface tension force is given by:

$$F_\sigma = \pi\sigma\,D_s \tag{3.44}$$

It is taken that the ejection angle is randomly distributed in the range $(0, \alpha_{max})$, where α_{max} is the specified spray semi-cone angle.

In order to determine the Saffman force, Eq.(3.43), a relative velocity, u_{rel}, and a radial velocity gradient, du/dy at the liquid jet surface are needed, and they are estimated according to [158] as:

$$u_{rel} = u_{ch}\left(1 - \frac{3}{4}\frac{x}{L_c}\right) \tag{3.45}$$

$$\frac{du}{dy} = \frac{2u_{rel}}{D - D_d} \tag{3.46}$$

$$Re_n = \frac{\rho_m\,u_{rel}D_s}{\mu_m} \tag{3.47}$$

The second mechanism responsible for atomisation is collision between the primary drops. This mechanism considered only for the two drops nearest to the tip of the liquid core, see Fig.3.5. If collision takes place, the leading primary drop, (subscript 1), disintegrates into two clouds of secondary droplets; the diameter of secondary droplets, D_s, and the droplet velocities in the clouds, $\mathbf{u}_{d,s1}$ and $\mathbf{u}_{d,s2}$ are

evaluated by:

$$D_s = 0.1\,D_{d1} \tag{3.48}$$

$$\mathbf{u}_{d,s1} = \mathbf{u}_{d,s} + |\mathbf{u}_{d1} - \mathbf{u}_{d2}|\,\mathbf{r} \tag{3.49}$$

$$\mathbf{u}_{d,s2} = \mathbf{u}_{d,s} - |\mathbf{u}_{d1} - \mathbf{u}_{d2}|\,\mathbf{r} \tag{3.50}$$

$$\mathbf{u}_{ds} = \frac{\mathbf{u}_{d1}m_{d1} + \mathbf{u}_{d2}m_{d2}}{m_{d1} + m_{d2}} \tag{3.51}$$

where **r** is the randomly chosen unit vector in the plane perpendicular to the injection direction, Fig.3.6.

All properties of the second drop involved in collision remain the same, except the drop velocity which is changed to:

$$\mathbf{u}_{d2}^n = \mathbf{u}_{ds} \tag{3.52}$$

This model of the collision process satisfies the overall mass and momentum conservation equations.

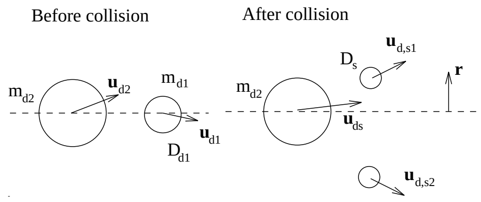

Figure 3.5: Collision in the liquid core

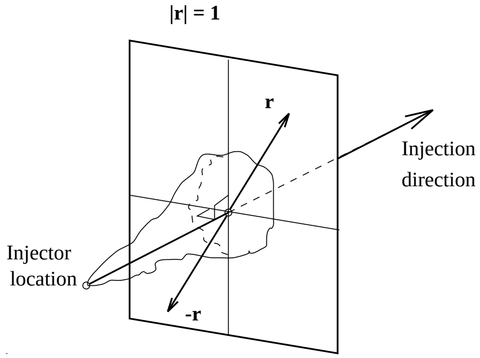

Figure 3.6: Random radial directions of droplets after collision

3.3 Droplet trajectory

Two main methods have been employed in the past to compute particle trajectories in turbulents flows: the gradient diffusion method and the stochastic method; see Faeth [68]. As the gradient diffusion method is less accurate for diesel sprays, and is not particularly convenient for implementation in a Lagrangian description of the droplet motion, in this study the stochastic approach is used. In this, a turbulence model provides the instantaneous properties of the gas environment of a droplet by random sampling.

The model employed here follows that of Gosman and Ioannides [83]. In this it is assumed that the turbulence is isotropic, and that the gas fluctuating velocity components obey a Gaussian probability density distribution with the zero mean value and standard deviation $\sigma_{u''} = (2\ k/3)^{1/2}$. Hence, the jth component of the fluctuating velocity, u''_j is selected randomly from a distribution function according to:

$$u''_j = \sigma_{u''}\ sign(2\ Y_{r,j} - 1)\ erf^{-1}(|2\ Y_{r,j} - 1|) \tag{3.53}$$

where $Y_{r,j}$ is random variable having uniform distribution in the range $(0, 1)$, and erf is the error function. The arguments of the $sign$ and erf functions are chosen in the way that their sign and magnitude determine the sign and magnitude of u''_j.

Thus, the instantaneous gas velocity, $\hat{\mathbf{u}}$ is calculated as:

$$\hat{\mathbf{u}} = \mathbf{u} + \mathbf{u}'' \tag{3.54}$$

The fluctuating velocity is taken to act on the droplet during a interaction time, τ_{int}. This is evaluated as the minimum of the eddy life time, τ_{eddy} and the transit time, τ_{tr} required for the droplet to cross the eddy. Assuming that the characteristic size of eddy is the dissipation length scale, given by:

$$L_e = C_\mu^{1/2}\,\frac{k^{3/2}}{\epsilon} \tag{3.55}$$

these times are calculated from:

$$\tau_{int} = min(\tau_{eddy}, \tau_{tr}) \tag{3.56}$$

$$\tau_{eddy} = \frac{L_e}{|\mathbf{u}''|} \tag{3.57}$$

$$\tau_{tr} = \frac{L_e}{|\hat{\mathbf{u}} - \mathbf{u}_d|} \tag{3.58}$$

where $\mathbf{u}_d$ is the droplet velocity.

There is a different way to estimate the eddy life time. Shuen et al. [188] calculate τ_{eddy} from the turbulence kinetic energy as $\tau_{eddy} = L_e/(2k/3)^{1/2}$. Both approaches yield the same results for heavier particles (diesel sprays belong to this group), since the interaction times in this case are mainly controlled by the transit times, which are computed in the same way; differences are bigger with the lighter particles, when the Gosman-Ioannides model tends to underpredict radial spreading of particles, [188].

The droplet trajectory equation, written in terms of the droplet position vector, $\mathbf{x}_d$ and velocity $\mathbf{u}_d$ reads:

$$\frac{d\mathbf{x}_d}{dt} = \mathbf{u}_d \tag{3.59}$$

As a result of our assumption that each computational parcel p is composed of a number of droplets N_p having the same location ($\mathbf{x}_p = \mathbf{x}_d$), and velocity ($\mathbf{u}_p = \mathbf{u}_d$), the parcel trajectory equation is given by:

$$\frac{d\mathbf{x}_p}{dt} = \mathbf{u}_p \tag{3.60}$$

The droplet/parcel velocity is calculated from the momentum conservation equation described in the following section.

3.4 Momentum conservation equation

The droplet momentum conservation equation used here neglects the gravitational, virtual, Bassett, Magnus and Saffman forces, and allows only for the drag forces, [68]. This simplification is justifiable due to the small influence of the other forces on the droplet motion in the diesel environment.

The gravitational forces are several orders of magnitude smaller than the drag forces; the virtual mass forces, which are proportional to the gas density (they measure the inertia of the fluid displaced by the drop motion), can be neglected on the basis of high liquid-gas density ratio (in diesel conditions $\rho_d/\rho \approx 40$), [68]. The Saffman forces depend on the velocity gradient in the gas, and are at least one order of magnitude smaller than the drag forces beyond 'a potential core' length, which is about ten nozzle diameters, [68]. In the near-injector region and regions close to the walls these forces could be important[1] (note that the MPI atomisation model allows for they effects, §(3.2.2)). The Bassett forces measure effects of unsteadiness in the relative velocity between drops and gas, and they are significant in hight turbulence ambient. Due to the complexity involved in the evaluation of these forces and the lack of their efficient numerical treatment they are neglected, [68] and [127]. The lack of evidence about drop rotating motion (spin) is the ground for neglecting the Magnus forces. It will be shown in the following section that evaluation of the dominant drag forces is not simple and suffer from uncertainties.

According to Newton's second law, the momentum conservation equation for an individual droplet, in the present framework, reads:

$$m_d \frac{d\mathbf{u}_d}{dt} = \frac{1}{2}\,\rho C_d A_d |\hat{\mathbf{u}} - \mathbf{u}_d| (\hat{\mathbf{u}} - \mathbf{u}_d) \tag{3.61}$$

where m_d, A_d and C_d are the mass, the cross-sectional area perpendicular to the relative velocity $(\hat{\mathbf{u}} - \mathbf{u}_d)$, and the drag coefficient for the droplet, respectively.

[1] Bai [17] found that the inclusion of Saffman forces gives better predictions of the droplet velocities in the near-wall region when compared with experimental results for both normal and oblique spray-wall impingement.

Drag coefficient

Determination of the droplet drag coefficient in a so complex environment as a diesel engine cylinder, where the droplets experience high temperatures (and hence high evaporation rates), pressures, and deformations, is very difficult and mainly founded on experimental studies[2]. On top of this, the proximity of neighbouring droplets, especially in the dense-spray region close to the injector, and high turbulence level in the surrounding gas, additionally affect the droplet drag coefficient. The last two effects have been almost invariably ignored in past spray models, mainly due to the lack of understanding of their mechanisms and lack of comprehensive experimental data. The works of Tsuji et al. [213] and Pei and Hayward [170] illustrate the effects of two adjacent spheres on the flow fields and transfer rates between the spheres and the surrounding gas. The numerical and experimental study of Liu et al. [131] on the droplet drag coefficient in monodispersed infinite droplet chain, showed a significant decrease of C_d compared to the value for a single droplet. In spray calculations, this effect was approximately taken into account by O'Rourke and Bracco [163], where C_d, obtained from fluidised bed results, was a function of the void fraction. They found that the influence of neighbouring droplets on the spray behaviour is already small when the inter-drop distance is not much larger than the drop diameter (inter-drop distances less than the drop diameter can be expected only in a region very close to injector). However, the motion of drops with different velocities and possible collision between drops, as well as formation of vortex wakes behind them, make the situation much more complex and beyond affordable mathematical treatment at least at present.

The influence of the gas turbulence on C_d has been the subject of intensive research, but unfortunately, at the present there are no conclusive results which can be easily implemented into mathematical models. Some studies suggest that C_d depends on the ratio between the drop diameter and turbulence length scale, see [44], and that the influence is negligible when the ratio is less than 1; others argue

[2] I wish to express my appreciation to Dr. I.Gökalp of Laboratoire de Combustion et Systèmes Réactifs, Centre National de la Recherche Scientifique - Orléans, for his valuable assistance in the matter of drop transfer coefficient correlations.

that the scale has only a secondary effect, [206] and [43]. The studies of Torobin and Clamen, [206] and [43], and those reported in them, have shown that with increasing turbulence intensity in gas, the critical Reynolds number (Re_c) above which the drag coefficient drops significantly (to 0.3), is reduced due to earlier transition from laminar to turbulent flow in the boundary layer around drop. At low turbulence intensity this transition occurs at $Re_c \approx 10^5$, which is well above the range of interest in diesel sprays; at high turbulence intensities, Re_c can drop to 400, [206]. Torobin and Gauvin, [206] found the following relation which links the critical Reynolds number and turbulence intensity:

$$Re_c \left(u'_{rms}/U_{rel}\right)^2 = 45$$

where u'_{rms} and U_{rel} are the rms value of gas velocity fluctuations, and magnitude of relative velocity between droplet and gas. In the regime $Re < Re_c$, C_d is generally found to increase with turbulence intensity.

The fact that there are no conclusive results and opinions about both effects, led us to ignore them in this study and adopt the broadly-accepted practice in spray calculations of using the drag coefficient for a single sphere and disregarding the influence of turbulence. Certainly, the effect of evaporation on the drag coefficient must be taken into account; below a number of proposed correlations are reviewed.

It is conventional to equate the drag coefficients of evaporating droplets with those of a smooth solid sphere moving in steady-state conditions. In this case C_d is a function of the approaching Reynolds number, i.e. the 'standard drag curve', [215] and [67]. Comparison of experimental results with the 'standard drag curve' have shown significant scattering. There are two main reasons for this difference:

- Evaporation changes the composition and temperature field of gas near the droplet surface; (in general, the viscosities of various fuel vapours are lower than air at the same temperature).
- Fuel vapour efflux from the droplet surface affects the velocity field around the droplet, causing the changes in friction and pressure (form) drag.

The discrepancies may also be due to the arbitrariness of the choice of mean conditions of the droplet surroundings (the temperature and gas composition).

Early drag measurements by Ingebo [109] on evaporating ethanol droplets in the Reynolds number range of 6 to 400 resulted in correlation:

$$C_d = 27 Re^{-0.84} \tag{3.62}$$

which lies below the 'standard curve'. The measurements of Eisenklam et al. [59] of free-falling, evaporating and burning droplets of various liquids in hot air have shown a reduction of the drag coefficient due to the mass transfer from the droplet surface. They have correlated the drag coefficient to the 'standard' drag based on the free stream conditions, and to the mass transfer number B, defined later on by Eq.(3.69). Hubbard et al. [107] have found for the case of evaporating droplets in a stagnant environment that the best agreement with measurements can be obtained when the viscosity is evaluated using the so-called '1/3 rule', described below. Yuen and Chen [225], in an experimental study in the Reynolds number range of 1 to 1000, confirmed Hubbard's findings. They found that the drag coefficient obtained from:

$$\begin{aligned} C_d &= \frac{24}{Re_r}\left(1 + \frac{1}{6}\, Re_r^{2/3}\right) \;;\; Re_r \leq 1000 \\ C_d &= 0.44 \;;\; Re_r > 1000 \end{aligned} \tag{3.63}$$

correlates well with the experimental results if the Reynolds number, Re_r is evaluated from :

$$Re_r = \frac{\rho |\hat{\mathbf{u}} - \mathbf{u}_d| D_d}{\mu_r} \tag{3.64}$$

where ρ is the free stream gas density, and μ_r is the gas viscosity based on the '1/3 rule' reference state, defined below as:

$$T_r = T_d + \frac{1}{3}(T_\infty - T_d) \tag{3.65}$$

$$Y_r = Y_d + \frac{1}{3}(Y_\infty - Y_d) \tag{3.66}$$

In these expressions T and Y denote the temperature and fuel vapour mass fraction, while the subscripts d and ∞ stand for the droplet and free stream conditions, respectively; see Fig.3.7. In the Reynolds number range of 10 to 260, they also

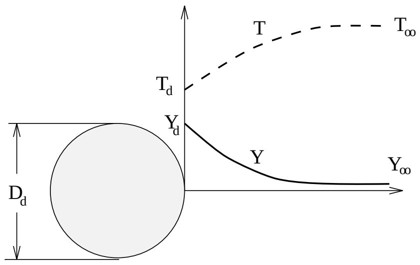

Figure 3.7: Temperature and fuel vapour mass fraction distributions arround an evaporating droplet

proposed the following correlation for the drag coefficient, [180]:

$$C_d = (1+B)^{-0.2}\frac{24}{Re}(1+0.2Re^{0.63}) \tag{3.67}$$

where Re and B are evaluated from:

$$Re = \frac{\rho|\hat{\mathbf{u}} - \mathbf{u}_d|D_d}{\mu} \tag{3.68}$$

$$B = \frac{c_p(T_\infty - T_d)}{L(T_d)} \tag{3.69}$$

Here, μ is the gas viscosity based on the film condition, i.e., at the arithmetic mean temperature and fuel vapour mass fraction. The disadvantage of this correlation is that it is only valid for values of the mass transfer number B in the narrow range from 0 to 3, which together with the limitation on the Reynolds number, makes this correlation unsuitable for diesel spray applications. (The maximum Reynolds number in diesel sprays is usually greater than 1000, and the mass transfer number for the droplets whose temperature approaches the critical fuel temperature, which is alway lower than the gas temperature in a cylinder, becomes large because the fuel latent heat, $L(T_d)$ then tends to zero; see Eq.(3.69).)

There have been many numerical studies of the drag coefficient of evaporating and burning droplets. Two recent ones which found the correlation given by Eq.(3.63) to be valid we will be mentioned here. Renksizbulut and Yuen, [180] in an analysis of variable-property flow past solid and liquid droplets, in the Reynolds number range from 1 to 100, have found a good agreement with experimental results. The same correlation is successfully used by Abramzon and Sirignano, [2] in their numerical studies of the vapourisation of a moving fuel droplet.

In spray calculations, Beshay [27] and Tabrizi, [200] have used the drag coefficient evaluated at the arithmetic mean temperature and composition, according to:

$$\begin{aligned} C_d &= \frac{24}{Re}(1+0.15Re^{0.687}) \;\; ; \; Re \le 1000 \\ C_d &= 0.44 \;\; ; \; Re > 1000 \end{aligned} \tag{3.70}$$

In this study, the correlations given by Eqs. (3.63) and (3.70) will both be used to assess the influence of different drag coefficients on the overall spray behaviour.

Momentum relaxation time

The drop momentum conservation equation (3.61) can be recast by introducing the momentum relaxation time, $\tau_{\mathbf{u}}$ defined as:

$$\tau_{\mathbf{u}} = \frac{2\, m_d}{\rho C_d A_d|\hat{\mathbf{u}} - \mathbf{u}_d|} = \frac{4}{3}\frac{\rho_d D_d}{\rho C_d|\hat{\mathbf{u}} - \mathbf{u}_d|} \tag{3.71}$$

into the working version of the drop momentum conservation equation:

$$\frac{d\mathbf{u}_d}{dt} = \frac{1}{\tau_{\mathbf{u}}}(\hat{\mathbf{u}} - \mathbf{u}_d) \tag{3.72}$$

or in the term of computational parcels:

$$\frac{d\mathbf{u}_p}{dt} = \frac{1}{\tau_{\mathbf{u}}}(\hat{\mathbf{u}} - \mathbf{u}_p) \tag{3.73}$$

The magnitude of the momentum relaxation time measures the mutual momentum interaction between the droplets and surrounding gas. High values of $\tau_{\mathbf{u}}$ mean practically undisturbed droplet motion (this is the case with the bigger droplets), while very low values denote a state when droplets almost completely follow the gas motion (typical of small droplets).

Momentum contribution to the gas phase

An additional source term, $\mathbf{s}^d_{\mathbf{u}}$, in the gas momentum conservation equation (see Eq.(2.44)) originates from the momentum exchange between the drops and gas via the drag force. A computational parcel contains N_d droplets, so its mass is $m_p = N_d m_d$. The ensemble-averaged value of the total momentum exchange rate at location $\mathbf{x}$ is therefore given by the following formula; see Appendix B.1:

$$\mathbf{s}^d_{\mathbf{u}}(\mathbf{x}) = - \lim_{\substack{\Delta t \to 0 \\ \delta V \to 0}} \frac{1}{\Delta t \delta V} \int_{\delta V} \left(\sum_{p=1}^{p=N_p} \int_t^{t+\Delta t} \delta(\mathbf{x} - \mathbf{x}_p) \frac{d}{dt}(m_p\, \mathbf{u}_p)\, dt \right) dV \qquad (3.74)$$

where δ denotes the Dirac delta function in the 3-D space, and the summation is performed over all N_p parcels.

3.5 Mass conservation equation

The droplet mass change due to evaporation is calculated from the mass conservation equation [31] given below:

$$\frac{dm_d}{dt} = -\pi D_d\, \mathcal{D} Sh\, \rho_v\, ln \frac{P - P_{v,\infty}}{P - P_{v,s}} \qquad (3.75)$$

where $\mathcal{D}$ is the mass diffusivity, Sh the Sherwood number, P the total pressure of gas mixture, and $P_{v,s}$ and $P_{v,\infty}$ stand for the partial fuel vapour pressure at the droplet surface and far from it, respectively. The fuel vapour density, ρ_v is evaluated from the ideal gas law for the fuel vapour as:

$$\rho_v = \frac{P}{R_v T_m} \qquad (3.76)$$

where T_m denotes the mean temperature ($T_m = \frac{1}{2}(T_d + T)$), and R_v stands for the fuel vapour gas constant.

The Sherwood number is calculated from the following correlation, [173]:

$$Sh = 2.0 + 0.6\, Re^{1/2}\, Sc^{1/3} \qquad (3.77)$$

where Sc is Schmidt number, defined below and calculated at the mean temperature T_m:

$$Sc = \frac{\mu}{\rho \mathcal{D}} \qquad (3.78)$$

It should be noted that Eq.(3.75) assumes that the mass diffusion results only from the fuel vapour concentration gradient, neglecting thermal diffusion. Errors incurred by this assumption and by neglecting the Dufour effect in the drop energy

equation are of the order of 10%, [67]. Therefore, complicating the model by including these effects, with respect to all uncertainties of empirical correlations and material properties involved in the model, is not justifiable within the context of the current study.

Evaporation relaxation time

An evaporation relaxation time τ can be defined by the following expression:

$$\tau = \frac{m_d}{\pi D_d\, \mathcal{D} Sh\, \rho_v\, ln \frac{P - P_{v,\infty}}{P - P_{v,s}}} = \frac{\rho_d D_d^2}{6\, \mathcal{D} Sh\, \rho_v\, ln \frac{P - P_{v,\infty}}{P - P_{v,s}}} \qquad (3.79)$$

Then, Eq.(3.75) can be cast into its operational form for the individual droplet and parcel respectively:

$$\frac{dm_d}{dt} = -\frac{m_d}{\tau} \qquad (3.80)$$

$$\frac{dm_p}{dt} = -\frac{m_p}{\tau} \qquad (3.81)$$

Mass contribution to the gas phase

The ensemble-averaged evaporation rate with which the spray locally contributes to the gas phase, changing the total mass and composition of the mixture is given by (see Appendix B.1):

$$s^d(\mathbf{x}) = - \lim_{\substack{\Delta t \to 0 \\ \delta V \to 0}} \frac{1}{\Delta t \delta V} \int_{\delta V} \left(\sum_{p=1}^{p=N_p} \int_t^{t+\Delta t} \delta(\mathbf{x} - \mathbf{x}_p) \frac{d}{dt} m_p\, dt \right) dV \qquad (3.82)$$

3.6 Energy conservation equation

During droplet evaporation, heat from the surrounding gas is transferred to the liquid surface. Part of this heat is spent heating up the liquid fuel, and the rest to overcome the latent heat of vapourisation.

The droplet temperature, T_d, is calculated from the drop energy conservation equation [31] given below:

$$m_d \frac{d}{dt} [\, c_l (T_d - T_{ref})] = \dot{Q}_d + \frac{dm_d}{dt}\, h_v(T_d) \qquad (3.83)$$

where c_l is the specific heat capacity of liquid fuel, the subscript ref denotes the reference state, and h_v is the latent heat of vapourisation.

The rate of heat transfer between the gas and the droplet, $\dot{Q}_d$ is calculated from:

$$\dot{Q}_d = \pi D_d \, k_h \, Nu \, f(T - T_d) \tag{3.84}$$

$$f = \frac{z}{e^z - 1} \tag{3.85}$$

$$z = -\frac{c_{p,v} \frac{dm_d}{dt}}{\pi D_d \, k_h \, Nu} \tag{3.86}$$

where f is a factor [61] which corrects the amount of heat exchange due to the presence of mass transfer, $c_{p,v}$ is the fuel vapour specific heat at constant pressure, k_h the mixture thermal conductivity, Nu the Nusselt number, and T the gas temperature.

The Nusselt number is evaluated according to the Ranz-Marshall correlation, [173] as:

$$Nu = 2.0 + 0.6 \, Re^{1/2} \, Pr^{1/3} \tag{3.87}$$

where Pr is the Prandtl number, defined below and calculated at the mean temperature T_m:

$$Pr = \frac{c_p \mu_m}{k_h} \tag{3.88}$$

Here, c_p denotes the specific heat capacity of the surrounding gas at constant pressure.

Heat transfer relaxation time

In order to simplify Eq.(3.83) the heat transfer relaxation time is introduced, defined as:

$$\tau_e = \frac{m_d c_l}{\pi D_d \, k_h \, Nu} = \frac{\rho_d \, D_d^2 \, c_l}{6 \, k_h \, Nu} \tag{3.89}$$

By using Eqs.(3.79) and (3.89) and after some rearrangement the drop energy conservation equations Eq.(3.83) can be recast into the following form:

$$\frac{dT_d}{dt} = \frac{f}{\tau_e}(T - T_d) - \frac{1}{c_l \, \tau} \, h_v(T_d) \tag{3.90}$$

In this equation, the argument of the correction function f is calculated from:

$$z = \frac{c_{p,v} \, \tau_e}{c_l \, \tau} \tag{3.91}$$

Because all droplets which belong to the same parcel p have equal properties, Eq.(3.90), written with the subscript p instead of d, is valid for the whole computational parcel, i.e.:

$$\frac{dT_p}{dt} = \frac{f}{\tau_e}(T - T_p) - \frac{1}{c_l \, \tau} h_v(T_p) \tag{3.92}$$

Energy contribution to the gas phase

The ensemble-averaged rate of the spray contribution to the gas energy at location $\mathbf{x}$ is calculated from the following expression:

$$s_e^d(\mathbf{x}) = - \lim_{\substack{\Delta t \to 0 \\ \delta V \to 0}} \frac{1}{\Delta t \delta V} \int_{\delta V} \left(\sum_{p=1}^{p=N_p} \int_t^{t+\Delta t} \delta(\mathbf{x} - \mathbf{x}_p) \, \dot{s}_{e,p} \, dt \right) dV \tag{3.93}$$

where

$$\dot{s}_{e,p} = \frac{d}{dt} [\, m_p \, c_l(T_p - T_{ref})] \tag{3.94}$$

or in terms of the mass and energy relaxation times:

$$\dot{s}_{e,p} = m_p \left\{ \frac{[c_l(T_p - T_{ref}) + h_v(T_p)]}{\tau} + \frac{c_l f \, (T - T_p)}{\tau_e} \right\} \tag{3.95}$$

3.7 Breakup model

Liquid drops detached from the jet liquid core, continuing their motion through the gas may, under certain conditions, be disintegrated into smaller droplets. This phenomenon is know in literature as the drop breakup or secondary atomisation. The exact mechanisms behind the drop breakup, despite numerous experimental and theoretical works, are still not completely understood. As a result of this, there are many uncertainties in the quantitative description of the process.

A simplified picture of the drop breakup process for the purpose of addressing relevant forces involved, can be summarised as follows. Relative motion between the drop and the surrounding gas causes a non-uniform pressure and shear stress distribution on the drop surface. These external forces, opposed by the internal (normal and shear) forces and surface tension forces, deform the drop causing further changes in the external stress distribution. At the moment when these external forces can not be balanced by the opposing forces, the drop breaks up into smaller droplets, which are much more efficient in resisting the external stress variations because of their smaller diameters (e.i. the surface tension forces are relatively stronger). However, it is possible that these droplets will also undergo further breakup, until a stable condition is reached when further breakup cannot occur.

From the picture above, it is clear that pressure and shearing forces at the droplet surface represent forces of disruption, while the surface tension and liquid viscous forces are the stabilising forces. The ratios of these forces, expressed in the form of Weber and Ohnesorge numbers[3] (the Weber and Ohnesorge numbers are the ratios of drag and liquid viscous forces to surface tension forces; ther definitions are given later), are usually used as the independent variables in correlations for distinguishing the various observed breakup modes.

According to Pilch and Erdman [171], there are five distinct breakup modes, but the two most important for the diesel spray are bag breakup and stripping breakup. While the cause of the bag-type breakup is attributed to the liquid deflection at the forward stagnation point due to the pressure distribution, followed by a creation of a bag-shape shell and its disintegration, the views regarding the mechanisms of stripping breakup point to the boundary layer separation process, and the formation and growth of the surface waves on the droplet surface; see [119], [221] and [222].

Many experiments have shown the existence of a critical Weber number below which drop breakup does not occur. From collected data from a wide literature search for a variety of fluids and both gas-liquid and liquid-liquid systems, Pilch and Erdman [171] obtained a correlation for the critical Weber number; see Fig.3.8. It is given as a function of the Ohnesorge number, which accounts for the liquid properties only, assuming that the viscosity of the gas phase is small compared to the liquid phase. When the Ohnesorge number is small ($On < 0.1$), the critical Weber number has an almost constant value of 6. The breakup of droplets under the diesel engine conditions belongs to this region. Drop breakup at higher Ohnesorge numbers, which mean a relatively stronger effect of the liquid viscosity, is progressively more difficult (Hsiang and Faeth [106] observed no breakup beyond $On \approx 4$).

[3] The Ohnesorge number is sometimes referred to as the viscosity number, the Laplace number or Z number.

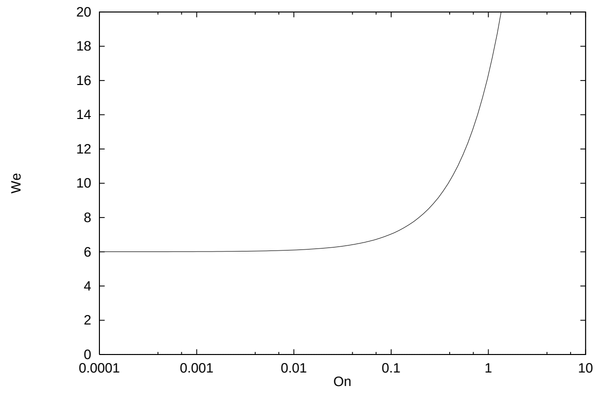

Figure 3.8: Critical Weber number versus Ohnesorge number; the curve is given by $We_c = 6(1 + 1.077On^{1.6})$; On - Ohnesorge number: $On = \mu_d/(\rho_d D_d \sigma)^{1/2}$.

For the purpose of modelling, it is desired to determine the rate of the droplet diameter change, the breakup time, and the properties of the created droplets. As a complete theoretical study of this problem, which would include the details of the drop deformation and the liquid motion inside the drop, has never been made, it was necessary to resort to the experiment and dimensional analysis. The result of this are empirical correlations which determine criteria for the breakup modes and other relevant parameters. In this study, two drop breakup models are implemented, the Reitz-Diwakar model and the model of Pilch and Erdman. Their descriptions are given below.

3.7.1 The Reitz-Diwakar model

The model adopted in this study is based on the correlations given in Nicholls [150], and reported by Reitz and Diwakar [178], [179], and Reitz [176]. The following two regimes are considered:

1. Bag breakup, when the Weber number is:

$$We = \frac{\rho_m u_{rel}^2 D_d}{2\sigma} > C_{bag} \tag{3.96}$$

and

2. Stripping breakup, when

$$\frac{We}{Re^{1/2}} > C_{strip} \tag{3.97}$$

Here C_{bag}, C_{strip} are the model coefficients, given in Table 3.2, and Re is the Reynolds number defined by Eq.(3.64).

The above criteria are used for the calculation of the stable diameters, below which breakup does not occur:

$$D_{s,bag} = 2\, C_{bag} \frac{\sigma}{\rho_m u_{rel}^2} \tag{3.98}$$

$$D_{s,strip} = 4\, C_{strip}^2 \frac{\sigma^2}{\rho_m u_{rel}^3 \mu_m} \tag{3.99}$$

If either of the two breakup criteria is satisfied, the droplet diameter changes according to the following diameter rate equation:

$$\frac{dD_d}{dt} = -\frac{D_d - D_s}{\tau_b} \tag{3.100}$$

where D_s and τ_b are the corresponding stable diameter and breakup time. The latter is estimated from:

$$\tau_{bag} = C_b D_d \sqrt{\frac{\rho_d D_d}{\sigma}} \tag{3.101}$$

or

$$\tau_{strip} = \frac{C_s D_d}{u_{rel}} \sqrt{\frac{\rho_d}{\rho_m}} \tag{3.102}$$

Here, C_b and C_s are the breakup time coefficients given in Table 3.2.

C_{bag}	C_{strip}	C_b	C_s
6.0	0.5	0.785	10.0

Table 3.2: Coefficients of the droplet breakup model

There is uncertainty about the values of the above coefficients. Reitz and Diwakar [179] used $C_s = 10$, Nicholls [150] gave $C_s = 4$ and O'Rourke and Amsden [164] have suggested that $C_s = \sqrt{3}/2$. Also, in [164] the authors criticise the use of the breakup criterion of Eq.(3.97) because the viscosity was not varied in an adequate range in the experiments from which it was derived. It has been observed in [164] and [176] that if only breakup criterion Eq.(3.99) is used for the determination of the stable drop size, instead of both (3.98 and 3.99), the resulting drop sizes in spray are very similar. Despite this simplification, in this study both criteria are used.

During the breakup process droplet mass and total mechanical energy - composed of the kinetic and surface energy - are conserved. The redistribution between the kinetic energy and the surface energy is calculated by the reduction of the droplet's three velocity components by the factor δu, evaluated from the following expression, [178]:

$$\delta u = 1 - \left(\frac{D_d}{D_d^n} - 1\right) \frac{3\,\sigma}{2\,\rho_d\, D_d\, (u_d)^2} \tag{3.103}$$

Here the superscript n denotes conditions after breakup. For consistency, the droplet momentum loss is added to the gas momentum.

3.7.2 Pilch-Erdman' correlations

This drop breakup model is based on correlations obtained from measurement data collected by an exhaustive literature survey by Pilch and Erdman [171]. They found correlations for the critical Weber number, shown in Fig.3.8, and breakup time. Their analysis included also data on the drop velocity history and drop sizes, which enabled them to propose a concept of the maximum stable diameter below which breakup does not take place. This concept challenges the conventional estimate of a stable drop diameter based on a critical Weber number, and allows for the effect of drop acceleration. They assume that the stable diameter is affected in two ways; (i) the decrease of droplet Weber number because of the new smaller droplet diameter, and (ii) the decrease in relative velocity between the droplets and the flow field, due to the changes in droplet acceleration (as a result of the decreased droplet diameter). They showed that this modified estimate produces larger droplets, which is in better agreement with the experimental results than the conventional practice.

The drop breakup occurs if the drop Weber number, We is greater than the critical Weber number, We_c. This critical Weber number, which allows for the viscous effects via the Ohensorge number On, is given by:

$$We_c = 6\,(1 + 1.077\, Oh^{1.6}) \tag{3.104}$$

$$Oh = \frac{\mu_d}{(\rho_d D_d \sigma_d)^{1/2}} \tag{3.105}$$

In the model five breakup regimes are distinguished, Fig.3.9. They are characterised by dimensionless total breakup times $\overline{\tau}_b$ given by the following formulae:

1. Vibrational breakup,

$$\overline{\tau}_b = 6\,(2\,We - 12)^{-0.25} \quad ; 6 < We \leq 9 \tag{3.106}$$

2. Bag breakup,

$$\overline{\tau}_b = 2.45\,(2\,We - 12)^{0.25} \quad ; 9 < We \leq 22 \tag{3.107}$$

3. Bag-and-stamen breakup,

$$\overline{\tau}_b = 14.1\,(2\,We - 12)^{-0.25} \quad ; 22 < We \leq 175 \tag{3.108}$$

4. Sheet stripping,

$$\overline{\tau}_b = 0.766\,(2\,We - 12)^{0.25} \quad ; 175 < We \leq 1335 \tag{3.109}$$

5. Wave crest stripping,

$$\overline{\tau}_b = 5.5 \quad ; 1335 < We \tag{3.110}$$

Here We and $\overline{\tau}_b$ are defined as:

$$We = \frac{\rho_m |\mathbf{u} - \mathbf{u}_d|^2 D_d}{2\,\sigma} \tag{3.111}$$

$$\overline{\tau}_b = \tau_b \frac{|\mathbf{u} - \mathbf{u}_d|}{D_d} \left(\frac{\rho_m}{\rho_d}\right)^{1/2} \tag{3.112}$$

The stable diameter is evaluated from:

$$D_s = 2\,We_c \frac{\sigma}{\rho_m |\mathbf{u} - \mathbf{u}_d|^2} \left(1 - \frac{V_d}{|\mathbf{u} - \mathbf{u}_d|}\right)^{-2} \tag{3.113}$$

where V_d is given by:

$$V_d = |\mathbf{u} - \mathbf{u}_d| \left(\frac{\rho_m}{\rho_d}\right)^{1/2} (B_1 \overline{\tau}_b + B_2 \overline{\tau}_b^2) \tag{3.114}$$

Coefficients B_1 and B_2 are chosen to fit experimental data; Their values are given in Table 3.3. The droplet diameter changes according to the Eq.(3.100).

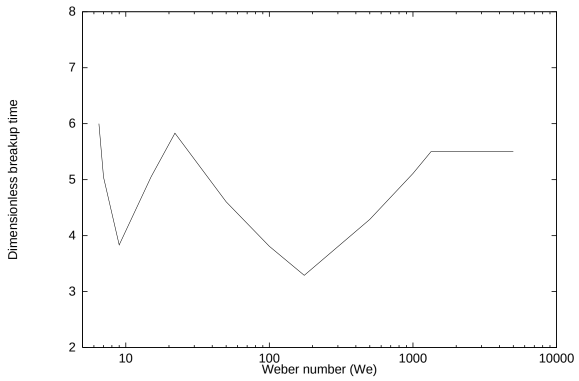

Figure 3.9: Dimensionless breakup time vs. Weber number

B_1	B_2
0.375	0.236

Table 3.3: Coefficients of Pilch-Erdman' breakup correlations

3.8 Droplet-droplet collision

It was shown by Bracco and co-workers [35], [163] that collision processes are important in sprays, especially in regions with high droplet number density. Collision is responsible for the growth of the droplets, due to the coalescence, and to the exchange of momentum between droplets. In this sense, the collision and breakup processes can be seen as a two competing mechanisms whose outcomes determine the local droplet size distribution. The results of collision can lead to the formation of a many new droplets (parcels) with different properties. Their numerical treatment could quickly fill computer storage, so some approach, satisfying the conservation principles, and avoiding this problem, must be adopted.

The model of droplet-droplet collisions used in this study follows that of O'Rourke, [162]. It is based on the proposals for computing collision processes in rain clouds by Brazier-Smith et al. [36], by the statistical discrete-particle method.

The model distinguishes three types of collision outcome: permanent coalescence, separation, and bouncing; see Fig.3.10. During collision droplets can exchange mass, momentum and energy. However, droplets which belong to the same computational parcel cannot collide mutually. This is the result of assumption that all the drops from the considered parcel behave exactly the same; i.e. they have not only the same sizes, velocities, temperatures, etc., but they also interact in the same way with the same turbulence eddy.

A statistical approach is used to avoid increasing the total number of parcels. In some cases during a coalescence the smaller diameter droplets are all absorbed, in which case the number of parcels is reduced by one. Once the type of collision has been resolved, then all the droplets in the parcel with larger diameter, called the collector, undergo collisions with the droplets from other parcel.

Probability of collision

It is assumed that for each pair of parcels, collisions only occur if they lie in the same computational cell. This assumption is a bit dubious because collision between two spatially very close parcels which reside in different computational cells is a priori excluded, in contrast to a pair of possibly more distant parcels in the same

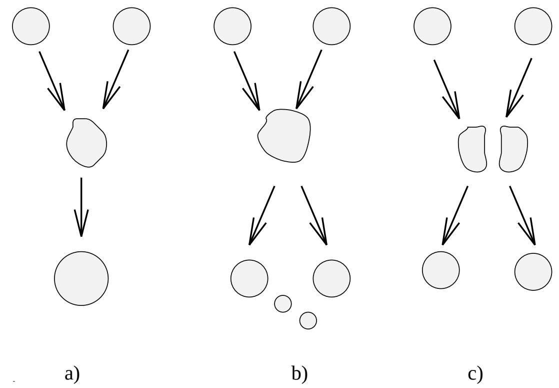

Figure 3.10: Types of collision; a) Permanent coalescence, b) Separation, c) Bouncing

computational cell. This feature of the collision model is one of the reasons for the strong mesh dependency of spray simulations[4].

The droplets in parcels are considered to be uniformly distributed through the cell where they currently reside. The collision frequency ν of the collector droplets, (these being the droplets with the bigger diameter), with all droplets in the other parcel is given by:

$$\nu = \frac{\pi}{4}\left(D_{d,1} + D_{d,2}\right)^2 \left|\mathbf{u}_{d,1} - \mathbf{u}_{d,2}\right| E_{1,2} \frac{N_{d,2}}{\delta V} \tag{3.115}$$

where the subscripts 1 and 2 refer to the collector and the droplet, respectively, $N_{d,2}$ is the number of droplets in the parcel, and δV is the cell volume. The term $N_{d,2}/\delta V$ evidently represents the droplet number density. Eq.(3.115) is 'borrowed' from the kinetic theory of gases, but because of the differences between droplet and molecular collisions[5], the collision efficiency, $E_{1,2}$ is introduced to allow for these effects.

[4] An alternative approach which could exclude this assumption, would be to introduce a dimension to the parcel cloud, to enable calculation of a parcel number density, needed for a probability calculation. However, this will require new assumptions, and the model will be very complex.

[5] There are two main differences. Firstly, the droplet motion is influenced by the gas, so the collision cross-section will differ from that calculated assuming straight-line trajectories. Secondly, collisions between droplets can result in a greater number of outcomes,(i.e. coalescence and separation), than collisions between molecules.

The collision efficiency is defined as the ratio of the effective collision cross-section to that obtained by assuming the straight-line trajectories of droplets, and is evaluated from [120] as:

$$E_{1,2} = \left(1 + \frac{3}{4}\, ln\, \frac{2\,W}{W - 1.214}\right)^{-2} \quad ; \quad W > 1.214 \tag{3.116}$$

$$E_{1,2} = 0.0 \quad ; \quad W \leq 1.214$$

where W is the dimensionless stopping distance given by:

$$W = \frac{\rho_{d,2}\, |\mathbf{u}_{d,1} - \mathbf{u}_{d,2}|\, D_{d,2}^2}{9\,\mu_m D_{d,1}} \tag{3.117}$$

Langmuir [120] found that when $W \ll 1.0$ then $E_{1,2} \approx 0.0$ because the small droplet is carried around the larger one by the gas flow, and collision will not occur. In the other extreme when $W > 1.0$, he found that $E_{1,2} \approx 1.0$.

The probability that the collector droplet undergoes n collisions with the droplets during a time interval δt, follows a Poisson distribution with the mean value $\overline{n} = \nu \delta t$:

$$P_n = \frac{(\overline{n})^n}{n!}\, e^{-\overline{n}} \tag{3.118}$$

The case $n = 0$ gives probability of no collisions $P_0 = e^{-\overline{n}}$. To determine whether collisions take place between the droplets in considered parcels, a random number $Y_{r,1}$ in the interval $(0, 1)$ is chosen. If $Y_{r,1} < P_0$, no collision occurs.

It should be noted that there is a characteristic time scale associated with collision, namely the collision time $1/\nu$, and the computational time step Δt must therefore be small compared to this. However, with the statistical approach employed here, as long as only a few collisions are so affected, this time step limit may be exceeded without either instability occurring, or the accuracy of the results being compromised, [162].

The outcomes of collision are illustrated in flow-chart in Fig.3.11, while the descriptions of the particular collision modes are given in the next section.

Separation

The experimental and theoretical study of Brazier-Smith et al. [36] was devoted to finding the criterion for distinguishing the separation type of collisions from the

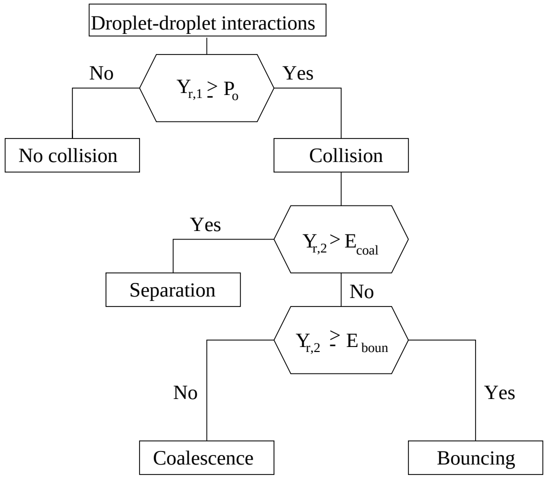

Figure 3.11: Droplet-droplet interactions

coalescence type. Their experiments have shown that when the collision involves the droplets of nearly equal size and the impact parameter exceeds some critical value, the droplets will separate. Often two or three smaller satellite droplets will be produced in the process.

In the theoretical part of their study they have found 'that in order for separation to occur the rotational energy must exceed the additional surface energy required to form the initial drops from the coalescence drop-pair'. In mathematical terms, this condition reads:

$$E \geq E_{coal} \tag{3.119}$$

where E and E_{coal} are the coalescence efficiency and its critical value, respectively, defined as:

$$E = \left(\frac{2\,X}{D_{d,1} + D_{d,2}}\right)^2 \tag{3.120}$$

$$E_{coal} = min\left[\frac{2.4\, f(\gamma)}{We_L}, 1\right] \tag{3.121}$$

$$f(\gamma) = \gamma^3 - 2.4\,\gamma^2 + 2.7\,\gamma \tag{3.122}$$

$$\gamma = \frac{D_{d,1}}{D_{d,2}} \tag{3.123}$$

In the above expressions, X is the distance between the centres of the droplets perpendicular to the relative velocity vector, see Fig.3.12, and We_L is the droplet Weber number, which measures the relation between the droplet inertial and surface tension forces, defined by:

$$We_L = \frac{\rho_{d,2} \left| \mathbf{u}_{d,1} - \mathbf{u}_{d,2} \right|^2 D_{d,2}}{2\, \sigma_2}. \tag{3.124}$$

where σ is the surface tension coefficient.

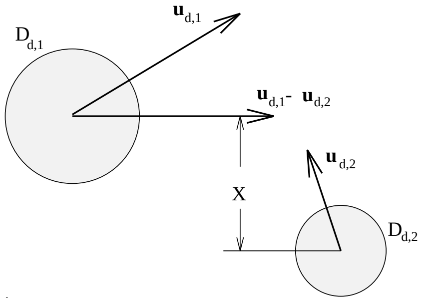

Figure 3.12: Collision; 1 - collector, 2 - droplet

To decide about the type of collision, i.e. whether it results in the coalescence or separation, a random value of E in the range $(0, 1)$, $Y_{r,2}$ is chosen. If

$$Y_{r,2} \geq E_{coal} \tag{3.125}$$

separation occurs. Note that this condition is equivalent to:

$$X \geq X_c \tag{3.126}$$

where X_c is the critical inter-drop distance when the separation is still possible, derived from Eqs.(3.120) and (3.121) as follows:

$$X_c = \frac{D_{d,1} + D_{d,2}}{2} E_{coal}^{1/2} \tag{3.127}$$

and X is the randomly chosen droplet distance given by:

$$X = \frac{D_{d,1} + D_{d,2}}{2} Y_{r,2}^{1/2} \tag{3.128}$$

As Brazier-Smith et al. did not measure the drop velocities after separation, O'Rourke [162] derived their values from the conservation of the linear and angular momentum and energy under assumption that the drops retain their original size. He obtained the following expressions for the droplet velocities after separation, denoted by the superscript n:

$$\begin{aligned} \mathbf{u}_{d,1}^n &= \frac{1}{m_{d,1} + m_{d,2}} \left[(m\mathbf{u})_{d,1} + (m\mathbf{u})_{d,2} + m_{d,2} (\mathbf{u}_{d,1} - \mathbf{u}_{d,2})\, f_{\mathbf{u}} \right] \\ \mathbf{u}_{d,2}^n &= \frac{1}{m_{d,1} + m_{d,2}} \left[(m\mathbf{u})_{d,1} + (m\mathbf{u})_{d,2} - m_{d,2} (\mathbf{u}_{d,1} - \mathbf{u}_{d,2})\, f_{\mathbf{u}} \right] \end{aligned} \tag{3.129}$$

where

$$f_{\mathbf{u}} = \frac{X - X_c}{\frac{D_{d,1} + D_{d,2}}{2} - X_c} = \frac{Y_{r,2}^{1/2} - E_{coal}^{1/2}}{1 - E_{coal}^{1/2}} \tag{3.130}$$

Coalescence

In the case that condition Eq.(3.125) is not satisfied, i.e.:

$$Y_{r,2} < E_{coal} \tag{3.131}$$

two different outcomes of collision are possible: permanent coalescence and bouncing. If the drops' kinetic energy is high enough to overcome the resistance of the air film trapped between them, the outcome of the collision will be coalescence. Then, the following condition will be satisfied:

$$Y_{r,2} < E_{boun} \tag{3.132}$$

where E_{boun} is the bouncing efficiency, defined, according to Jayaratne [111] as:

$$E_{boun} = \left(\frac{We_L}{2.4\, f(\gamma)} \right)^{1/3} \tag{3.133}$$

The number of droplets M which take part in the coalescence with each collector droplet is determined by:

$$\sum_{i=0}^{i=M-1} P_i \; < Y_{r,2} \; < \sum_{i=0}^{i=M} P_i \tag{3.134}$$

and they are removed from their associated parcel until the complete depletion of the parcel, when M is recomputed so that all droplets take part in coalescence. The remaining number of droplets in parcel 2, $N^n_{d,2}$ is calculated from:

$$N^n_{d,2} = N_{d,2} - M\, N^o_{d,1} \tag{3.135}$$

where $N_{d,1}$ is the number of collector droplets, and superscripts n denotes the value after coalescence. The other droplet properties in parcel 2, (velocity and temperature) stay the same.

The new properties of the collector droplet are estimated from the conservation of mass, m_d momentum, $(m\mathbf{u})_d$ and energy, $(mc_pT)_d$ according to:

$$\begin{aligned} m^n_{d,1} &= m_{d,1} + m_{d,2}M \\ (m\mathbf{u})^n_{d,1} &= (m\mathbf{u})_{d,1} + (m\mathbf{u})_{d,2}M \\ (mc_lT)^n_{d,1} &= (mc_lT)_{d,1} + (mc_lT)_{d,2}M \end{aligned} \tag{3.136}$$

However, the number of droplets in the collector remains unchanged; $N^n_{d,1} = N_{d,1}$, and the new drop diameter is calculated based on the new drop mass.

Bouncing

The bouncing type of collision occurs at low drop velocities and is accompanied by the deformation of each of the approaching droplet pair approximately into the shape of an oblate spheroid due to the air film trapped between them. A threshold condition for bouncing is given by:

$$Y_{r,2} \geq E_{boun} \tag{3.137}$$

where E_{boun} is determined by Eq.(3.133). As the drops involved in bouncing do not touch each other, they retain their size and internal energy, and exchange only momentum.

The drop velocities after bouncing are determined in the same manner as in the case of separation, and the same expressions (3.129) are used. However, the coefficient $f_{\mathbf{u}}$ has now different value given by the following formula:

$$f_{\mathbf{u}} = \frac{Y^{1/2}_{r,2} - E^{1/2}_{boun}}{1 - E^{1/2}_{boun}} \tag{3.138}$$

3.9 Droplet-wall interactions

Spray-wall interactions in diesel engines have become the subject of intensive research in the past twenty years, from the time that DI diesel engines began to find wider application to passenger cars. Until then, little attention was paid to the phenomenon of spray-wall interaction, although earlier research was done in the fields of cloud physics, soil erosion and aerospace industry, where they mainly considered water drop splashing. The works of Engel, [65] and [66] deal with splashing of water drops on dry and wet surfaces. In these studies, the outcome of splashing is correlated to the impact velocity, drop size and the surface roughness. Hobbs and Alkezweeny, [104] and Hobbs and Osheroff [105] investigated drop splashing on deep and shallow liquid layers, and the dependence of the number of newly-created drops on the layer thickness. The size distribution of droplets produced by water drop impact has been measured by Levin [128] and Levin and Hobbs [129], who found it to be approximately lognormal. Very detailed measurements of the products of water drop splashing with respect to the impact velocity, drop size, surface tension, roughness and curvature of target surface, and depth of liquid film, were done by Stow and Stainer [195]. They also correlated the number of splash products in terms of impact conditions.

The need for studying the spray-wall impingement in engine field comes from the fact that some engine designs exploit spray-wall interaction to control fuel evaporation and combustion, as the M.A.N. injection system [100], or because the impingement is blamed for the high unburned hydrocarbon emission level, especially in a small DI engine, [135]. The latter become important after many governments introduced legislative restriction on the permitted level of engine emissions, see §(1.1), forcing engine manufacturers to find answers to emission reduction.

One of the first models of spray-wall impingement implemented in a multidimensional numerical code, was developed by Naber and Reitz, [148]. In their model, drops striking the walls are assigned a velocity parallel to the wall in a manner of a jet-wall impingement. Smaller drops approaching the wall are deflected away, while the larger drops stick to the wall and form there a liquid film. The drop shattering process and the model of liquid film were not considered. The model showed qualitatively good predictions compared to photographs from engine and bomb measurements, in respect to various swirl flow conditions, chamber pressures (densities) and spray impact angle relative to the wall. Watkins and Wang [218] developed a spray-wall impingement model based on an extension of the drop collision model of O'Rourke and Bracco [163], accompanied by an empirical correlation for the momentum change of the impacting drops. When attachment between drop and wall occurs, the drop retains its tangential velocity relative to the wall, while its normal velocity is set to zero. To simulate the shattering process, the drop size after impact is reduced by an empirical factor of 4. The model gives reasonable good predictions for normal spray impactions for walls near injector, but failed for angled injection and injector far from the wall.

The recent extensive measurements of drop- and spray-wall interaction at the Max Planck Institut reported in [39], [152], [153], [154] and [155], resulted in a model of this phenomenon developed by Obermeier and Chaves [156]. The measurements were performed in a number of pressure and temperature conditions, varying fuels, incidence angle, wall temperature and wall roughness. They measured the velocity of the droplets, their sizes and reflection angles, as well as the volume of ejected drops and then correlated these quantities to the incidence Weber number and a newly-introduced dimensionless quantity. The model also allows for the multiple droplet impact. This model is implemented in this study and its description is given below.

3.9.1 MPI model

All mechanisms involved in the spray-wall processes are not known, and knowledge about them is mainly based on observation, dimensional analysis and intuition. The picture of the dynamics of these processes, given below, comes from photographs of single droplet impact on a wall.

When a drop hits the wall, it will experience deformation, firstly spreading and then flowing along the wall. The final result of impact depends on the drop kinetic energy before collision with the wall, and drop internal forces which oppose deformation - viscous and surface tension forces, as well as on the wall conditions such

as wall temperature, wall roughness, and on whether the wall is dry or wet. If the drop kinetic energy is high enough, part of the drop will be ejected from the wall, forming an irregular shape similar to a crown. In a further phase, due to surface tension forces, this shape disintegrates into a number of small (secondary) droplets, which continue traveling from the wall. For the purpose of modelling, it is important to know the criteria determining when this transition takes place, and the sizes, velocities and the total volume of secondary droplets. However, if instead of one single droplet, there is a chain of drops which hits the wall (which roughly mimics spray-wall impingement), the situation will be changed and should be allowed for in a model.

Experiments have shown that the wall temperature is, together with the drop velocity, one of the most influential factor, since it affects heat transfer between the drops and wall, causing, if the wall temperature is high enough, boiling and evaporation of drop. Two characteristic wall temperatures are observed, the Leidenfrost temperature, when the drop levitates above a cushion of its own vapour and does not make direct contact with the wall (the drop then has a relatively large life time), and the Nukiyama temperature, when the drop life time reaches its minimum value. Since both temperatures are beyond the boiling point of liquid, the above regimes are not of interest for diesel engines because the temperature of chamber walls is normally lower than the boiling temperature of fuel.

The model presented here, developed by Obermeier and Chaves, [156], accounts for the multiple drop impacts (i.e. for a drop chain), and neglects the effects of roughness and curvature of the target surface, possible formation of a liquid film, and heat transfer between the wall and the droplets on the wall. Three different regimes are distinguished:

1. **Splashing**. The incident drop breaks up into smaller droplets which are reflected with characteristic velocity magnitude and direction.

2. **Fragmentation**. The drop is fragmented into smaller droplets which adhere to the wall.

3. **Sticking on the wall**. The incidence drop remains unbroken and adheres to

the wall where it subsequently evaporates.

During the above processes a liquid film will be formed, but this is not considered in the model, and is beyond the scope of the present thesis.

It follows from the above physical picture that the relevant forces governing drop impingement are the inertial, surface tension and viscosity forces, so the dimensionless criteria for the onset of the regimes are given in terms of the drop incidence Weber number, We_d and the dimensionless drop diameter, d^*, defined as:

$$We_d = \frac{\rho_d\, D_d\, u_{d,n}^2}{\sigma} \tag{3.139}$$

$$d^* = \frac{\rho_d D_d \sigma}{\mu_d^2} \tag{3.140}$$

Here $u_{d,n}$ is the normal component of drop velocity relative to the wall; see Fig.3.13. It should be noted that the Weber number in Eq.(3.139) is based on the drop density (not on the gas density) since the drop inertia (kinetic energy) plays the important role; also, only the normal component of drop incidence velocity is of importance for the impact, therefore it is present in the equation. In Eq.(3.140), d^* represents ratio of the surface tension and viscous forces (note that $d^* = 1/On^2$; Eq.(3.105)).

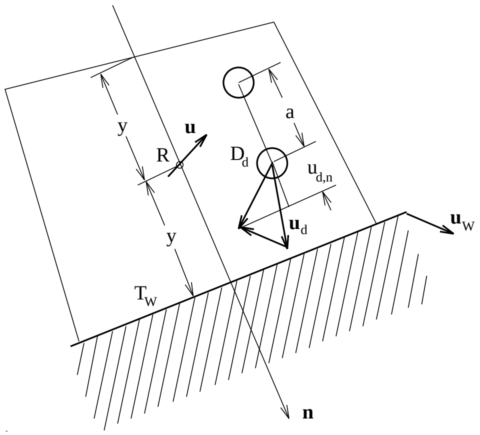

Figure 3.13: Drop-wall interactions

Since it is assumed that all drops in the incidence parcel share the same 'fate', the descriptions of the impingement regimes will be given for one member of the considered computational parcel. In the case of the splashing regime, two new computational parcels are assumed to be created, while for other two regimes the number of parcels remains the same. The parcel mass is conserved, and the drop temperatures before and after impingement are assumed equal (a consequence of the neglected heat transfer between drop and wall). However, as a result of impingement, the drop size, the number of drops in the parcel and the drop velocity can be changed.

Splashing

Splashing occurs when $We_d > We_{spl}$, where We_{spl} is evaluated from the empirical relation [216] :

$$We_{spl} = \begin{cases} 2.5 \cdot 10^3\,(d^*)^{-0.2} & ; T_W \leq T_{Leid} \\ \\ 7.9 \cdot 10^{10}\,(d^*)^{-1.4} & ; T_W > T_{Leid} \end{cases} \tag{3.141}$$

where T_{Leid} is the Leidenfrost temperature, and T_W is the temperature of the target wall.

A drop which hits the wall and satisfies above conditions will be broken into two parts; one which stays on the wall, and another which reflects from the wall as a 'cloud' of droplets ('splash droplets'). The total volume of the latter droplets, V_s is given by the following expression:

$$\frac{V_s}{V_d} = \begin{cases} 0 & ; Ch < 2000 \\ \\ 5.3 \cdot 10^{-4}\,Ch - 1.06 & ; 2000 \leq Ch \leq 3500 \\ \\ 0.8 & ; Ch > 3500 \end{cases} \tag{3.142}$$

where V_d is the volume of incoming drop, Ch is a dimensionless characteristic number defined as:

$$Ch = We_d^{2/3}\, Re_d^{1/3}\, St^{-1} \tag{3.143}$$

and Re_d and St are the drop Reynolds and Strouhal numbers:

$$Re_d = \frac{\rho_d\, u_{d,n}\, D_d}{\mu_d} \tag{3.144}$$

$$St = f\,\frac{D_d}{u_{d,n}} = \frac{D_d}{a} \tag{3.145}$$

In Eq.(3.145), f is the frequency of impingement, and a is the average distance normal to the wall between incoming drops, Fig.3.13. This distance is calculated under assumption of homogeneous distribution of drops in the computational cell adjacent to the wall where the incident parcel resides and where the splashing occurs[6], as:

$$a = 2y\ N_d^{-1/3} \tag{3.146}$$

where y is the normal distance of cell centre from the wall, and N_d is the number of drops in the parcel.

The diameter of the droplets in the splash cloud, D_s and their number, N_s are calculated from the correlation given below, and from the conservation of drop mass:

$$D_s = 0.12\ D_d \tag{3.147}$$
$$N_s = \frac{6}{\pi}\frac{V_s}{D_s^3} \tag{3.148}$$

The remainder of the drop mass, $\rho_d(V_d - V_s)$ is assumed to remain on the wall in a shape of a droplet with the new diameter, D_d^n calculated from mass conservation as:

$$D_d^n = \sqrt{\frac{6}{\pi}\left(V_d - V_s\right)} \tag{3.149}$$

and later evaporates there. This assumption about the shape and diameter of the remaining drop has no justification, but since the formation of liquid film is not considered in the model, and in the order to preserve the individuality of droplet, this practice arose 'naturally'.

The velocity of the splashed droplets is composed of two components; the first is parallel to the wall and assumed to be equal to the tangential component of incoming drop relative to the wall, and the second is taken to be in the randomly sampled direction determined by the reflection angle α, Fig. 3.14. The magnitude of the latter component is taken to be $u_s = u_{d,n}$.

The reflection angle of the splashed droplet α is assumed to be uniformly distributed in the range $(0, \alpha_s)$, and is randomly sampled from this range as:

$$\alpha = Y_r\ \alpha_s \tag{3.150}$$

[6]This assumption is made without justification, but is consistent with the same assumption adopted in the collision model, see §(3.8)

where Y_r is a random number in the range $(0, 1)$, and α_s is the maximum reflection angle calculated from the following empirical correlation:

$$\alpha_s = \begin{cases} \frac{Ch-2000}{1500}\ 60^o & ; 2000 \le Ch \le 3500 \\ \\ 60^o & ; Ch > 3500 \end{cases} \tag{3.151}$$

All splashed droplets from the considered parcels are divided into two computational parcels each containing half the total number of splashed droplets[7]. These droplets have equal diameters, but different velocities determined from the assumed conservation of tangential velocity component (Fig.3.14), from:

$$\begin{aligned} \mathbf{u}_{s,1} &= \mathbf{u}'_{s,1} + \mathbf{u}_W = u_{d,t}\mathbf{t}_1 + u_{d,n}\mathbf{t}_2 + \mathbf{u}_W \\ \\ \mathbf{u}_{s,2} &= \mathbf{u}'_{s,2} + \mathbf{u}_W = u_{d,t}\mathbf{t}_1 + u_{d,n}\mathbf{t}'_2 + \mathbf{u}_W \end{aligned} \tag{3.152}$$

Here, $\mathbf{t}_1$, $\mathbf{t}_2$ and $\mathbf{t}'_2$ are unit vectors.

Fragmentation

This regime happens if the drop Weber number is in the range:

$$We_{frg} < We_d < We_{spl} \tag{3.153}$$

and the temperature of the target wall is greater than the Leidenfrost temperature, i.e.:

$$T_W > T_{Leid} \tag{3.154}$$

This regime does not occur in diesel conditions, but is modelled for the sake of completeness. The threshold Weber number for onset of fragmentation is taken to be $We_{frg} = 80$. The result is breakup into a number of smaller droplets, whose diameter is given by:

$$D_{frg} = D_d/3 \tag{3.155}$$

All these droplets are assumed to adhere to the wall and evaporate there.

[7]The splashed droplets eject from the wall forming an irregular cone cloud. Here, this cone shape is simulated with two directions (to limit the number of newly-formed parcels because of the demands on computer memory and computational time; see also discussion on the parcel injection rate in §(3.10)), $\mathbf{t}_2$ and $\mathbf{t}'_2$ in Fig.3.14, and two corresponding computational parcels.

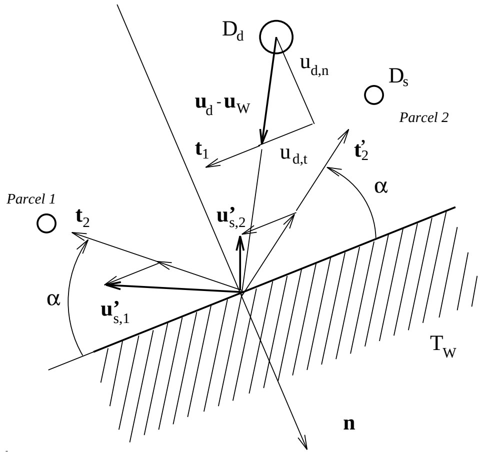

Figure 3.14: Droplet splashing

Sticking on the wall

If the above criteria for splashing and/or fragmentation are not satisfied, the drop sticks to the wall and adopts the wall velocity. It is assumed that this drop keeps its spherical shape and that there is no heat transfer between the wall and the drop. However, the drop evaporates and exchanges mass and energy with the surrounding air, in a manner of an ordinary 'freely-flying' drops. This assumption is taken without justification.

In the treatment of the sticking droplets the drop Reynolds number in the correlations for the heat and mass transfer, Eqs.(3.77) and (3.87), is evaluated with a velocity $|\mathbf{u}_R - \mathbf{u}_d|$, where $\mathbf{u}_R$ is the gas velocity adjacent to the wall. However, it is taken that the sticking drops do not participate in the collision and breakup processes. In the case of collision calculation, the droplet number density is needed which is not defined for the droplets on the wall since they lie in the wall surface and cannot participate in collision with free-flying drops; on the other hand, these droplets are inside a wall boundary layer, and taking into account their sizes (which can be in the range $1-100\mu m$), it is clear that the gas velocity relative to the wall in this region is very small, and any breakup due to aerodynamic forces is impossible.

3.10 Initial conditions

In order to fix the spray injection conditions, the following quantities must be known:

1. The injection rate history, given as a volumetric (or mass) flow rate versus time, $\dot{Q}(t)$,
2. The type of fuel and its temperature,
3. The nozzle geometry, including its characteristic dimensions L and D, and discharge coefficient c_d (see Fig3.1). In the case of the MPI atomisation model c_d is not needed, but the nozzle hole wall roughness, k_r and entrance area contraction coefficient C_c must be known.
4. The spray cone angle, α_{max} for the MPI model must be specified; for Huh's model this angle, Θ, is calculated from Eq.(3.15).

The injection rate history may be estimated, in the absence of direct measurement, from the measurements of the fuel supply pressure, pressure at the nozzle exit, and the needle lift, using the known fuel properties. The values of the discharge coefficient, c_d used in this calculation are sometimes based on the measured values at the steady-state conditions at the different nozzle openings varying the needle lift, which is the most accurate procedure. The spray cone angle is determined by the atomisation model in the case of Huh's model, or empirically specified in the case of the MPI model.

The total fuel mass injected in the time interval $(t, t+\Delta t)$ is distributed over N_p parcels, so the mass of each parcel and the number of droplets, N_d in it is given by following expressions:

$$m_p = \rho_d \frac{1}{N_p} \dot{Q}(t) \Delta t \qquad (3.156)$$

$$N_d = \frac{6\, m_p}{\pi\, \rho_d D_d} \qquad (3.157)$$

where the initial drop diameter is equal to the injector diameter. The specified number of parcels injected per time step affects the spray predictions and computational time. Its value of about 1 parcel/μs represents optimum value when the prediction independence is almost reached at the reasonable computational cost, [227] and [200].

The initial location of the parent droplets corresponds to the injector location, and the magnitude of their initial velocity is determined from $\dot{Q}(t)$ as:

$$u_d(t) = \frac{4}{\pi D^2} \frac{\dot{Q}(t)}{C_{ch}} \tag{3.158}$$

In the case of Huh's atomisation model, the coefficient C_{ch} in the above expression is equal to 1. The direction of velocity is randomly sampled inside the spray cone, see Fig.3.15. It is assumed that the probability of the directions inside the cone are equal, i.e. that there are no preferential directions.

The initial velocity of the secondary droplets is determined as described, for the Huh' model in §(3.2.1), and for the MPI model in §(3.2.2).

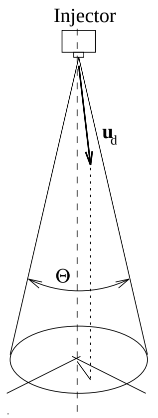

Figure 3.15: Initial drop velocity

3.11 Closure

In this chapter, a model of the spray has been presented. The spray is represented by a discrete-particle model, in which each computational parcel represents a number of droplets of the same properties.

The model of spray includes the submodels of the following spray processes: atomisation, drop breakup, drop collision, interphase transfer of mass, momentum and energy, and spray-wall interactions.

Two atomisation models for round-hole diesel injectors have been described; Huh's atomisation model in §(3.2.1) and the model developed at the Max Planck Institut in §(3.2.2).

The drop breakup has been modelled by the Reitz-Diwakar model, §(3.7.1), and by the Pilch-Erdman correlations, §(3.7.2). The latter distinguishes five regimes which in diesel engine conditions lessen to the same two regimes modelled by the Reitz-Diwakar model. The most important difference between the models is the practice how they estimate drop stable diameter.

The droplet collision has been modelled according to O'Rourke [162], §(3.8). It distinguishes three collision modes: coalescence, separation and bouncing.

The interphase transfer of mass, momentum and energy for individual drop/parcel has been described by a set of ordinary differential equations in §(3.5), §(3.4), and §(3.6), respectively. They express the general conservation laws in the Lagrangian frame of reference. The transfer coefficients used in these equations have been extensively reviewed in the corresponding sections. The coupling source terms associated with the interactions between the spray and the gas have been given at the end of each of the above sections. The effect of turbulence on the trajectories of the droplets has been modelled by a random walk technique in §(3.3).

The correlations obtained from the extensive measurements at the Max Planck Institut has been used for the modelling of the spray-wall impingement, §(3.9). The model allows for the multiple droplet impact, and distinguishes the following three regimes: splashing, fragmentation and sticking on the wall. Finally, the spray initial conditions have been explained in §(3.10).

With this chapter the mathematical description of the gas and the spray has been completed. The following chapter will deal with the discretisation of the governing equations.

Chapter 4

Discretisation

4.1 Introduction

In the previous chapters, the equations expressing the conservation laws for the in-cylinder flow of gas and spray have been given. In chapter 2, the following transport equations of the gas phase have been assembled: §(2.3.1) - continuity equation for the gas and fuel vapour, §(2.3.2) - momentum equation, and §(2.3.3) - energy equation. The turbulence model equations were given in §(2.3.4).

The spray process models have been gathered in chapter 3: two atomisation models in §(3.2.1) and §(3.2.2), parcel trajectory calculation in §(3.3), parcel momentum equation in §(3.4), and mass and energy conservation equations in §(3.5) and §(3.6), respectively. Breakup models were given in §(3.7), droplet collision model in §(3.8), and model of spray-wall interactions in §(3.9).

All these equations, together with the initial and boundary conditions (for the gas phase given in §(2.4), and for the spray in §(3.10)), define a closed system of mutually-coupled non-linear equations. As this system can not be solved by analytical methods, a numerical procedure must be deviced.

The equations describing the gas flow were given in the integro-differential form, where the dependent variables are considered as continuous functions of time and 3D geometrical space in an Eulerian frame of reference. Various numerical methods are available to solve these equations. They can be grouped into the following three main categories: finite element, finite difference, and finite volume. All these methods are based on replacement of the exact, unknown, continuous solution with the numerical values at the finite number of points in the solution domain. The derivation of the relations between these values, a procedure usually called discretisation, must employ some assumptions about the spatial and temporal variation of the variables, and must 'map' features of the original equations. In this way, the original equations are transformed into a set of simultaneous algebraic equations, whose solution approximates the exact solution to a required order of accuracy.

The first part of this chapter is devoted to the discretisation of the gas governing equations. In this study, the finite-volume method is used, and its basis is presented in §(4.2). The discretisation of the general conservation equation, Eq.(2.21), and formation of its algebraic counterpart will first be given in detail in §(4.3). The procedure presented, oriented to general unstructured meshes, mainly follows Theodoropoulos [204]. Then, in §(4.4), the discretised forms of the particular equations will be assembled.

The second part of the chapter deals with the discretisation of the spray governing equations (§(4.5)). As these equations belong to the group of ordinary differential equations, their discretisation is much simpler and the standard Eulerian implicit method is adopted.

4.2 Basis of the finite volume method

The finite volume method was made popular in the field of computational fluid dynamics by the works of Gosman et al. [87], McDonald [133] and MacCormac and Paulay [132], among others. The main characteristics of the method which make it attractive and widely used are:

- local and global conservation of physically-conserved properties can be ensured,
- applicable to complex geometries, with stationary and/or moving boundaries,
- easy implementation of boundary conditions,
- clear physical meaning,

- efficient methods of solution of the resulting simultaneous algebraic equations.

Other equally-important features of the method are the control it offers over boundness, accuracy and the stability of the solution procedure, which can be realised by appropriate measures during the discretisation.

4.2.1 Spatial and temporal discretisation

In order to form an algebraic set of equations which will properly represent the original governing integro-differential equations, the following steps must be performed:

1. **Discretisation of computational domain**

   The computational domain is defined by the space and time coordinates. The geometrical domain has to be divided into a finite number of non-overlapping control volumes or cells. There must be no gaps between cells, and each cell face can only be shared by the two neighbouring cells[1]. There are no requirements on the resulting mesh or grid concerning its topological structure, i.e. both structured and unstructured meshes can be used.

   The time domain must be divided into a finite number of time intervals; the time steps between intervals have to be small enough to assure the required time resolution.

2. **Selection of interpolating functions**

   The spatial and temporal interpolation functions by which the mid-values of dependent variables in the discretised space-time computational domain can be evaluated, must be selected.

3. **Discretisation of the transport equation**

   The governing transport equation has to be applied to each control volume in the geometrical domain. The result of that is a set of simultaneous algebraic equations, where the number of unknowns are the values of the dependent variables in the cells. The number of these simultaneous equations is equal to the number of cells.

[1] This restriction can be avoided by adopting some interpolation scheme for the fluxes between the cells at that face.

It is intuitively obvious that the final accuracy of the numerical solution directly depends on the fineness of the mesh and temporal resolution. Although the cell shape, i.e the number of cell faces, is arbitrary, in this study only six-sided cells (i.e.hexahedra) are used. This results in a computational molecule with seven points: one central point and six neighbours. It is taken that representative values of all the variables are located in the cell centres, i.e. the collocated arrangement is used.

In unsteady flow problems, the discretisation of time derivatives necessarily leads to an algebraic system of equations which links the unknowns at a given time to the values at current and previous times. There are three families of methods to approach this problem, namely, *explicit* and *implicit* methods, which can be regarded as two extremes, and their combination, usually called a *semi-implicit* method; see Patankar [165].

Explicit methods lead to a simple diagonal system of equations with a trivial matrix inversion. However, this advantage is paid for by a severe restriction on the permissible time step size required to satisfy stability and convergence conditions; the Courant-Friedrich-Lewy condition ([47] and [103]). In engine calculations, application of this method will, according to [24], impose restriction on the time step of the order of 10^{-7}s (10^{-3} crank angles degrees).

In implicit methods, the resulting coefficient matrix is not diagonal and its inversion requires more complex algorithms. This disadvantage is compensated for by an absence of stability and convergence limitations on the time step size. However, the time step restriction due to time scales of the physical/chemical processes remains.

Among semi-implicit methods the best known is the Crank-Nicolson scheme, [48]. Although it is unconditionally stable (in the mathematical sense), this does not ensure solutions without oscillations or physically plausible solutions; see Patankar and Baliga [167]. More information on the methods can be found in Patankar [165] and Begleris [24].

As the implicit method is simple to implement, gives physically desirable behaviour, and does not suffer from the severe time step size restrictions, it is generally preferred in the fluid flow class of problems. Therefore, this method is adopted in this study.

4.2.2 Notation

A typical cell arrangement with the notation used here is shown in Fig.4.1. The considered cell is denoted by the capital letter P, and its faces by $\mathcal{S}_f^P$, where $f \in \{\pm 1, \pm 2, \pm 3\}$, represents the six directions in the local cell coordinate system centred at P. The $\pm$ sign denotes the two opposite directions, so $\mathcal{S}_f^P$ and $\mathcal{S}_{-f}^P$ represent two opposite faces of the cell P. In this sense, we will talk about the cell face f and $-f$. The neighbouring cells to the cell P are denoted by N, where $N = N(f)$ links neighbouring cell to the considered direction; $N(f)$ is the f neighbour of P. NN represents the neighbouring cells of N.

The values of variables in the cell centre and at the cell faces are denoted by the corresponding subscript, ϕ_P and ϕ_f respectively.

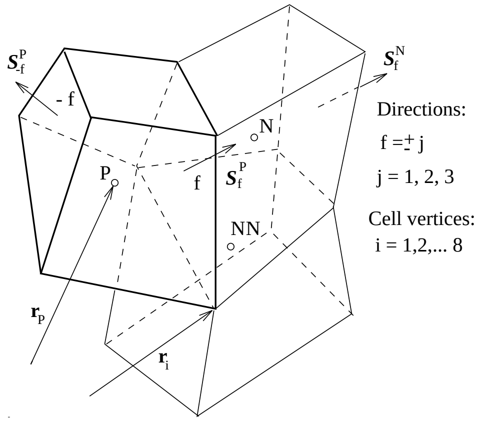

Figure 4.1: Cell notation

Each cell is defined by its eight vertices whose locations are given by the position vectors $\mathbf{r}_i$ ($i = 1, \ldots 8$) in the global Cartesian coordinate system. For the cell P, its cell centre $\mathbf{r}_P$ and the centre of the face f, $\mathbf{r}_f$, are defined as the arithmetic average of the position vectors of all cell vertices, $\{i\}_P$ and all vertices $\{i\}_f$ which belong to the considered face f, respectively:

$$\mathbf{r}_P = \frac{1}{8} \sum_{\{i\}_P} \mathbf{r}_i \quad (4.1)$$

$$\mathbf{r}_f = \frac{1}{4} \sum_{\{i\}_f} \mathbf{r}_i \tag{4.2}$$

The face vector $\mathcal{S}_f^P$ is calculated via the vector product of the two face diagonals, and it points outwards[2]. When there cannot be confusion, the superscript P will be omitted.

The cell volume V_P is calculated from the volumes of the six pyramids whose bases are the cell faces, and apexes are the cell centre P, giving the following expression:

$$V_P = \frac{1}{3} \sum_{\{f\}_P} \mathcal{S}_f \cdot (\mathbf{r}_f - \mathbf{r}_P) \tag{4.3}$$

where $\sum_{\{f\}_P}$ stands for the summation over all six directions in the cell P.

The values of the dependent variables at the cell faces are estimated by the following spatial interpolation scheme:

$$\phi_f = \lambda_f^P \, \phi_P + (1 - \lambda_f^P) \, \phi_N \tag{4.4}$$

where λ_f^P represents the interpolation (weighting) factor of the cell P in the direction f, defined in Fig.4.2. The same interpolation scheme is used for the evaluation of

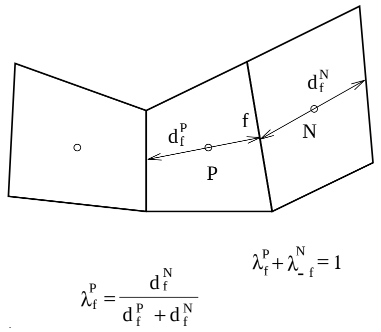

Figure 4.2: Definition of interpolation function

the other gas properties, such as viscosity, at the cell face.

A quick look at the governing transport equations shows the frequent appearances of the nabla operator ∇, so this is the reason why we now introduce its

[2] See in Theodoropoulos [204] on the problem of faces which are not plane, so-called 'warped' faces, and their treatment.

finite-volume counterpart, $\mathbf{N}$ defined by:

$$(\mathbf{N}\phi)_P = \frac{1}{V_P} \sum_{\{f\}_P} \mathcal{S}_f \, \phi_f = \frac{1}{V_P} \sum_{\{f\}_P} \mathcal{S}_f \, (1 - \lambda_f^P)(\phi_N - \phi_P) \tag{4.5}$$

This formula results from the Gauss theorem:

$$\int_V \nabla\phi \, dV = \int_S d\mathcal{S} \, \phi \tag{4.6}$$

and the mean-value theorem:

$$\nabla\phi = \lim_{V \to 0} \frac{1}{V} \int_V \nabla\phi \, dV = \lim_{V,S \to 0} \frac{1}{V} \int_S d\mathcal{S} \, \phi \tag{4.7}$$

In Eg.(4.5), ϕ can be a tensor of arbitrary order. Then, the gradient of an arbitrary scalar field ψ, the divergence and gradient of a vector field $\mathbf{u}$, and the divergence of a tensor field $\mathbf{T}$, are given respectively by the following formulae:

$$\begin{aligned}
(\nabla\psi)_P &\approx (\mathbf{N}\psi)_P \\
&= \frac{1}{V_P} \sum_{\{f\}_P} \mathcal{S}_f \, (1 - \lambda_f^P)(\psi_N - \psi_P) && (4.8) \\
(\nabla \cdot \mathbf{u})_P &\approx (\mathbf{N} \cdot \mathbf{u})_P \\
&= \frac{1}{V_P} \sum_{\{f\}_P} \mathcal{S}_f \cdot (1 - \lambda_f^P)(\mathbf{u}_N - \mathbf{u}_P) && (4.9) \\
(\nabla \mathbf{u})_P &\approx (\mathbf{N}\mathbf{u})_P \\
&= \frac{1}{V_P} \sum_{\{f\}_P} \mathcal{S}_f \, (1 - \lambda_f^P)(\mathbf{u}_N - \mathbf{u}_P) && (4.10) \\
(\nabla \cdot \mathbf{T})_P &\approx (\mathbf{N} \cdot \mathbf{T})_P \\
&= \frac{1}{V_P} \sum_{\{f\}_P} \mathcal{S}_f \cdot (1 - \lambda_f^P)(\mathbf{T}_N - \mathbf{T}_P) && (4.11)
\end{aligned}$$

4.3 Discretisation of the general transport equation

The conservation of the general gas property ϕ in the arbitrary control volume was given by Eq.(2.21). This equation, when the convection and diffusion terms are collected together, reads:

$$\frac{d}{dt} \int_V \rho\phi \, dV + \int_S d\mathcal{S} \cdot (\rho \mathbf{u}_r \phi - \rho \, \Gamma_\phi \nabla\phi) = \int_V (s_\phi + s_\phi^d) \, dV \tag{4.12}$$

When this equation is applied to the hexahedral control volume P, the individual terms are approximated as follows.

4.3.1 The unsteady term

In order to discretise the unsteady term, the following assumptions are made:

- The content of the property ϕ in the control volume can be expressed by the product of the mass content in this cell and the representative value ϕ_P at the cell centre:
$$\int_{V_P} \rho\phi \, dV \approx (\rho\phi V)_P \approx (\rho V)_P \; \phi_P \tag{4.13}$$
- The local rate of change of ϕ can be approximated by an average change during the finite time step Δt.

The discretised unsteady term is then:

$$\begin{aligned}\frac{d}{dt}\int_{V_P} \rho\phi \, dV &\approx \frac{(\rho\phi V)_P - (\rho\phi V)_P^o}{\Delta t} \\ &\approx \frac{(\rho V)_P \; \phi_P - (\rho V)_P^o \; \phi_P^o}{\Delta t}\end{aligned} \tag{4.14}$$

where the superscript o denotes the 'old' time values.

4.3.2 The convection-diffusion terms

These two terms are considered together because their proper discretisation is essential for the preservation of the conservation, bounding and transportive properties of the original transport equation. The total flux of ϕ through the entire cell boundary S_P is equal to the sum of the fluxes over all the cell faces:

$$\int_{S_P} d\mathcal{S} \cdot (\rho \mathbf{u}_r \phi - \rho \; \Gamma_\phi \nabla\phi) = \sum_{\{f\}_P} \int_{S_f} d\mathcal{S} \cdot (\rho \mathbf{u}_r \phi - \rho \; \Gamma_\phi \nabla\phi) \tag{4.15}$$

Assuming that the convective and diffusive fluxes of ϕ at the cell face can be expressed in terms of mass flux and diffusion counterparts at the face, and some average, representative values of ϕ and $\nabla\phi$ at the face, the flux of ϕ through the cell face f is:

$$\int_{S_f} d\mathcal{S} \cdot (\rho \mathbf{u}_r \phi - \rho \; \Gamma_\phi \nabla\phi) \approx F_f \tag{4.16}$$

where F_f is the flux of ϕ through cell face f, given by:

$$F_f = \mathcal{S}_f \; \cdot [\, (\rho \mathbf{u}_r \phi)_f - (\rho \; \Gamma_\phi \nabla\phi)_f \,] \tag{4.17}$$

The convective flux of ϕ through the face f is evaluated as:

$$\begin{aligned}\mathcal{S}_f \; \cdot (\rho \mathbf{u}_r \; \phi)_f &= \mathcal{S}_f \; \cdot (\rho \mathbf{u}_r)_f \; \phi_f \\ &= \mathcal{C}_f \; [\, w_f \phi_P + (1 - w_f)\phi_N \,] \qquad (4.18) \\ \mathcal{C}_f &= \mathcal{S}_f \cdot (\rho \mathbf{u}_r)_f \qquad (4.19)\end{aligned}$$

where $\mathcal{C}_f$ is the mass flux, and w_f is a weighting factor whose specification will be given later on.

In the case of the diffusion flux, its vector $(\rho \; \Gamma_\phi \nabla\phi)_f$ is resolved into two components. One, in the direction f, is called the 'normal diffusion' component, $\mathbf{d}_f^{nor}$; and the other is called the 'cross diffusion' component, $\mathbf{d}_f^c$:

$$(\rho \; \Gamma_\phi \nabla\phi)_f = \mathbf{d}_f^{nor}(\phi) + \mathbf{d}_f^c(\phi) \tag{4.20}$$

The components are defined as:

$$\begin{aligned}\mathbf{d}_f^{nor}(\phi) &= \lambda_f^P \left(\frac{\rho \; \Gamma_\phi}{V}\right)_P \sum_{\{l=\pm f\}_P} \mathcal{S}_l \; \phi_l \; + \\ &+ \; (1 - \lambda_f^P) \left(\frac{\rho \; \Gamma_\phi}{V}\right)_N \sum_{\{l=\pm f\}_N} \mathcal{S}_l \; \phi_l\end{aligned} \tag{4.21}$$

$$\begin{aligned}\mathbf{d}_f^c(\phi) &= \lambda_f^P \left(\frac{\rho \; \Gamma_\phi}{V}\right)_P \sum_{\{l\neq\pm f\}_P} \mathcal{S}_l \; \phi_l \; + \\ &+ \; (1 - \lambda_f^P) \left(\frac{\rho \; \Gamma_\phi}{V}\right)_N \sum_{\{l\neq\pm f\}_N} \mathcal{S}_l \; \phi_l\end{aligned} \tag{4.22}$$

where the summation is performed over the faces in the $+f$ and $-f$ directions for $\mathbf{d}_f^{nor}$, and over all faces excluding $+f$ and $-f$ in the case of the cross diffusion component $\mathbf{d}_f^c$.

In the above splitting, the gradient of ϕ at the cell face is interpolated from the gradients at the two adjacent cell centres as:

$$(\nabla\phi)_f = \lambda_f^P \; (\nabla\phi)_P + (1 - \lambda_f^P) \; (\nabla\phi)_N \tag{4.23}$$

while the cell-centre gradients are approximated according to Eq.(4.8) by:

$$\begin{aligned}(\nabla\phi)_P &\approx (\mathbf{N}\phi)_P \qquad (4.24) \\ (\nabla\phi)_N &\approx (\mathbf{N}\phi)_N \qquad (4.25)\end{aligned}$$

After some manipulation (see Apendix §(C.1)), the normal diffusion component can be recast into the following compact form:

$$\begin{aligned}
\mathbf{d}_f^{nor}(\phi) &= \overline{\mathcal{S}_f}^P(\phi_N - \phi_P) && (4.26)\\
\overline{\mathcal{S}_f}^P &= \lambda_f^P(1-\lambda_f^P)\left[(\mathcal{S}_f^P - \mathcal{S}_{-f}^P)(\frac{\rho\,\Gamma_\phi}{V})_P + (\mathcal{S}_f^N - \mathcal{S}_{-f}^N)(\frac{\rho\,\Gamma_\phi}{V})_N\right] && (4.27)
\end{aligned}$$

which involves only the ϕ values at P and its neighbour N. This allows a completely implicit treatment of the normal diffusion term.

The discretisation of the cross-diffusion part necessarily involves the values of ϕ at the 'next-nearest' neighbouring cells, and its implicit treatment would therefore, not only expand the computational molecule beyond the present six nearest neighbours, but could deteriorate the boundness of the solution (for very non-orthogonal meshes)[3]. The resulting set of equations is much more difficult to solve, and so the alternative procedure is adopted of evaluating the cross-diffusion term at the old time level (or with the currently available values); i.e. this term is treated explicitly. Expressed in terms of the old time ϕ values, the cross diffusion component at the face f is:

$$\begin{aligned}
\mathbf{d}_f^c(\phi^o) &= \lambda_f^P(\frac{\rho\,\Gamma_\phi}{V})_P \sum_{\{l\neq\pm f\}_P} \mathcal{S}_l\,(1-\lambda_l)(\phi_N^o - \phi_P^o) + \\
&+ (1-\lambda_f^P)(\frac{\rho\,\Gamma_\phi}{V})_N \sum_{\{l\neq\pm f\}_N} \mathcal{S}_l\,(1-\lambda_l)(\phi_{NN}^o - \phi_N^o) && (4.28)
\end{aligned}$$

After substitution of Eqs.(4.18),(4.20), (4.26), and (4.28) into Eq.(4.17), the total flux through the face f is:

$$\begin{aligned}
F_f &= (\mathcal{C}_f w_f + \mathcal{D}_f)\phi_P - \\
&- [\mathcal{C}_f(w_f - 1) + \mathcal{D}_f]\phi_N - \\
&- D_f^c && (4.29)
\end{aligned}$$

where

$$\begin{aligned}
\mathcal{D}_f &= \mathcal{S}_f^P \cdot \overline{\mathcal{S}_f}^P && (4.30)\\
D_f^c &= \mathcal{S}_f^P \cdot \mathbf{d}_f^c(\phi^o) && (4.31)
\end{aligned}$$

[3]The latter is affected by the numerical values of the coefficients of ϕ.

4.3.3 The source terms

In general, the source terms are non-linear functions of the dependent variables, and in their discretisation linearisation is employed; see [165]. Thus, the discretised source term reads:

$$\int_{V_P} s_\phi\, dV = (S_\mathcal{U}^\phi)_P + (S_\mathcal{P}^\phi)_P\,\phi_P \qquad (4.32)$$

where $S_\mathcal{U}$ and $S_\mathcal{P}$ are the coefficients which depend on the particular source expression.

The same approach is taken for the spray source contribution, hence:

$$\int_{V_P} s_\phi^d\, dV = (S_\mathcal{U}^{\phi,d})_P + (S_\mathcal{P}^{\phi,d})_P\,\phi_P \qquad (4.33)$$

The linearisation must be done in a manner that assures that the linear coefficients $S_\mathcal{P}^\phi$ and $S_\mathcal{P}^{\phi,d}$ are always negative or equal to zero, to avoid instabilities and physically unrealistic solution.

It is important to emphasize an essential difference between the $S_\mathcal{U}$ and $S_\mathcal{P}$ terms. While $S_\mathcal{P}$ is always a scalar, $S_\mathcal{U}$ must be a tensor of the same order as ϕ.

4.3.4 Discretised form of the transport equation

Substitution of all the above terms into Eq.(4.12) yields:

$$\begin{aligned}
\mathcal{A}_P^\phi\phi_P &= \sum_N \mathcal{A}_N^\phi\phi_N + b_P^\phi && (4.34)\\
\mathcal{A}_P^\phi &= \sum_{\{f\}_P}[\,\mathcal{C}_f w_f^\phi + \mathcal{D}_f^\phi\,] + \frac{(\rho V)_P}{\Delta t} - (S_\mathcal{P}^\phi)_P - (S_\mathcal{P}^{\phi,d})_P \\
&= \sum_N \mathcal{A}_N^\phi + \frac{(\rho V)_P^o}{\Delta t} - (S_\mathcal{P}^\phi)_P - (S_\mathcal{P}^{\phi,d})_P + (S^d)_P && (4.35)\\
\mathcal{A}_N^\phi &= [\,\mathcal{C}_f(w_f^\phi - 1) + \mathcal{D}_f^\phi\,] && (4.36)\\
b_P^\phi &= \frac{(\rho V)_P^o}{\Delta t}\phi_P^o + \sum_{\{f\}_P} D_f^{\phi,c} + (S_\mathcal{U}^\phi)_P + (S_\mathcal{U}^{\phi,d})_P && (4.37)
\end{aligned}$$

where the additional superscript ϕ on b_P^ϕ, $\mathcal{D}_f^\phi$, w_f^ϕ and $D_f^{\phi,c}$ is used to emphasize their dependence on the dependent variable, and the summation over directions $\sum_{\{f\}_P}$ is replaced with the equivalent summation over the neighbours, $\sum_N$.

The final form of Eq.(4.35) was obtained by the usage of the discretised mass conservation equation Eq.(4.55) by replacing $(\rho V)_P/\Delta t$ in terms of the 'old' time value, $(\rho V)^o_P/\Delta t$, and the spray evaporation rate S^d, i.e.:

$$\frac{(\rho V)_P}{\Delta t} = \frac{(\rho V)^o_P}{\Delta t} - \sum_{\{f\}_P} \mathcal{C}_f + (S^d)_P \tag{4.38}$$

When Eqs.(4.34-4.37) are written for all N_c cells in the solution domain, the result is a system of N_c non-linear algebraic equations:

$$\mathcal{A}^\phi_P \phi_P = \sum_N \mathcal{A}^\phi_N \phi_N + b^\phi_P \quad , P = 1, \ldots, N_c \tag{4.39}$$

where $\mathcal{A}^\phi_P$ and $\mathcal{A}^\phi_N$ are the diagonal and off-diagonal coefficients of the system, respectively, and b^ϕ_P is the source term.

In a matrix form Eq.(4.39) reads:

$$\mathbf{A}^\phi \underline{\phi} = \underline{b}^\phi \tag{4.40}$$

where $\mathbf{A}^\phi$ is the $N_c \times N_c$ (N_c is the total number of cells) coefficient matrix, and $\underline{\phi}$ and $\underline{b}^\phi$ are the column vectors of the unknowns and the source, respectively.

4.3.5 Differencing schemes

The coefficients of ϕ_P and ϕ_N in Eq.(4.29) have crucial affects on the boundness and transportive properties of the original equation, [165]. In order to preserve these properties, these coefficients must be non-negative. Therefore, the assumed variation of ϕ between neighbouring nodes P and N, dictated by the weighting factor w_f, Eq.(4.18), plays such important role.

There are many different schemes (see for example Patankar [165] and a review in Collins [46]), but here, two schemes used in this study, namely, a hybrid differencing scheme and self-filtered central differencing scheme (SFCD), will only be described.

Hybrid differencing

This scheme which always preserves those aforementioned desirable features, was proposed by Spalding [192]. It combines the upwind differencing and central differencing schemes. The value of the weighting factor w_f is given by the following formulae, [165]:

$$w_f = \begin{cases} 1, & Pe_f \geq \frac{1}{1-\lambda^P_f} \\ 0, & Pe_f \leq -\frac{1}{\lambda^P_f} \\ \lambda^P_f, & -\frac{1}{\lambda^P_f} < Pe_f < \frac{1}{1-\lambda^P_f} \end{cases}$$

where Pe_f is the cell-face Peclet number, representing the ratio of the strength of convection and the diffusion:

$$Pe_f = \frac{\mathcal{C}_f}{\mathcal{D}_f} \tag{4.41}$$

From the above expressions, it can be seen that the fluxes are uniquely defined at the cell face. This assures local conservation of fluxes between the neighbouring cells, and as a consequence, global conservation as well.

Self-filtered central differencing

This scheme of Ziman [230], is a conservative higher order discretisation scheme that switches, depending on the local ϕ-profile, between central differencing (CD) and blended upwind (UD) and linear upwind differencing (LUD). In this way, the scheme reduces the amount of numerical diffusion present in the scheme as UD, and switches to UD only when a local extremum exists. In regions where very steep gradients are present, a special parameter limits the CD usage, and the scheme then blends UD and LUD. A brief description of the scheme is presented below.

In the SFCD, the value of ϕ at a face f, ϕ_f, Fig.4.3a, is evaluated by:

- if $\mathcal{C}_f \geq 0$:

$$\phi_f = \phi_P + (\phi_P - \phi_{N(-f)})(1 - \lambda^P_f)\beta_f \tag{4.42}$$

where β_f is given by:

$$\beta_f = \max\left[0, \min\left(\frac{\phi_N - \phi_P}{\phi_P - \phi_{N(-f)}}, \beta_{max}\right)\right] \tag{4.43}$$

- if $\mathcal{C}_f < 0$:

$$\phi_f = \phi_N + (\phi_N - \phi_{NN(f)})\, \lambda^P_f \, \beta_f \tag{4.44}$$

where β_f is:

$$\beta_f = \max\left[0, \min\left(\frac{\phi_N - \phi_P}{\phi_{NN(f)} - \phi_N}, \beta_{max}\right)\right] \tag{4.45}$$

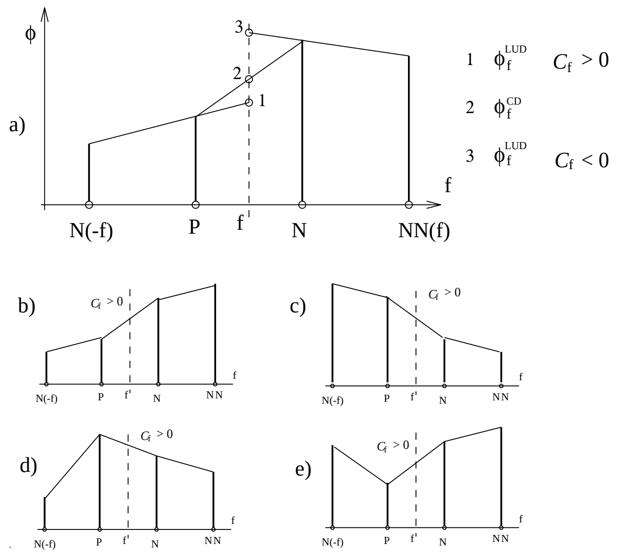

Figure 4.3: SFCD scheme

There are basically three different operating modes of this scheme, which will now be explained, for the case $\mathcal{C}_f \geq 0$:

1. $\beta_f = (\phi_N - \phi_P)/(\phi_P - \phi_{N(-f)})$; SFCD is equivalent to CD. This occurs if $0 < (\phi_N - \phi_P)/(\phi_P - \phi_{N(-f)}) \leq \beta_{max}$, Figs.4.3b and (4.3c).

2. $\beta_f = 0$; SFCD is equal to UD. This happens if either $\beta_{max} = 0$, or $(\phi_N - \phi_P)/(\phi_P - \phi_{N(-f)}) \leq 0$, i.e. when ϕ has a local extremum, Figs.4.3d and 4.3e,

3. $\beta_f = \beta_{max}$; SFCD operates as a blend between UD and LUD. This happens if $(\phi_N - \phi_P)/(\phi_P - \phi_{N(-f)}) > \beta_{max}$; then, β_{max} can be interpreted as a weighting factor between UD and LUD .

The parameter β_{max} has the task to put the upper limit on the usage of the CD scheme; beyond this value SFCD blends UD and LUD. It is recommended that β_{max} be set to unity. A schematic presentation of the functioning of the scheme is shown in Fig.4.4.

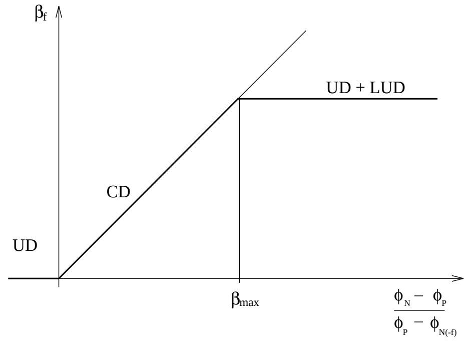

Figure 4.4: Functioning of the SFCD scheme

Implementation of SFCD

As can be seen, the SFCD in the general case uses ϕ-values at the next-nearest neighbours (NN), where implicit treatment would expand the computational molecule. In order to avoid this, an partially-explicit method is implemented, in which the upwind part is treated implicitly, while the rest is evaluated with the currently available ϕ-values and added to the source as an explicit term. Expressed in term of the weighting factor, w_f, Eq.(4.18), the implementation comprises the following two actions:

1. Evaluation of the $\mathcal{A}_N^\phi$ coefficients in Eq.(4.36), according to the UD scheme, with the following weighting factor:

$$w_f = 1 + \min[\,0, sign(\mathcal{C}_f)] \tag{4.46}$$

2. Calculation of the explicit part by:

$$(S_\mathcal{U}^\phi)_P^{SFCD} = \sum_{\{f\}_P} \phi_f' \, \mathcal{C}_f \tag{4.47}$$

where ϕ_f' is defined by:

$$\phi_f' = \begin{cases} (\phi_P - \phi_{N(-f)})(1-\lambda_f^P)\beta_f & ;\mathcal{C}_f \geq 0 \\ \\ (\phi_N - \phi_{NN(f)})\,\lambda_f^P\,\beta_f & ;\mathcal{C}_f < 0 \end{cases} \tag{4.48}$$

and addition to the overall source term.

4.3.6 The boundary conditions

The expressions for the evaluation of the convective and diffusive fluxes given in §(4.3.2) are valid for all interior cell faces. On these cell faces which lie on the boundary of the solution domain a modified treatment is imposed to account for the boundary conditions there. It consists of the introduction of additional boundary source term and setting the corresponding $\mathcal{A}_N^\phi$ coefficient to zero. In this respect, two kinds of boundary conditions are distinguished: (1) the fluxes at the boundary are known, in which case they are added to the source term of the adjacent cells, or (2) the boundary values of the dependent variables are known; then, the fluxes are calculated based on the boundary values and the values in the cells adjacent to the boundary.

The general form of the linearised boundary source term of the cell P adjacent to the boundary is:

$$(S_b^\phi)_P = (S_{\mathcal{U},b}^\phi)_P + (S_{\mathcal{P},b}^\phi)_P\ \phi_P \tag{4.49}$$

and the terms $S_{\mathcal{U},b}^\phi$ and $S_{\mathcal{P},b}^\phi$ are added to the 'real' source terms $S_\mathcal{U}^\phi$ and $S_\mathcal{P}^\phi$, respectively.

In this section, the boundary conditions for the inflow/outflow boundaries, symmetry planes and cyclic boundaries are described. The wall boundary conditions, since they are more complex and specific to the particular property ϕ, are given at the end of the description of the corresponding discretised transport equation.

Inflows and outflows

Here it is assumed that the boundary mass inflow or outflow rate is known. In the cells adjacent to the such boundaries, the boundary source term, split in the $(S_{\mathcal{P},b}^\phi)_P$ and $(S_{\mathcal{U},b}^\phi)_P$ parts, reads:

$$(S_{\mathcal{P},b}^\phi)_P = \begin{cases} \dot{m}_b & ; \dot{m}_b \le 0 \\ 0 & ; \dot{m}_b > 0 \end{cases} \tag{4.50}$$

$$\phi = \mathbf{u}, e, Y_{ft}, k, \epsilon$$

$$(S_{\mathcal{U},b}^\phi)_P = \begin{cases} -\ \dot{m}_b\ \phi_b & ; \dot{m}_b \le 0 \\ 0 & ; \dot{m}_b > 0 \end{cases} \tag{4.51}$$

where $\dot{m}_b$ is the mass flow rate ($\dot{m}_b < 0$ means inflow) at a cell face b, and ϕ_b is the value of ϕ at this face.

Symmetry plane

At a symmetry plane, since the fluxes are zero (§2.4.3), the boundary source term is set to zero:

$$(S_b^\phi)_P = 0 \quad ; \phi = \mathbf{u}, e, Y_{ft}, k, \epsilon \tag{4.52}$$

Cyclic boundaries

Cyclic boundary conditions and the relations which will be used here, were defined earlier in §(2.4.4). Suppose we have a situation shown in Fig.4.5, where two cells, P and S, adjacent to corresponding locations at the cyclic boundary pair are illustrated. If cell P is considered, a fictitious cell N, which is cell S rotated through the angle α, is positioned as a b-neighbour of P. Values of all the scalar quantities in cell N are equal to those of cell S, while the gas velocity in N is equal to the rotated velocity in S for the angle α, i.e.:

$$\phi_N = \phi_S \qquad ; \phi \neq \mathbf{u} \tag{4.53}$$

$$\mathbf{u}_N = \mathbf{R}^\alpha \cdot \mathbf{u}_S \tag{4.54}$$

where $\mathbf{R}^\alpha$ is the rotation matrix. Now cell P can be treated as an ordinary internal cell, and all fluxes at b are accordingly calculated, see §(4.3.2) and §(4.3.4). Cell S is treated in the same way, i.e., its 'cyclic' neighbour T is the rotated cell P through $-\alpha$, with the equal scalar values to those of P, and the velocity vector equal to the rotated velocity of P for the same angle.

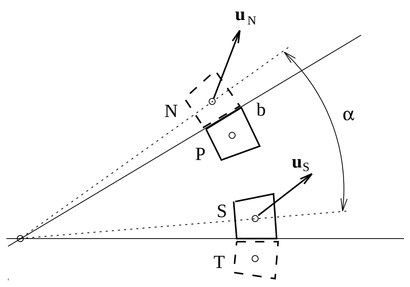

Figure 4.5: Cells at the cyclic boundaries

4.4 Discretised gas equations

In the previous section, the discretised form of the general transport equation and boundary conditions, apart from wall boundary conditions, were presented. Here, the discretised counterparts of all the governing equations of the gas field assembled in §(2.3) and the corresponding wall boundary conditions will be given in turn.

4.4.1 Mass conservation equations

The discretised form of the mass conservation equation, Eq.(2.39) is:

$$\frac{(\rho V)_P - (\rho V)_P^o}{\Delta t} + \sum_{\{f\}_P} \mathcal{C}_f = (S^d)_P \tag{4.55}$$

where $\mathcal{C}_f$ and $(S^d)_P$ are the convective flux at the cell face f and the spray evaporation rate in the cell P, respectively. The latter is calculated from the discretised form of Eq.(3.82) as:

$$(S^d)_P = -\frac{1}{\Delta t}\int_{V_P} \sum_{p=1}^{p=N_p} \sum_{i=1}^{i=N_s} \delta(\mathbf{x}-\mathbf{x}_p^i)\,(m_p^i - m_p^{i-1})\,dV \tag{4.56}$$

where the summation is performed over all spray computational parcels N_p and over N_s subcycling time steps. Integration of $\delta(\mathbf{x}-\mathbf{x}_p^i)$ over the control volume V_P assures that only parcels which are in V_P during the time step Δt make contribution to this cell. More details about the discretisation of the spray source terms are given in Appendix B.1 and in §(4.5.1) and §(4.5.2).

The discretised version of the fuel vapour mass conservation equation Eq.(2.42) reads:

$$\mathcal{A}_P^{Y_{ft}}(Y_{ft})_P = \sum_N \mathcal{A}_N^{Y_{ft}}(Y_{ft})_N + b_P^{Y_{ft}} \quad , \; P = 1, \ldots N_c \tag{4.57}$$

$$\mathcal{A}_P^{Y_{ft}} = \sum_N \mathcal{A}_N^{Y_{ft}} + \frac{(\rho V)_P^o}{\Delta t} + (S^d)_P \tag{4.58}$$

$$\mathcal{A}_N^{Y_{ft}} = [\mathcal{C}_f(w_f^{Y_{ft}} - 1) + \mathcal{D}_f^{Y_{ft}}] \tag{4.59}$$

$$b_P^{Y_{ft}} = \frac{(\rho V)_P^o}{\Delta t}(Y_{ft})_P^o + \sum_{\{f\}_P} D_f^{Y_{ft},c} + (S^d)_P \tag{4.60}$$

4.4.2 Momentum conservation equation

Although the gas momentum conservation, Eq.(2.44) is a special case of the general transport equation, the presence of the unknown pressure gradient in this equation differentiates it from the other, scalar equations. In anticipation of the later derivation of a pressure equation, the pressure gradient and spray source terms are separated from the rest of the source term.

The discretised momentum equation reads:

$$\mathcal{A}^{\mathbf{u}}_P \mathbf{u}_P = \sum_N \mathcal{A}^{\mathbf{u}}_N \mathbf{u}_N + \mathbf{b}^{\mathbf{u}}_P + (\mathbf{S}^{\mathbf{u},d}_{\mathcal{U}})_P - (V\vartheta \mathbf{N}p)_P \quad , P = 1,\dots N_c \tag{4.61}$$

$$\mathcal{A}^{\mathbf{u}}_P = \sum_N \mathcal{A}^{\mathbf{u}}_N + \frac{(\rho V)^o_P}{\Delta t} - (S^{\mathbf{u},d}_{\mathcal{P}})_P + (S^d)_P \tag{4.62}$$

$$\mathcal{A}^{\mathbf{u}}_N = [\,\mathcal{C}_f(w^{\mathbf{u}}_f - 1) + \mathcal{D}^{\mathbf{u}}_f\,] \tag{4.63}$$

$$\mathbf{b}^{\mathbf{u}}_P = \frac{(\rho V)^o_P}{\Delta t}\mathbf{u}^o_P + \sum_{\{f\}_P} \mathbf{D}^{\mathbf{u},c}_f + (\mathbf{S}^{\mathbf{u}}_{\mathcal{U}})_P \tag{4.64}$$

The notation in Eq.(4.61) stands for:

$$\begin{aligned}\mathcal{A}^{u_i}_P (u_i)_P = & \sum_N \mathcal{A}^{u_i}_N (u_i)_N + (b^{u_i}_i)_P \\ & + (S^{u_i,d}_{\mathcal{U},i})_P - (V\vartheta N_i p)_P \quad , i = 1,2,3\end{aligned} \tag{4.65}$$

In the above discretisation, the contribution of the remaining part of stress tensor, i.e. the part without the pressure gradient term (see Eqs.(2.23) and (2.30)), which, after substitution of Eq.(2.24) reads:

$$\mathbf{T}_m + \mathbf{T}_t = \underbrace{\rho\, \nu_{eff} \nabla \mathbf{u}}_{I} + \underbrace{\rho\, \nu_{eff} (\nabla \mathbf{u})^T - \tfrac{2}{3}\,\rho\, \nu_{eff} \nabla\cdot \mathbf{u}\,\mathbf{I} - \tfrac{2}{3}\rho\, k\,\mathbf{I}}_{II} \tag{4.66}$$

is split into two parts.

The first part (I), is resolved into its normal and cross-diffusive parts according to Eq.(4.20). The normal diffusion at f, $\mathcal{S}_f \cdot \mathbf{d}^{nor}_f(\mathbf{u})$ forms the diffusion part of the coefficient (see Eq.(4.30)):

$$\mathcal{S}_f \cdot \mathbf{d}^{nor}_f(\mathbf{u}) = \mathcal{D}^{\mathbf{u}}_f(\mathbf{u}_N - \mathbf{u}_P) \tag{4.67}$$

$$\mathcal{D}^{\mathbf{u}}_f = \mathcal{S}_f \cdot \overline{\mathcal{S}_f}^P \tag{4.68}$$

The cross diffusion contribution of I for the whole cell forms the cross-diffusion vector $\mathbf{D}^{\mathbf{u},c}_f$ (Eq.(4.64)). It is given according to Eq.(4.31) by:

$$\mathbf{D}^{\mathbf{u},c}_f = \sum_{i=1}^{3} \mathcal{S}_f \cdot \mathbf{d}^c_f(u^o_i)\, \mathbf{e}_i \tag{4.69}$$

where $\mathbf{e}_i$ stands for the unit base vector in the global Cartesian coordinate system.

The second part (II) is treated explicitly, as follows:

$$\begin{aligned}(\mathbf{S}^{\mathbf{u}}_{\mathcal{U}})_P = & \left\{V\,\mathbf{N}\cdot\left[\rho\,\nu_{eff}\mathbf{N}(\mathbf{u}^o)^T\right]\right\}_P - \\ - & \frac{2}{3}\,[\,V\,\mathbf{N}\,(\rho\,\nu_{eff}\mathbf{N}\cdot\mathbf{u}^o)]_P - \\ - & \frac{2}{3}\,[\,V\,\mathbf{N}(\rho k^o)]_P\end{aligned} \tag{4.70}$$

The spray contribution term to the gas momentum conservation equation is obtained from Eq.(3.74). After its discretisation (see §(4.5.1), §(4.5.2) and Appendix B.1), this term is linearised and split into $(\mathbf{S}^{\mathbf{u},d}_{\mathcal{U}})_P$ and $(S^{\mathbf{u},d}_{\mathcal{P}})_P$ as:

$$\begin{aligned}(\mathbf{S}^{\mathbf{u},d}_{\mathcal{U}})_P = & -\frac{1}{\Delta t}\int_{V_P}\sum_{p=1}^{p=N_p}\sum_{i=1}^{i=N_s}\delta(\mathbf{x}-\mathbf{x}^i_p) \\ & \left[m^i_p\left(\frac{\tau_{\mathbf{u}}\mathbf{u}_p + \Delta t'\mathbf{u}''(\mathbf{x}_p)}{\tau_{\mathbf{u}} + \Delta t'}\right)^{i-1} - (m_p\mathbf{u}_p)^{i-1}\right] dV\end{aligned} \tag{4.71}$$

$$(S^{\mathbf{u},d}_{\mathcal{P}})_P = -\frac{1}{\Delta t}\int_{V_P}\sum_{p=1}^{p=N_p}\sum_{i=1}^{i=N_s}\delta(\mathbf{x}-\mathbf{x}^i_p)\left(\frac{m_p\,\Delta t'}{\tau_{\mathbf{u}} + \Delta t'}\right)^i dV \tag{4.72}$$

In the above equations, the summation is performed over all spray particles N_p and over N_s subcycling time steps.

Concerning Eg.(4.71), it should be recall that the fluctuating gas velocity $\mathbf{u}''(p)$ belongs to the eddy where the parcel p temporarily resides.

In the cells adjacent to the wall boundaries, the boundary source term $\mathbf{S}^{\mathbf{u}}_b$, according to Eqs. (2.61) and (2.68), is:

$$(\mathbf{S}^{\mathbf{u}}_b)_P = (F^{\mathbf{u}}_w)_P\left[\mathbf{u}_P - \mathbf{u}_W - (\mathbf{u}_P - \mathbf{u}_W)\cdot\frac{\mathcal{S}_b}{|\mathcal{S}_b|^2}\,\mathcal{S}_b\right]|\mathcal{S}_b| \tag{4.73}$$

where $\mathbf{u}_W$ is the wall velocity and $\mathcal{S}_b$ is the cell face vector at the wall boundary pointing out of the domain. Its $\mathbf{S}^{\mathbf{u}}_{\mathcal{U}b}$ term, given here in component form, and $S^{\mathbf{u}}_{\mathcal{P},b}$ term are:

$$(S^{u_i}_{\mathcal{U}b})_P = -(F^{\mathbf{u}}_w)_P\left[|\mathcal{S}_b| - \frac{(\mathcal{S}_b\cdot\mathbf{e}_i)^2}{|\mathcal{S}_b|}\right] u_{i,W} -$$

$$- (F^{\mathbf{u}}_w)_P \, \frac{(\mathcal{S}_b \cdot \mathbf{e}_i)^2}{|\mathcal{S}_b|} \left[\sum_{j \neq i} (u_{j,P} - u_{j,W}) \, \mathcal{S}_b \cdot \mathbf{e}_j \right] \qquad (4.74)$$

$$(S^{u_i}_{\mathcal{P},b})_P = (F^{\mathbf{u}}_w)_P \left[|\mathcal{S}_b| - \frac{(\mathcal{S}_b \cdot \mathbf{e}_i)^2}{|\mathcal{S}_f|} \right] \qquad (4.75)$$

where $\mathbf{e}$ is a unit base vector in the global coordinate system, and i and j denote coordinate directions ($i, j = 1, 2, 3$).

4.4.3 Energy conservation equation

The discretised form of the energy conservation equation, Eq.(2.39) is:

$$\mathcal{A}^e_P (e)_P = \sum_N \mathcal{A}^e_N (e)_N + b^e_P \quad , \; P = 1, \ldots N_c \qquad (4.76)$$

$$\mathcal{A}^e_P = \sum_N \mathcal{A}^e_N + \frac{(\rho V)^o_P}{\Delta t} - (S^{e,d}_{\mathcal{P}})_P + (S^d)_P \qquad (4.77)$$

$$\mathcal{A}^e_N = [\, \mathcal{C}_f (w^e_f - 1) + \mathcal{D}^e_f \,] \qquad (4.78)$$

$$b^e_P = \frac{(\rho V)^o_P}{\Delta t} (e)^o_P + \sum_{\{f\}_P} D^{e,c}_f + (S^e_{\mathcal{U}})_P + (S^{e,d}_{\mathcal{U}})_P + (S^d)_P \qquad (4.79)$$

The source terms are as follows:

$$(S^e_{\mathcal{U}})_P = - \frac{[p + (p)^o]_P}{2} \, (\vartheta \; V \, \mathbf{N} \cdot \mathbf{u})_P \qquad (4.80)$$

$$(S^{e,d}_{\mathcal{P}})_P = - \frac{1}{e^o_P} \frac{1}{\Delta t} \int_{V_P} \sum_{p=1}^{p=N_P} \sum_{i=1}^{i=N_s} \delta(\mathbf{x} - \mathbf{x}^i_p) \, m^i_p \left(\frac{c_l f}{\tau_e} \right)^{i-1} T(\mathbf{x}^i_p) \Delta t' \, dV \qquad (4.81)$$

$$(S^{e,d}_{\mathcal{U}})_P = \frac{1}{\Delta t} \int_{V_P} \sum_{p=1}^{p=N_P} \sum_{i=1}^{i=N_s} \delta(\mathbf{x} - \mathbf{x}^i_p)$$

$$m^i_p \left\{ \frac{\left[c^{i-1}_l (T^i_p - T_{ref}) + h_v (T^{i-1}_p) \right]}{\tau^{i-1}} + \left(\frac{c_l f}{\tau_e} \right)^{i-1} T^i_p \right\} \Delta t' \, dV \qquad (4.82)$$

In the case of heat transfer at a wall, the boundary source term in a cell adjacent to the wall, expressed via the wall function (see Eq.(2.62)), reads:

$$(S^e_b)_P = - \, \mathcal{S}_b \cdot \mathbf{q}_W$$

$$= - \, |\mathcal{S}_b| \, (F^e_w)_P \, (e_W - e_P) \qquad (4.83)$$

where $\mathbf{q}_W$ stands for the vector of the heat flux at the wall, and $\mathcal{S}_b$ and T_W are the cell face vector at the wall (pointing out of the domain), and wall temperature,

respectively. The $(S^e_{\mathcal{U},b})$ and $(S^e_{\mathcal{P},b})$ terms of Eq.(4.83) are then given by:

$$(S^e_{\mathcal{U},b})_P = -|\mathcal{S}_b| \, (F^e_w)_P \, e_W \qquad (4.84)$$

$$(S^e_{\mathcal{P},b})_P = |\mathcal{S}_b| \, (F^e_w)_P \qquad (4.85)$$

4.4.4 Turbulence equations

Turbulence energy

The turbulence energy conservation equation Eq.(2.49) is discretised as shown below:

$$\mathcal{A}^k_P k_P = \sum_N \mathcal{A}^k_N k_N + b^k_P \quad , \; P = 1, \ldots N_c \qquad (4.86)$$

$$\mathcal{A}^k_P = \sum_N \mathcal{A}^k_N + \frac{(\rho V)^o_P}{\Delta t} - (S^k_{\mathcal{P}})_P - (S^{k,d}_{\mathcal{P}})_P + (S^d)_P \qquad (4.87)$$

$$\mathcal{A}^k_N = [\, \mathcal{C}_f (w^k_f - 1) + \mathcal{D}^k_f \,] \qquad (4.88)$$

$$b^k_P = \frac{(\rho V)^o_P}{\Delta t} (k)^o_P + \sum_{\{f\}_P} D^{k,c}_f + (S^k_{\mathcal{U}})_P + (S^{k,d}_{\mathcal{U}})_P \qquad (4.89)$$

The gas-related $S_{\mathcal{P}}$ and $S_{\mathcal{U}}$ terms are:

$$(S^k_{\mathcal{P}})_P = -C_\mu (V \rho \, k^o)_P \left[\frac{2}{3} \frac{1}{\epsilon^o} (\mathbf{N} \cdot \mathbf{u})^2 + \frac{1}{\nu_t} \right]_P$$

$$+ \; \frac{2}{3} (V \rho)_P \; \min[\, 0, (\mathbf{N} \cdot \mathbf{u})_P] \qquad (4.90)$$

$$(S^k_{\mathcal{U}})_P = G_1 + \frac{2}{3} (V \rho \, k^o)_P \; \max[\, 0, (\mathbf{N} \cdot \mathbf{u})_P] \qquad (4.91)$$

$$G_1 = (V \rho \, \nu_t)_P \left\{ \left[\mathbf{N}\mathbf{u} + (\mathbf{N}\mathbf{u})^T \right] : \mathbf{N}\mathbf{u} \right\}_P \qquad (4.92)$$

where the term linearly dependent on the divergence of velocity ($\mathbf{N} \cdot \mathbf{u}$) is treated implicitly or explicitly according to its sign. This is accomplished by the max and min functions in the above expressions.

The same approach is used with $S_{\mathcal{P}}$ and $S_{\mathcal{U}}$ terms which represent the direct spray contribution (see Eqs.(2.51) and (A.46)):

$$(S^{k,d}_{\mathcal{P}})_P = \frac{1}{k^o_P} \min[\, 0, (\dot{S}^d_k)_P] \qquad (4.93)$$

$$(S^{k,d}_{\mathcal{U}})_P = \max[\, 0, (\dot{S}^d_k)_P] \qquad (4.94)$$

$$(\dot{S}^d_k)_P = - \frac{1}{\Delta t} \int_{\delta V} \sum_{p=1}^{p=N_P} \sum_{i=1}^{i=N_s} \delta(\mathbf{x} - \mathbf{x}^i_p)$$

$$\left\{(m_p\mathbf{u}_p)^i - (m_p\mathbf{u}_p)^{i-1} - [\hat{\mathbf{u}}^i - \frac{1}{2}(\mathbf{u}'')^i]\,(m_p^i - m_p^{i-1})\right\}\cdot$$
$$\cdot(\mathbf{u}'')^i\,\Delta t'\,dV \tag{4.95}$$

The cells adjacent to the wall boundaries are specially treated. In these cells the average energy dissipation rate over the control volume, [123], is calculated using the wall functions (§(2.4)). This is accomplished by evaluating the $(S^k_{\mathcal{P}})_P$ term in Eq.(4.90) using the following expression of ν_t:

$$\nu_t = \begin{cases} \nu_m\,; & y^+ \le y_c^+ \\ \frac{C_\mu^{1/4}\,k^{1/2}\,\kappa\,y}{\ln(E\,y^+)} & y^+ > y_c^+ \end{cases} \tag{4.96}$$

and by modifying that part of the generation term in Eq.(4.92) caused by the work of the wall shear stress, τ_W. In the case of the turbulent Couette flow, the generation rate in the cell adjacent to the wall, $(G_w)_P$, is given by the following formula ([203]):

$$(G_w)_P = \int_{V_P} \tau_W\,(-\frac{\partial u}{\partial \mathbf{n}})\,dV \tag{4.97}$$

where u is the velocity parallel to the wall and $\mathbf{n}$ a normal vector shown in Fig.2.2.

After substituting Eq.(2.61) into the above formula, and discretisation, the result obtained is:

$$(G_w)_P = -\int_{V_P} F_w^{\mathbf{u}}\,u'_P\frac{u'_P}{y_P}\,dV \tag{4.98}$$
$$\approx -\frac{F_w^{\mathbf{u}}}{y_P}\,\mathbf{u}'_P\cdot\mathbf{u}'_P\,V_P \tag{4.99}$$

where $F_w^{\mathbf{u}}$ is the wall function given in §(2.4.1) by Eqs.(2.63) and (2.64), y_P is the normal distance from the cell centre to the wall, and $\mathbf{u}'_P$ is the component of the relative velocity parallel to the wall; see Fig.2.2.

Since there is no diffusion of k at the wall boundary, §(2.4.1), the boundary source term, S_b^k (Eg.(4.49)), is set to zero, i.e.:

$$(S_b^k)_P = 0 \tag{4.100}$$

Turbulence dissipation

The system of algebraic equations which represents the conservation of the turbulence dissipation, obtained by discretisation of Eq.(2.52), is given by:

$$\mathcal{A}_P^\epsilon\epsilon_P = \sum_N \mathcal{A}_N^\epsilon\epsilon_N + b_P^\epsilon \quad,\ P=1,\dots N_c \tag{4.101}$$
$$\mathcal{A}_P^\epsilon = \sum_N \mathcal{A}_N^\epsilon + \frac{(\rho V)_P^o}{\Delta t} - (S_{\mathcal{P}}^\epsilon)_P - (S_{\mathcal{P}}^{\epsilon,d})_P + (S^d)_P \tag{4.102}$$
$$\mathcal{A}_N^\epsilon = [\,\mathcal{C}_f(w_f^\epsilon - 1) + \mathcal{D}_f^\epsilon\,] \tag{4.103}$$
$$b_P^\epsilon = \frac{(\rho V)_P^o}{\Delta t}(\epsilon)_P^o + \sum_{\{f\}_P} D_f^{\epsilon,c} + (S_{\mathcal{U}}^\epsilon)_P + (S_{\mathcal{U}}^{\epsilon,d})_P \tag{4.104}$$

The gas and spray source terms are respectively:

$$(S_{\mathcal{P}}^\epsilon)_P = -(V\rho\,\frac{1}{k^o})_P\left[\frac{2}{3}\,C_{\epsilon1}\,\nu_t\,(\mathbf{N}\cdot\mathbf{u})^2 + C_{\epsilon2}\,\epsilon^o\right]_P$$
$$+\ (C_{\epsilon3} - \frac{2}{3}\,C_{\epsilon1})\,(V\rho)_P\ \min[\,0,(\mathbf{N}\cdot\mathbf{u})_P] \tag{4.105}$$
$$(S_{\mathcal{U}}^\epsilon)_P = C_{\epsilon1}G_1\left(\frac{\epsilon}{k}\right)_P^o$$
$$+\ (C_{\epsilon3} - \frac{2}{3}\,C_{\epsilon1})\,(V\rho\,\epsilon^o)_P\ \max[\,0,(\mathbf{N}\cdot\mathbf{u})_P] \tag{4.106}$$

$$(S_{\mathcal{P}}^{\epsilon,d})_P = C_{\epsilon4}\,\frac{1}{k_P^o}\min[\,0,(\dot{S}_k^d)_P] \tag{4.107}$$
$$(S_{\mathcal{U}}^{\epsilon,d})_P = C_{\epsilon4}\left(\frac{\epsilon}{k}\right)_P^o\max[\,0,(\dot{S}_k^d)_P] \tag{4.108}$$
$$\tag{4.109}$$

The above mentioned spray source term is derived from Eqs.(2.53), (A.52) and (A.46).

In the cells adjacent to the walls, the dissipation rate is calculated from the wall function, Eq.(2.69), as:

$$\epsilon_P = C_\mu^{3/4}\,\frac{k_P^{3/2}}{\kappa y_P} \tag{4.110}$$

This is accomplished by setting the boundary source term, Eq.(4.49), to:

$$(S_{\mathcal{U},b}^\epsilon)_P = L\,C_\mu^{3/4}\,\frac{k_P^{3/2}}{\kappa y_P} \tag{4.111}$$
$$(S_{\mathcal{P},b}^\epsilon)_P = -L \tag{4.112}$$

where L is a very large number.

4.5 Discretised spray equations

As already noted in §(3) the equations which describe spray behaviour are the ordinary differential equations. All of them are discretised in first-order implicit Euler form, apart from the parcel trajectory equation and the equation of boundary layer development in the nozzle model which are treated explicitly, and the diameter rate equation in the breakup model which is exactly solved.

4.5.1 Temporal subcycling

In order to distinguish the time step used in the integration of the spray equations from that used in the integration of the gas conservation equations, here the former will be denoted by $\Delta t'$. This is usually called the subcycling time step and is set at the minimum of the relevant spray time scales; ie:

$$\Delta t' = min(\tau, \tau_{\mathbf{u}}, \tau_e, \tau_b, \tau_c) \tag{4.113}$$

where all the time scales have already been defined in §(3), apart from τ_c. The latter is the parcel residence time, i.e. the time parcel spends in the current cell. It is calculated from the characteristic cell length ($L_c = V^{1/3}$; V is the cell volume) and parcel velocity as:

$$\tau_c = \frac{L_c}{|\mathbf{u}_p|} \tag{4.114}$$

This practice, when the time step used in the integration of the gas transport equation is divided into N_s ($N_s = \Delta t/\Delta t'$) subcycling time steps for the integration of spray equations, will be called temporal subcycling[4]. The subsequent values of variables at times t and $t + \Delta t'$ will be denoted by the superscript $i-1$ and i, respectively.

4.5.2 Spatial interpolation

Since the spray governing equations need gas properties along the drop/parcel trajectory ($\mathbf{u}$, T, etc.) the following linear interpolation scheme for the estimation of

[4]Since N_s in the general case is not an integer, it is evaluated from $N_s = int(\Delta t/\Delta t')$ and one additional subcycling step with the time step equal to $\Delta t - int(\Delta t/\Delta t')\Delta t'$ is performed.

these values is used. In term of general property ϕ, its value at parcel location $\mathbf{x}_p$, $\phi(\mathbf{x}_p)$, is evaluated from:

$$\phi(\mathbf{x}_p) = \phi_P + (\mathbf{N}\phi)_P \cdot (\mathbf{r}_P - \mathbf{x}_p) \tag{4.115}$$

where $\mathbf{r}_P$ is the position vector of cell center in which the parcel temporarily resides.

4.5.3 Spray governing equations

The equations which describe spray behaviour, (3.60) for trajectory, (3.81) for mass conservation, (3.73) and (3.92) for momentum and energy conservation, (3.30) and (3.33) for nozzle flow, and (3.16) and (3.100) for atomisation and breakup processes, are discretised as follows.

Parcel trajectory

Explicit discretisation of Eq.(3.60) yields:

$$\mathbf{x}_p^i = \mathbf{x}_p^{i-1} + \mathbf{u}_p^{i-1}\,\Delta t' \tag{4.116}$$

Parcel mass conservation equation

The parcel mass conservation equation (3.81) is discretised in the implicit way as:

$$\frac{m_p^i - m_p^{i-1}}{\Delta t'} = -\frac{m_p^i}{\tau^{i-1}} \tag{4.117}$$

which results in the following final form:

$$m_p^i = \frac{\tau^{i-1}}{\tau^{i-1} + \Delta t'} m_p^{i-1} \tag{4.118}$$

Parcel momentum conservation equation

The discretisation of Eq.(3.73), after the instantaneous gas velocity is expressed via Eq.(3.54), gives the following:

$$\mathbf{u}_p^i = \frac{\Delta t'[\mathbf{u}(\mathbf{x}_p^{i-1}) + \mathbf{u}''(\mathbf{x}_p^{i-1})] + (\tau_{\mathbf{u}}\mathbf{u}_p)^{i-1}}{\Delta t' + \tau_{\mathbf{u}}^{i-1}} \tag{4.119}$$

Parcel energy conservation equation

Implicit discretisation of Eq.(3.92) yields:

$$T_p^i = \frac{1}{\tau_e^{i-1} + f^{i-1}\Delta t'}\left[f^{i-1}\Delta t'\, T(\mathbf{x}_p^i) + (\tau_e\, T_p)^{i-1} - \Delta t' \left(\frac{\tau_e h_v(T_p)}{\tau\, c_l}\right)^{i-1}\right] \quad (4.120)$$

Atomisation and breakup equations

The diameter rate equation in the atomisation model, Eq.(3.16), is discretised as:

$$D_d^i = D_d^{i-1} - \left(\frac{L_A}{\tau_A}\right)^{i-1} \Delta t'' \quad (4.121)$$

The above equations is integrated by a separate subscycling time step $\Delta t'' = \tau_A/10$, because atomisation is calculated at the beginning of each time step, prior to the calculation of the gas transport equations and the rest of spray equations.

In the breakup model, under assumption that the stable diameter D_s and the breakup time τ_b are constant during $\Delta t'$, the exact integration of equation (3.100) which describes droplet diameter change during $\Delta t'$, yields:

$$D_d^i = D_s^{i-1} - (D_d - D_s)^{i-1} \exp(\frac{\Delta t'}{\tau_b^{i-1}}) \quad (4.122)$$

Nozzle flow equations

Equations (3.30) and (3.33), which describe nozzle flow, are both of the form:

$$\frac{dy}{dx} = F(y) \quad (4.123)$$

The equation is discretised explicitly as:

$$y^i = y^{i-1} + F(y^{i-1})\Delta x \quad (4.124)$$

and integrated with Δx of the order of 10^{-4}, which assures that the total error is of the order of 10^{-3}, [147].

4.5.4 Initial conditions

The initial drop diameter is set to the injector hole diameter, and its location (position vector) is the injector location. The drop has the initial, prescribed temperature and corresponding density, and its velocity is randomly chosen as described in §(3.10).

The number of drops in the computational parcel is calculated based on the fuel mass injected in the considered time step, and the specified parcel injection rate, i.e. the number of parcel injected in the current time step, see also §(3.10).

4.6 Closure

In this chapter the discretised counterparts of the gas transport equations, assembled in §(2), and the spray governing equations, presented in §(3), have been given.

The gas transport equations have been discretised by the finite volume method, on an arbitrary unstructured mesh, composed of the hexahedral cells. The collocated variable arrangement and fully-implicit temporal discretisation practice have been used. The latter ensures linear stability of the solution for an arbitrary time step size.

In section (4.3), the detailed discretisation of the general transport equation has been described, together with the assembly of the algebraic system of equations. In section (4.3.5) two differencing schemes, hybrid and SFCD, have been explained. The treatment of the boundary conditions, apart from the wall boundary conditions, has been given in section (4.3.6). The discretised forms of the gas transport equations, together with the wall boundary conditions, have been described in the subsequent sections, namely §(4.4.1) - mass conservation equations, in §(4.4.2) - momentum conservation equation, and in §(4.4.3) and (4.4.4) the energy and the turbulence equations, respectively. The same sections present the discretised spray source contributions to the gas equations. They have been resolved into explicit and implicit parts to enhance diagonal dominance of gas phase equations for stability reasons.

The spray equations have been discretised in the first-order implicit Eulerian fashion in section (4.5). They have been discretised in time with a different time step from the gas equations, to allow for the smaller time scales of spray processes; a technique known as the temporal subcycling.

The final result of discretisation is a system of simultaneous non-linear algebraic equations. In the following chapter the solution procedure for solving this system will be given.

Chapter 5

Solution procedure

5.1 Introduction

The system of equations obtained by the discretisation process given in the previous chapter is complex. The equations are non-linear and mutually coupled. The solution procedure is also burdened with problems arising from the relatively large global changes of pressure, density and temperature compared to the local spatial variations of these quantities due to the piston and valve motions, flow through valve curtains, and also, but not so strongly, by the heat transfer between the gas and the cylinder walls. This is the reason why the solution procedure is split into two stages: a bulk adjustment stage, which deals with the global adjustment of the gas fields, and a predictor-corrector stage, which resolves the coupling between equations. The operator-splitting method called PISO [110] was chosen for the latter stage.

An iterative method which combines these steps, applied to single-phase in-cylinder flow, was first developed by Watkins, [217]. Later on the PISO algorithm was modified for this task by Begleris [24] and given the name 'EPISO'. In the present study, due to the presence of the liquid phase and the transfer processes between phases, the EPISO method had to be modified. Also, the incorporation of the fuel vapour mass fraction and energy conservation equations into the predictor-corrector sequence was necessary to allow for the existence of large density and temperature gradients. All these features have demanded significant restructuring of the original algorithms presented in [110] and [24], as described in the following sections [1].

The main features of the adopted solution algorithm are:

- Use of an operator splitting technique (PISO) to temporarily decouple the flow equations, enabling sequential solution (segregated approach).

- Linearisation of the individual set of equations by assuming that their coefficients and source terms are constant, and evaluated from the currently-available values of the dependent variable prior to the solution of the system.

- Enforcement of mass conservation by a pressure equation, derived by combining the discretised mass and momentum conservation equations.

- Use of a solution procedure involves a predictor step in which the fuel vapour mass fraction equation as well as the energy equation are solved in implicit form together with the gas momentum conservation equations. These fields are then refined in the corrector steps.

- In the corrector steps, the field-dependent coefficients arising from the coupling and nonlinearities are updated. This is done after the continuity-based pressure equation is solved to ensure mass conservation.

- The above corrector sequence is repetitively performed until the required accuracy of the solution is reached.

- The spray calculation is fully embedded in the predictor-corrector sequence.

The first part of this chapter is devoted to the solution sequence. In §(5.2.1) the bulk adjustment stage is described, and in §(5.2.2) and §(5.2.3) the predictor and corrector steps of the algorithm are given. In section (5.2.4) a methodology for the solution of the turbulence equations is presented.

The second part of the chapter, §(5.3), deals with the solvers for the linear algebraic equations and convergence criteria. The individual linearised equations are

[1]The modifications to the algorithm also make it suitable for reacting flows, where even larger gradients of all variables are present.

solved by conjugate gradient methods ([97]), and to improve computational efficiency the matrices are preconditioned which significantly reduces the number of iterations required for the solution. Brief descriptions of the above topics are given in §(5.3.1). In §(5.3.2), the convergence criteria used in this study are presented.

5.2 Solution sequence

A flow chart of the solution algorithm is given in Fig.5.1, and the description of its particular blocks can be summarised as follows.

1. **Initialisation**
   Here, all the necessary geometrical characteristics of the mesh are evaluated, and the initial values of the dependent variables are set. The field values at this point are denoted by the superscript '^{o}'.

2. **Mesh motion**
   Calculates the new locations of cell vertices, the volumes of cells and the spatial interpolation factors, after the time has advanced by Δt.

3. **Valve flow**
   Determines the inlet/outlet mass and ϕ-fluxes through the valve curtains.

4. **Bulk adjustment**
   Determines the bulk values of p, ρ and e (T) due to the mesh motion, heat transfer and valve flow, and updates the local values of these quantities and the effective viscosity. The updated values of the pressure, density and viscosity, at this stage are denoted by the superscript '$^{(1)}$' ($p^{(1)}$, $\rho^{(1)}$, and $\mu_{eff}^{(1)}$). Intermediate values of the internal energy, and temperature, which are also calculated at this stage (from the gas equation of state), are denoted by $'$, i.e. e' and (T'); these quantities will be letter denoted by the superscript '$^{(1)}$' after the predictor step, in which the gas internal energy conservation equation is solved, producing new values for the gas energy and temperature.

5. **Predictor step**

   Calculates the spray contributions to the source terms in the gas momentum, mass and energy conservation equations; assembles and solves the equations for the fuel vapour mass fraction ($Y_{ft}^{(1)}$), gas internal energy ($e^{(1)}$) and velocity ($\mathbf{u}^{(1)}$), employing the currently-available pressure and mass fluxes.

6. **Corrector steps**

   Finds the corrected spray contributions to the gas, and calculates a new estimate of the pressure field ($p^{(2)}$). Then, updates the mass fluxes, density ($\rho^{(2)}$) and corrects the gas velocity ($\mathbf{u}^{(2)}$). After this, assembles and solves the equations for the fuel vapour mass fraction ($Y_{ft}^{(2)}$) and gas internal energy ($e^{(2)}$).

   This step is repeated until specific criteria have been satisfied as described later.

7. **Drop-drop interactions**

   Calculates collision between drops. Note that the drop-drop interactions are not allowed to effect the gas phase in the current time step, but only modify the properties of liquid phase.

8. **Turbulence calculation**

   Assembles and solves the conservation equations for the turbulence kinetic energy and its dissipation rate.

The field values obtained from the above sequence, denoted by the superscript ^{n}, represent the numerical solution of the governing equations at $t = t_o + \Delta t$. For the next time step, the solution sequence is repeated using the just obtained results as the initial values. The calculation is terminated when the required, total elapsed time (or crank angle) has been reached.

A detailed explanation of the main blocks of the solution algorithm is given in the following sections.

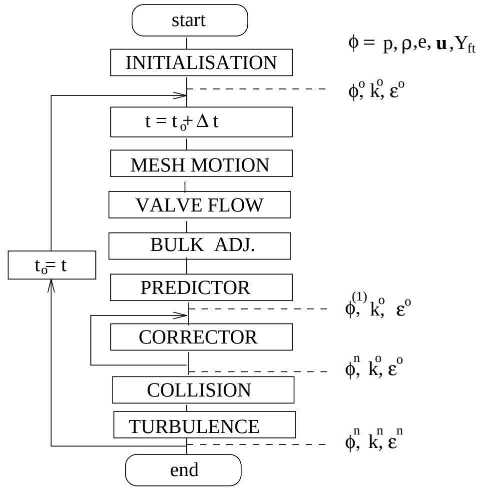

Figure 5.1: Solution algorithm

5.2.1 Bulk adjustment

This block comprises two stages. The first deals with the estimation of average (bulk) properties, namely, the average (cylinder) pressure and density. In the second stage, local adjustment of the pressure and density is performed.

Bulk properties

The pressure field is split into the two components, an average (cylinder) pressure (p_{cyl}) and the relative pressure (p'). The evolution of the average pressure is calculated from overall conservation balances prior to the three-dimensional flow solution. This is done because the absolute pressure is large compared to the spatial variations due to the piston motion, heat transfer and valve flow, and the solution tolerance required for the three-dimensional pressure calculation is very much finer for the absolute pressure, [24].

The global calculation is based on mass and enthalpy balances for the entire cylinder contents. In the general case, the bulk quantities p_{cyl} and ρ_{cyl} at $t = t_o + \Delta t$, derived from these laws (see Appendix D.1 for derivation), are:

Energy

$$p_{cyl} = \frac{\left[\left(\frac{c_p}{R}\right)_{cyl} - 1\right] \overline{V}_{cyl}\, p^o_{cyl} + [\dot{Q}_b - e_v\, \dot{m}_v]\Delta t}{\left[\left(\frac{c_p}{R}\right)_{cyl} - 1\right] \overline{V}_{cyl} + \left(\frac{c_p}{R}\right)_{cyl} (V_{cyl} - V^o_{cyl})} \tag{5.1}$$

Mass

$$\rho_{cyl} = \frac{\left(\rho^o_{cyl} V^o_{cyl} - \dot{m}_v \Delta t\right)}{V_{cyl}} \tag{5.2}$$

where $\left(\frac{c_p}{R}\right)_{cyl}$ is the volume-averaged value of $\frac{c_p}{R}$ [2], e_v and $\dot{m}_v$ are the specific internal energy and mass flow rate of the valve flow (negative $\dot{m}_v$ means inflow); $\dot{Q}_b$ is the total heat transfer rate at the cylinder surface, and $\overline{V}_{cyl} = (V^o_{cyl} + V_{cyl})/2$ is the average cylinder volume. In Eq.(5.1), the first term of the numerator of RHS represents the effect of the change of cylinder volume, and the second term the effects of the valve flow and heat transfer on the bulk cylinder pressure.

Local corrections

Uniform global corrections, marked by superscript '$^+$', are made to the old time level local density and relative pressure values as:

$$\rho^{(1)}_i = \rho^o_i + \rho^+ \tag{5.3}$$

$$(p')^{(1)}_i = (p')^o_i + p^+ \tag{5.4}$$

where ρ^+ and p^+ are evaluated from the mass and energy balance in the cylinder, see Appendix D.1, as:

$$\rho^+ = \rho_{cyl} - \frac{1}{V_{cyl}} \sum_{i=1}^{N_c} \rho^o_i V_i \tag{5.5}$$

[2] c_p and R are the specific heat capacity at constant pressure and gas constant, respectively. The volume averaged ratio $\left(\frac{c_p}{R}\right)_{cyl}$ is calculated as follows:

$$\left(\frac{c_p}{R}\right)_{cyl} = \frac{1}{V_{cyl}} \sum_{i}^{N_c} V_i \frac{c_p(T_i)}{R_i}$$

$$p^+ = -\frac{1}{\vartheta_{cyl} V_{cyl}} \sum_{i=1}^{N_c} (p')^o_i \vartheta_i V_i \tag{5.6}$$

Here, ϑ_{cyl} is the average (cylinder) void fraction defined as:

$$\vartheta_{cyl} = \frac{1}{V_{cyl}} \sum_{i=1}^{N_c} \vartheta_i V_i \tag{5.7}$$

The local gas temperature is corrected based on the gas equation of state:

$$T'_i = \frac{\vartheta_i\, [p_{cyl} + (p')^{(1)}_i]}{R_i \rho^{(1)}_i} \quad , \qquad i = 1, \ldots, N_c \tag{5.8}$$

The above values are then used to update the local gas internal energy and viscosity:

$$e' = e(T', Y^o_{ft}) \tag{5.9}$$

$$\mu_{eff} = C_\mu\, \rho^{(1)} \frac{(k^o)^2}{\epsilon^o} + \mu_m \tag{5.10}$$

In Eqs.(5.8) and (5.9) the intermediate values of T and e have superscript $'$, since these quantities will be further modified in the predictor stage (see item 4 in §(5.2)). The superscript $^{(1)}$ is reserved to mark the quantities at the end of the predictor stage; see also Fig.5.1.

5.2.2 Predictor step

The solution sequence of the predictor step is shown in Fig.5.2. Two main blocks can be seen, labelled 'spray predictor' and 'gas predictor'. In the spray predictor the spray equations are solved to determine the local void fraction $\vartheta^{(1)}$ as well as the spray contributions to the source/sink terms of the gas mass, fuel vapour mass fraction, momentum, and energy conservation equations (see \$ (4.4)), i.e.:

$$(S^d)^{(1)}, (\mathbf{S}^{\mathbf{u},d}_{\mathcal{U}})^{(1)}, (S^{\mathbf{u},d}_{\mathcal{P}})^{(1)}, (S^{e,d}_{\mathcal{U}})^{(1)}, (S^{e,d}_{\mathcal{P}})^{(1)}$$

These equations are solved by temporal subcycling (see §4.5) during which the gas fields are kept 'frozen'.

Then, in the gas predictor, the coefficient matrices of the conservation equations for the fuel vapour mass fraction, energy and momentum are assembled and solved in their implicit form with the above spray contribution terms, as follows:

$$\mathcal{A}^{Y_{ft}}_P (Y_{ft})^{(1)}_P = \sum_N \mathcal{A}^{Y_{ft}}_N (Y_{ft})^{(1)}_N + (b^{Y_{ft}}_P)^{(1)} \tag{5.11}$$

$$\mathcal{A}^e_P e^{(1)}_P = \sum_N \mathcal{A}^e_N e^{(1)}_N + (b^e_P)^{(1)} \tag{5.12}$$

$$\begin{aligned}\mathcal{A}^{\mathbf{u}}_P \mathbf{u}^{(1)}_P &= \sum_N \mathcal{A}^{\mathbf{u}}_N \mathbf{u}^{(1)}_N + \mathbf{b}^{\mathbf{u}}_P + \\ &+ (\mathbf{S}^{\mathbf{u},d}_{\mathcal{U}})^{(1)} - \left[V\vartheta^{(1)}\mathbf{N}(p')^{(1)} \right]_P \end{aligned} \tag{5.13}$$

In Eqs.(5.11) and (5.12) the source terms are marked with the superscript $^{(1)}$ to denote that they include corresponding spray contributions mentioned above.

The local gas temperature is calculated from $e^{(1)}$ and $Y^{(1)}_{ft}$ via the inverse function of that given by Eq.(5.9), i.e. e^{-1}, as:

$$T^{(1)}_i = e^{-1}(e^{(1)}_i, Y^{(1)}_{ft}) \tag{5.14}$$

and the effect of the spray on the average cylinder pressure, due to the heat and mass transfer between phases and change in the void fraction, is determined from the following relation:

$$p_{cyl} = \frac{1}{\vartheta^{(1)}_{cyl} V_{cyl}} \sum_i^{N_c} (\rho\, V R\, T)^{(1)}_i \tag{5.15}$$

At the end of this step, provisional values of all the field variables have been obtained. However, at this stage the predicted velocity field does not satisfy the continuity equation. In order to fulfill this requirement, a new pressures and velocities have to be calculated. This is done in the corrector steps.

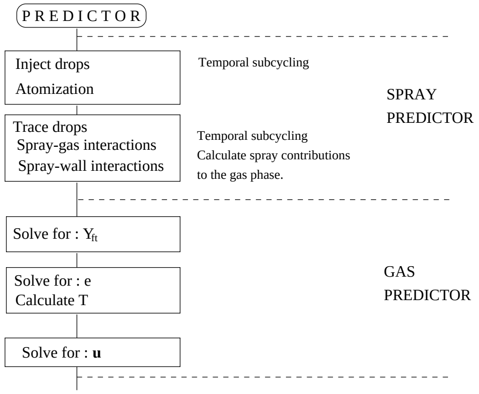

Figure 5.2: Predictor sequence

5.2.3 Corrector step

The corrector stage comprises a number of steps; see Fig.5.3. As in the predictor step, here, two blocks of operations labelled spray corrector and gas corrector can be distinguished. The following description explains the k-th corrector step which is denoted by the superscript $^{(k)}$; $k = 2$ represents the first corrector step.

Firstly, in the spray corrector, the new local void fraction is determined ($\vartheta^{(k)}$), as well as the spray contributions to the gas phase sources:

$$(S^d)^{(k)}, (\mathbf{S}^{\mathbf{u},d}_{\mathcal{U}})^{(k)}, (S^{\mathbf{u},d}_{\mathcal{P}})^{(k)}, (S^{e,d}_{\mathcal{U}})^{(k)}, (S^{e,d}_{\mathcal{P}})^{(k)}$$

Then, the gas corrector is performed, with the following sequence of calculations:

1. Solution of the pressure equation, with updating of the convective fluxes and densities.
2. Correction of the velocities.
3. Solution of the fuel vapour mass fraction equation.
4. Solution of the energy equation.

This procedure, starting with the spray corrector and followed by the above steps in the gas corrector, is repeated until a convergence criterion is reached, see §(5.3.2).

Below, details of the gas corrector sequence are given.

The new pressure and the new velocity field are found solving a continuity-based pressure equation set (see Appendix D.2 for derivation):

$$\mathcal{A}^p_P (p')^{(k)}_P = \sum_N \mathcal{A}^p_N (p')^{(k)}_N + (b^p_P)^{(k)} \quad, \; P = 1, \dots N_c \tag{5.16}$$

$$\mathcal{A}^p_P = \sum_N \mathcal{A}^p_N + \frac{1}{\Delta t}\left(\frac{V\vartheta}{RT}\right)^{(k-1)}_P \tag{5.17}$$

$$\mathcal{A}^p_N = \mathcal{D}^p_f \tag{5.18}$$

$$\begin{aligned}(b^p_P)^{(k)} &= -\sum_{\{f\}_P} (\rho_f)^{(k-1)} \left[\mathbf{H}^{(k-1)} - \mathbf{u}_b \right]_f \cdot \mathcal{S}_f + \\ &+ (S^d)^{(k)}_P - \frac{1}{\Delta t}\left(\frac{V\vartheta p_{ref}}{RT}\right)^{(k-1)}_P + \\ &+ \frac{(\rho V)^o_P}{\Delta t} + \sum_{\{f\}_P} D^{p,c}_f \end{aligned} \tag{5.19}$$

Here $\mathbf{H}^{(k-1)}$ is defined as:

$$\mathbf{H}_P^{(k-1)} = \frac{1}{\mathcal{A}_P^{\mathbf{u}}} \left[\sum_N \mathcal{A}_N^{\mathbf{u}} \mathbf{u}_N^{(k-1)} + \mathbf{b}_P^{\mathbf{u}} + (\mathbf{S}_{\mathcal{U}}^{\mathbf{u},d})_P^{(k)} \right] \tag{5.20}$$

The new convective fluxes are then evaluated from:

$$\mathcal{C}_f^{(k-1)} = \mathcal{S}_f \cdot \left[\rho^{(k-1)} \left(\mathbf{H}^{(k-1)} - \mathbf{u}_b - \frac{1}{\mathcal{A}^{\mathbf{u}}} V \vartheta^{(k)} \mathbf{N}(p')^{(k)} \right) \right]_f \tag{5.21}$$

where $\mathcal{A}^{\mathbf{u}}$ denotes the central coefficient.

The updating of the density field, $\rho^{(k)}$, which follows next, is based on the local mass conservation equation:

$$\rho_P^{(k)} = \left[\frac{(\rho V)_P^o}{\Delta t} + (S^d)_P^{(k)} - \sum_{\{f\}_P} \mathcal{C}_f^{(k-1)} \right] \frac{\Delta t}{V_P} \tag{5.22}$$

After this, the velocities are updated from the following explicit relation (see Appendix D.2):

$$\mathbf{u}_P^{(k)} = \left(\frac{\rho^{(k-1)}}{\rho^{(k)}} \right)_P \left[\mathbf{H}_P^{(k-1)} - \frac{1}{\mathcal{A}_P^{\mathbf{u}}} \vartheta_P^{(k)} \sum_{\{f\}_P} \mathcal{S}_f (p')_f^{(k)} \right] \tag{5.23}$$

When this is finished, the following discretised fuel vapour mass fraction and energy conservation equations (see sections (4.4.1) and (4.4.3)) are solved:

$$\mathcal{A}_P^{Y_{ft}} (Y_{ft})_P^{(k)} = \sum_N \mathcal{A}_N^{Y_{ft}} (Y_{ft})_N^{(k)} + (b_P^{Y_{ft}})^{(k)} \tag{5.24}$$

$$\mathcal{A}_P^e \, e_P^{(k)} = \sum_N \mathcal{A}_N^e \, e_N^{(k)} + (b_P^e)^{(k)} \tag{5.25}$$

in which the coefficients are calculated from the latest available values.

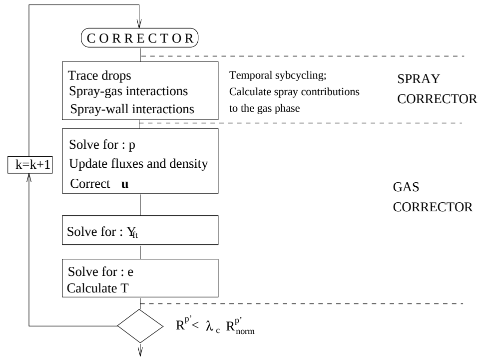

Figure 5.3: Corrector step

5.2.4 Turbulence calculation

The calculation of turbulence fields is performed outside the gas predictor-corrector sequence after the last corrector step is completed; see flow chart in Fig.5.1. Because of the strong source coupling between k and ϵ equations via their source terms, it is necessity to devise a procedure which takes this into account. The predictor-corrector sequence described by Theodoropoulos [204], was adopted in this study, with appropriate modifications to account for the additional spray terms. Details are given below.

Turbulence predictor

The source terms for the k-ϵ equations are first calculated immediately after the last gas corrector. They are here denoted by the superscript 1. The k-ϵ equations are solved in their implicit form as:

$$\mathcal{A}_P^k \, k_P^{(1)} = \sum_N \mathcal{A}_N^k \, k_N^{(1)} + (b_P^k)^{(1)} \tag{5.26}$$

$$\mathcal{A}_P^\epsilon (\epsilon)_P^{(1)} = \sum_N \mathcal{A}_N^\epsilon (\epsilon)_N^{(1)} + (b_P^\epsilon)^{(1)} \tag{5.27}$$

and the predicted values of k and ϵ are obtained.

Algebraic turbulence corrector

The strong dependence of the source terms on k and ϵ means that Egs.(5.26) and (5.27) need further corrections, because in the predictor stage they are solved with lagged source terms. Among the various approaches to this problem, two methods will here be mentioned: a single-corrector method proposed by Issa [110], and 'algebraic corrector method' of Theodoropoulos [204]. In this study the latter method is applied.

The single-corrector method has one corrector step, namely:

$$\left[(\mathcal{A}_P^k)' - (S_\mathcal{P}^k)_P^{(1)}\right] k_P^{(2)} = \sum_N \mathcal{A}_N^k \, k_N^{(1)} + (b_P^k)^{(1)} \tag{5.28}$$

$$\left[(\mathcal{A}_P^\epsilon)' - (S_\mathcal{P}^\epsilon)_P^{(1)}\right] \epsilon_P^{(2)} = \sum_N \mathcal{A}_N^\epsilon \, \epsilon_N^{(1)} + (b_P^\epsilon)^{(1)} \tag{5.29}$$

where the coefficients $S_\mathcal{P}^k$ and $S_\mathcal{P}^\epsilon$, as well as the source terms, (b^k) and (b^ϵ), are evaluated with the predicted values of k and ϵ, i.e. with $k^{(1)}$ and $\epsilon^{(1)}$. The above equations represent Eqs.(4.86) and (4.101) written in a different form, where the central coefficient $\mathcal{A}_P$ is split into the part which does not include $S_\mathcal{P}$, $(\mathcal{A}_P)'$, and $S_\mathcal{P}$ itself. Since equations (5.28) and (5.29) are explicit, they are then easely solved for each cell individually. However, the problem of the lagged source terms remains, because Eqs.(5.28) and (5.29) are uncoupled.

The algebraic corrector method, initiated by Tsui [210] and completed by Theodoropoulos [204], consists of a number of corrector steps, in which the **coupled** system of the equations for k and ϵ is iteratively solved for each cell. Since there are differences in the treatment of internal cells from cells adjacent to the wall boundaries, the description below is split accordingly.

Internal cells

For the purpose of this procedure, the discretised k-ϵ equations, (4.86) and (4.101), are rewritten, for the jth-correction ($j \geq 2$), in the form:

$$\left[(\mathcal{A}_P^k)' - (S_\mathcal{P}^k)'_P\right] k_P^{(j)} = \sum_N \mathcal{A}_N^k \, k_N^{(j-1)} + (b_P^k)^{(j)} \tag{5.30}$$

$$[(\mathcal{A}_P^\epsilon)' - (S_\mathcal{P}^\epsilon)'_P] \, \epsilon_P^{(j)} = \sum_N \mathcal{A}_N^\epsilon \, \epsilon_N^{(j-1)} + (b_P^\epsilon)^{(j)} \tag{5.31}$$

where $(\mathcal{A}_P)'$, $(S_\mathcal{P})'_P$ and $(b_P)^{(j)}$ are defined, for k equation by:

$$(\mathcal{A}_P^k)' = \sum_N \mathcal{A}_N^k + \frac{(\rho V)_P^o}{\Delta t} + (S^d)_P \tag{5.32}$$

$$\begin{aligned}(S_\mathcal{P}^k)'_P = & - \frac{2}{3} \, C_\mu \left[\frac{V \rho \, k^{(j-1)}}{\epsilon^{(j-1)}} (\mathbf{N} \cdot \mathbf{u})^2 \right]_P + \\ & + \frac{1}{k_P^{(j-1)}} \min[\, 0, (\dot{S}_k^d)_P] + \\ & + \frac{1}{k_P^{(j-1)}} \min(0, \sum_{\{f\}_P} D_f^{k,c})\end{aligned} \tag{5.33}$$

$$\begin{aligned}(b_P^k)^{(j)} = & \frac{(\rho V)_P^o}{\Delta t} \, k_P^o + \max(0, \sum_{\{f\}_P} D_f^{k,c}) + \\ & + C_\mu \, (V \rho \, \frac{k^{(j)} k^{(j-1)}}{\epsilon^{(j)}})_P \left\{ \left[\mathbf{Nu} + (\mathbf{Nu})^T \right] : \mathbf{Nu} \right\}_P + \\ & + \frac{2}{3} (V \rho \, k^{(j-1)} \, \mathbf{N} \cdot \mathbf{u})_P - \\ & - (V \, \rho \, \epsilon^{(j)})_P + \max[\, 0, (\dot{S}_k^d)_P]\end{aligned} \tag{5.34}$$

and for ϵ-equation by:

$$(\mathcal{A}_P^\epsilon)' = \sum_N \mathcal{A}_N^\epsilon + \frac{(\rho V)_P^o}{\Delta t} + (S^d)_P \tag{5.35}$$

$$\begin{aligned}(S_\mathcal{P}^\epsilon)'_P = & -(V \rho \, \frac{1}{k^{(j-1)}})_P \, \frac{2}{3} \, C_{\epsilon 1} \, \nu_t \, (\mathbf{N} \cdot \mathbf{u})_P^2 - \\ & - C_{\epsilon 2} \, (V \rho \frac{\epsilon^{(j)}}{k^{(j)}})_P + \\ & + C_{\epsilon 4} \, \frac{1}{k_P^{(j-1)}} \min[\, 0, (\dot{S}_k^d)_P] + \\ & + \frac{1}{\epsilon_P^{(j-1)}} \min(0, \sum_{\{f\}_P} D_f^{\epsilon,c})\end{aligned} \tag{5.36}$$

$$\begin{aligned}(b_P^\epsilon)^{(j)} = & \frac{(\rho V)_P^o}{\Delta t} \, \epsilon_P^o + \max(0, \sum_{\{f\}_P} D_f^{\epsilon,c}) + \\ & + C_{\epsilon 1} G_1 \left(\frac{\epsilon}{k} \right)_P^{(j-1)} + \\ & + (C_{\epsilon 3} - \frac{2}{3} \, C_{\epsilon 1}) \, (V \rho \, \epsilon^{(j-1)} \, \mathbf{N} \cdot \mathbf{u})_P + \\ & + C_{\epsilon 4} \, \left(\frac{\epsilon}{k} \right)_P^{(j-1)} \max[\, 0, (\dot{S}_k^d)_P]\end{aligned} \tag{5.37}$$

Multiplication of Eq.(5.30) by $\epsilon_P^{(j)}$ and Eq.(5.31) by $k_P^{(j)}$ yields:

$$a_0^k \, k^{(j)} \, \epsilon^{(j)} = a_1^k \, \left[\epsilon^{(j)}\right]^2 + a_2^k \, \epsilon^{(j)} + a_3^k \, k^{(j)} \tag{5.38}$$

$$a_0^\epsilon \, k^{(j)} \, \epsilon^{(j)} = a_1^\epsilon \, \left[\epsilon^{(j)}\right]^2 + a_2^\epsilon \, k^{(j)} \tag{5.39}$$

In the above and in the following equations the subscript P is omitted.

The coefficients of Eqs.(5.38) and (5.39) are given by the following expressions:

$$
\begin{aligned}
a_1^k &= \left\{\frac{2}{3}\left(\frac{k}{\epsilon}\right)^{(j-1)} \min[\,0, \mathbf{N}\cdot\mathbf{u}] - 1\right\}(\rho\, V) && (5.40)\\
a_2^k &= \sum_N \mathcal{A}_N^k k_N^{(j-1)} + \frac{(\rho V)^o}{\Delta t}\, k^o + \max(0, \sum_{\{f\}} D_f^{k,c}) + \\
&+ \frac{2}{3} V\, \rho\, k^{(j-1)} \max[\,0, (\mathbf{N}\cdot\mathbf{u})] + \\
&+ \max[\,0, \dot{S}_k^d] && (5.41)\\
a_3^k &= C_\mu\, V \rho\, k^{(j-1)} \left[\mathbf{Nu} + (\mathbf{Nu})^T\right] : \mathbf{Nu} && (5.42)\\
a_0^k &= \sum_N \mathcal{A}_N^k + \frac{(\rho V)^o}{\Delta t} - \frac{1}{k^{(j-1)}} \min(0, \sum_{\{f\}} D_f^{k,c}) + \\
&+ \frac{2}{3} C_\mu\, V\, \rho\, \frac{k^{(j-1)}}{\epsilon^{(j-1)}} (\mathbf{N}\cdot\mathbf{u})^2 - \\
&- \frac{1}{k^{(j-1)}} \min[\,0, \dot{S}_k^d] + S^d && (5.43)
\end{aligned}
$$

$$
\begin{aligned}
a_1^\epsilon &= -C_{\epsilon 2}\, V \rho + (C_{\epsilon 3} - \frac{2}{3} C_{\epsilon 1})\, V \rho\, \min[\,0, (\mathbf{N}\cdot\mathbf{u})]\, \frac{k^{(j-1)}}{\epsilon^{(j-1)}} && (5.44)\\
a_2^\epsilon &= \sum_N \mathcal{A}_N^\epsilon \epsilon_N^{(j-1)} + \frac{(\rho V)^o}{\Delta t}\, \epsilon^o + \max(0, \sum_{\{f\}} D_f^{\epsilon,c}) + \\
&+ C_{\epsilon 1} V\, \rho k^{(j-1)} C_\mu \left[\mathbf{Nu} + (\mathbf{Nu})^T\right] : \mathbf{Nu} + \\
&+ (C_{\epsilon 3} - \frac{2}{3} C_{\epsilon 1})\, V \rho \epsilon^{(j-1)} \max[\,0, (\mathbf{N}\cdot\mathbf{u})] + \\
&+ C_{\epsilon 4}\, \frac{\epsilon^{(j-1)}}{k^{(j-1)}} \max[\,0, \dot{S}_k^d] && (5.45)\\
a_0^\epsilon &= \sum_N \mathcal{A}_N^\epsilon + \frac{(\rho V)^o}{\Delta t} + S^d - \frac{1}{\epsilon^{(j-1)}} \min(0, \sum_{\{f\}} D_f^{\epsilon,c}) + \\
&+ \frac{2}{3} C_{\epsilon 1}\, C_\mu\, V\, \rho\, \frac{k^{(j-1)}}{\epsilon^{(j-1)}} (\mathbf{N}\cdot\mathbf{u})^2 - \\
&- C_{\epsilon 4}\, \frac{1}{k^{(j-1)}} \min[\,0, \dot{S}_k^d] && (5.46)
\end{aligned}
$$

It was shown by Theodoropoulos in [204] that Eqs.(5.38) and (5.39) represent hyperbolas in the k-ϵ space, and that one intersection, among all possible intersections, is the required solution. The same author has also developed a procedure which always leads to the physically acceptable solution, i.e. that both, k and ϵ are positive (§(2.46)). Here, the procedure will only be briefly described.

From Eqs.(5.38) and (5.39), the local (cell) value of k can be expressed by:

$$k^{(j)} = \frac{(A_1^k - A_1^\epsilon)(\epsilon^{(j)})^2 + A_2^k \epsilon^{(j)}}{A_2^\epsilon + A_3^k} \tag{5.47}$$

and after substituting Eq.(5.47) into Eq.(5.38), the following relation is obtained:

$$\epsilon^{(j)}\, [\, B_1 (\epsilon^{(j)})^2 + B_2 \epsilon^{(j)} + B_3\,] = 0 \tag{5.48}$$

where A coefficients in Eq.(5.47) are given by:

$$A_i^\phi = a_i^\phi / a_0^\phi\,; \quad i = 1,2,3;\;\; \phi = k, \epsilon \tag{5.49}$$

and B coefficients in Eq.(5.48) by:

$$
\begin{aligned}
B_1 &= A_1^k - A_1^\epsilon \\
B_2 &= A_2^k - A_1^k A_2^\epsilon + A_3^k A_1^\epsilon \\
B_3 &= -A_2^k A_2^\epsilon
\end{aligned} \tag{5.50}
$$

The positive and non-trivial solution of Eq.(5.48) is:

$$\epsilon^{(j)} = \frac{-B_2 + \sqrt{B_2^2 - 4 B_1 B_3}}{2 B_1} \tag{5.51}$$

The iterative solution procedure, based on the above formulae, comprises the following steps ($j \geq 2$):

1. Calculate A and B coefficients from Eqs.(5.49) and (5.50),
2. Estimate ϵ from Eq.(5.51), with the currently available k and ϵ values; symbolically:

$$\epsilon^{(j)} = F^\epsilon(k^{(j-1)}, \epsilon^{(j-1)}) \tag{5.52}$$

3. Calculate k from Eq.(5.47), using the latest available ϵ; symbolically:

$$k^{(j)} = F^k(k^{(j-1)}, \epsilon^{(j-1)}, \epsilon^{(j)}) \tag{5.53}$$

4. Repeat steps $1 \rightarrow 3$ for all cells in the domain,
5. Check convergence criterion, and if they are not reached, continues with iteration, starting with a point 1 ($j = j + 1$); otherwise, terminates further calculation.

Near-wall cells

The k-ϵ equations for the near-wall cells (see §(4.4.4) and Eqs.(4.86), (4.96) and (4.110)), are rearranged into the following form:

$$
\begin{aligned}
\left[(\mathcal{A}_P^k)' - (S_{\mathcal{P}}^k)'_P\right]\, k_P^{(j)} &= \sum_N \mathcal{A}_N^k\, k_N^{(j-1)} + (b_P^k)^{(j)} && (5.54)\\
\epsilon_P^{(j)} &= C_\mu^{3/4}\, \frac{(k_P^{(j)})^{3/2}}{\kappa y_P} && (5.55)
\end{aligned}
$$

where $(\mathcal{A}_P)'$, $(S_{\mathcal{P}})'_P$ and $(b_P)^{(j)}$ are defined as:

$$
\begin{aligned}
(\mathcal{A}_P^k)' &= \sum_N \mathcal{A}_N^k + \frac{(\rho V)_P^o}{\Delta t} + (S^d)_P && (5.56)\\
(S_{\mathcal{P}}^k)'_P &= -\frac{2}{3}\left[V\rho\,\nu_t\,\frac{(\mathbf{N}\cdot\mathbf{u})^2}{k^{(j-1)}}\right]_P +\\
&+ \frac{1}{k_P^{(j-1)}}\min(0, \sum_{\{f\}_P} D_f^{k,c})\\
&+ \frac{2}{3}(V\rho)_P\ \min[0, (\mathbf{N}\cdot\mathbf{u})_P] && (5.57)\\
(b_P^k)^{(j)} &= \frac{(\rho V)_P^o}{\Delta t}\, k_P^o + \max(0, \sum_{\{f\}_P} D_f^{k,c}) +\\
&+ \left\{V\rho\,\nu_t\,\left[\mathbf{Nu} + (\mathbf{Nu})^T\right] : \mathbf{Nu}\right\}_P +\\
&+ \frac{2}{3}(V\rho\, k^{(j-1)})_P\ \max[0, (\mathbf{N}\cdot\mathbf{u})_P] -\\
&- \left[V\rho\,\frac{C_\mu}{\nu_t}\,(k^{(j)})^2\right]_P && (5.58)
\end{aligned}
$$

In Eqs.(5.57) and (5.58), ν_t is evaluated from Eq.(4.96). Depending on the cell centre distance from the wall, two outcomes are possible; the node (cell centre) is in the viscous sublayer, or it is in the inertial sublayer.

If the node is in the viscous sublayer, i.e.:

$$
\begin{aligned}
y^+ &\le y_c^+ \Rightarrow && (5.59)\\
\nu_t &= \nu_m && (5.60)
\end{aligned}
$$

Eq.(5.54), after omitting the subscript P, is rearranged to read:

$$
a_{v,1}^k\, \left[k^{(j)}\right]^2 + a_{v,2}^k\, k^{(j)} - a_{v,3}^k\ = 0 \qquad (5.61)
$$

where

$$
\begin{aligned}
a_{v,1}^k &= V\rho\,\frac{C_\mu}{\nu_m} && (5.62)\\
a_{v,2}^k &= (\mathcal{A}^k)' - (S_{\mathcal{P}}^k)' && (5.63)\\
a_{v,3}^k &= \sum_N \mathcal{A}_N^k k_N^{(j-1)} + \frac{(\rho V)^o}{\Delta t}\, k^o + \max(0, \sum_{\{f\}_P} D_f^{k,c}) +\\
&+ \left\{V\rho\,\nu_m\left[\mathbf{Nu} + (\mathbf{Nu})^T\right] : \mathbf{Nu}\right\} +\\
&+ \frac{2}{3}V\rho\, k^{(j-1)}\ \max(0, \mathbf{N}\cdot\mathbf{u}) && (5.64)
\end{aligned}
$$

The only positive root of Eq.(5.61) is:

$$
k^{(j)} = \frac{-a_{v,2}^k + \sqrt{(a_{v,2}^k)^2 + 4a_{v,1}^k\, a_{v,3}^k}}{2a_{v,1}^k} \qquad (5.65)
$$

and corresponding ϵ can be evaluated by Eq.(5.55).

The iterative solution procedure can then be described as:

$$
\begin{aligned}
k^{(j)} &= F_v^k(k^{(j-1)}) && (5.66)\\
\epsilon^{(j)} &= F_v^\epsilon(k^{(j)}) && (5.67)
\end{aligned}
$$

where F_v^k and F_v^ϵ stand for Eqs.(5.61) and (5.55), respectively.

In the case that the cell node is in the inertial sublayer ($y^+ > y_c^+$), the k and ϵ equations read:

$$
\begin{aligned}
\left[(\mathcal{A}_P^k)' - (S_{\mathcal{P}}^k)'_P\right]\, k_P^{(j)} &= \sum_N \mathcal{A}_N^k\, k_N^{(j-1)} + (b_P^k)^{(j)} && (5.68)\\
\epsilon_P^{(j)} &= C_\mu^{3/4}\, \frac{(k_P^{(j)})^{3/2}}{\kappa y_P} && (5.69)
\end{aligned}
$$

where $(\mathcal{A}_P)'$, $(S_{\mathcal{P}})'_P$ and $(b_P)^{(j)}$ are defined as:

$$
\begin{aligned}
(\mathcal{A}_P^k)' &= \sum_N \mathcal{A}_N^k + \frac{(\rho V)_P^o}{\Delta t} + (S^d)_P && (5.70)\\
(S_{\mathcal{P}}^k)'_P &= -\frac{2}{3}\left[V\rho\,(k^{(j)})^{1/2}\,\frac{C_\mu^{1/4}\kappa y}{ln(Ey^+)}\,\frac{(\mathbf{N}\cdot\mathbf{u})^2}{k^{(j)}}\right]_P +\\
&+ \frac{1}{k_P^{(j-1)}}\min(0, \sum_{\{f\}_P} D_f^{k,c})\\
&+ \frac{2}{3}(V\rho)_P\ \min[0, (\mathbf{N}\cdot\mathbf{u})_P] && (5.71)\\
(b_P^k)^{(j)} &= \frac{(\rho V)_P^o}{\Delta t}\, k_P^o + \max(0, \sum_{\{f\}_P} D_f^{k,c}) +\\
&+ \left\{V\rho\,(k^{(j)})^{1/2}\,\frac{C_\mu^{1/4}\kappa y}{ln(Ey^+)}\left[\mathbf{Nu} + (\mathbf{Nu})^T\right] : \mathbf{Nu}\right\}_P +
\end{aligned}
$$

$$
\begin{aligned}
&+ \frac{2}{3}(V\rho\, k^{(j-1)})_P \;\max[0,(\mathbf{N}\cdot\mathbf{u})_P] - \\
&- \left[V\rho\, \frac{C_\mu^{3/4}\, ln(Ey^+)}{\kappa y}\,(k^{(j-1)})^{1/2}\, k^{(j)}\right]_P \qquad (5.72)
\end{aligned}
$$

One can rewrite Eq.(5.68) as:

$$
a_{i,1}^k\;\left[q^{(j)}\right]^2 + a_{i,2}^k\, q^{(j)} - a_{i,3}^k \;= 0 \qquad (5.73)
$$

where q and the coefficients are defined by:

$$
\begin{aligned}
q^{(j)} &= (k^{(j)})^{1/2} && (5.74)\\
a_{i,1}^k &= (\mathcal{A}^k)' - \frac{2}{3}V\rho\,\min(0,\mathbf{N}\cdot\mathbf{u}) - \\
&- \frac{1}{k^{(j-1)}}\min(0,\sum_{\{f\}_P} D_f^{k,c}) + \\
&+ V\rho\,\frac{C_\mu^{3/4}\, ln(Ey^+)}{\kappa y}\,(k^{(j-1)})^{1/2} && (5.75)\\
a_{i,2}^k &= \frac{2}{3}\,V\rho\,\frac{C_\mu^{1/4}\kappa y}{ln(Ey^+)}\,(\mathbf{N}\cdot\mathbf{u})^2 \;- \\
&- V\rho\,\frac{C_\mu^{1/4}\kappa y}{ln(Ey^+)}\,\left[\mathbf{Nu} + (\mathbf{Nu})^T\right] : \mathbf{Nu} && (5.76)\\
a_{i,3}^k &= \sum_N \mathcal{A}_N^k k_N^{(j-1)} + \frac{(\rho V)^o}{\Delta t}\,k^o + \max(0,\sum_{\{f\}_P} D_f^{k,c}) + \\
&+ \frac{2}{3}V\rho\, k^{(j-1)}\,\max(0,\mathbf{N}\cdot\mathbf{u}) && (5.77)
\end{aligned}
$$

The positive root of Eq.(5.73) is:

$$
q^{(j)} = (k^{(j)})^{1/2} = \frac{-a_{i,2}^k + \sqrt{(a_{i,2}^k)^2 + 4a_{i,1}^k\, a_{i,3}^k}}{2a_{i,1}^k} \qquad (5.78)
$$

and corresponding ϵ is evaluated by Eq.(5.69).

The solution procedure can then be symbolically described as:

$$
\begin{aligned}
k^{(j)} &= F_i^k(k^{(j-1)}) && (5.79)\\
\epsilon^{(j)} &= F_i^\epsilon(k^{(j)}) && (5.80)
\end{aligned}
$$

where F_i^k stands for the composition of functions defined by Eqs.(5.73) and (5.74), and F_i^ϵ represents (5.69).

Convergence criteria

The convergence criteria for the k-ϵ equations used in this study are based on the following normalised and cell-averaged residuals (N_c is the number of cells):

$$
(r^\phi)^{(j)} = \frac{1}{N_c}\sum_{P=1}^{N_c}\frac{(\phi_P^{(j)} - \phi_P^{(j-1)})}{\max(\phi_P^{(j)},\phi_P^{(j-1)})}\;; \qquad \phi = k,\;\epsilon \qquad (5.81)
$$

It is taken that the convergence is reached when

$$
(r^\phi)^{(j)} < \lambda \qquad (5.82)
$$

where λ is a value of the order 10^{-3}.

In [204], the author argues that a relatively small number of the corrector steps ($\approx$ 10) is usually enough to reach the above convergence criteria. The present experience on a variety of test cases confirms this.

5.3 Solution of linear algebraic equations

It has been shown that the discretisation of the transport equations and their linearisation lead to systems of simultaneous linear algebraic equations, which for a general variable ϕ can be written as:

$$
\mathcal{A}_P^\phi \phi_P = \sum_N \mathcal{A}_N^\phi \phi_N + b_P^\phi \quad , P = 1,\ldots N_c \qquad (5.83)
$$

There are many different methods for solving this system. The choice of method depends mainly on the characteristics of the coefficient matrix **A**. Taking into account that **A** is sparse, asymmetric (except in the case of the pressure equation) and strongly diagonally dominant, the conjugate gradient method (CG), [175], is believed to be the optimum choice. It will now be briefly outlined.

5.3.1 Conjugate gradient method

Originally, the CG method was proposed by Hestenes and Stiefel [97] to solve a symmetric system of linear equations. The procedure starts with an arbitrary (approximate) solution and, in the case of symmetric **A**, is able to find the 'exact' solution in at most N_c iterations. (For this reason the CG method has also been regarded as a direct solver.) The method received little attention until Reid [175] recognised its potential as an iterative method for the solution of large and sparse systems.

Many different methods have been developed to extend the applicability of the CG algorithm to asymmetric systems. The one used in this study is the bi-conjugate gradient (BCG) method of Fletcher [72].

A very important characteristic of solvers is their convergence rate, i.e. the number of iterations needed to reach the solution. In a typical CFD calculation, where N_c is of the order $10^4 - 10^5$, the number of iterations to obtain the solution required by the CG method would not be economical. This can be avoided by the use of the preconditioning.

The convergence rate depends on the dispersion of the eigenvalues of the matrix **A**, [142]. Preconditioning modifies the system to obtain a similar system with a smaller spectral radius which converges faster. In the case of CG solver used for solving the pressure equation, the incomplete Cholesky decomposition is applied (see Kershaw [116]), while for the other transport equations the BCG solver with diagonal preconditioning is used. Detailed presentations of the preconditioning methods and solvers can be found in Theodoropoulos [204] and Demirdzic [54].

5.3.2 Convergence criteria

As can be seen in Fig.5.3, two solution levels in the corrector sequence can be distinguished; one for the solution of individual transport equation, and another for the complete corrector sequence. The solution process is taken to converge when pre-specified convergence criteria, at both levels, are satisfied.

In this study, a convergence criterion based on the normalised absolute residual sum is used, where the residual sum is defined as:

$$R^\phi = \sum_{P=1}^{N_c} |R_P^\phi| \qquad (5.84)$$

and

$$R_P^\phi = \sum_N \mathcal{A}_N^\phi \phi_N + b_P^\phi - \mathcal{A}_P^\phi \phi_P \qquad (5.85)$$

The convergence test requires that R^ϕ must fall below a specified level; i.e.:

$$R^\phi < \lambda\, R^\phi_{norm} \qquad (5.86)$$

where λ is a value of the order 10^{-3}, and R^ϕ_{norm} is a suitable normalisation factor specified in Table 5.1.

ϕ	R^ϕ_{norm}	Symbols
$\mathbf{u}$	$u_{ref}\ \frac{m_{cyl}}{\tau_{ref}}$	m_{cyl} - current mass of gas in cylinder
p'	$\frac{m_{cyl}}{\tau_{ref}}$	u_{ref} - average piston velocity
e	$c_v\, T_{ref}\ \frac{m_{cyl}}{\tau_{ref}}$	T_{ref} - reference temperature
Y_{ft}	$s_{f,a}\ \frac{m_{cyl}}{\tau_{ref}}$	$\tau_{ref} = \frac{60}{n}$; n - engine speed
k	$u^2_{ref}\ \frac{m_{cyl}}{\tau_{ref}}$	$s_{f,a}$ - stoichiometric fuel-air mass ratio
ϵ	$\frac{u^3_{ref}}{0.1\, V_{cyl}^{1/3}}\ \frac{m_{cyl}}{\tau_{ref}}$	V_{cyl} - cylinder volume

Table 5.1: Normalisation factors for individual transport equations

The normalisation factor is taken to be proportional to the characteristic mass flow rate ($\frac{m_{cyl}}{\tau_{ref}}$) and some reference value of the particular property ϕ; for the momentum equation it is taken to be the average piston velocity (u_{ref}), for the energy equation - the reference internal energy ($c_v\, T_{ref}$), and for the fuel vapour mass equation - the stoichiometric fuel-air mass ratio. For the k equation, it is taken that k_{ref} is proportional to the square of the reference velocity ($k_{ref} \propto u^2_{ref}$), and for the ϵ equation, the reference dissipation rate, $\epsilon_{!ref}$ is taken to vary as $\epsilon_{ref} \propto k_{ref}^{3/2}\Lambda$. The integral length scale Λ, is assumed to be proportional to $0.1\,L$ (see [102] and [207]), where L is a characteristic dimension, $L = V_{cyl}^{1/3}$; V_{cyl} is the instantaneous volume of the cylinder.

The convergence criterion for the hole corrector sequence is based on the absolute residual sum in the pressure equation at the beginning of each corrector step. In the case of the kth-corrector step, convergence is taken to be reached when the following condition is satisfied:

$$(R^{p'})^{(k)} < \lambda_c \, R^{p'}_{norm} \tag{5.87}$$

where λ_c is the overall corrector convergence tolerance with a value of the order of 10^{-2}.

5.4 Closure

In this chapter a solution procedure for solving a system of discretised gas and spray equations assembled in §(4) has been described. The solution procedure has been split into two stages; the adjustment of the average cylinder thermodynamic variables, called the bulk adjustment stage (§(5.2.1)), and the predictor-corrector stage with full embedment of spray calculations (§(5.2)). The flow equations have been decoupled by the EPISO operator splitting technique, which has enabled sequential solution of the equations, and then linearised, forming a system of linear algebraic equations.

Mass conservation has been enforced by a pressure equation (derivation in §(D.2)). The predictor step, which comprises the spray and gas predictors and provides provisional values of the dependent variables, have been described in §(5.2.2). In section §(5.2.3), the corrector step has been explained, which, similar to the predictor, has spray and gas parts. In both predictor and corrector, in addition to the pressure and momentum equations, the energy and fuel mass conservation equations have also been incorporated. This takes care of the variation of the matrix coefficients due to steep density gradients.

Calculation of turbulence takes place outside this main predictor-corrector sequence. The solution algorithm contains two parts, a turbulence predictor and an algebraic turbulence corrector, and its description was given in section (5.2.4).

In section (5.3), brief descriptions have been given of the solver for the linear

algebraic equations and the convergence criteria.

With this chapter the numerical solution of the coupled gas and spray equations has been concluded. In the following chapter, results obtained using the method and the various submodel options, will be presented.

Chapter 6

Predictions of Diesel sprays

6.1 Introduction

The previous chapters have delt with the mathematical models of the gas and the dispersed phases, §(2) and §(3), and with the discretisation methods and solution procedure adopted in this study, §(4) and §(5).

This chapter presents the results of the sensitivity and validation studies. The activities are concentrated into two directions. Firstly, to investigate effects on the spray predictions of the different spray submodels and the empirical correlations used in them (the MPI and the Huh atomisation models, correlations for the droplet drag coefficient, droplet breakup time and stable diameter, the turbulence modulation and the spray-wall impingement model). Secondly, to assess the quality of predictions by their comparison with available measurements.

The chapter begins with definitions of physical quantities which are used for the comparison of results, §(6.2).

A series of measurements carried out as a part of the SPRAY and IDEA projects[1] are used for the validation purpose. The measurements were performed with the various fuels, under different injection regimes and gas conditions.

Three different test cases are considered and their detailed descriptions are pre-

[1]The SPRAY project was financed by the Joint Research Committee of European Engine Manufacturers (JRC), Commission of the European Communities (CEC), and the IDEA project by the JRC, CEC and the Swedish National Board for Technical Development.

sented in corresponding sections. The sections are organised in a similar way. They begin with the description of the test rig, initial and boundary conditions, and the computational parameters used in the calculations. This is followed by the presentation of results and their discussion. At this place only the summaries of the test cases are given.

The first test case considers injection of a spray through a single-hole injector into a chamber filled with quiescent air. This test case, since the measurements were accomplished at the Institut für Thermodynamik, Aachen, will be referred to as the Aachen pressure chamber case (APC). The air temperature and pressure conditions correspond to those in real diesel engines, and measurements were performed with different injection regimes and different types of fuels. The test case is used for both sensitivity studies and validation, §(6.3).

The effects of the computational mesh on the predictions are investigated in §(6.3.2).

The measurements done in the Aachen pressure chamber as a part of the SPRAY project are used to investigate the effects of the drag coefficient correlations, breakup models and turbulence modulation on spray behaviour; these results are presented in §(6.3.3). The other set of pressure chamber measurements accomplished under the IDEA project is used to compare predictions of the two atomisation models; the results are given in §(6.3.4). The same computational mesh, with a different injector location and injection specifications, is employed to illustrate the predictions of the MPI spray-wall impingement model, §(6.3.5).

Two other two test cases involve measurements in the direct injection experimental engines; one investigation took place at the Institut Français du Pétrole, Rueil-Malmaison, and this will be referred to as IFP (optical) engine, §(6.4), and the other at Volkswagen AG, Wolfsburg. The latter will be called VW (transparent) engine and the results are presented in §(6.5).

The IFP optical engine is a specially-designed research diesel engine which enables optical access to the combustion chamber through a window in the piston. The single-hole injector is located in the liner, and oriented to inject perpendicular to the cylinder axis. The injection takes place into a specially formed, rectangular

passage in the piston.

In the case of the VW experimental engine, a five-hole injector situated in the cylinder head (the same arrangement as in the series engines) injects fuel into the piston bowl. Optical access is achieved by the replacement of the original omega piston bowl (used in the series engines) by a flat bottomed transparent bowl.

In all the above calculations the physical properties of air and fuels are calculated based on the data in [53], [10] and [97]; see also [193].

6.2 Definitions

The numerical experiments have at their disposal a number of quantities which are difficult or impossible to measure, but are easily accessible in the mathematical models and useful in performance comparisons. Examples of these quantities are the fuel vapour distribution and its formation rate, the local gas temperature and the temperature of droplets. On the other hand, experiments provide data about quantities which have no unique numerical counterparts; the spray penetration, for example. These result in of difficulties and uncertainties in the validation of spray models.

The quantities used in this study are defined as follows; see [185], [228], and [27].

Spray penetrations

The spray penetration is measured from photographs which capture differences in density of various regions of spray and gas. The photographs are obtained by high-speed cinematography in combination with the Schlieren technique. The disadvantages of the method are the absence of direct link between the transparency (visibility) of the gas-vapour mixture and fuel vapour mass fraction, and blurred edge of the spray liquid core due to the presence of droplets, [185]. This introduces uncertainty in the measurements.

The instantaneous fuel vapour penetration has been defined as the distance of axially farthest point from the injector where the fuel vapour mass fraction has reached 0.05.

The liquid penetration has been defined as the distance from the injector where the void fraction (see its definition in §(2.2.2)) has value of 99%; this represents a reduction of 1% of the void fraction from the pure single-phase fluid for which the void fraction is equal to 1. Occasionally, the so-called 'leading droplet' penetration, defined as the farthest axial distance of the leading droplet in the spray from the injector, will also be used.

Cumulative evaporation ratio $Evap$

This quantity is useful for the sensitivity studies of various submodels. It is defined as a ratio of the total amount of fuel vapour in the computational domain at a particular time t, to the total (cumulative) amount of injected fuel from the start of injection to time t, i.e.:

$$Evap(t) = \frac{m_{fv}(t)}{m_f(t)} \tag{6.1}$$

where

$$m_{fv}(t) = \int_V \rho(t)\, Y_t(t)\, dV \approx \sum_{i=1}^{N_c} [\, \rho(t)\, Y_t(t) \Delta V(t)\,]_i \tag{6.2}$$

$$m_f(t) = \int_{t_{SOI}}^{t} \rho_d(t)\, \dot{Q}(t)\, dt \approx \sum_{j=1}^{N_t} [\, \rho_d\, \dot{Q}\,]_j\, \Delta t_j \tag{6.3}$$

where N_t is the total number of subcycling time steps from t_{SOI} to t.

The cumulative evaporation cannot be directly measured, but it can be very roughly assessed from the photographs of the spray liquid core and surrounding fuel vapour. It can be roughly calculated as the ratio of the volume occupied by the vapour to the total volume of the spray, [228]. However, this leads to a lot of uncertainties and inaccuracies, so here, only the 'exact' quantity defined by Eq.(6.1) will be used.

Sauter mean diameter

To characterise a mean droplet size in a spray it is common to use the Sauter mean diameter defined by, [223]:

$$SMD = \frac{\int D_d^3\, dn}{\int D_d^2\, dn} = \sum_{p=1}^{p=N_p} N_{p,d} D_d^3 \;/\; \sum_{p=1}^{p=N_p} \mathrm{N_{p,d} D_d^2} \tag{6.4}$$

where dn is the number of droplets with diameter in the range $(D_d, D_d + dD_d)$ and the integration is over the whole range of droplet sizes. The Sauter mean diameter is the diameter of the droplet that has the same volume/surface ratio as the whole spray.

Local field value

There are test cases considered in the study, where field properties, such as gas velocity or fuel vapour mass fraction, are measured at fixed locations in the domain. They will be compared with the predicted values obtained in the computational cells where the measuring locations reside. More details will be given later in the chapter.

6.3 Aachen pressure chamber

6.3.1 Description

The pressure chamber is specially designed to allow optical access to the in-chamber space for non-intrusive measurements. The compressed air passes through heaters and straightening blades at the top of the chamber, and enters into its observation part, Fig. 6.1. The fuel is injected along the chamber axis through a single-hole, water-cooled injector, [185]. All parts of the chamber are thermally insulated.

The main part of the chamber is a rectangular measuring section equipped by up to four quartz glass windows of $100mm$ length and $40mm$ width for optical access. The distance between the window is $90mm$, so that the wall influences on the spray can be neglected. The maximum mean axial air velocity measured in the chamber, in the absence of spray injection is lower than 0.1 m/s, so that it can be considered nearly quiescent, [185]. Other details about the geometry of pressure chamber and experimental set-up can be found in [185] and the works cited later on in this section.

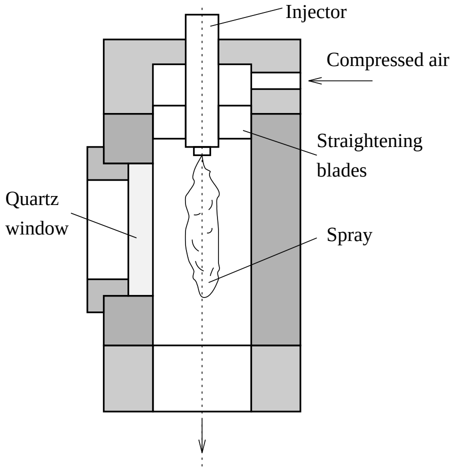

Figure 6.1: Sketch of the Aachen pressure chamber.

6.3.2 Computational mesh

Introduction

The actual chamber domain is approximated by a cylinder with dimensions given in Fig. 6.2. The computational domain is taken to be a 30^o sector of the cylinder.

The fact that the quality of numerical predictions depends to a large extent on the resolution of the computational mesh, [27] and [228] necessitated a sensitivity study on this matter. For this purpose five different computational meshes were built by varying the number of cells and the mesh aspect ratio in the axial and radial directions. (The mesh aspect ratio is defined as the ratio of the maximum to the minimum lengths of cells in considered direction). The parameters of the meshes are summarised in Table 6.1; they are ordered from the coarsest mesh (Mesh 1) towards the finest (Mesh 5). Note that meshes 2 and 3, and 4 and 5 have the same radial and axial cell distribution, respectively.

It is important to emphasize that the volume of the smallest cell in the domain is restricted by the requirement that the void fraction in the cell should not be $\ll 1$ or negative. That would violate the assumption that the gas is a continuum, or the

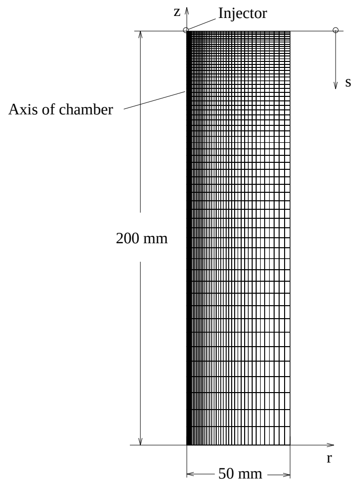

Figure 6.2: Example of computational mesh (Mesh 5).

Mesh No.	Directions					
	Radial			Axial		
	Number of cells	Aspect ratio	Min. Δr [mm]	Number of cells	Aspect ratio	Min. Δz [mm]
1	23	1.0	2.17	95	1.0	2.1
2	40	1.0	1.25	60	1.0	3.3
3	40	1.0	1.25	60	11.1	0.78
4	40	6.1	0.44	60	1.0	3.3
5	40	6.1	0.44	60	11.1	0.78

Table 6.1: Parameters of computational meshes.

physical concept that the liquid phase cannot occupy more space in the cell than is available; §§(2.1) and (2.2.2). Note that this requirement involves the time step size because the amount of fuel injected in the considered time step depends on the size of the time step and the injection rate. (The size of the time step will be discussed in the following section). The dimensions of the smallest cell are therefore chosen from the ranges recommended in [163] and [200].

Calculation parameters

Fig. 6.3 depicts the injection rate history, taken from [185], and Tables 6.2 and 6.3 show the spray submodels and computational parameters used in the calculations.

The size of the time step, Δt is selected based on the droplet trajectory analysis of Beshay [27]. The chosen value of $2\mu s$ assures that the droplet Courant number, defined by $Co = U\Delta t/\Delta z_{min}$, is always less than 1. In the calculations presented in this section the maximum value of Co is 0.62.

The parcel injection rate $\dot{N}_p$ is chosen to be 4 parcels/time-step. This complies with the recommendations of Dukowicz, [58] and Tabrizi, [200], who found that the dynamics of spray are not very sensitive to variation in this parameter if $\dot{N}_p > 2$ parcels/time-step.

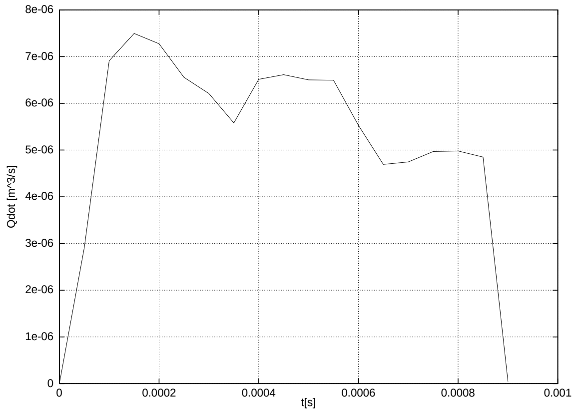

Figure 6.3: Fuel injection flow rate.

Spray process	Submodel/correlation
Atomisation	Huh
- discharge coeff.	$c_d = 0.68$
- injector diam.	$d_{inj} = 0.2$ mm
- hole length	$L = 0.8$ mm
Breakup	Reitz-Diwakar
Collision	O'Rourke
Momentum exchange	Yuen & Chen drag correlation
Impingement	Not included
Turbulence modulation	Not included

Table 6.2: Spray submodels used in calculations.

Parameter	Value
Ambient gas	air
Time step, Δt	2.0 μs
Max. Courant number, Co	0.62
Parcel injection rate, $\dot{N}_p$	4 parcels/time-step
Convergence tolerance, λ_c	$1.0 \cdot 10^{-4}$
Max. number of correctors	4
Discretisation scheme	SFCD

Table 6.3: Calculation parameters.

The initial and boundary conditions are given in Table 6.4. The fuel temperature was not measured and its assumed value is taken to be $300K$. (Note that the injector was cooled by water, [185]).

The initial value of the turbulence energy, in the absence of the measured data, is assumed according to [179] and [200]. The turbulence dissipation rate is calculated based on a characteristic length of the chamber, taken to be a half of the chamber width ($0.045m$). It should be noted that the spray predictions are rather insensitive to these initial values; see [179] and [163]. The same initial values of k and ϵ are used in all the pressure chamber calculations presented latter on in this study.

Spray		
T_{SOI}	0.00	ms
T_{EOI}	0.90	ms
Fuel	n-dodecane	
Inj. quantity	5.00	mm^3
T_{inj}	300.0	K
Field variables		
$\mathbf{u}$	0.00	m/s
P	50.0	bar
T	800.0	K
k	$1.0 \cdot 10^{-3}$	m^2/s^2
ϵ	$7.0 \cdot 10^{-4}$	m^2/s^3

Table 6.4: Initial and boundary conditions used in the calculations.

Comparison of the predictions

The comparisons of predictions of the fuel vapour and liquid penetrations, and evaporation are shown in Figs. 6.4, 6.5 and 6.6. The maximum difference in fuel vapour penetration of about 20 mm is observed between the coarsest mesh, Mesh 1, and the finest, Mesh 5. It can be seen that the prediction of penetration is affected by the mesh resolution in both directions, radial and axial. The influence of radial

resolution is evidently stronger than the axial; compare the curves Mesh 3 and Mesh 5, and Mesh 4 and Mesh 5 in Fig. 6.4.

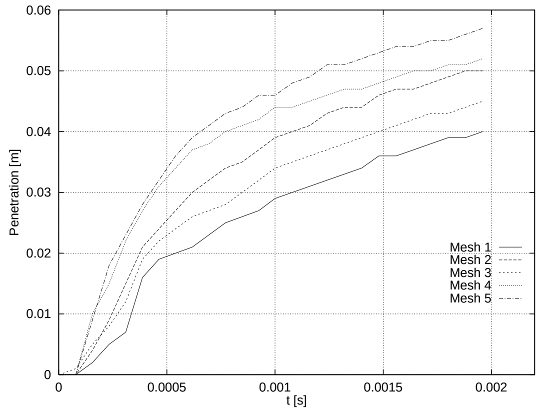

Figure 6.4: Effects of computational meshes on the prediction of fuel vapour penetration (5% fuel vapour mass fraction criterion).

The predictions of liquid penetration show the same trend, Fig. 6.5. It is interesting to note the time delays of about 0.15 and 0.1 ms in curves Mesh 1 and Mesh 2 until the first detection of penetration. This is caused by the relatively big minimal volumes of cells in these meshes (these are the two coarsest meshes), which delays the void fraction in these cells from reaching the threshold value. This dependency on the mesh density points out a disadvantage of the usage of void fraction as a measure of the liquid penetration. The disadvantage, however, disappears when the comparisons are made on the same mesh, as it is a case in the calculations presented later on in the chapter.

The fuel evaporation ratio $Evap$, Fig. 6.6, is not so sensitive on mesh density as penetration. Here too, the maximum observed difference is between the predictions on the coarsest and finest meshes, and it reaches about 20%.

The curves in all the aforementioned figures show a clear tendency to cluster as the mesh density increases. Since it is impossible to achieve a completely grid-independent solution, as was shown by Dukowicz, [58] and Beshay, [27], and taking into account the restriction on the further increase of the mesh density due

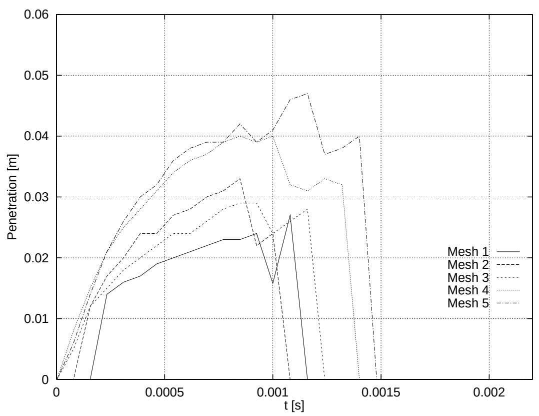

Figure 6.5: Effects of the mesh density on the liquid penetration (99% void fraction criterion).

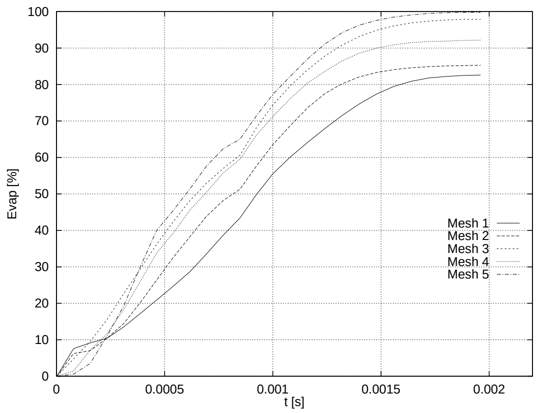

Figure 6.6: Effects of computational meshes on the prediction of spray evaporation.

to the reasons mentioned in §(6.3.2), the finest mesh, Mesh 5 (Fig 6.2) is chosen for all the further calculations. These two properties, the impossibility to achieve a grid-independent solution and the restriction on the void fraction, are the main disadvantages of the discrete droplet method.

6.3.3 The HMN results

Description

The injection system consists of a modified in-line injection pump (Bosch Type MW, JRC III), an injection line and a commercial Bosch single-hole nozzle (No. 502-3) with characteristics given in Table 6.5. The fuel injection rate was monitored by

Injector		
d_{inj}	0.2	mm
L	0.8	mm
c_d	0.68	

Table 6.5: Injector data.

measuring the injection pressure in the injection line and needle lift, with a pressure transducer and a needle lift sensor. From these data the fuel injection rate history is calculated, [185].

The measurements were carried out for a number of operating points and the one with the most measurement data is selected for the validation purpose. This operating point has internal (Aachen) designation JH001.

Operating point and measurement data

The parameters of the operating point are summarised in Table 6.6. The injected fuel was heptamethylnonane[2] (HMN), and the corresponding injection rate history and injection specifications are shown in Fig.6.7 and Table 6.7 respectively.

OP	T_{air} [K]	p [bar]	Q [mm^3/cycle]	Fuel
JH001	800	50	5	HMN

Table 6.6: Aachen pressure chamber; operating point JH001.

[2]This fuel was used, because of its very low ignition quality (cetane number 15), to avoid ignition during the experiments.

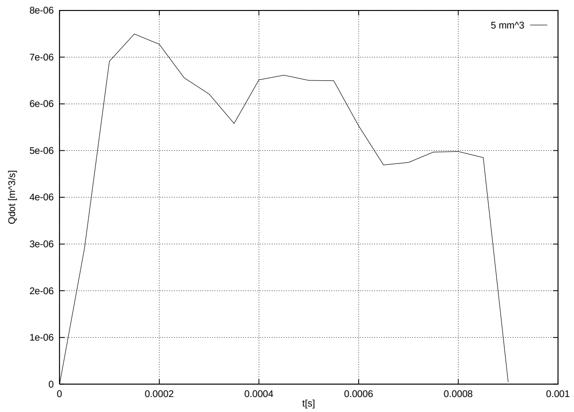

Figure 6.7: Injection rate history.

Spray		
T_{SOI}	0.00	ms
T_{EOI}	0.90	ms
Fuel	HMN	
Inj. quantity	5.00	mm^3
T_{inj}	300.0	K

Table 6.7: Injection specifications used in the calculations.

The spray penetration was calculated from photographs obtained by high-speed cinematography in combination with the Schlieren technique, [185]. The temporal variation of the local gas velocity, fuel vapour mass fraction, and turbulence intensity were measured at two axial distances and several radial positions, as shown in Fig.(6.8), using laser-doppler velocimetry (LDV) and Raman spectroscopy. The data, reported in [185], represent the ensemble average of approximately 50 samples per point in time and space.

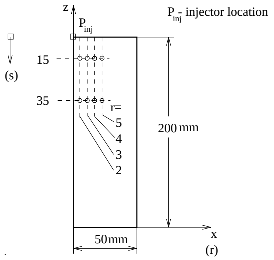

Figure 6.8: Locations of the measuring points.

Calculation parameters

The calculations were performed with four different combinations of spray submodels summerised in Table 6.8. The combination employed as a standard for comparison (baseline) uses the 'standard drag curve' for the droplet drag coefficient, Eg.(3.70), and the Reitz-Diwakar breakup model. It does not include turbulence modulation. The other cases, called variants, differ from the baseline case in only one different submodel they employed, as indicated in Table 6.8; so Variant 1 uses the Yuen & Chen drag correlation Eg.(3.63) instead of the 'standard drag curve', Variant 2 uses Pilch-Erdman instead of the Reitz-Diwakar breakup model, and Variant 3 includes the turbulence modulation in contrast to the baseline.

The comparisons between the baseline results and those obtained with the variants are presented in the following sections, together with the measurements when they were available. In all the calculations the same computational parameters shown in Table 6.9 are adopted.

Spray process	Baseline	Variant 1	Variant 2	Variant 3
Atomisation	Huh			
Breakup	Reitz-Diwakar		Pilch-Erdman	
Collision	O'Rourke			
Momentum	Eg.(3.70)	Eg.(3.63)		
Impingement	Not included			
Turbulence mod.	Not included			Included

Table 6.8: Spray submodels/correlations used in the calculations.

Parameter	Value
Time step, Δt	2.0 μs
Max. Courant number, Co	0.62
Parcel injection rate, $\dot{N}_p$	2 parcels/μs
Convergence tolerance, λ_c	$1.0 \cdot 10^{-3}$
Max. number of correctors	4
Discretisation scheme	SFCD

Table 6.9: Calculation parameters.

Baseline results

Development of the gas velocity is depicted in Fig.6.9 by the axial-section vector plots at four characteristic times, two during injection (0.5 and 0.75 ms) and two after the end of injection (1.0 and 1.5 ms). The maximum velocity is found along the spray axis. As expected, during injection the maximum gas velocity is located near the injector and is of the order of $100m/s$ (the average injection velocity is about $177m/s$). Later on, when injection ceases, the location of maximum velocity moves downstream with the spray, and the velocity magnitude decreases. Careful inspection of the plots reveals a toroidal vortex formed at the outer edge of the spray.

Contours of the fuel vapour mass fraction (FVMF) and gas temperature at the same viewing planes and times, are given in Figs.6.10 and 6.11. The maximum concentration of the fuel vapour is around the tip of the spray (see Fig.6.12 for the distribution of the parcels). This approximately corresponds to the region of minimum gas temperature; this is because the evaporation of fuel droplets extracts heat from the surrounding gas. The plots in Fig.6.10 contain lines labelled Meas. which designate the fuel vapour penetration measured by the raman method.

The spray evolution with time is presented in Figs.6.12 and 6.13, where the former figure depicts the locations of the droplets/parcels and their diameters, and the latter their temperature. It can be seen that the bigger and cooler droplets are located near the injector. As the droplet heat transfer and breakup processes advance, they become smaller and hotter. The majority of the droplet population has diameter less than $30\mu m$.

In order to compare the predictions of the liquid penetration with the measurements and to illustrate the difficulty of its assessing, the penetrations inferred from the photographs are also depicted in Fig.6.12. Note that the droplet size in the plot are not scaled which to some extent can bias impression on the (dis)agreement[3]. Inspection of Figs.6.10 and 6.12 leads to the conclusion that the computational results, for both vapour and liquid penetrations, overpredict the measurements; the detailed comparison of the penetrations vs. time will be given later on in this section.

[3]Because of the wide range of the droplet sizes, the droplets in the figures are plotted with the constant diameter, i.e. they are not scaled; if scaled, the smallest droplets will be practically invisible.

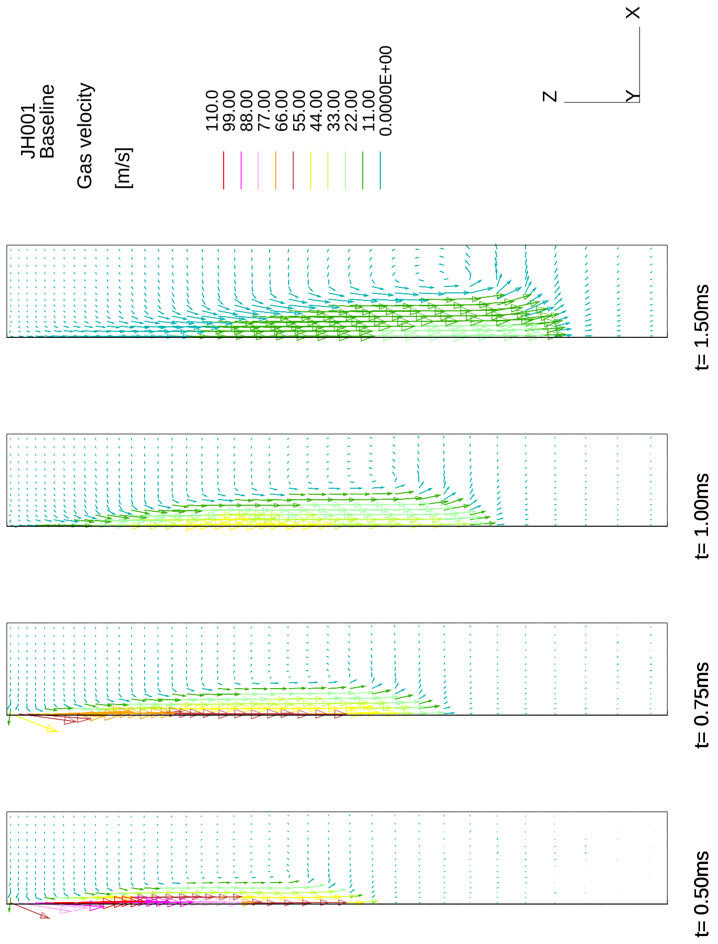

Figure 6.9: Gas velocity at 0.5, 0.75, 1.0 and 1.5 ms. Injection terminates at 0.9 ms.

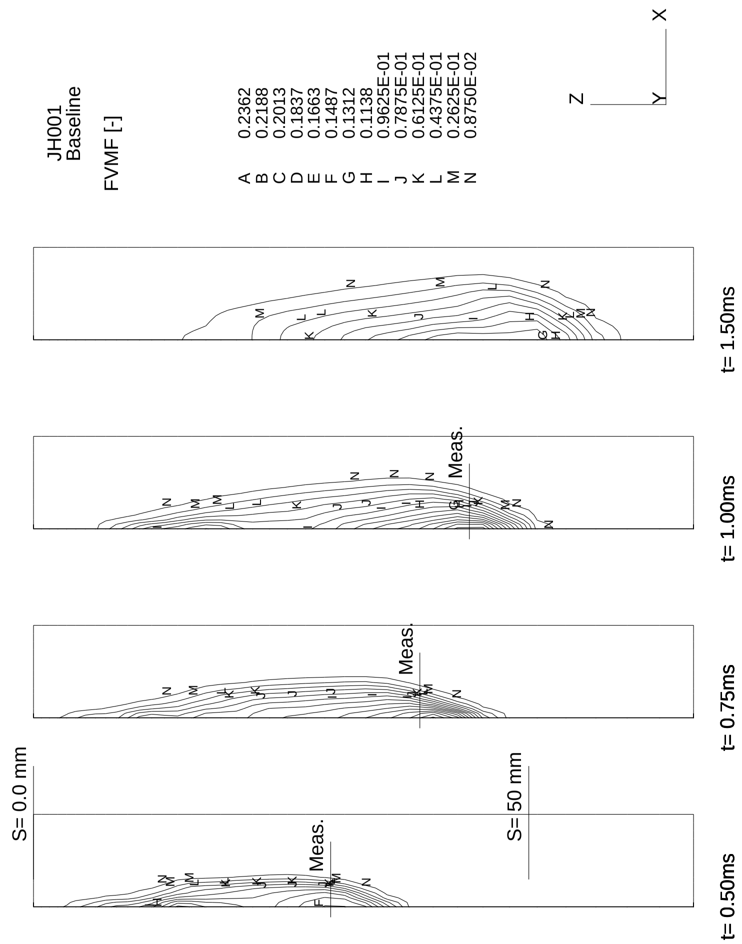

Figure 6.10: Contours of the fuel vapour mass fraction at 0.5, 0.75, 1.0 and 1.5 ms; Meas. denotes the fuel vapour penetration inferred from spray Schlieren photographs.

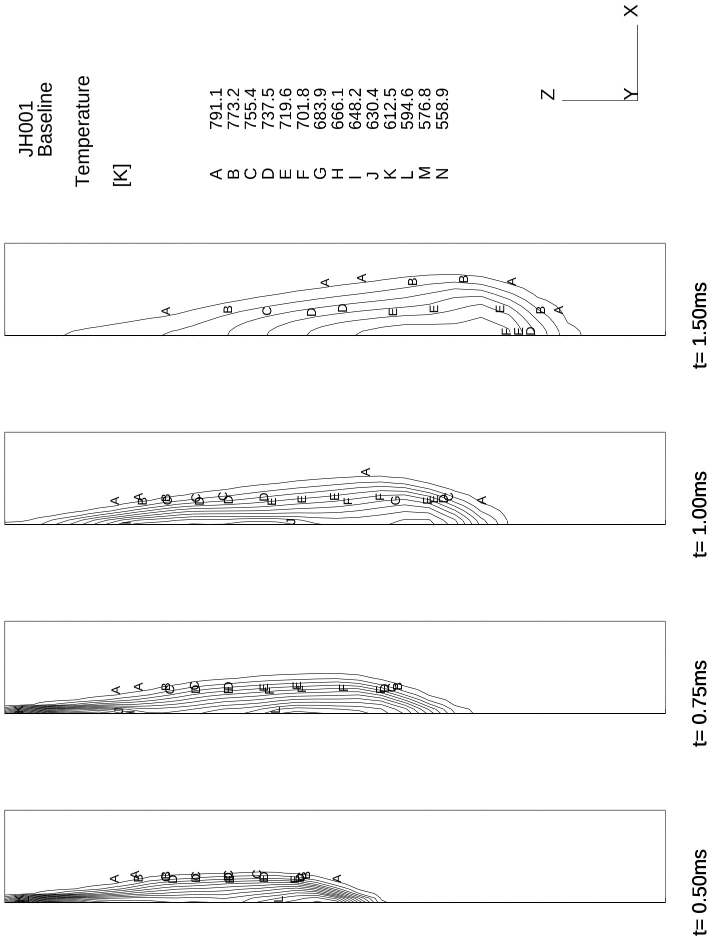

Figure 6.11: Contours of the gas temperature at 0.5, 0.75, 1.0 and 1.5 ms.

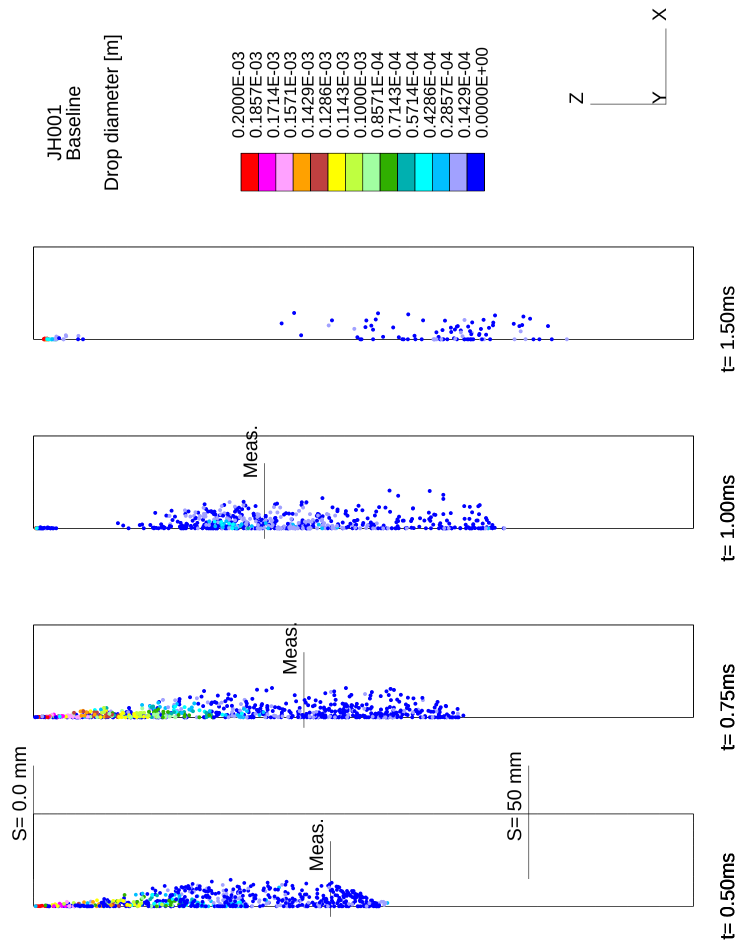

Figure 6.12: View on the spray and distribution of the droplet/parcel diameters at 0.5, 0.75, 1.0 and 1.5 ms; Meas. denotes the liquid penetration inferred from the spray photographs.

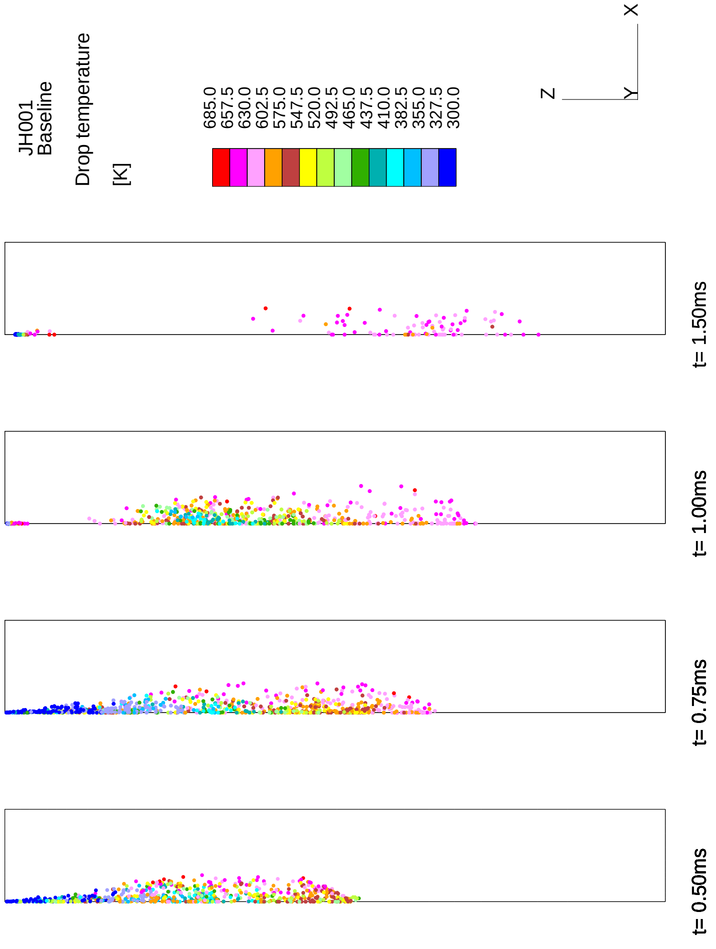

Figure 6.13: Drop/parcel temperature at 0.5, 0.75, 1.0 and 1.5 ms.

Effects of the drag coefficient correlations (Variant 1)

The effects of the droplet drag coefficient correlations proposed in §(3.4) on the spray behaviour are minimal. Fig.6.14 shows the predictions of the fuel vapour penetration by the baseline and the Variant 1 cases, together with the measurements. The predictions of Variant 1 are always less or equal than the baseline's, and the maximum differences between them are about 1-2mm. They both overpredict the measurements and the maximum overshoot is about 7mm. The predictions of the liquid penetration, Fig.6.15 follow each other, and both significantly overpredict the measurements; moreover, they both failed to predict the decrease of the liquid penetration in the range from 0.6ms up to the end of injection.

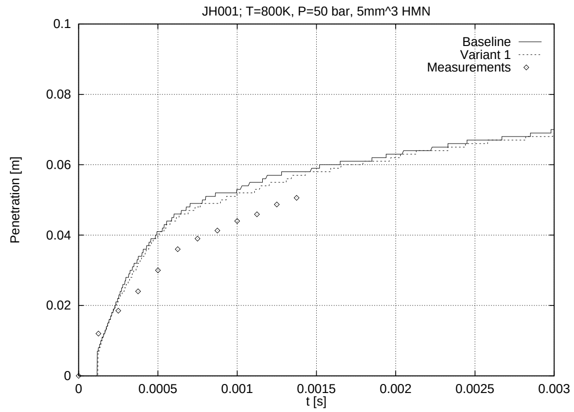

Figure 6.14: JH001; Effects of drag correlations on the fuel vapour penetration (penetration based on 5% fuel vapour mass fraction criterion).

Further evidence that both correlations produce very similar results are given in Figs.6.16 and 6.17, which compare the spray evaporation and Sauter mean diameter, respectively. In the former, the maximum difference is about 2-3%; the Sauter mean diameter is practically equal up to 2.0ms, 1.1ms after the end of injection. Beyond 2.0ms the differences between the Sauter mean diameters become bigger, but this is the result of the evaporation of the parcels when their total number is reduced (small statistical sample). Note that the amount of the liquid phase at that time is

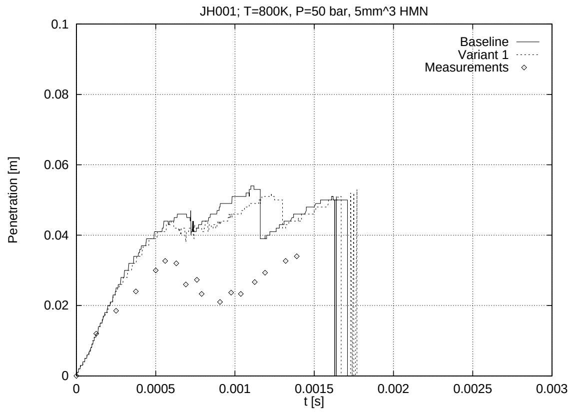

Figure 6.15: JH001; Effects of drag correlations on the liquid penetration (penetration based on 99% void fraction).

less than 1% of the total injected mass.

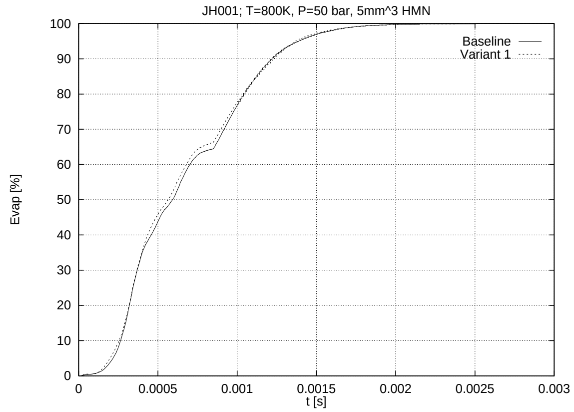

Figure 6.16: JH001; Effects of drag correlations on the spray evaporation vs. time.

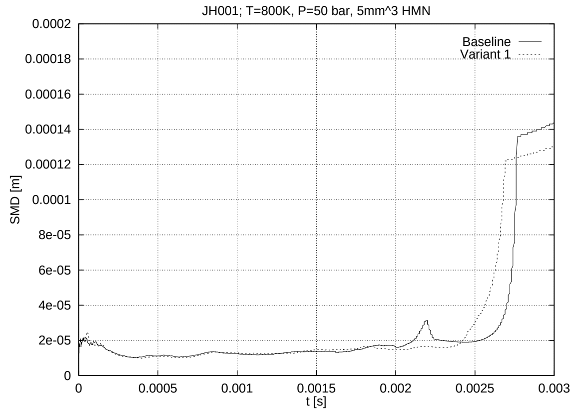

Figure 6.17: JH001; Effects of drag correlations on the spray Sauter mean diameter.

Effects of the breakup correlations (Variant 2)

In contrast to the previous case the correlations employed for the calculation of the breakup process strongly affect the spray predictions.

The predictions of the fuel vapour penetration start to differ from the baseline predictions noticeably from the end of injection and $1ms$ later the difference reaches almost $10mm$, Fig.6.18.

In the case of the liquid penetration prediction, Fig.6.19, the variant results part ways sooner, at approximately half of the injection duration, and from then the overprediction of Variant 2 steadily increases. Another significant difference is that the penetration of Variant 2 can be detected up to the end of calculation ($3ms$), while in the baseline case it ceases to be found from $1.7ms$. This indicates that the instantaneous amount of the liquid phase in Variant 2 is greater (i.e. the evaporation of the fuel is slower) than in the baseline case, Fig.6.20. The same figure shows that at the end of injection the baseline case predicts that 64% of the total injected fuel is evaporated, which is more than 20% higher than calculated by Variant 2. The reason for this lies in the bigger Sauter mean diameter, Fig.6.21, which is in the Variant 2 case almost twice as big as in the baseline case for the most of the time. This results from the prediction of the bigger stable diameter by the Pilch-Erdman model than by the Reitz-Diwakar correlation, a fact already mentioned in §(3.7.2) and noted elsewhere, [171].

The consequence of the bigger drop diameters in Variant 2 is the reduced evaporation rate of these droplets due to their larger evaporation relaxation times (which is proportional to D_d^2) than in the baseline case. This explains overprediction and the existence of liquid penetration up to the end of calculation.

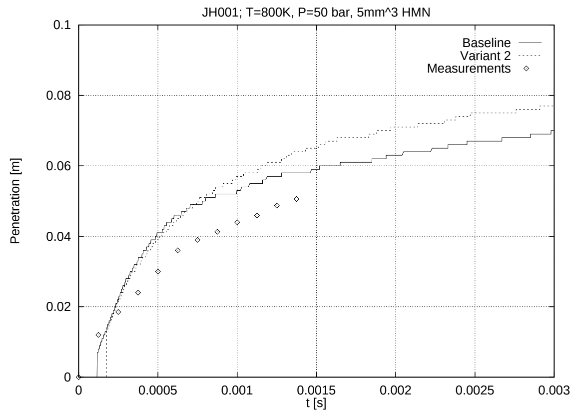

Figure 6.18: JH001; Effects of the breakup models on the fuel vapour penetration (penetration based on 5% fuel vapour mass fraction criterion).

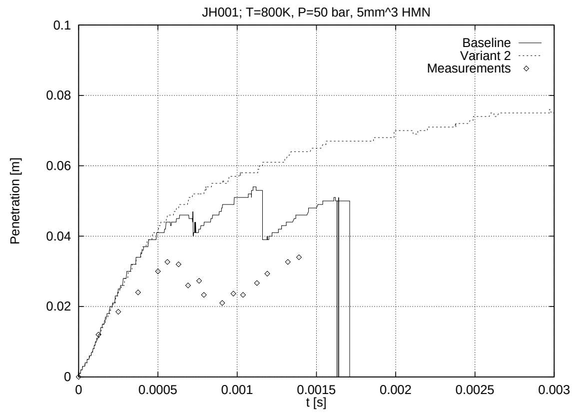

Figure 6.19: JH001; Effects of the breakup models on the liquid penetration (penetration based on 99% void fraction).

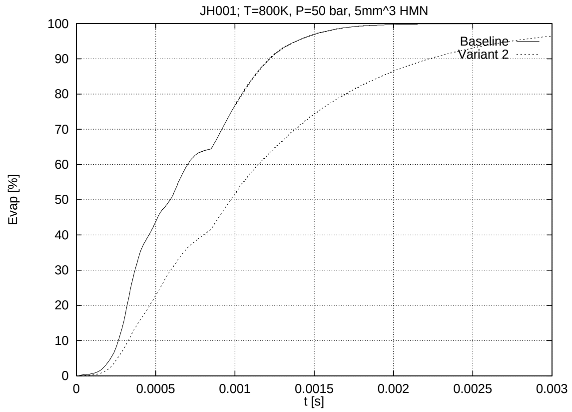

Figure 6.20: JH001; Effects of the breakup models on the spray evaporation.

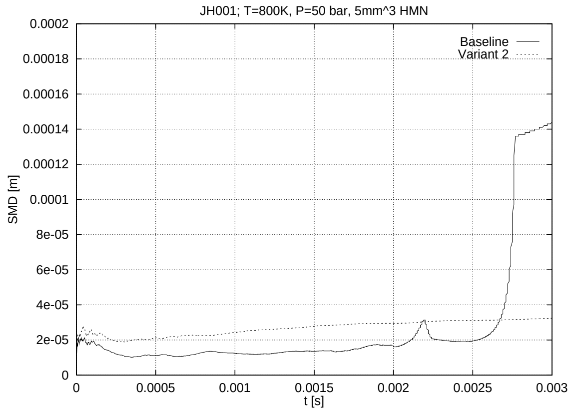

Figure 6.21: JH001; Effects of the breakup models on the spray Sauter mean diameter.

Effects of the turbulence modulation (Variant 3)

The inclusion of the turbulence modulation in the modelling of the gas-spray interaction produces even bigger overpredictions of the fuel vapour and liquid penetrations than the breakup model shown in the previous section. At the end of injection, the predictions of the vapour and liquid penetrations of Variant 3 are greater than the baseline's by about 7 mm, Figs.6.22 and 6.23. 0.5 ms later, the overprediction increases to about 13 mm, in the case of the fuel vapour penetration, and to 22 mm in the liquid penetration. Comparison of the turbulence viscosity of the baseline

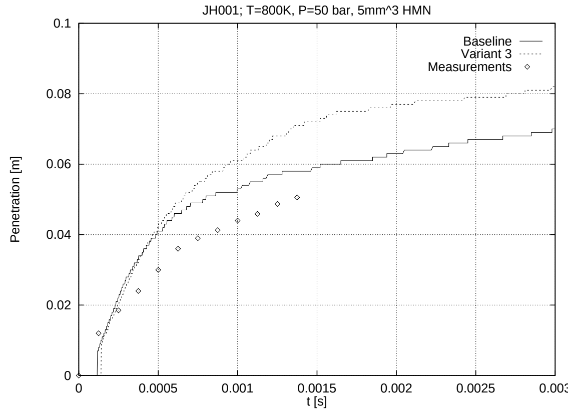

Figure 6.22: JH001; Effects of the turbulence modulation on the fuel vapour penetration (penetration based on 5% fuel vapour mass fraction criteria).

and Variant 3 cases, shown in Figs.6.24 and 6.25 respectively, gives explanation for this behaviour. As can be seen, the inclusion of the turbulence modulation terms in the gas-spray model significantly reduces the turbulence viscosity, as found by others; see §(2.3.4). (Details will be shown later in the section). This has two consequences. Firstly, the radial spreading of spray is diminished due to the smaller sizes of characteristic eddies, which play important role in the droplet random-walk calculation (§(3.3)), caused by a lessen level of turbulence kinetic energy. In this way the smaller (narrower) region of gas takes part in the exchange of momentum (and mass and energy) with the spray, which results in the lower rate of transfer

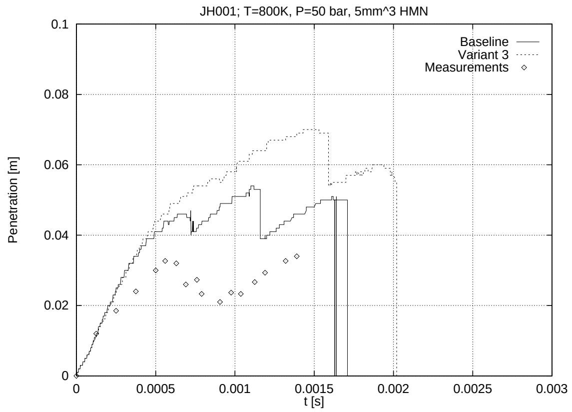

Figure 6.23: JH001; Effects of the turbulence modulation on the liquid penetration (penetration based on 99% void fraction).

of momentum from the spray to the gas. This is the reason of the enhanced spray penetration. Secondly, the reduced turbulence viscosity causes slower diffusion of the momentum, fuel vapour and temperature in the gas.

The fuel evaporation prediction is less than the baseline's, and the difference reaches about 12% at the end of injection, Fig.6.26. This discrepancy, compared with the baseline results, is less than the previous case, implying that the differences in the prediction of the Sauter mean diameter must be smaller. This is indeed the case as shown in Fig.6.27. The slightly bigger Sauter mean diameter can be attributed to the increased collisions and coalescences due to the more closely packed droplets.

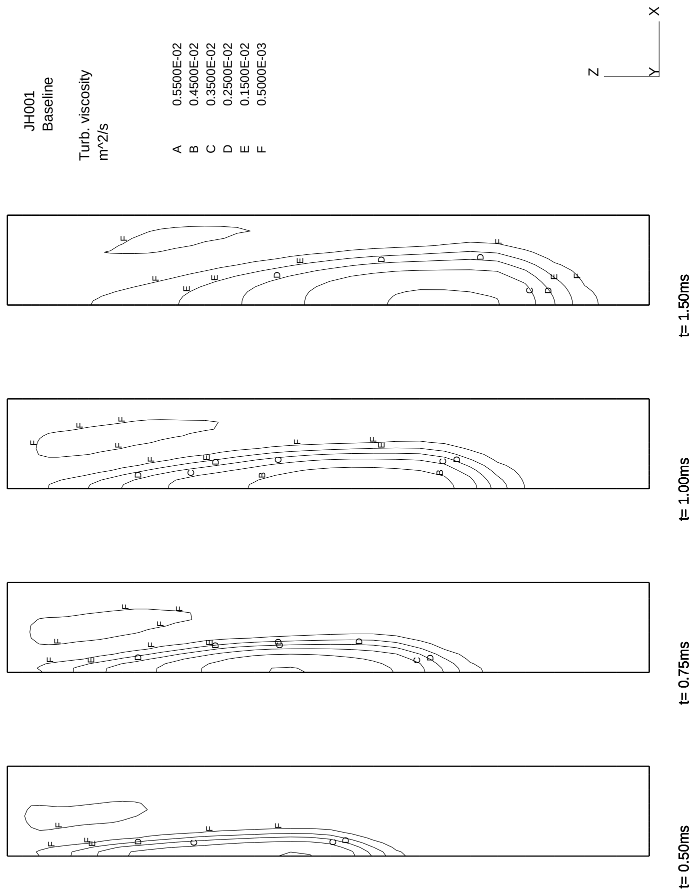

Figure 6.24: Baseline; contours of the turbulence kinematic viscosity at 0.5, 0.75, 1.0 and 1.5 ms.

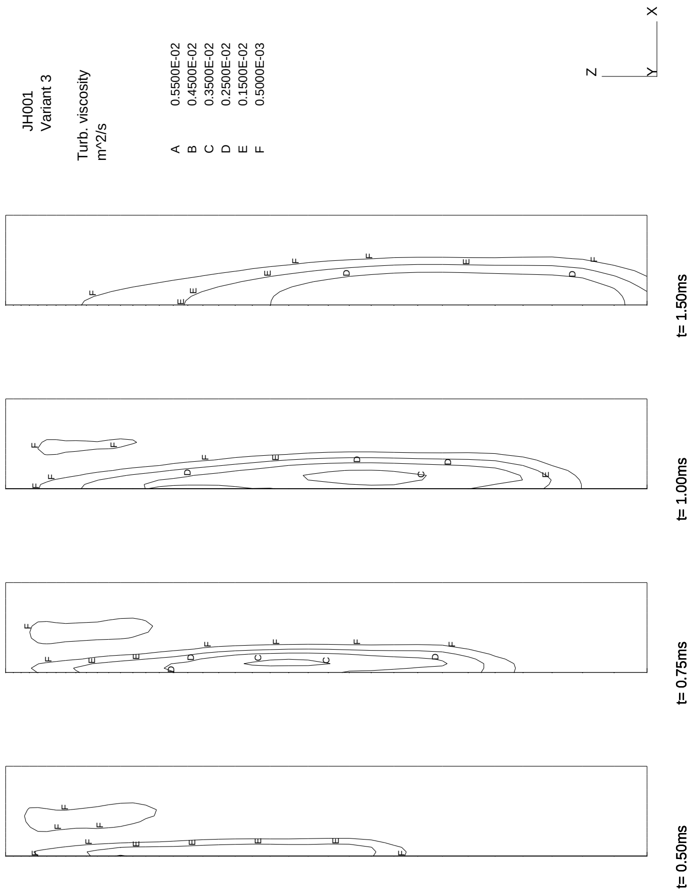

Figure 6.25: Variant 3; contours of the turbulence kinematic viscosity at 0.5, 0.75, 1.0 and 1.5 ms.

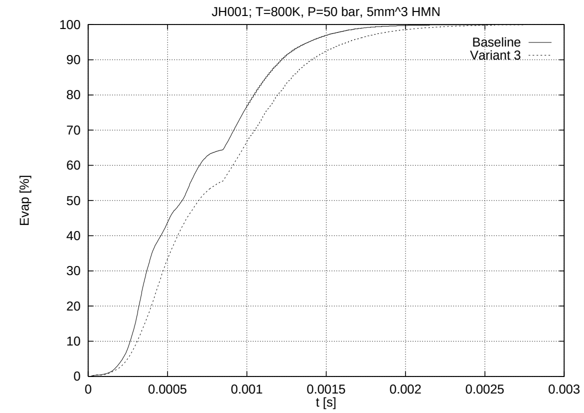

Figure 6.26: JH001; Effects of the turbulence modulation on the spray evaporation.

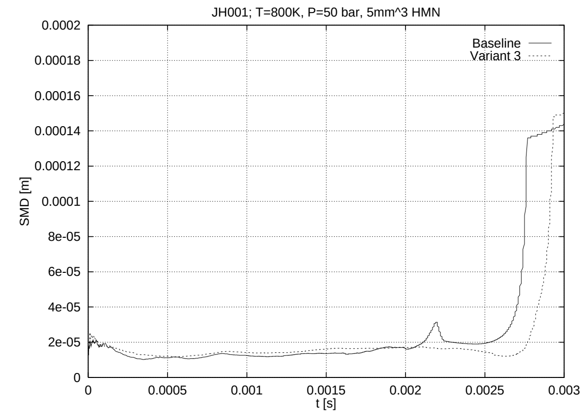

Figure 6.27: JH001; Effects of the turbulence modulation on the spray Sauter mean diameter.

This test case is also used to compare the predictions of the fuel vapour mass fraction, gas velocity, and turbulence intensity with the measurements.

Figs.6.28 and 6.29 depict the fuel vapour mass fraction at three radial positions, 15 and 35 mm below the injector. The predictions at s=15 mm, Fig.6.28 can be assessed as poor, especially at the points farther from the injector axis, at r=3 and 4 mm. The predicted fuel vapour mass fraction there is almost zero, which is caused by the fact that no spray droplets are detected in the simulations at these sites for the whole injection period. A possible explanation for this may be that the injection velocity in the experiment is greater than that computed in the calculations due to the cavitation phenomenon in the nozzle, [151]. With this smaller injection velocity, the atomisation model would produce bigger droplets less prone to dispersion by turbulence (causing smaller radial spreading), and with the smaller evaporation rates. However, the predictions of other gas properties at these points must be also affected, as will be shown below.

The predictions of the fuel vapour mass fraction at s=35 mm are slightly better, Fig.6.29. After overprediction in the early period, in the later period the results of both the baseline and Variant 3 calculations show relatively good agreement with the measurements, particularly at r=3 and 4 mm. The Variant 3 overshoots are somewhat smaller. The predicted arrival times are shorter then measured. The Variant 3 predictions shows longer arrival time when compared to the baseline's, and it increases with the distance from the injector axis. This can be explained by the slower diffusion due to the smaller predicted turbulence viscosity than in the baseline case.

Comparison of the axial gas velocities at the same two planes below the injector is presented in Figs.6.30 and 6.31. As expected, significant discrepancy between the measurements and predictions is present at the first set of plots for s=15 mm, Fig.6.30. The measured gas velocity is of the order of $10 m/s$ which is significantly greater than in the predictions which is about $2 m/s$. The same explanation given above for the underprediction of the fuel vapour mass fraction can be applied here. The agreement is little better at the measurement locations 35 mm below the injector, Fig.6.31.

In order to illustrate the effects of turbulence modulation on the predictions of the turbulence intensity u' ($u' = (3/2\ k)^{1/2}$), comparisons of the computational results obtained by the baseline and Variant 3 cases with the measurements, are given in Figs.6.32 and 6.33. In general, the Variant 3 case predicts significantly smaller turbulence intensity and longer arrival time than the baseline case. The found evidence of the reduction of the turbulence intensity agrees, taking into account that the size of the majority of droplets/particles is less than $20 \mu m$, i.e. $D_d/l_e <$ 0.1 (l_e is the integral length scale), with the findings of Gore and Crowe, [76]. When compared with the measurements, the predictions at s=15 mm are worse than those at s=35 mm. At s=35 mm, especially closer to the injector axis, the predictions can be assess as good. The figures also indicate a noticeable delay in the building up of turbulence intensity.

The above suggests that turbulence modulation affects the spray in the following ways: it enhances the vapour and liquid penetrations, reduces evaporation and spray radial spreading, and moderately increases the Sauter mean diameter. In the gas phase, turbulence modulation reduces the turbulence intensity and viscosity. This, however, decreases diffusion of all the gas properties.

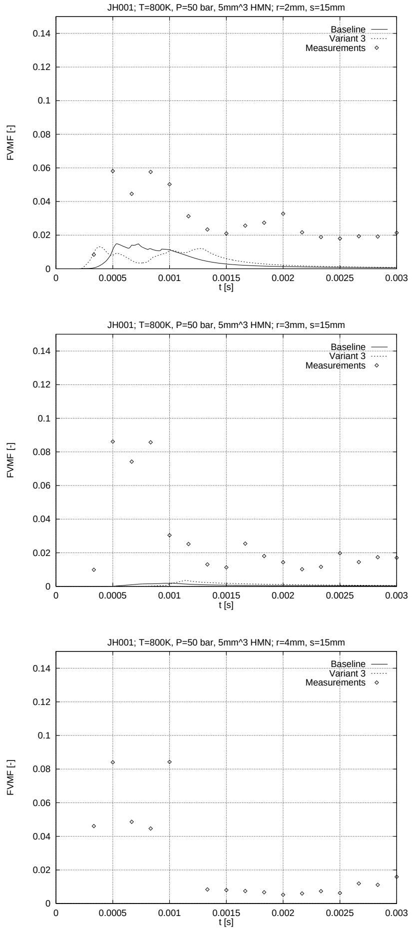

Figure 6.28: JH001; Fuel vapour mass fraction vs. time at s= 15.0 mm and at three radial positions; from top to bottom: r= 2.0, 3.0 and 4.0 mm.

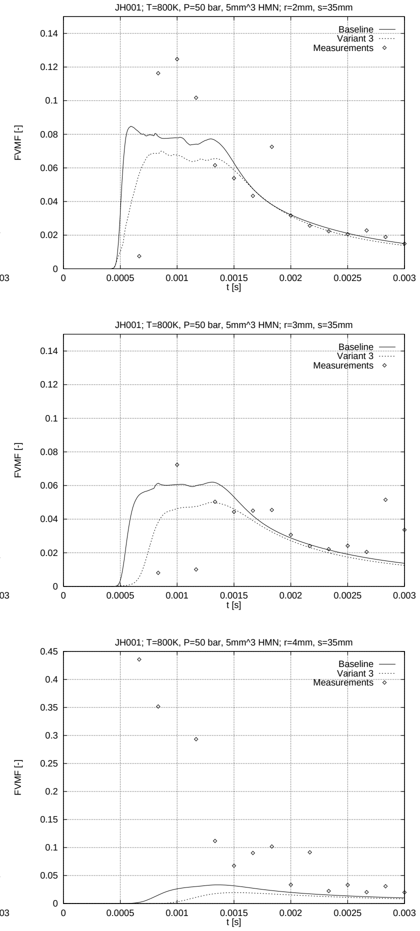

Figure 6.29: JH001; Fuel vapour mass fraction vs. time at s= 35.0 mm and at three radial positions; from top to bottom: r= 2.0, 3.0 and 4.0 mm.

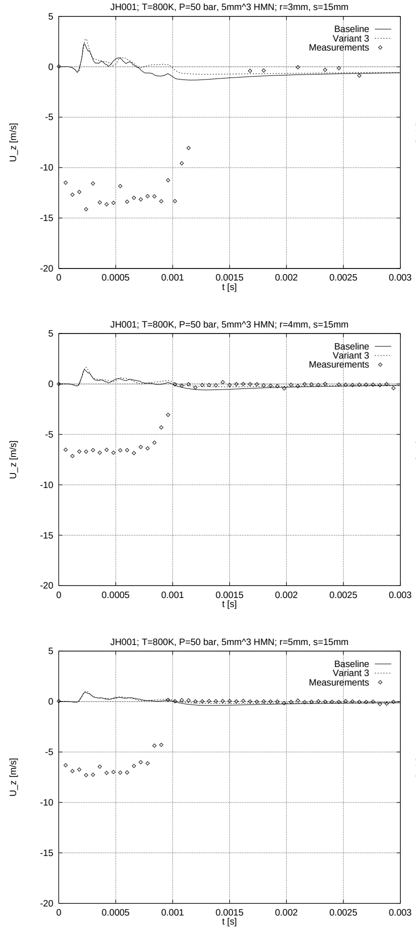

Figure 6.30: JH001; Gas velocity vs. time at s= 15.0 mm and at three radial positions; from top to bottom: r= 3.0, 4.0 and 5.0 mm.

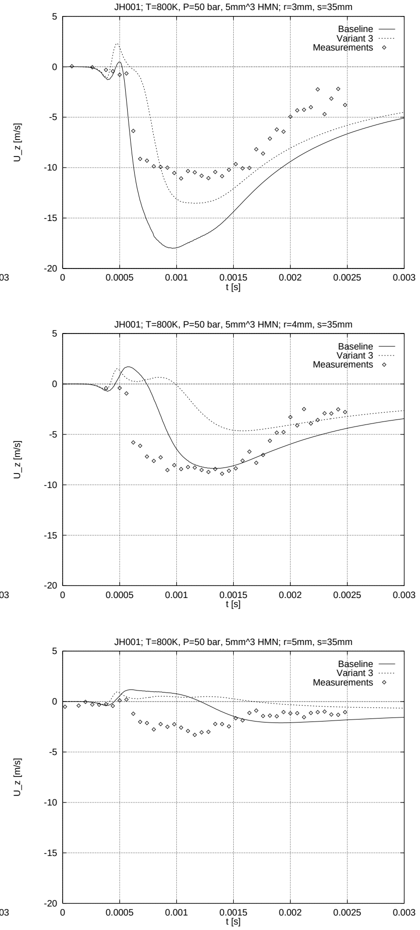

Figure 6.31: JH001; Gas velocity vs. time at s= 35.0 mm and at three radial positions; from top to bottom: r= 3.0, 4.0 and 5.0 mm.

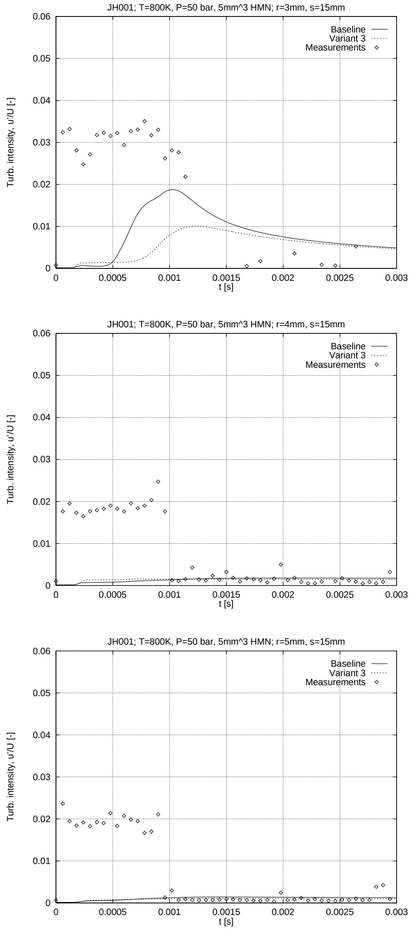

Figure 6.32: JH001; Turbulence intensity (normalised by the average injection velocity) vs. time at s= 15.0 mm and at three radial positions; from top to bottom: r= 3.0, 4.0 and 5.0 mm.

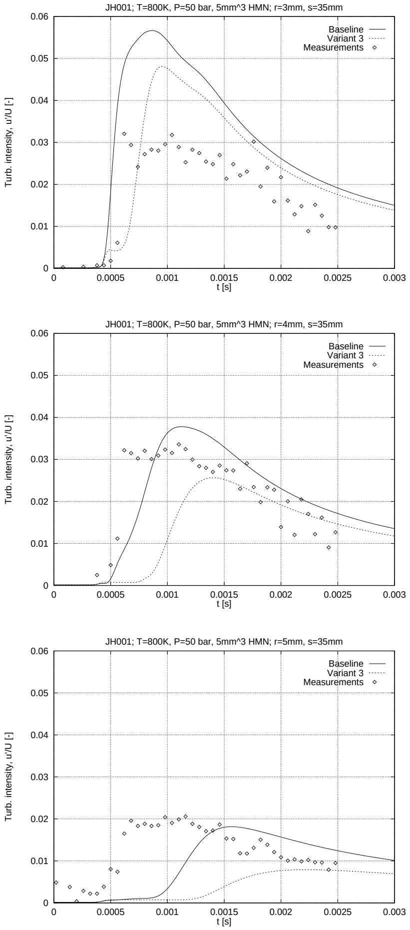

Figure 6.33: JH001; Turbulence intensity (normalised by the average injection velocity) vs. time at s= 35.0 mm and at three radial positions; from top to bottom: r= 3.0, 4.0 and 5.0 mm.

Summary

It was found out that the two correlations tested for the droplet drag coefficient, the 'standard drag curve' and Yuen and Chen correlation given by Eqs. (3.70) Eqs. (3.63) respectively, produce very similar results. The maximum difference in the predictions of the spray penetration is about $2mm$, and the evaporation differs by 2-3%. The predictions obtained by the Yuen and Chen correlation slightly better agree with the measurements then the baseline's.

The two tested breakup submodels, Reitz-Diwakar and Pilch-Erdman, induce substantial differences in the spray predictions. The spray penetrations differ by maximum $10mm$, the evaporation by 20%, and the spray Sauter mean diameter by a ratio of 2, because the Pilch-Erdman model predicts bigger droplet stable diameter. When compared with the measurements the Reitz-Diwakar model is preferred.

The inclusion of turbulence modulation in the gas-spray model causes reduction in the gas turbulence intensity and spray radial spreading. This enhences spray penetration so that the differences with the baseline case and measurements are the biggest of all the previous cases. The differences in the spray evaporation are smaller than in the previous case, and the Sauter mean diameter differs slightly from that predicted by the baseline case. This indicates increased coalescences between the more closely packed droplets.

Among all the cases, the spray prediction is best matched by `Variant 1` which employs the Yuen and Chen correlation for the drop drag coefficient and the Reitz-Diwakar breakup model, and does not include the turbulence modulation.

None of the combinations gives very good predictions of the local gas velocity, fuel vapour mass fraction and turbulence intensity, especially near the injector and farther from its axis. The predictions are somewhat better near the injector axis at axial distances greater than $100d_{inj}$.

6.3.4 The n-heptane results

Description

The injection system consists in this case of a modified in-line injection pump (Bosch Type PES 4 MW 80), an injection line and a commercial Bosch single-hole nozzle with characteristics given in Table 6.10, [118]. The fuel injection rate history is

Injector		
d_{inj}	0.2	mm
L	0.8	mm
c_d	0.65	

Table 6.10: Injector data.

calculated by the Institut für Thermodynamik, Aachen, from the measured injection and chamber pressures and needle lift. The injector discharge coefficient has been measured at a constant pressure difference varying the needle lift. The data can be found in Appendix E.1.

The computation is performed with the MPI and Huh's atomisation models. In the case of the MPI atomisation model, the two values of the spray semi-cone angle were used in order to assess its effects on the spray predictions.

Operating points and measurement data

The experiments were carried out under different air conditions, and the three operating points (OP) listed in Table 6.11 comprise all necessary input data for the numerical simulation. Two different amounts of fuel per cycle were injected and corresponding injection rate histories are shown in Fig.6.34, [118]. The fuel used in the experiments was n-heptane (C_7H_{16}). In the specified operating regimes n-heptane ignites, but the fact that the average measured ignition delay was $1.8ms$ after the start of injection, [16], allows us to use the measurements for the comparison. The operating points are designated here according to the practice used by the Institut für Thermodynamik, Aachen.

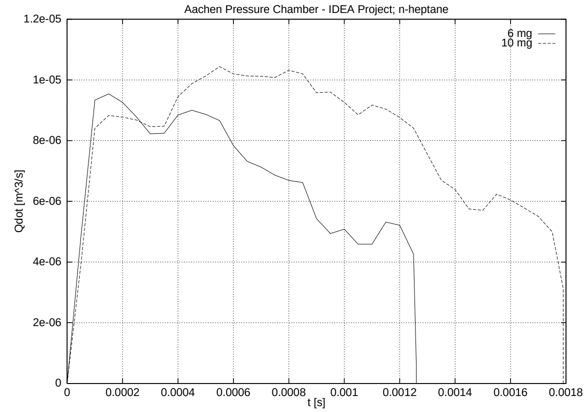

Figure 6.34: Injection rate curves.

The available types of measurement data are indicated in Table 6.12. The variations of fuel vapour mass fraction with time were measured at six locations in the chamber, see Fig.(6.35), by the Raman spectroscopy, [118]. The reported data represent the ensemble average of approximately 50 samples.

The spray penetration was analysed by a high-speed cinematography in combination with the Schlieren technique, [16].

OP	T_{air} [K]	p [bar]	Q [mg/cycle]	Fuel
1	800	50	6	n-heptane
3	800	50	10	n-heptane
4	600	30	6	n-heptane

Table 6.11: Aachen pressure chamber operating points - IDEA project.

OP	FVMF	Liquid penetration	Vapour penetration
1	+[1]	+	+
3	+[1]		
4	+[1]	+	+

[1] - measurement at six locations; see Fig. 6.35

Table 6.12: Available measurement data.

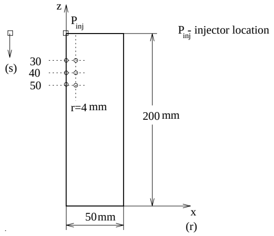

Figure 6.35: Locations of the measuring points.

Calculation parameters

As already noted, the calculations were performed with the Huh and MPI atomisation models, at the three operating conditions, Table 6.11. The spray models and computation parameters used in the calculations of all the three operating points are given in Tables 6.13 and 6.14. Since the maximum injection rate is about 1.4 times greater than that in the previous case, §(6.3.3), the time step size, Δt is chosen to be 1.25 μs; this ensures that the droplet Courant number is always less than 1.

The initial and boundary conditions specific to particular operating point are given at the beginning of sections which describe the comparison with the measurements.

Spray process	Submodel/correlation
Atomisation	Huh
discharge coeff.	$c_d = 0.65$
Atomisation	MPI
contraction ratio	$C_c = 0.7$
spray angle	$\alpha_{max} = 6.5^o$ or 10.0^o
hole wall roughness	$k_r = 1.0\ \mu m$
Breakup	Reitz-Diwakar
Collision	O'Rourke
Momentum exchange	Yuen & Chen drag correlation
Impingement	Not included
Turbulence modulation	Not included

Table 6.13: Spray submodels used in the calculations.

Parameter	Value
Time step, Δt	1.25 μs
Max. Courant number, Co	0.535
Parcel injection rate, $\dot{N}_p$	1 parcel/μs
Convergence tolerance, λ_c	$1.0 \cdot 10^{-3}$
Max. number of correctors	5
Discretisation scheme	SFCD

Table 6.14: Calculation parameters.

Comparison with measurements

The following figures show comparisons with experimental results for the spray penetration (liquid and vapour) and fuel vapour mass fraction for each operating point. In the figures r and s denote the radial and axial distances of measuring points from the injector, respectively. In the case of the MPI atomisation model, two values of the spray semi-cone angle, 6.5 and 10.0 degrees, were used to asses its effects on the spray behaviour; corresponding curves are denoted as MPI/6.5 deg and MPI/10.0 deg.

Operating point No. 1

The injection conditions for this operating point are given in Table 6.15.

Spray		
T_{SOI}	0.00	ms
T_{EOI}	1.26	ms
Fuel	n-heptane	
Inj. quantity	6.00	mg
T_{inj}	300.0	K

Table 6.15: OP1; Injection specifications used in the calculations.

The fuel vapour penetration for both atomisation models shows reasonably good agreement with the measurements, Fig.6.36. While the Huh model slightly overpredicts penetration (by maximum 4 mm) in the range t=0.4-1.2 ms, the MPI model, in the same range, shows very small underprediction; less than 1 mm. Both models overpredict penetration in the range t=0-0.4 ms, and underpredict for t>1.4 ms. In the initial stage of injection, up to 0.2 ms, the MPI predicts greater penetration than the Huh, what indicates that the injection velocity in the former model is higher. This is caused by cavitation in the injector nozzle which the MPI model takes into account. As the spray develops, the differences in penetration become smaller, and after $t = 0.3ms$ the Huh model predicts slightly greater penetration than the MPI.

This can be the result of the more intensive secondary breakup of the 'MPI' droplets due to their higher velocity.

Despite difficulties in assessing the quality of liquid penetration prediction due to the oscillations of results[4], Fig.6.37, it can be concluded that the MPI model shows better agreement with the measurements. Both models overpredict the measurements.

This penetration behaviour has its background in the droplet size distribution. As can be seen in Fig.6.38, the MPI model produces spray with significantly smaller Sauter mean diameter than Huh's model. This means that the MPI droplets experience relatively higher drag force with the consequences on the liquid penetration described above.

Although there are no measurements of the cumulative evaporation, it is interesting to compare predictions of the models. The MPI model shows substantially higher evaporation ratio than the Huh's model, Fig.6.39. This is consistent with the aforementioned predictions of the spray Sauter mean diameter.

Inspection of the above figures reveals that the influence of the spray semi-cone angle in the MPI case on the spray predictions is weak; the similar behaviour was observed by [179]. This can be explained by two facts. Firstly, the size of the secondary droplets, D_s is slightly affected by the spray angle since $D_s \propto \alpha^{-1/3}$ (see 3.2.2); the evidence of this is almost equal Sauter mean diameter predicted with both spray angles up to $t = 0.6ms$, Fig.6.38. Secondly, these droplets, due to their very small sizes, have small momentum and short life time.

In the later period of injection, for $t > 0.6ms$, the Sauter mean diameter predicted with the smaller spray angle is greater than that obtained with the angle 10 ^{o}. This can be attributed to the higher probability for the droplet coalescence in the narrower spray.

The comparison of the fuel vapour mass fraction at six locations is given in Figs.6.40-6.44. Both atomisation models, Huh's and MPI, overpredict the measurements, although in the case of the MPI, this overprediction is lower than with the

[4]The oscillations are result of complete evaporation of droplets in some computational cells, which causes abrupt changes of void fraction there.

Huh's model. The fuel vapour mass fraction curves show the distinguish peak in the early stage of injection. This is probably caused by the local depletion of small droplets whose temperature at that instant of time reaches the critical temperature of the fuel.

The analysis of the arrival times of the fuel vapour to the measured sites shows that the Huh model predicts in average 0.1 ms shorter arrival times than the MPI model. The agreement between the MPI predictions and the measurements is somewhat better up to s=40 mm; beyond this point the calculations give arrival times shorter by approximately 0.1-0.15 ms. The influence of the spray semi-cone angle, which is the input for the MPI model, on the predictions of fuel vapour mass fraction and spray arrival time is small. The maximum observed difference in the prediction of the local fuel vapour mass fraction is less than 7%.

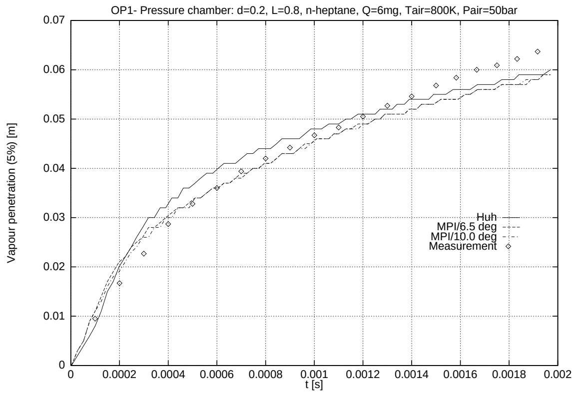

Figure 6.36: OP1; Fuel vapour penetration based on the 5% FVMF criterion.

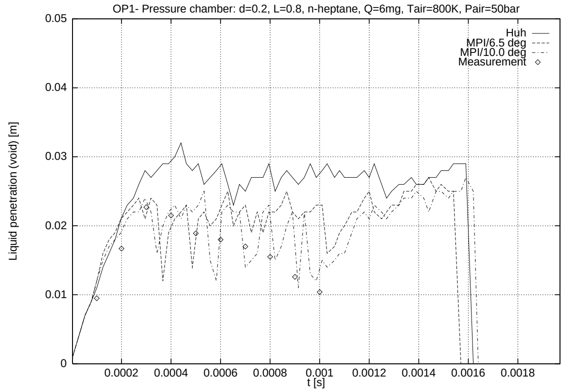

Figure 6.37: OP1; Liquid penetration based on the 99% void fraction criterion.

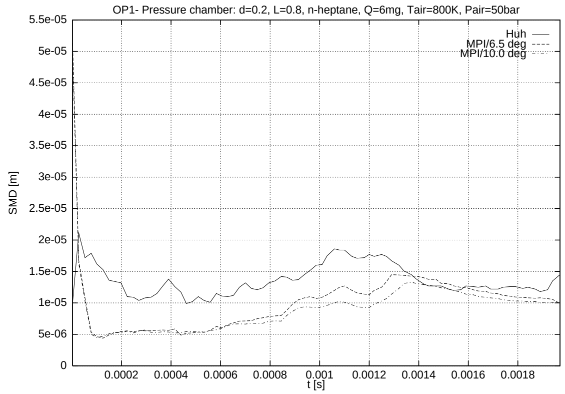

Figure 6.38: OP1; Predicted spray Sauter mean diameter.

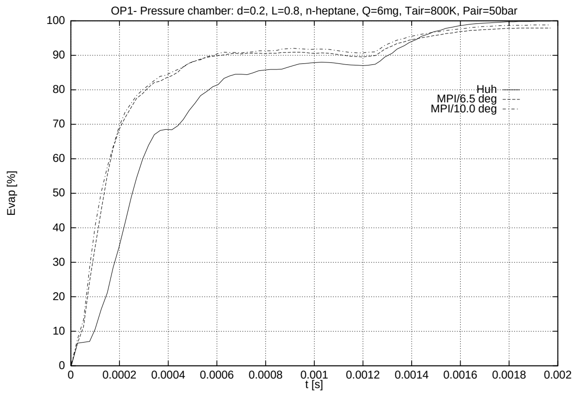

Figure 6.39: OP1; Fuel evaporation vs. time.

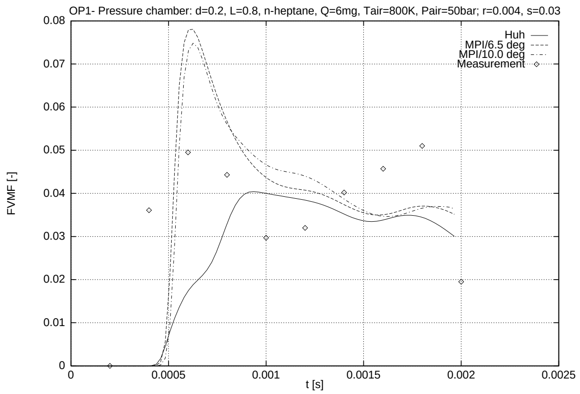

Figure 6.40: OP1; Fuel vapour mass fraction vs. time at r=4.0 mm, s= 30.0 mm.

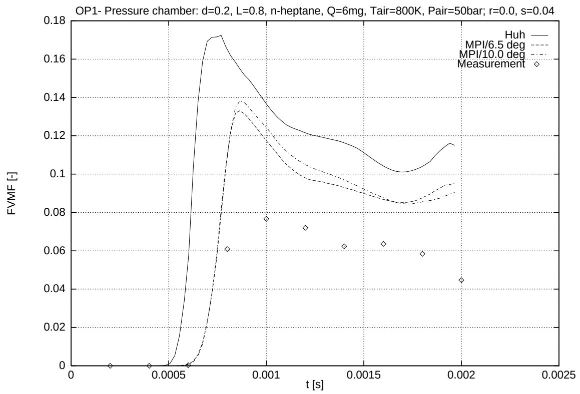

Figure 6.41: OP1; Fuel vapour mass fraction vs. time at r=0.0 mm, s= 40.0 mm.

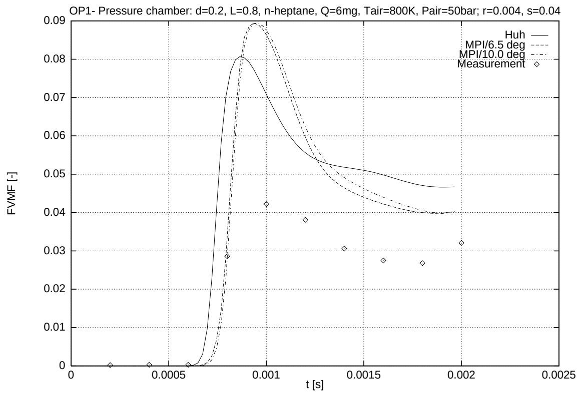

Figure 6.42: OP1; Fuel vapour mass fraction vs. time at r=4.0 mm, s= 40.0 mm.

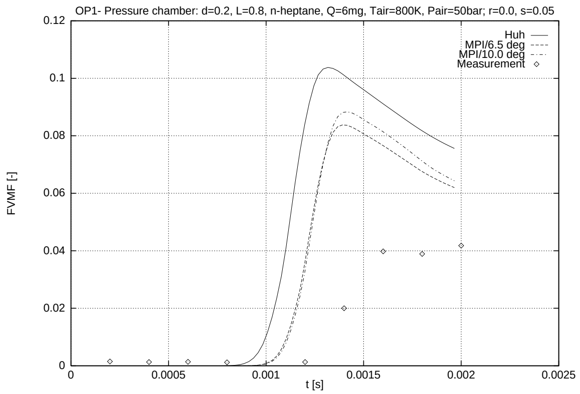

Figure 6.43: OP1; Fuel vapour mass fraction vs. time at r=0.0 mm, s= 50.0 mm.

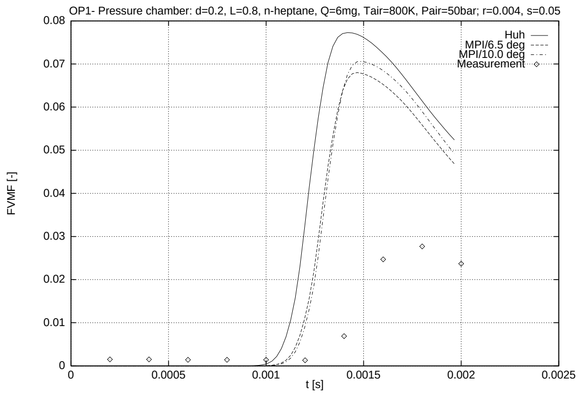

Figure 6.44: OP1; Fuel vapour mass fraction vs. time at r=4.0 mm, s= 50.0 mm.

Operating point No. 3

The injection conditions for this operating point are given in Table 6.16.

Spray	
T_{SOI}	0.00 ms
T_{EOI}	1.79 ms
Fuel	n-heptane
Inj. quantity	10.00 mg
T_{inj}	300.0 K

Table 6.16: OP3; Injection specifications used in the calculations.

In the absence of experimental spray penetrations data for this operating point, only comparisons of the computational predictions are depicted in Figs.6.45-6.46. Compared to operating point OP1, the differences between the predictions produced by the models are smaller, especially in the case of liquid penetration. As was the case in the previous operating point, in the early stage of injection, up to 0.25 ms, the MPI model predicts greater penetration than the Huh model; this is caused by the higher injection velocity predicted by the MPI nozzle model.

Comparison of the MPI predictions obtained with the different spray angles reveals that the spray angle affects the penetration, both vapour and liquid, slightly stronger than in the previous operating point. The maximum observed difference in the prediction of the fuel vapour penetration is about $3mm$. As expected, the MPI model with the spray angle of 10 ^{o} produces somewhat smaller penetrations, due to its bigger radial spreading.

The predictions of the cumulative evaporation and the Sauter mean diameter show the same trend as in the previous operating point; see Figs.6.48 and 6.47. The MPI model produces significantly smaller Sauter mean diameter, and therefore bigger evaporation, than the Huh model.

The comparison of fuel vapour mass fraction for this operating point is given in Figs.6.49-6.54. As in the previous operating point the calculations overpredict measurements. The spray arrival times predicted by the MPI model are more affected by the spray angle than in the OP1 case, what can be the result of the significantly bigger injection velocity than in OP1. As expected, the MPI model with the bigger spray angle predicts longer arrival time, and as the measuring points are farther from the injector, it differs more from that of the 6.5 ^{o} case.

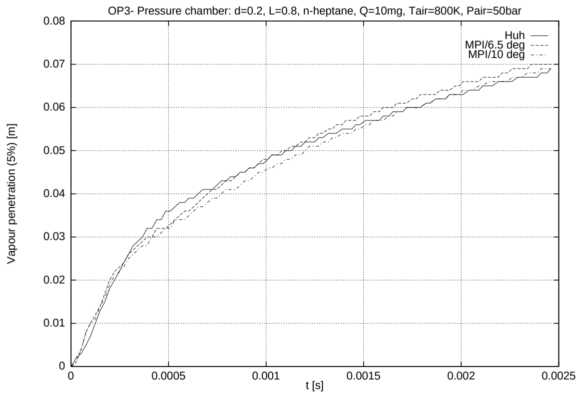

Figure 6.45: OP3; Fuel vapour penetration based on the 5% FVMF criterion.

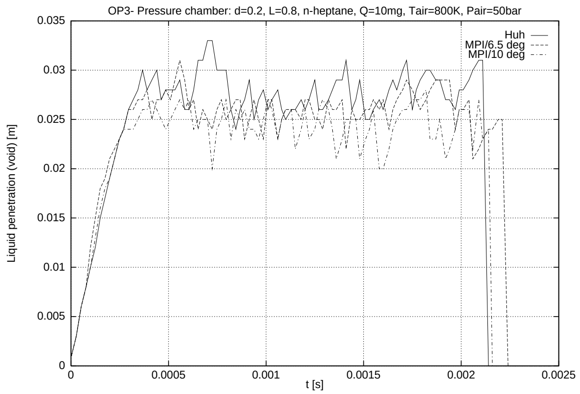

Figure 6.46: OP3; Liquid penetration based on the 99% void fraction criterion.

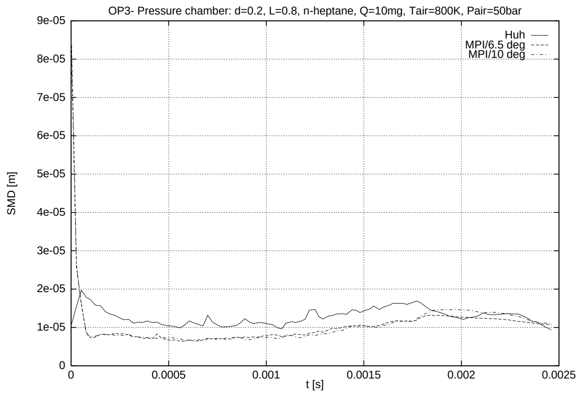

Figure 6.47: OP3; Predicted spray Sauter mean diameter.

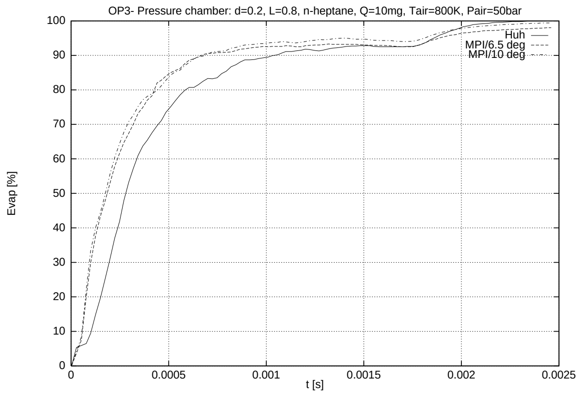

Figure 6.48: OP3; Fuel evaporation vs. time.

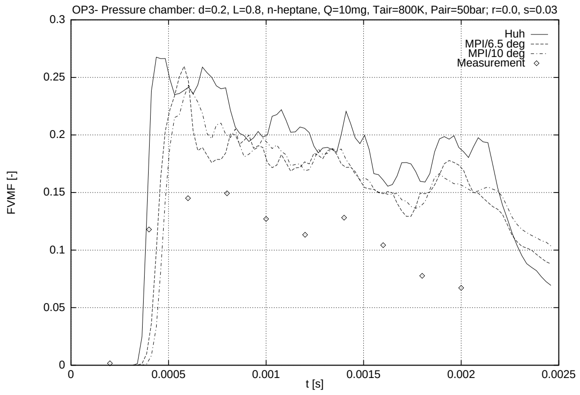

Figure 6.49: OP3; Fuel vapour mass fraction vs. time at r=0.0 mm, s=30.0 mm.

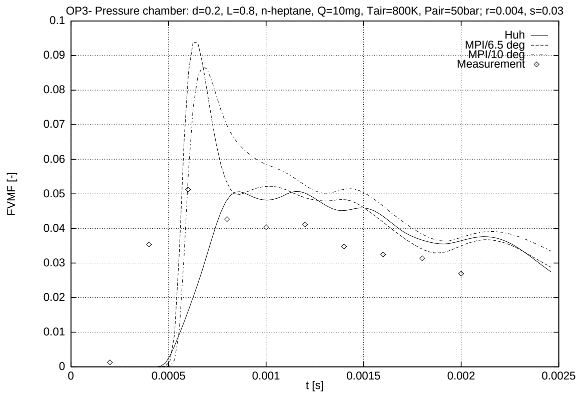

Figure 6.50: OP3; Fuel vapour mass fraction vs. time at r=4.0 mm, s= 30.0 mm.

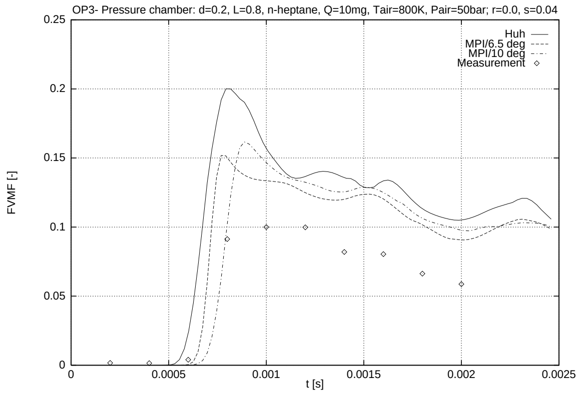

Figure 6.51: OP3; Fuel vapour mass fraction vs. time at r=0.0 mm, s= 40.0 mm.

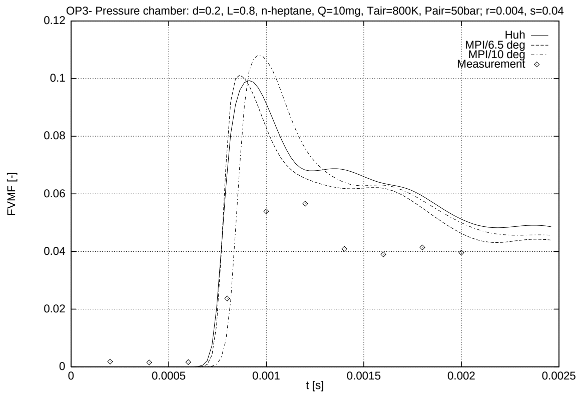

Figure 6.52: OP3; Fuel vapour mass fraction vs. time at r=4.0 mm, s= 40.0 mm.

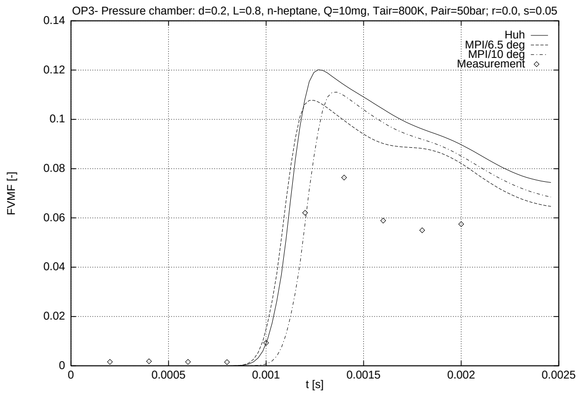

Figure 6.53: OP3; Fuel vapour mass fraction vs. time at r=0.0 mm, s= 50.0 mm.

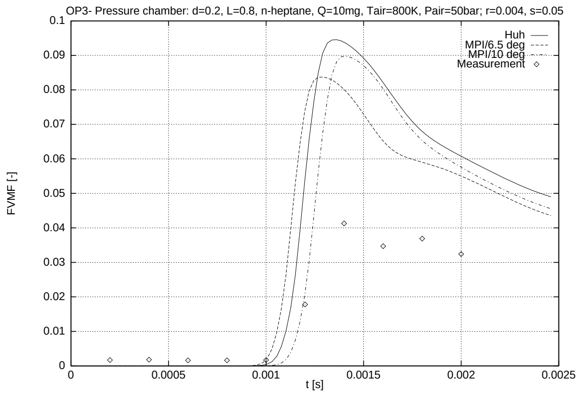

Figure 6.54: OP3; Fuel vapour mass fraction vs. time at r=4.0 mm, s= 50.0 mm.

Operating point No. 4

This operating point has the same injection rate as OP1, and differs from OP1 in the pressure and temperature of air. Since the gas density and temperature in the chamber are lower than in the OP1 case, the spray penetration is expected to be higher. The injection conditions for this operating point are given in Table 6.17.

Spray		
T_{SOI}	0.00	ms
T_{EOI}	1.26	ms
Fuel	n-heptane	
Inj. quantity	6.00	mg
T_{inj}	300.0	K

Table 6.17: OP4; Injection specifications used in the calculations.

Fig.6.55 depicts the fuel vapour penetration. The overprediction is bigger than in OP1 and the maximum deviations from the measurements are 10 and 7 mm for the Huh and MPI model, respectively. The biggest overprediction is in the time range 0.2-1.0 ms, and afterward the differences become smaller.

The results of the MPI model for liquid penetration, Fig.6.56, shows reasonably good agreement with the measurements. The Huh model predicts notable bigger penetration than the MPI, which indicates that its Sauter mean diameter is also bigger, Fig. 6.57.

As can be seen in Figs.6.58 and 6.57 the cumulative evaporation and the Sauter mean diameter show the same trend as in the previous cases. The predicted Sauter mean diameter, by both models, are smaller than in OP1 due to the longer life time of small droplets caused by the reduced heat transfer from the gas to the droplets, as a consequence of the lower ambient gas temperature than in the OP1 case.

The effect of the spray angle on the prediction of all the above quantities is small, less than 5%; the same explanation given for the OP1 case can be applied.

The comparisons of the measured and calculated fuel vapour mass fractions show similar overpredictions as in both the previous operating points (Figs.6.59-6.64).

Particularly good agreement with the MPI predictions can be seen in Fig.6.60 for t>0.5ms. The arrival time is predicted better than in OP1, especially by the MPI model.

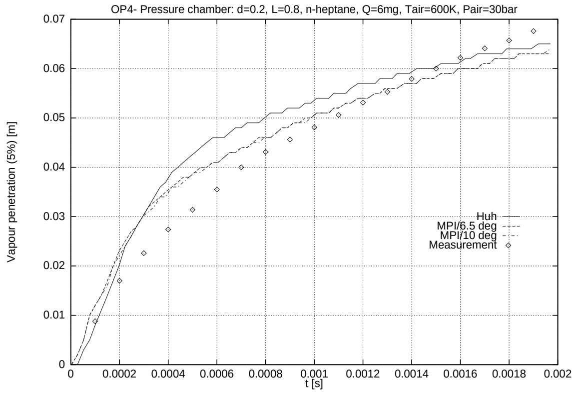

Figure 6.55: OP4; Fuel vapour penetration based on the 5% FVMF criterion.

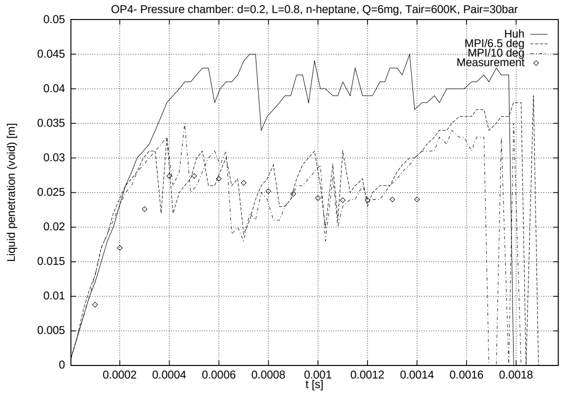

Figure 6.56: OP4; Liquid penetration based on the 99% void fraction criterion.

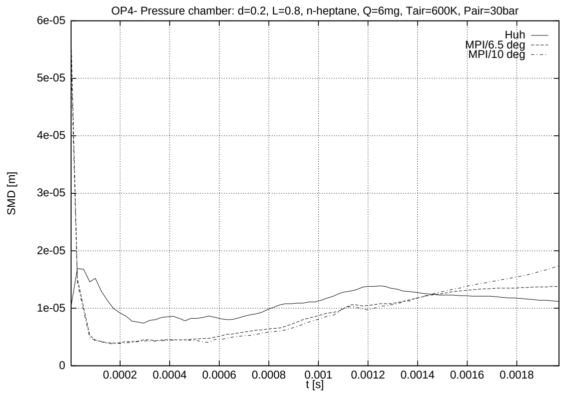

Figure 6.57: OP4; Predicted spray Sauter mean diameter.

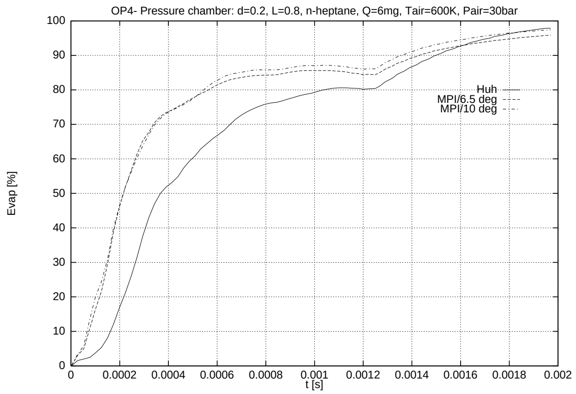

Figure 6.58: OP4; Fuel evaporation vs. time.

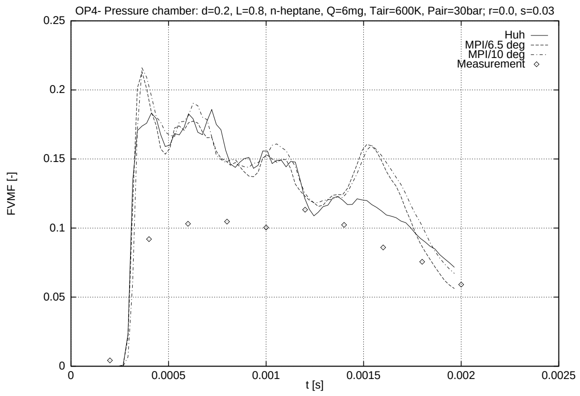

Figure 6.59: OP4; Fuel vapour mass fraction at r=0.0 mm, s=30.0 mm.

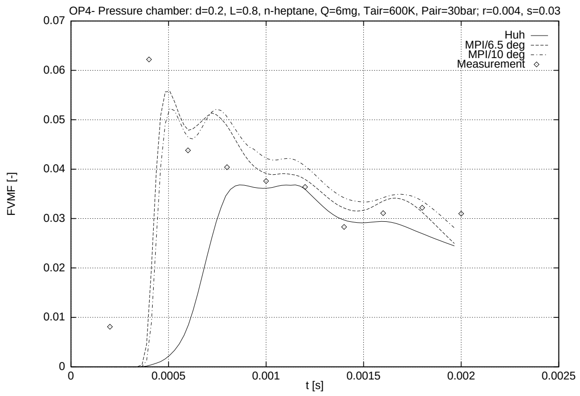

Figure 6.60: OP4; Fuel vapour mass fraction at r=4.0 mm, s= 30.0 mm.

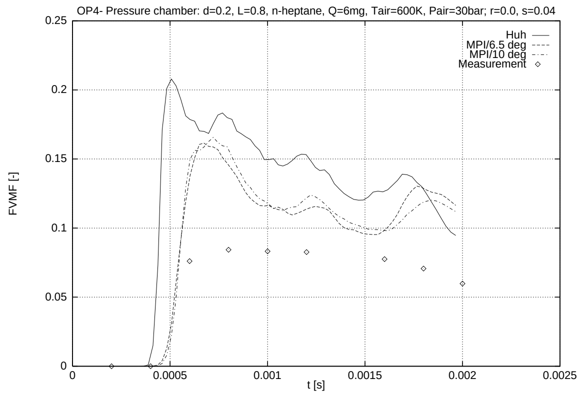

Figure 6.61: OP4; Fuel vapour mass fraction at r=0.0 mm, s= 40.0 mm.

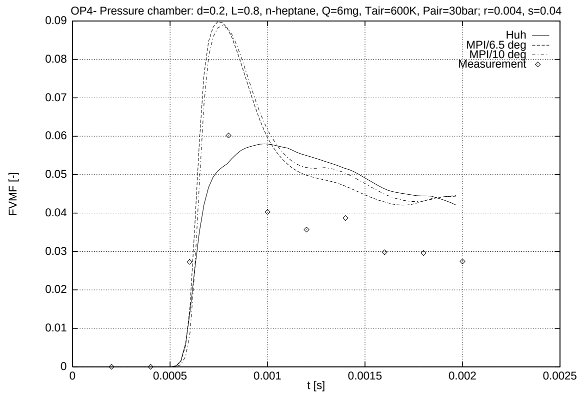

Figure 6.62: OP4; Fuel vapour mass fraction at r=4.0 mm, s= 40.0 mm.

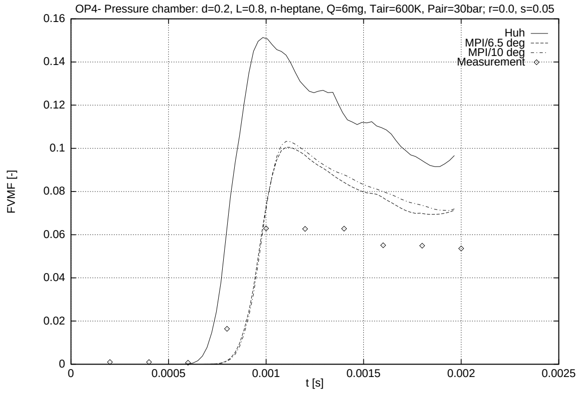

Figure 6.63: OP4; Fuel vapour mass fraction at r=0.0 mm, s= 50.0 mm.

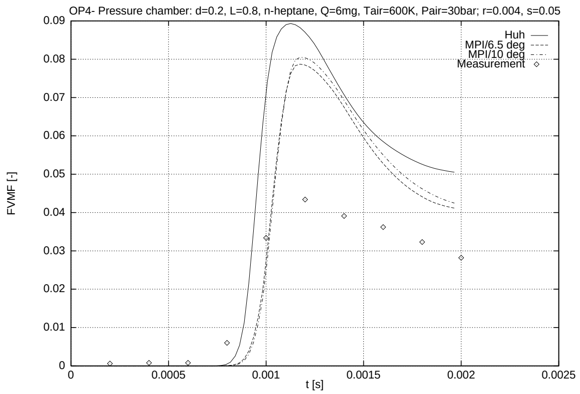

Figure 6.64: OP4; Fuel vapour mass fraction at r=4.0 mm, s= 50.0 mm.

Summary

The comparisons of the computational results and measurements presented in this section for the three operating regimes enable the following conclusions.

The fuel vapour penetration is slightly better predicted by the MPI model. Both the models slightly overpredict penetration at the early stage of injection, and toward the end of injection this overprediction vanishes. In the later period, after the end of injection, both models slightly underpredict vapour penetration.

Despite the difficulties in assessing predictions of the liquid penetration, the predictions of the MPI model are significantly closer to the measurements than the Huh model. Generally, both models overpredict the measurements and none of the models can be judged as successful.

The worst-predicted quantity is the time development of the fuel vapour mass fraction at particular measurement locations. Big overpredictions are common to both the models and neither the MPI nor Huh model can be assessed as better. The exception to this behaviour are the predictions of the Huh model at point $r = 4mm, s = 30mm$ in all the operating regimes, see Fig.6.40, 6.50 and 6.60. This can be explained as a result of the bigger droplets produced by atomisation and by their smaller radial spreading in the initial stage of injection than in the case of the MPI model. The further evidence of this is the behaviour at the beginning of injection of the Sauter mean diameter (Figs.6.38, 6.47 and 6.57), which is almost three times bigger than in the MPI case, and spray evaporation (Figs.6.39, 6.48 and 6.58) which is about 2.5 times smaller than in the MPI case. However, these differences become smaller with time.

6.3.5 Spray-wall impingement

Description

The aim of this section is much to illustrate the predictions of the MPI spray-wall impingement model without any detailed comparison with measurements, since this is beyond the scope of the present study. For this purpose a dummy test case[5] was

[5]The specifications for the test case were selected in collaboration with C.Bai, who at the time worked on his own impingement model [18]. I wish to express my appreciation for his valuable

created, and its arrangement is shown in Fig.6.65. The injector is positioned $25mm$ above the wall and injects a fuel, n-dodecane, normal to the wall at an average speed of about $200m/s$. The ambient gas is air with pressure of $1bar$, and with a zero initial velocity. The temperatures of the fuel, air and the wall are taken to be equal, so the heat transfer between the spray and surrounding air does not take place and the calculation of evaporation is disabled[6].

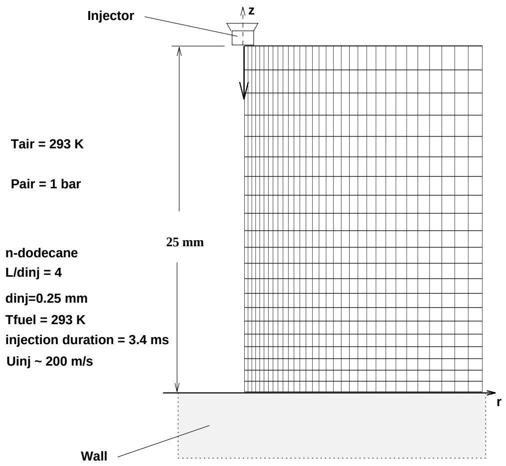

Figure 6.65: Spray-wall impingement; lay-out and injection conditions.

Calculation parameters

The computational mesh used for the calculation is the same one used for the Aachen pressure chamber, see §(6.3.2); the part of the mesh is shown in Fig.6.65. The initial conditions and the spray submodels employed in calculation are given in Tables 6.18, and 6.19. The computational parameters are listed in Table 6.20.

assistance.

[6]Even for these conditions there is a difference between the partial fuel vapour pressures at the drop surface and in the surrounding air which acts as a driving force for the evaporation, but because of the low fuel temperature it is small and the evaporation can be neglected.

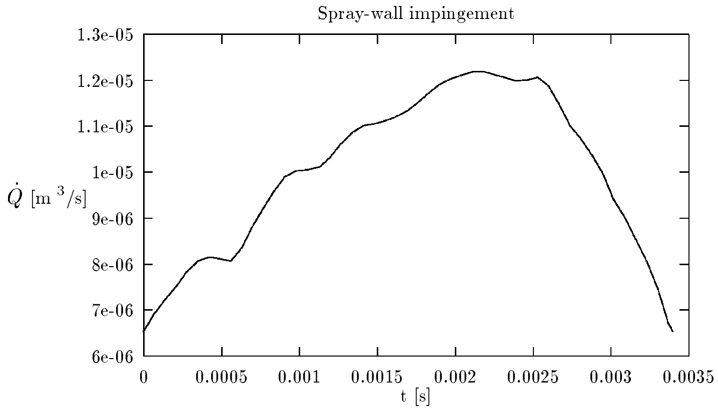

Figure 6.66: Injection rate history.

Spray		
T_{SOI}	0.00	ms
T_{EOI}	3.5	ms
Fuel	n-dodecane	
T_{inj}	293.0	K
Field variables		
$\mathbf{u}$	0.00	m/s
P	1.00	bar
T	293.0	K
k	0.1	m^2/s^2
ϵ	4.0	m^2/s^3

Table 6.18: Initial conditions used in calculation.

Spray process	Submodel/correlation
Atomisation	Huh
discharge coeff.	$c_d = 0.61$
Breakup	Reitz-Diwakar
Collision	O'Rourke
Momentum exchange	'standard drag curve'
Impingement	MPI
Turbulence modulation	Not included

Table 6.19: Spray submodels/correlations used in calculation.

Parameter	Value
Time step, Δt	5.0 μs
Parcel injection rate, $\dot{N}_p$	1 parcel/μs
Convergence tolerance, λ_c	$1.0 \cdot 10^{-4}$
Max. number of correctors	2
Discretisation scheme	SFCD

Table 6.20: Calculation parameters.

Results

Figs. 6.67 and 6.68 depict the development of the gas velocity and the spray at six different times. In the first plot, at $t = 0.25ms$, which is just about $30\mu s$ after the spray reaches the wall, the first droplets reflected from the wall can be observed near the impact point, pushing the air in front of them. The air motion towards the wall caused by the injection become deflected at the wall and starts forming a vortex whose evidence can be seen at $t = 0.50ms$. Subsequent plots of the gas velocity depict the motion of the vortex along the wall further from the point of spray impact.

From the moment spray hits the wall, reflected droplets form a cloud which propagates along the wall, partly due to its own inertia, and partly dragged by the air. As the droplets in the cloud lose their initial momentum, by transferring it to the surrounding air, they are captured by the air and from then on practically follow its motion. The distinct evidence of this are the droplets at the outer (radial) edge of the cloud, Fig. 6.68, at time $1.0, 1.25$ and $1.5ms$, which match the shape of the vortex.

The spray radial penetration is shown in Fig. 6.69. The sharp discontinuity of the curve at $t = 0.22ms$ indicates the moment when the spray hits the wall. The evidence of the impact can also be seen in Fig. 6.70, which depicts the number of spray parcels, as a disruption in the slope of the curve. The greater slope of the curve from the time of impact indicates increasing rate of droplets production due to the splashing process.

During splashing, part of the droplets stay at the wall and that can be observed as a cluster of droplets in the vicinity of the spray axis, Fig. 6.68. In the same region there are also droplets whose Weber number is less than critical (the small-size secondary droplets produced by atomisation or breakup) which stick at the wall without splashing. In the same figure, there is an evidence of a number of small droplets stuck to the wall radially farther from the spray axis; these droplets are initially produced by splashing and later carried away by the air to the wall.

The spray Sauter mean diameter is shown in Fig. 6.71. After an initial period of about $0.3ms$, the Sauter mean diameter adopts an approximately constant value.

It must be remembered here that the MPI impingement model does not consider the formation of the liquid film on the wall and its flow. This omission can result in accumulation of droplets in a few near-wall cells, producing there a small or, in the extreme case, negative void fraction which can prevent further calculation. In order to avoid this, in the present study the volume of the droplets stuck on the wall was not taken into account in the void calculation. This measure ensured that the void fraction was never less than 0.89.

Another important fact, from computational point of view, is a high rate of production of the computational parcels, which slows down computations and can cause the overflow of the 'drop arrays' in the code. Fortunately, in the diesel engine conditions both the above mentioned issues are not very likely to occur because of the high ambient temperature leads to fast evaporation of the droplets.

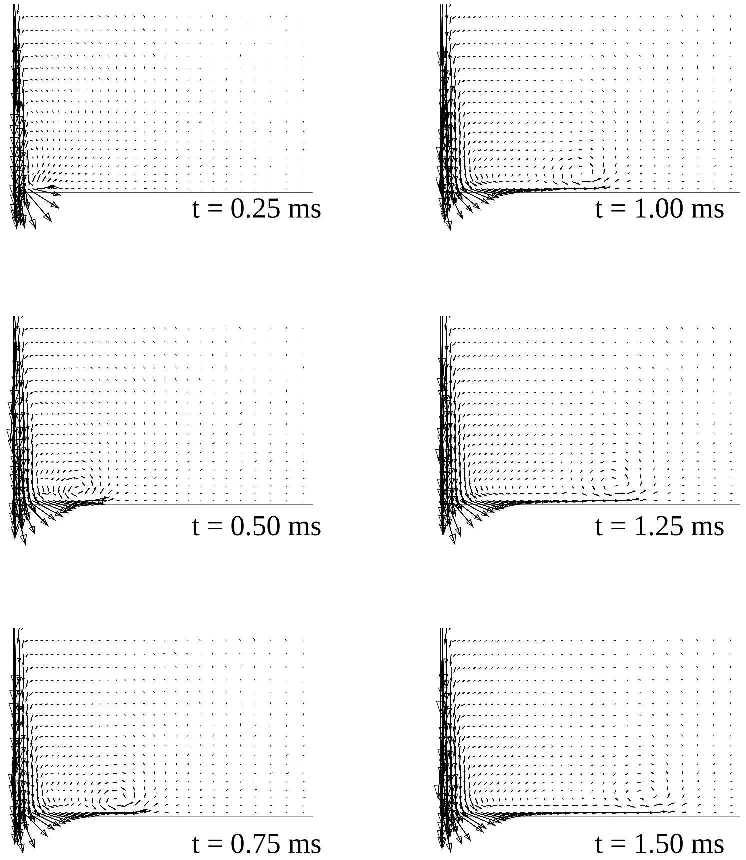

Figure 6.67: Gas velocity at 0.25, 0.5, 0.75, 1.0, 1.25, and 1.5 ms.

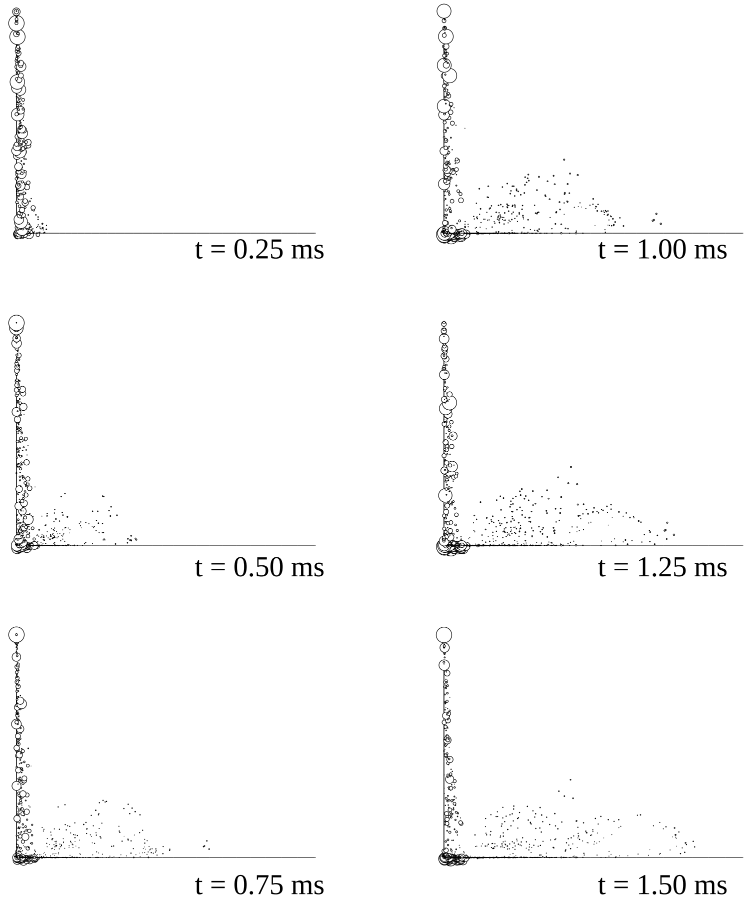

Figure 6.68: Spray at 0.25, 0.5, 0.75, 1.0, 1.25, and 1.5 ms.

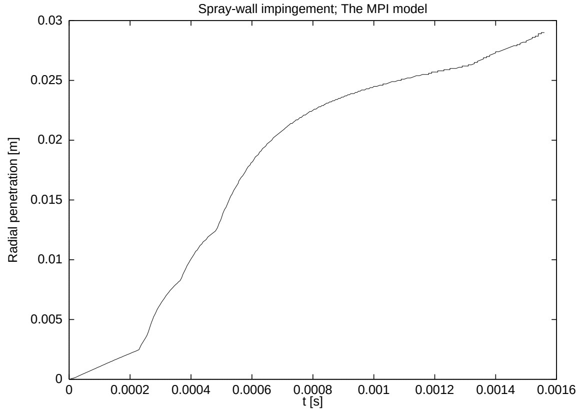

Figure 6.69: Spray radial penetration vs. time.

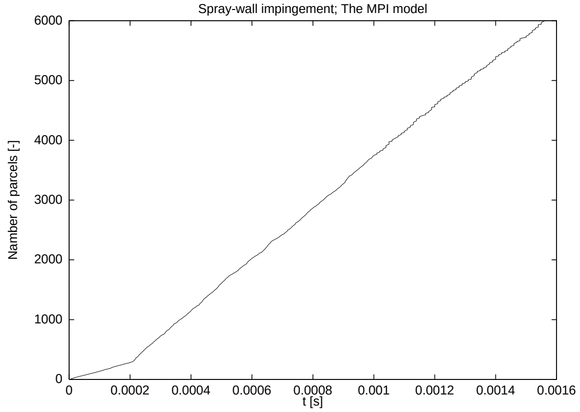

Figure 6.70: Number of parcels vs. time.

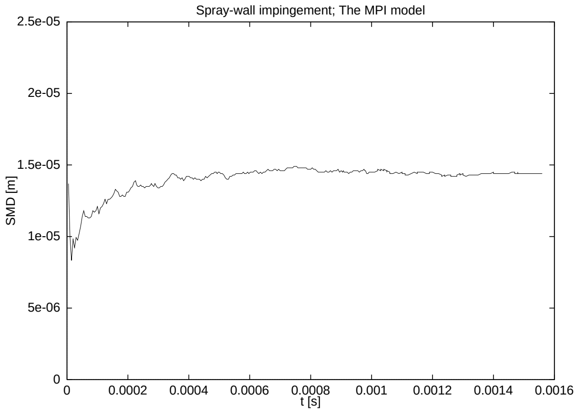

Figure 6.71: Sauter mean diameters vs. time.

6.4 IFP Engine

6.4.1 Description

This engine, developed and built by the Institute Francais du Petrole (IFP), is specially designed to enable a full optical view of the in-cylinder space through a fused silica window in the piston and a side window opposite to the injector, Fig. 6.72. The objective of the experiments was to collect data on spray and combustion in a DI diesel engine to support the development of spray and ignition/combustion modelling. Pressure and temperature levels in the engine are similar to those of the typical diesel engine, and at the top dead centre (TDC) they can reach 70 bar and 900 K. The injection takes place in a rectangular canal formed in the piston; this region will also be referred in this study as the 'duct'. The engine configuration is almost symmetrical, except for the slight offset of the side window and the inlet/outlet valve assemblage. The injection system comprises a single-hole Bosch injector and an in-line injector pump. These and other details about the engine and experimental set-up can be found in [22] and [21].

The engine operating conditions were varied to study different effects. For spray measurements, the engine was fed with nitrogen to suppress ignition, under the operating conditions given in §(6.4.2). This operating point is called a 'Reference' operating point (REF). In a numerical simulation air is used instead of nitrogen, assuming that the differences in properties important for spray calculation between air and nitrogen are not significant (nitrogen makes almost 79% of air by volume). The liquid fuel and fuel vapour were visualised with the planar laser induced 'EXCIPLEX' fluorescence[7]. Experimental data were inferred from recorded images with image processing and ensemble averaging.

[7]This method allows simultaneous observation of the fuel liquid and fuel vapour distribution. The EXCIPLEX mixture consists of a fuel (solvent) and two other species which under laser excitation form an exited state complex (EXCIPLEX). Under certain conditions, the EXCIPLEX exists only in the liquid phase, and this fact is exploited in the measurements (more details can be found in [21]).

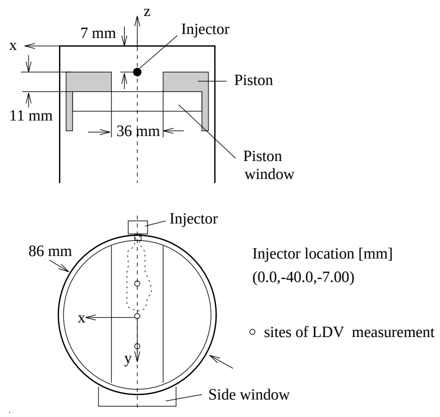

Figure 6.72: Sketch of the IFP optical engine.

6.4.2 Initial and boundary conditions

The relevant engine and injector data are given in Table 6.21, and parameters for the operating point REF in Table 6.22. The data about valve motion, gas conditions in the inlet/outlet valve ports or at the valve curtains is not available, so the valves are not modelled in the computational mesh, nor is the flow through the valves calculated. Instead, it is assumed that the initial gas fields at the BDC, where the numerical simulation starts, are spatially uniform, with the values given in Table 6.23. The values of gas pressure and temperature are taken from [22], while the values of other quantities are assumed.

Injector			Engine		
d_{inj}	0.2	mm	Compression ratio	10.55	
L	0.8	mm	Bore, B	86.00	mm
c_d	0.8		Stroke	82.00	mm
			Connecting rod	547.90	mm

Table 6.21: IFP optical engine data.

The chamber wall temperatures were not measured. In the numerical simulation

IFP optical engine; REF		
Speed	1200	rpm
V_p	3.28	m/s
Charge	N_2/air	
T_{BDC}	333	K
t_{SOI}	351.0	CA
t_{EOI}	371.0	CA
Fuel	n-heptane	
Inj. quantity	14.00	mm^3
T_{inj}	310.0	K

Table 6.22: IFP optical engine; operating point REF. (V_p is the average piston velocity).

the wall temperature is taken as constant at $400K$ over the whole chamber surface consisting of the piston, liner and cylinder head patches.

Initial conditions at BDC		
u	0.00	m/s
P	1.95	bar
T	333.00	K
k/V_p^2	0.11	
$\epsilon\ B/V_p^3$	0.175	

Table 6.23: Initial conditions at BDC used in calculations.

Injection rate

The injection system was fitted with a needle lift sensor and injection line pressure transducer. The cylinder pressure was measured by a piezo-electric pressure transducer, and the adjustment of the fuel injection quantity was done with a micrometer coupled with the pump governor. One cycle measurement of the injection line pressure, chamber pressure, and needle lift vs. time, for the operating point REF, are given in Figs. 6.73 and 6.74, [20]. The ensemble-averaged data of the above quantities were not available, therefore the existing single-cycle measurements were used for the injection rate calculation. This, however, represents a serious weakness for the simulation and can be one of the reasons for rather poor prediction of the fuel vapour penetration reported later in the study.

The injection flow rate is calculated from the needle lift data and the pressure difference between the injection and cylinder pressures. In the absence of other data, it is assumed that the flow cross-sectional area varies linearly with the needle lift[8], and that the nozzle discharge coefficient is constant (see Table 6.22). It is assured by an appropriate scaling factor that the total amount of injected fuel per cycle, obtained by the integration of calculated injection rate over the injection period, is equal to its measured value specified in Table 6.22. The injection volumetric flow rate calculated in the aforementioned fashion is shown in Fig. 6.75.

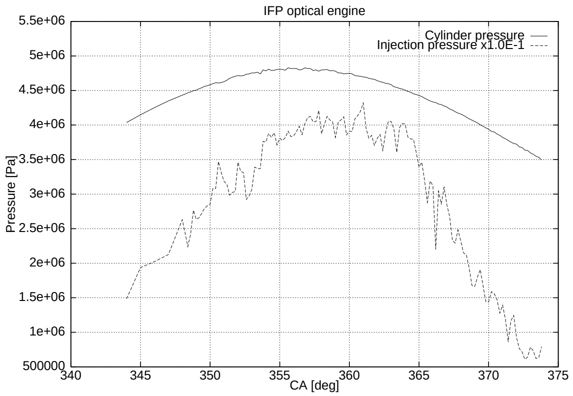

Figure 6.73: Cylinder and injection pressures vs. time; single cycle measurement.

[8]Taking into account almost constant value of the needle lift for the most of injection period, Fig. 6.74, the error introduced by this assumption is presumablely small.

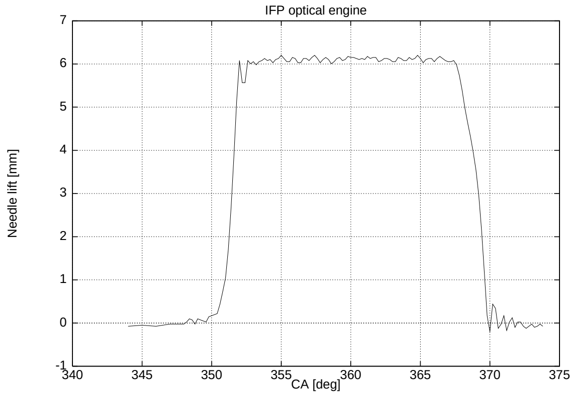

Figure 6.74: Single cycle measurement of the needle lift vs. time.

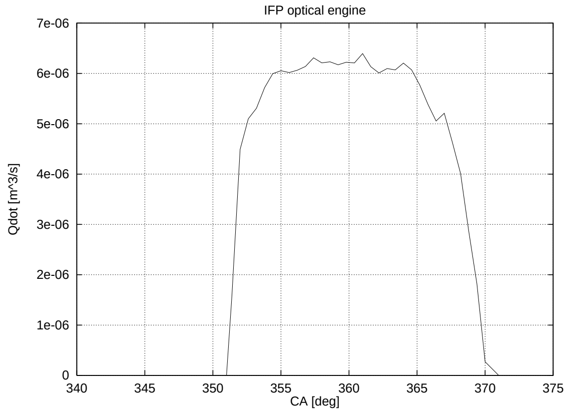

Figure 6.75: Calculated injection flow rate history.

6.4.3 Computational mesh

The sensitivity of spray predictions to the mesh density, shown earlier in §(6.3.2), demands a special care in designing the computational mesh in the region where the spray injection takes place. In this test case it is in the canal (duct) region of the piston. However, there is a limit on the total number of cells in the computational domain affordable to the simulation with respect to the computer storage capacity and CPU time.

In order to find a suitable computational mesh a series of different meshes for the piston duct region alone (without the rest of the chamber) was created, and the influence of the various mesh densities on the key relevant spray parameters was investigated, [79]. The mesh density was varied by two means, by changing the number of cells in particular spatial directions, and by varying the mesh aspect ratio, Table 6.24. The initial and boundary conditions, injection rate specification and the measurement of the fuel vapour penetration for the Aachen pressure chamber operating point No. 1, §(6.3) were used for this mesh-density sensitivity study[9]. The same time step of $2.5\mu s$ was employed in these calculations.

Mesh No.	Directions					
	X		Y		Z	
	Number of cells	Aspect ratio	Number of cells	Aspect ratio	Number of cells	Aspect ratio
1	36	1.0	43	1.0	12	1.0
2	36	3.7	43	1.0	12	6.1
3	36	3.7	43	11.1	12	6.1
4	36	3.7	60	1.0	12	6.1

Table 6.24: Computational meshes of the piston duct region.

The predictions of the fuel vapour penetration and cumulative evaporation for the different meshes are presented in Figs. 6.76 and 6.77, respectively. It can be

[9]The assistance of B.Peters in preparing the numerical set-ups is gratefully acknowledged.

seen that the cumulative evaporation is not so sensitive on the mesh density as the penetration. The maximum difference between the predictions of evaporation is about 10%, and it occurs at the very beginning of injection during the first crank angle degree after the start of injection. From then on the differencies practically vanish.

In contrast to the prediction of evaporation, the fuel vapour penetration prediction shows a strong mesh-density dependency, Fig.6.76. The maximum difference observed between predictions of penetration is about $15mm$. It occurs between the coarsest and the finest meshes. The comparison with the measurements shows that the coarser meshes produce a bigger underprediction of penetration (this may be taken as a general rule). Further mesh refinement will not change penetration significantly. Therefore the duct mesh No. 4, given in Fig.6.78, is taken as the mesh for the piston canal region.

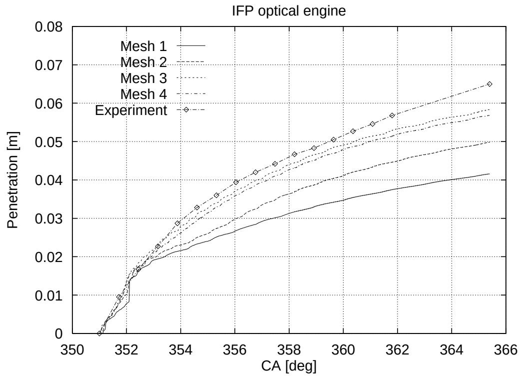

Figure 6.76: Effects of the mesh density on the fuel vapour penetration.

The complete computational mesh of the engine at the BTD and at the start of injection ($351.0\,^oCA$) is depicted in Figs.6.79 and 6.80. As can be noticed from these figures the number of cells in the mesh varies with time since the cell (layer) removal/addition feature is used; some details about this feature can be found in §(6.5.3). Also, a special adaptive mesh-movement feature was developed and used in the calculations, which, during the injection period, automatically adjusts the

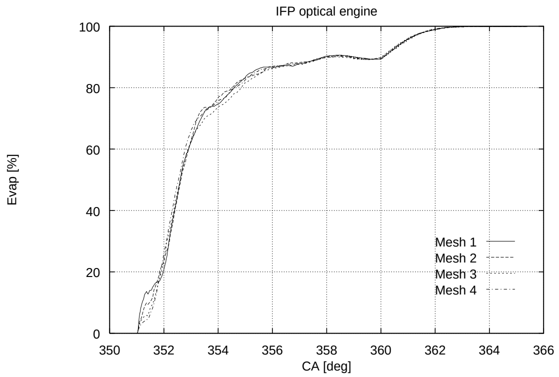

Figure 6.77: Effects of the mesh density on the cumulative evaporation.

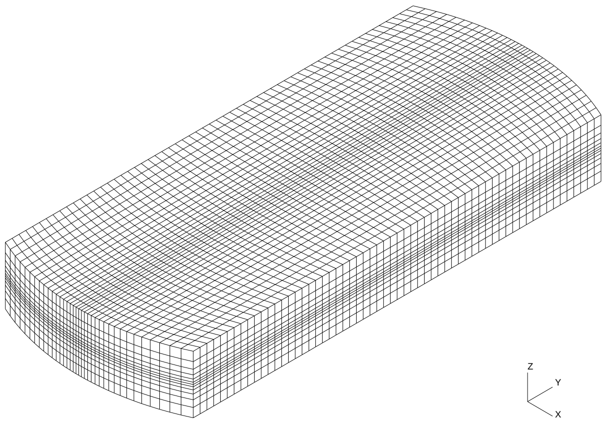

Figure 6.78: Computational mesh of the piston duct region (Mesh No. 4).

highest mesh density region of the duct to the injector location. This is done as a part of our efforts to find the causes of significant underprediction of the fuel vapour penetration, as will be reported in §(6.4.5).

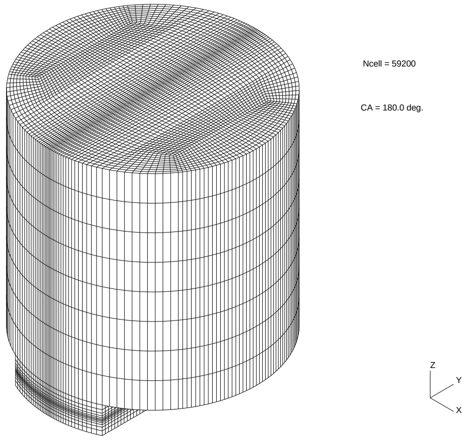

Figure 6.79: IFP optical engine; computational mesh at CA=180.0^o.

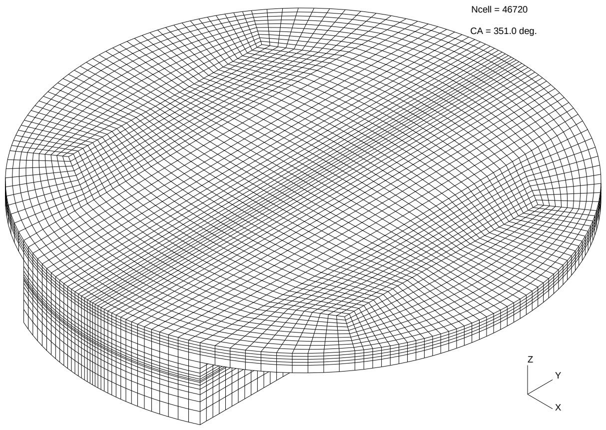

Figure 6.80: Computational mesh at the start of injection (CA=351.0^o).

6.4.4 Calculation parameters

The spray submodels/correlations listed in Table 6.25 are used in the numerical simulation. Both atomisation models (Huh and MPI) are employed to compare their predictions with the measurements.

The computational parameters used in the calculations are given in Table 6.26. In the calculation from the BDC up to the start of injection ('cold flow') a time step of 1.0^o CA (138.8μs) is used. From the start of injection two different time steps, 0.1^o (13.8μs) and 0.02^o (2.7μs) CA, are used to investigate their effects on spray predictions. The maximum number of correctors is 8 and it was sufficient to satisfy the overall convergence tolerance $\lambda_c = 10^{-2}$ (see §(5.3.2)).

Spray process	Submodel/correlation
Atomisation	Huh
Atomisation	MPI
contraction ratio	$C_c = 0.7$
spray angle	$\alpha_{max} = 6.5^o$
hole wall roughness	$k_r = 1.0\ \mu m$
Breakup	Reitz-Diwakar
Collision	O'Rourke
Momentum exchange	Yuen & Chen drag correlation
Impingement	Not included
Turbulence modulation	Not included

Table 6.25: Spray submodels/correlations used in the calculation.

Parameter	Value
Time step (cold flow), Δt	1.0^o CA
Time step (spray calc.), Δt	0.1 and 0.02^o CA
Parcel injection rate	$1.0 \cdot 10^6$ parcels/s
Convergence tolerance, λ_c	$1.0 \cdot 10^{-2}$
Max. number of correctors	8
Discretisation scheme	SFCD

Table 6.26: Calculation parameters.

6.4.5 Predictions and comparison with measurements

In the first part of this section the contour plots of the fuel vapour mass fraction and gas temperature, and the vector plots of gas velocity and views of spray are presented. Since there are no measurement data, the presented plots are used only to illustrate the distribution of these quantities. They are given for a one time step, at CA= 361.0^o, i.e. in the middle of the injection period.

Two sets of cutting planes are used to represent spatial distribution of the gas fields; three planes parallel to the piston crown (called here horizontal planes), and three planes parallel to the injection direction and cylinder axis (vertical planes). The distance between the planes is $2.5mm$ and the presented plots correspond to the calculation with the Huh's atomisation model.

The second part of the section deals with the global spray data and comparison with measurements. The predictions of both atomisation models and the comparison with the measurements are given. At the end, an explanation for the substantial underprediction of the fuel vapour penetration is proposed.

Gas fields and spray

This subsection shows plots of the gas fields and spray obtained with the Huh's atomisation model. Fig.6.81 depicts the fuel vapour mass fraction and gas temperature predictions in the three horizontal planes. It can be noticed that the contours of the fuel vapour mass fraction and temperature are topologically similar. This is because the region with the higher fuel vapour concentration corresponds to the region with a lower gas temperature due to the heat taken from the gas and used for the fuel vapourisation. The top plot in Fig.6.82 shows the gas velocities at the three horizontal planes. The maximum observed gas velocity is about $100m/s$. The characteristic air entrainment along the spray and formation of the toroidal vortex round the spray are clearly visible. The bottom plot in Fig.6.82 shows three views of the spray. The first presents parcel diameter distributions, the second parcel temperature, and the third (at the bottom of the figure) shows parcels scaled and coloured according to their droplet diameters.

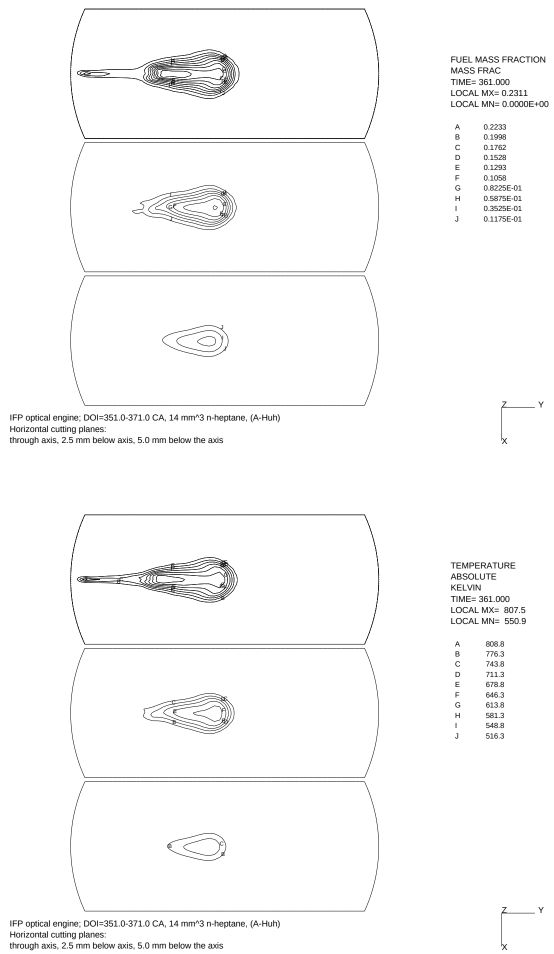

Figure 6.81: Contours of the fuel vapour mass fraction and gas temperature at CA=361.0^o in three cross-section planes parallel to the piston crown; Top, through the injector axis; middle, $2.5mm$ below the injector; bottom, $5mm$ below the injector.

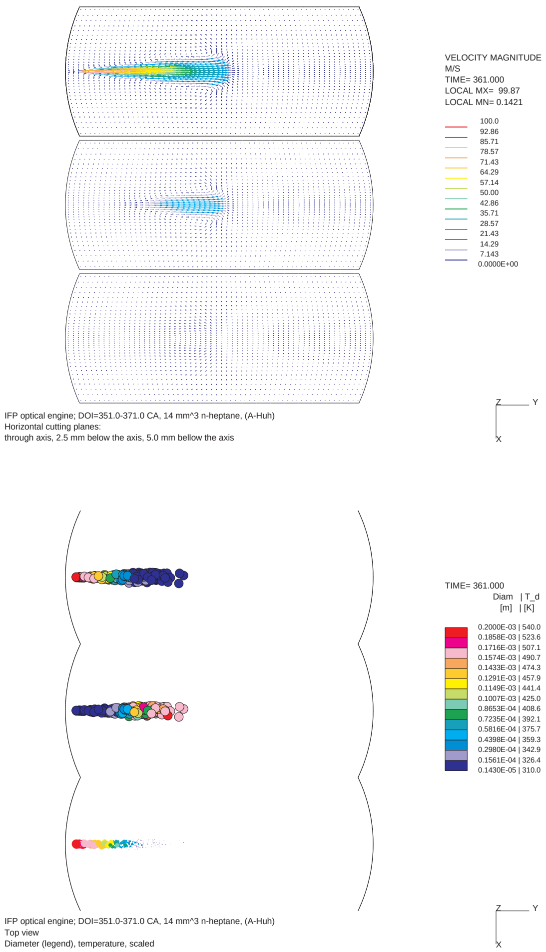

Figure 6.82: Top: gas velocity at CA=361.0^o in three cross-section planes parallel to the piston crown; through the injector axis, 2.5mm below the injector, 5mm below the injector. Bottom: view of spray; top, drop diameter distribution; middle, drop temperature distribution; bottom, scaled drop diameter.

The above plots show a high degree of symmetry with respect to the duct symmetry plane, since the geometry is symmetric and the gas initial and boundary conditions are uniform so the resulting gas fields, up to the start of injection, are symmetric too. However, the start of injection designates the beginning of asymmetry in the gas field properties due to the randomisation in the atomisation calculation, and due to the random walk technique adopted for the parcel trajectory calculation. Figs.6.83, and 6.84 show the same gas and spray properties as the previous figures, but in the vertical cross-section planes.

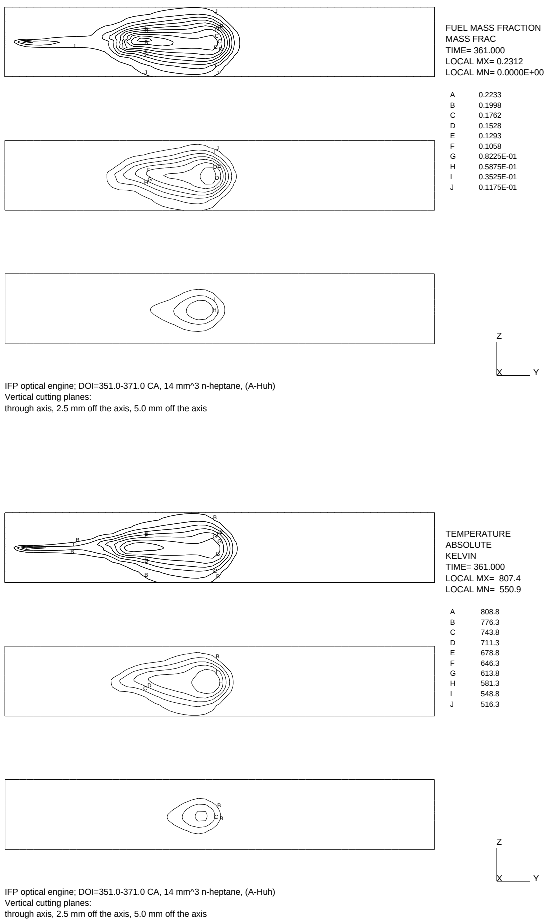

Figure 6.83: Contours of the fuel vapour mass fraction and temperature at CA=361.0^o in three cross-section planes parallel to the injector axis; Top, through the injector axis; middle, 2.5mm off the axis; bottom, 5mm off the axis.

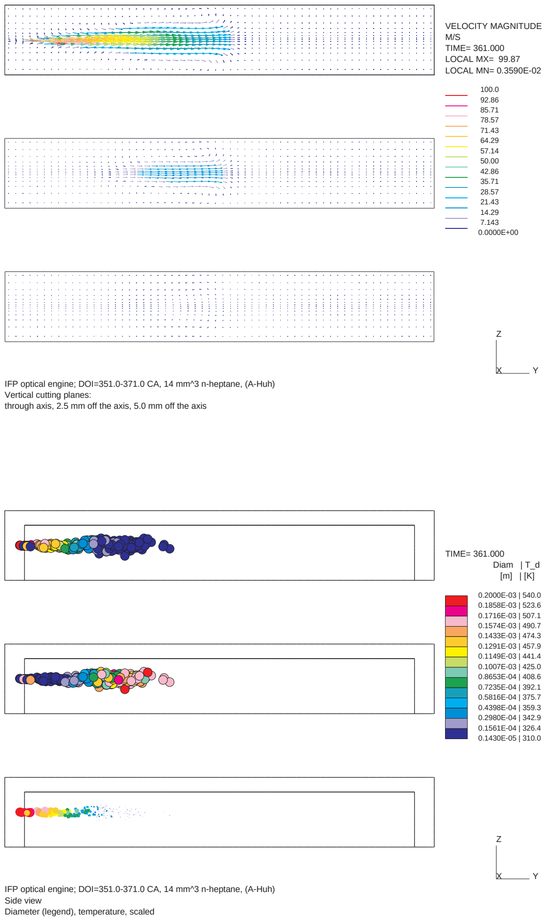

Figure 6.84: Top: gas velocity at CA=361.0^o in three cross-section planes parallel to the injector axis; through the injector axis, 2.5mm off the axis, 5mm off the axis. Bottom: view of spray; top, drop diameter distribution; middle, drop temperature distribution; bottom, scaled drop diameter.

Comparison with measurements

The comparison of spray penetration is given in Figs. 6.85 and 6.86. Fig. 6.85 depicts the effects of different time steps on the predictions obtained with the Huh atomisation model. It can be seen that both the time steps selected for the calculations produce almost the same fuel vapour penetration. The prediction of the liquid penetration shows little more sensitivity on the size of the time step.

The comparison of the Huh and the MPI results is shown in Fig. 6.86. As can be seen in the figure, both the atomisation models substantially underpredict the fuel vapour penetration. The maximum difference with respect to the measurement is about $15mm$, while the maximum difference between the MPI and Huh's predictions is about $5mm$. A similar underprediction in the fuel vapour penetration was obtained by the IFP group, [20], using the KIVA code. The proposed explanation for this large underprediction not experienced in other test cases, apart from the uncertainties about the fuel injection rate already mentioned in §(6.4.2), will be given in the following section. It is based on a supposition that the initial gas velocity field is not correctly assumed.

The prediction of the liquid penetration, taking into account its dependency on the definition, is reasonable. During injection, the maximum overprediction in the liquid penetration is about $5mm$, for both the atomisation models. The difference between predictions produced by the atomisation models is significant in the early stage of injection, in the period of 355-357 ^{o} CA, and after the end of injection. At the early stage, the Huh atomisation model gives larger liquid penetration than the MPI, because the former produces larger drop sizes than the latter, as evidenced in Fig.6.87.

Explanation for the fuel vapour underprediction

As was mentioned above, one of the proposed explanation for the large underprediction in the fuel vapour penetration is attributed to the lack of knowledge of the initial gas velocity field[10]. This can be corroborated by the better predictions

[10] An exhaustive study of various parameter changes and mesh refinement which did not significantly improve predictions can be found in [79].

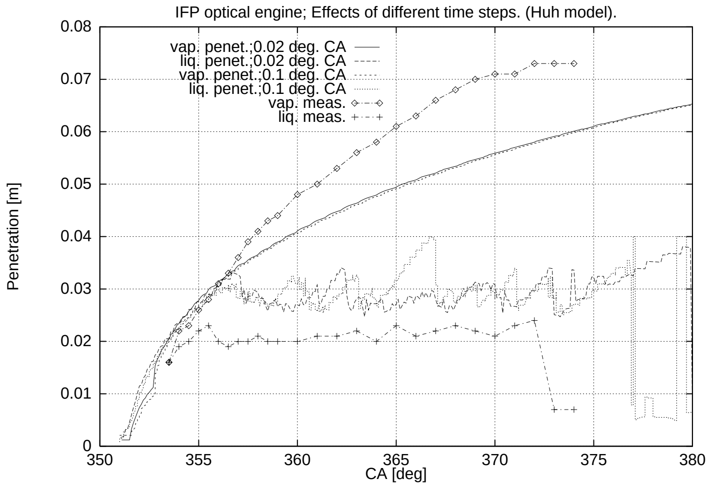

Figure 6.85: IFP optical engine; effects of different time steps on spray penetration; predictions obtained with the Huh atomisation model).

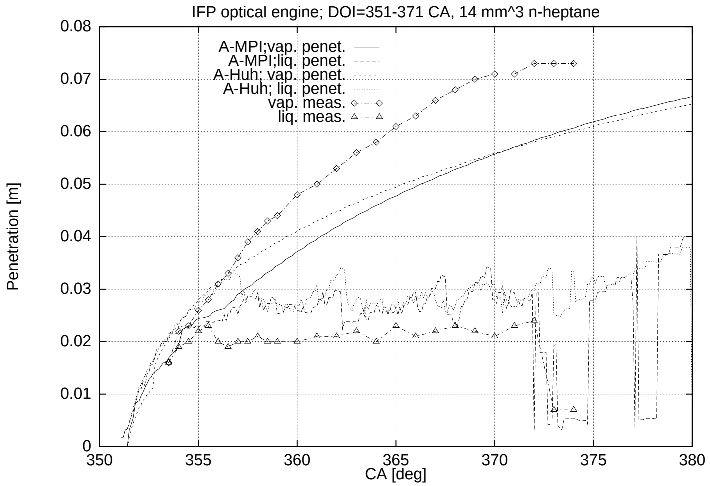

Figure 6.86: IFP optical engine; penetration comparison.

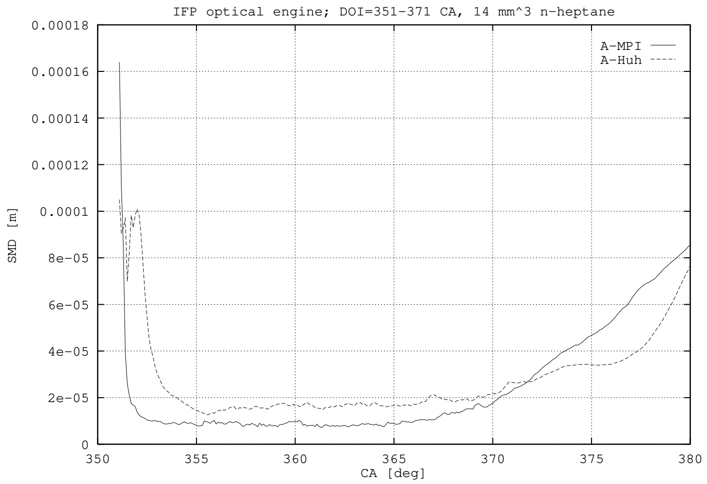

Figure 6.87: IFP optical engine; comparison of the Sauter mean diameter predictions.

obtained on the same computational duct mesh with the Aachen chamber set-up (Fig.6.76), and the evidence presented below from the gas velocity measurements. However, without further measurements, the explanation is not conclusive.

The gas velocity was measured by a single component LDV technique in the forward scatter mode at three locations along the injection direction; see Fig.6.72. During these measurements the engine was operated in the motored regime without spray injection since the injector hole was used for laser access, [21]. Only the gas velocity component perpendicular to the cylinder axis and injection direction (radial component) was measured. The time variation of the gas mean radial velocity, calculated by ensemble-averaging 200 cycle measurements, is shown in Fig.6.88, [21].

Although it is impossible to reconstruct the flow field in the cylinder from velocity measurements at only three different spatial locations, the data in Fig.6.88 can be used in such a way to give a rough pattern of gas flow, as shown in Fig.6.89. The plots presented in Fig.6.89 are obtained by drawing the measured radial velocity

components at the site of their measurement at four characteristic time steps. From

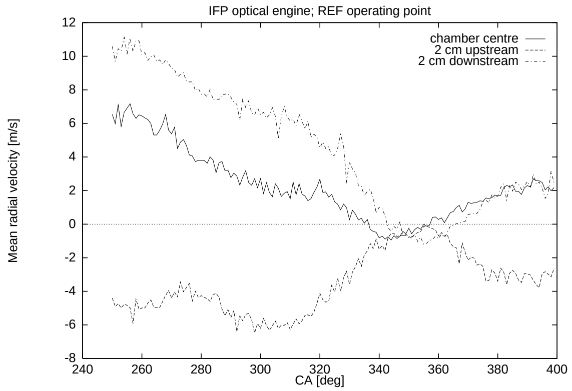

Figure 6.88: IFP optical engine; measurement of the mean radial gas velocity component at three locations in the duct.

this figure, the presence of a significant swirl flow is suggested in the first two time steps, at 260 and 300^o CA, with the swirl centre pushed off the cylinder axis towards the injector. The swirl is probably induced during the induction stroke by the intake valve flow (the engine has single shrouded intake valves [23]). As the piston approaches the TDC, the swirl is being rapidly destroyed; see Fig.6.88 and Fig.6.89, at CA = 340.0^o and 380.0^o when the radial gas velocity is of the order of $1m/s$. This swirl destruction can be explained by the unusual piston shape, with no piston bowl suitable to sustain the rotating gas motion. The fact that there is a swirl motion means that the gas must have velocity component parallel to the injection direction (axial component), which affects spray development, and the convective transport of the gas quantities. It can be roughly estimated that the average axial gas velocity of about 3.6m/s to transport fuel vapour, is sufficient to compensate 15mm of the penetration underprediction over a period of 30^o CA ($u_a = 0.015 * (6 * rpm)/30$).

Additional support to the proposed explanation is the series of spray photographs in [21] showing the spray pushed slightly off the duct axis in the swirl direction. However, only measurements of the gas axial velocity can confirm the hypothesis.

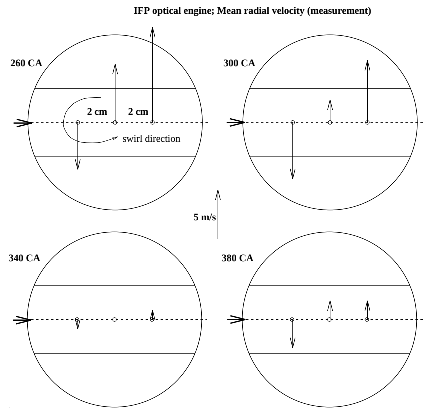

Figure 6.89: Radial gas velocity component vs. time.

6.5 VW Engine

6.5.1 Description

The Volkswagen four-cylinder DI 1.9 l engine is a modified version of the standard VW research engine which allows detailed experimental investigation of the in-cylinder flow, spray development, auto-ignition and combustion processes. To enable optical access to the cylinder chamber, the original omega shape bottom region of the bowl-in-piston chamber is modified to a transparent flat one. This modification does not affect the compression ratio of the engine, [94]. The injection system consists of a distributor pump and a five-hole injector, positioned slightly off the bowl centre. A sketch of the cylinder with the transparent piston is shown in Fig.6.90.

Measurements on this engine were made by several research groups involved in the IDEA project, namely those at the Volkswagen AG, Wolfsburg, Imperial College (IC), London and Lerstul für Angewandte Thermodynamik (LAT), Aachen. Their measurements are reported in [94], [95] and [96] (VW), [12] (IC), and [186] (LAT). Among several operating points, one denoted as EOP1a comprises the most complete data set for the spray aspects, thus this operating point is chosen for the numerical simulation.

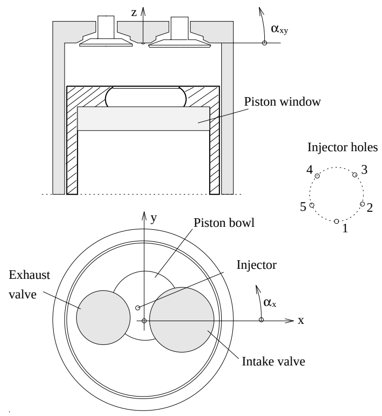

Figure 6.90: Schematic drawing of the VW transparent engine.

6.5.2 Initial and boundary conditions

The general engine data are given in Table 6.27, [94], and the locations of the injector holes and injection directions are given in Table 6.28, [196]. The data for the EOP1a operating point and initial and boundary conditions used in the calculation are given in Tables 6.29, 6.30 and 6.31; see [79].

Injector			Engine		
d_{inj}	0.2	mm	Compression ratio	19.0	
L	0.8	mm	Bore	79.5	mm
c_d	$0.65-0.75$		Stroke	95.5	mm
			Connecting rod	144.0	mm
			IV diameter	36.0	mm
			OV diameter	31.5	mm

Table 6.27: VW engine data.

Injector No.	x [mm]	y [mm]	z [mm]	α_{xy} [^{o}]	α_x [^{o}]
1	-1.90	6.38	-2.35	-14.0	270.0
2	-0.458	7.40	-2.54	-14.6	339.0
3	-0.901	9.04	-2.98	-15.8	52.0
4	-2.90	9.04	-2.98	-15.8	128.0
5	-3.34	7.40	-2.54	-14.6	201.0

Table 6.28: Injector hole locations and injection directions; see Fig.6.90.

Valve curtain

In the absence of experimental data for the velocity at the valve curtains and valve discharge coefficients for the EOP1a operating point, the valve velocity profiles and valve discharge coefficients measured for the same cylinder head under stationary

VW; EOP1a		
Speed	2000	rpm
Charge	*air*	
t_{SOI}	358.2	CA
t_{EOI}	365.4	CA
Fuel	n-dodecane	
Inj. quantity	8.0	mg
T_{inj}	373.0	K

Table 6.29: VW engine; operating point EOP1a.

flow conditions are used, [13]. The valve lift diagram and valve discharge coefficient are shown in Figs. 6.91 and 6.92, taken from [13] and [197].

The radial, axial and azimuthal (swirl) components of the gas velocity, in a local coordinate system centered on the inlet valve axis, Fig. 6.93, at the inlet valve curtain were measured at six circumferential sites, A, B, C, D, E and F, and along the valve axial direction $\overline{z}$, for three valve lifts. The normalised gas radial velocity, normalised by the maximum radial velocity at the corresponding circumferential section, and the velocity direction, characterised by two angles, one measured from the radial direction (α_v) and another measured from the valve axis (β_v), for six time steps, are given in Figs. 6.94, 6.95 and 6.96. As can be seen from these figures, the radial velocity has a plug profile for smaller valve lifts (correspond to crank angles: -26.0, 25.0, 184.0 and 250.0 ^{o}). For larger valve openings (corresponding to the crank angles 50.0 and 162.0 ^{o}) the axial variation of the radial velocity is taken into account. The normalised radial velocity and angles α_v and β_v are linearly interpolated in the axial and azimuthal directions; also their values at the intermediate times are linearly interpolated, [193].

The velocity profile at the outlet valve curtain is taken to be uniform with a zero azimuthal angle β_v and with the axial angle α_v set to 45^o.

The turbulence parameters of flow at the valve curtains, i.e a turbulence kinetic energy, k_v and its dissipation, ϵ_v, are evaluated according to Begleris, [24] and

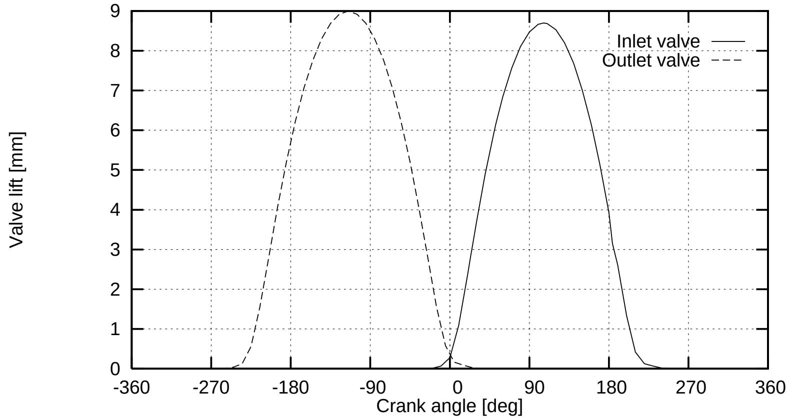

Figure 6.91: VW engine; valve lifts vs. time.

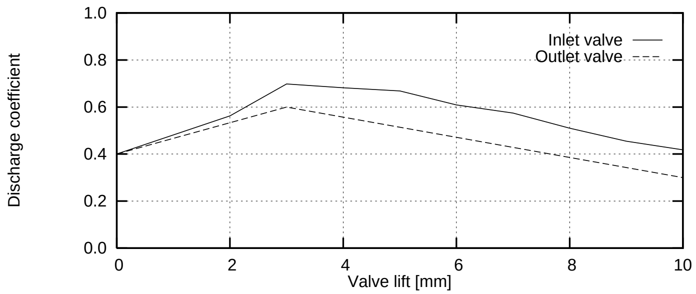

Figure 6.92: VW engine; valve discharge coefficients.

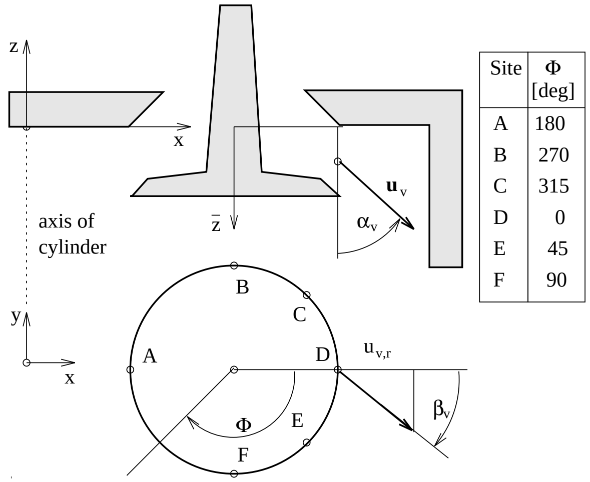

Figure 6.93: Valve local coordinate system and measurement sites; $\bar{z}$- axial direction (normalised by the current valve lift), α_v- axial flow angle, measured from the valve axis, β_v- azimuthal (swirl) angle, measured from the radial direction. (Note the location of the global coordinate system in this figure and in Fig. 6.90.)

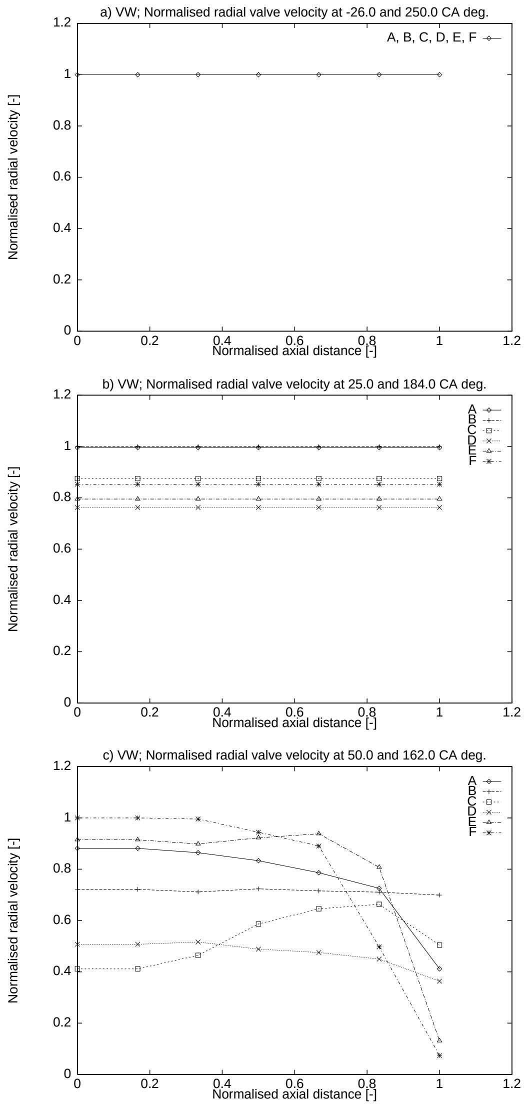

Figure 6.94: Inlet valve; normalised radial velocity profiles at: a) CA = -26.0 and 250.0 deg., b) CA = 25.0 and 184.0 deg., c) CA = 50.0 and 162.0 deg.

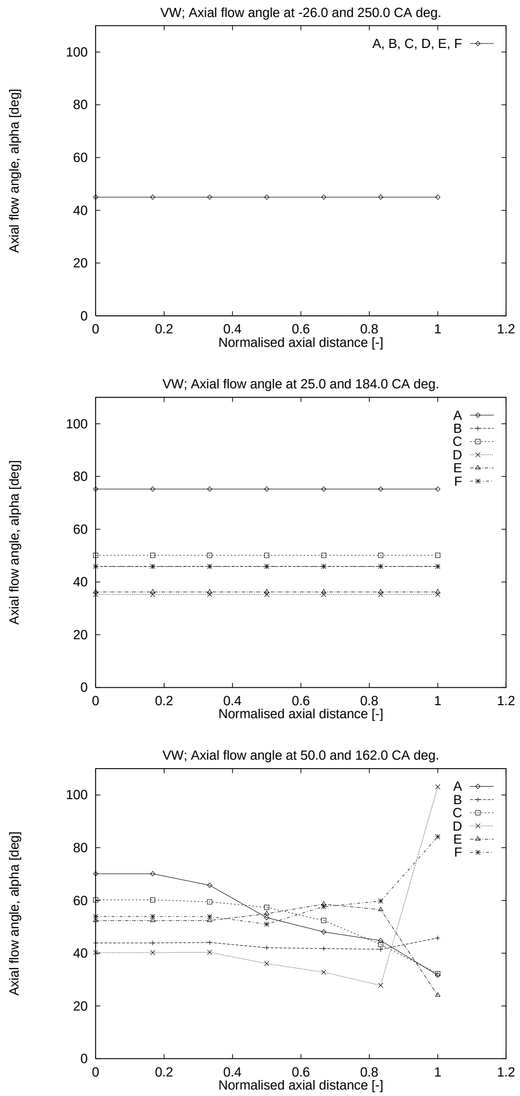

Figure 6.95: Inlet valve; axial flow angle at: a) CA = -26.0 and 250.0 deg., b) CA = 25.0 and 184.0 deg., c) CA = 50.0 and 162.0 deg.

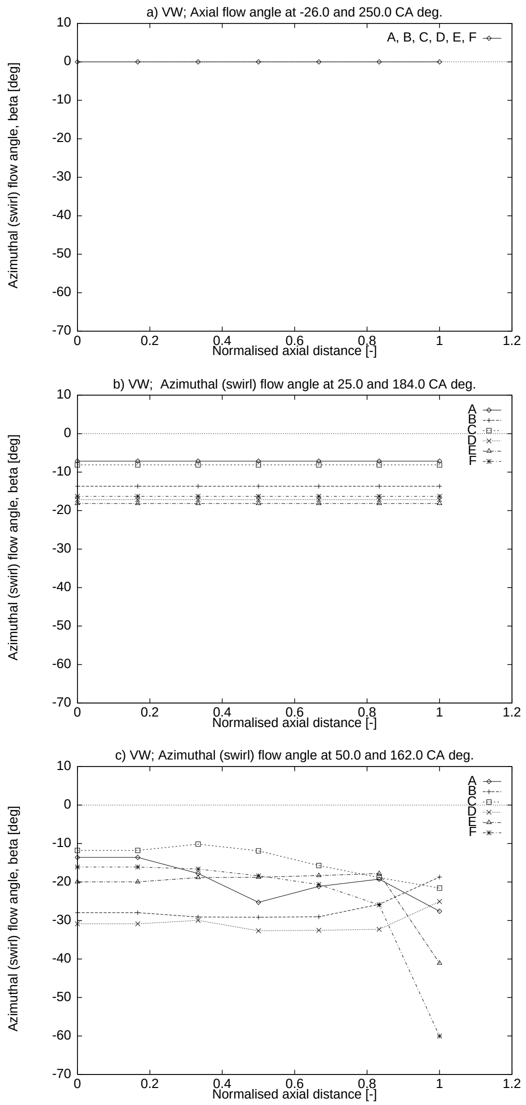

Figure 6.96: Inlet valve; azimuthal (swirl) flow angle at: a) CA = -26.0 and 250.0 deg., b) CA = 25.0 and 184.0 deg., c) CA = 50.0 and 162.0 deg.

Ahmadi-Befrui [6] as:

$$k_v = K_v^k \, u_{v,r}^2$$
$$\epsilon_v = C_\mu^{3/4} \, \frac{k_v^{3/2}}{l_v}$$

where $u_{v,r}$ is the average radial gas velocity at the valve curtain ($u_{v,r} = \dot{Q}_v / S_v$; $\dot{Q}_v$ and S_v are the volumetric flow rate through the valve curtain and the valve curtain cross-section area, respectively), L_v is the valve lift, Fig. 6.91, and l_v is a characteristic turbulence length scale given by:

$$l_v = K_v^\epsilon \, L_v$$

Coefficients K_v^k and K_v^ϵ are assumed to be constant and in the absence of the measured data, the values taken from [6] are used in the calculations, Table 6.30. It is worth mentioning that the in-cylinder level of turbulence is rather insensitive to these boundary conditions, since most of the turbulence production takes place in the cylinder due to the piston motion; see [6].

Property	Inlet port	Outlet port
Pressure, $[bar]$	0.833	1.167
Temperature, $[K]$	291	340
Turbulence kinetic energy coefficient K_v^k	0.01	0.01
Turbulence dissipation coefficient K_v^ϵ	0.045	0.045

Table 6.30: VW engine; conditions at the inlet and outlet valve ports.

Wall temperatures

The chamber wall temperatures were not measured. They are specified according to experience and directions given by the VW, [198], and their values can be found in Table 6.31. It is taken that the temperature is uniformly distributed over each of the chamber walls.

Wall	Temperature $[K]$
Cylinder head	350
Cylinder liner	360
Piston crown	390
Piston bowl	400
Head of inlet valve	340
Head of outlet valve	390

Table 6.31: VW engine; wall temperatures.

Injection rate

The fuel injection rate history was provided by the VW, [95] and [196]. For the purpose of numerical calculation, this measured injection rate is approximated by a set of straight lines labelled 'linear', shown in Fig.6.97. Calculations with this injection rate produced small, dubious, injection velocities of less than $50 m/s$ at the beginning and at the end of injection period, due to the small $d\dot{Q}/dt$ in these region, a behaviour not found in other injection rate data. Usually, $\dot{Q}$-curves are very steep at the start and at the end of injection, see for example Figs.6.7 and 6.75, and [5]. Moreover, the spray measurements indirectly suggest that the initial injection velocity is higher than that suggested by the $\dot{Q}$-curve b, as can be revealed from the spray- and cycle-averaged spray tip velocity for the EOP1a, [96]. The spray tip velocity is calculated from photographs of spray development taken by laser-sheet high-speed photography, and at $0.24\,^o$ CA ($20 \mu s$) after start of injection it has a value of about 90 m/s. Note that this velocity is always lower than the injection velocity due to spray retardation caused by the ambient gas.

In order to have a plausible injection velocity, which in diesel sprays should be in a range of 100-300 m/s, [108] and [100], an alternative injection rate history shown in Fig.6.97 as a line a 'histogram' is proposed. It is calculated in such a way that the injection period is split into four characteristic intervals, and the constant injection rate in each of these intervals is calculated based on the conservation of the fuel mass injected in the intervals. This assures that the total injection mass is equal to

the original one. The effects of these two injection rate specifications on the spray behaviour will be briefly discussed in §(6.5.5).

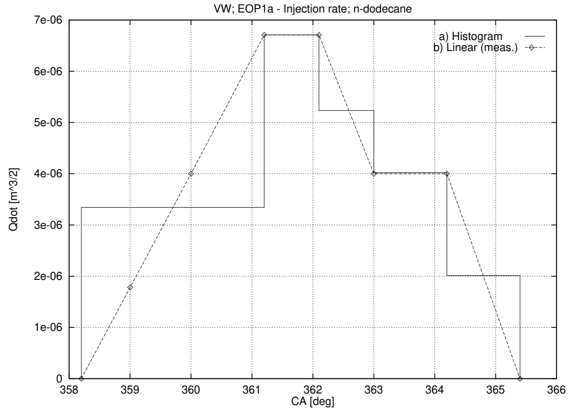

Figure 6.97: VW engine; injection rate per injector hole vs. CA.

6.5.3 Computational mesh

The computational meshes at a bottom and top dead centre, are shown in Fig.6.98. Together with the view of the mesh, cross-sections through the cylinder axis are also depicted in the figure to emphasize the valve curtain locations and piston-bowl shape. The original research engine has a glow plug in the direction of nozzle hole No. 3, which is not modelled in the computational mesh because the glow plug during compression protrudes into the piston bowl, i.e. into the cells in the bowl. This phenomenon is not allowed in the present version of the code.

As the chamber shape changes with the piston and valve motions, cells between the piston crown and cylinder head and/or valve heads become distorted. If the cell distortion becomes extreme, in the case of highly squashed cells during compression/exhaust stroke or highly elongated cells during expansion/induction stroke for instance, the convergence of numerical solution may be slowed down or even impossible; see [204]. On the other hand, during the compression/exhaust stroke the spatial resolution of the mesh squish region in the direction of cylinder axis becomes, needlessly, much more finer than in the other parts of mesh or than in the mesh when the piston is at the BDC. Thus, the removal of these cells will not corrupt the previously accepted spatial resolution but, because of the less number of cells in the domain and devoid of highly distorted cells, the removal of cells may enhance convergence and save the computational time. An opposite action, i.e. the addition of cells is needed or desirable during the expansion/exhaust stroke; this, however, increases the computational effort.

Because of the both above reasons, a cell removal/addition feature, developed by Adamson [193] was used in this calculation. The removal and addition of cells take place if the cell distortion, defined as a ratio of the longest cell dimension to its shortest one, is greater than a user-specified value. The cell removal or addition includes all the cell in the concerned layer. The result of the action is that the number of cells in the mesh varies with time, as can be seen in Fig.6.98. At BDC, the number is 11768, and at the TDC, 4164. During the removal/addition action all the extensive gas properties are conserved.

Inspection of the computational mesh shows that the mesh density does not comply with the recommendations for the spray simulation; see [27] and [200], and §§(6.3.2) and (6.4.3). During injection, in the near-injector region the dimensions of cells vary from 3 to 5 mm in the injection directions, and from 0.5 to 2 mm radially. (The characteristic cell length based on the cell volume, $V_{cell}^{1/3}$, is in the range of 1-3 mm). Since it was beyond affordable time and computational resources, the present mesh was used, knowing that the quality of spray predictions will be affected[11].

[11] The implementation of adaptive mesh refinement in such a complex geometry will be extremely useful. It will reduce the time-consuming task of mesh generation and improve the accuracy of predictions.

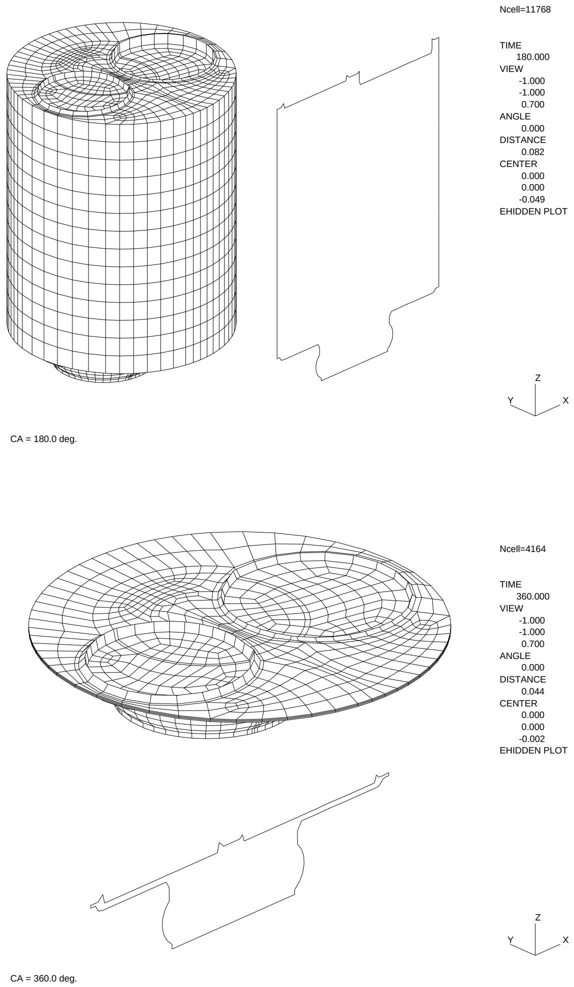

Figure 6.98: Computational mesh of the VW engine at 180^o and 360^o CA; view and cross section through the cylinder axis.

6.5.4 Calculation parameters

In the calculation of the EOP1a operating point, the spray submodels/correlations listed in Table 6.32, and calculation parameters given in Table 6.33 are used. Prior to the start of injection a time step of 1.0^o CA (83.3 μs) is employed; during injection and up to the end of calculation a smaller time step of 0.05^o CA (4.17 μs) is used.

The overall convergence tolerance, λ_c (see §(5.3.2)) is usually reached in less than 8 corrector steps, see Fig.6.99. At only few time steps the chosen maximum number of correctors (16) was insufficient to ensure demanded convergence criterion. In these cases the achieved residuals were already reduced to a level of about 10^{-3}, i.e. the convergence was almost satisfied so the calculation was not repeated.

Spray process	Submodel/correlation
Atomisation	MPI;
contraction ratio	C_c = 7.00E-01
spray angle	$\alpha_{max} = 7.0^o$
hole wall roughness	$k_r = 1.0\ \mu m$
Breakup	Reitz-Diwakar
Collision	O'Rourke
Momentum exchange	Yuen & Chen drag correlation
Impingement	MPI
Turbulence modulation	Not included

Table 6.32: Spray submodels/correlations used in the calculation.

6.5.5 Predictions and comparison with measurements

This section is divided into three parts. The first deals with the effects on spray behaviour of the different injection rate specifications, the second presents the evolutions of the gas fields and the spray, and the last shows comparisons with available measurements.

Parameter	Value
Time step (cold flow), Δt	1.0^o CA
Time step (spray calc.), Δt	0.05^o CA
Parcel injection rate	$6.0 \cdot 10^5$ parcels/s
Convergence tolerance, λ_c	$1.0 \cdot 10^{-3}$
Max. number of correctors	16
Discretisation scheme	SFCD

Table 6.33: Calculation parameters.

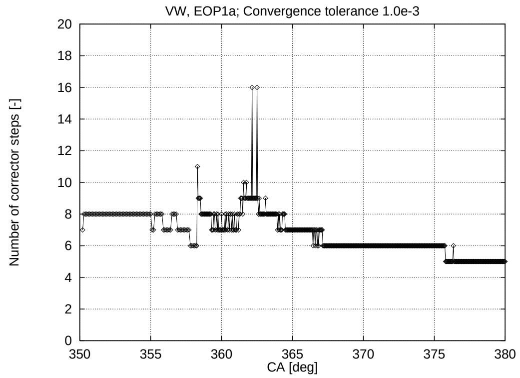

Figure 6.99: Number of corrector steps required to reach convergence vs. CA.

Effects of injection rates

The problem of injection rate specification mentioned in §(6.5.2) is investigated here and the outcomes are briefly described. Comparison between spray predictions obtained with both injection specifications a and b, Fig.6.97, shows significant differences. The results discussed are for spray No. 1, Fig.6.90. The other sprays, since they all have the same injection rate and nozzle-hole geometry, are affected in the same manner.

A comparison of the leading droplet penetrations, measured from the injector hole location in the injection direction (see explanation in Fig.6.100), is depicted in Fig.6.101. The same figure shows the measured spray- and cycle-averaged vapour tip penetration[12], [96]. It can be seen that a curve a, i.e. the one obtained with the modified injection curve, is closer to the measured result. A maximum difference in penetration between the predictions obtained with the different injection specifications in the initial stage of injection is about 10 mm.

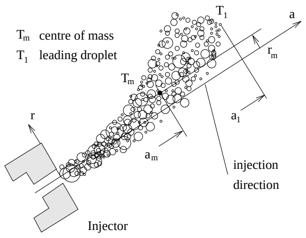

Figure 6.100: Local injector coordinates; the spray mass centre and leading droplet.

The small initial injection velocity produced by a injection curve b, Fig.6.97, is much lower than injection velocities typically encountered in diesel sprays, and therefore outside the range of injection velocities for which the atomisation models are developed, see §§(3.2.1) and (3.2.2). Some important consequences of this are

[12]These data were calculated from photographs obtained by a technique known as a laser-sheet high-speed photography, where the laser sheet was parallel to the piston crown; therefore the angle of spray injection direction with respect to the laser sheet (α_{xy}) has to be taken into account.

the decline of atomisation and drop secondary breakup, manifested by the order of magnitude bigger Sauter mean diameter, Fig.6.102, than the values obtained with injection curve a. The bigger droplets evaporate much more slowly, especially during the first crank angle degree of injection[13]; see curve b in Fig.6.103. These are the reasons why the injection specification a is used for the further spray calculations.

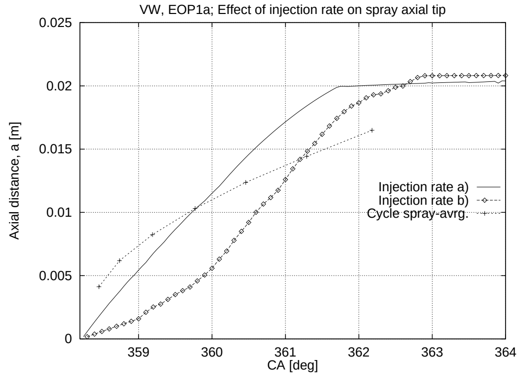

Figure 6.101: Effects of different injection rates on the leading droplet penetration. The curve denoted as 'Cyclic- and spray-avrg.' represents the cyclic- and spray-averaged spray penetration measured from photographs.

[13]Phenomena like this are very unlikely to occur in normal diesel conditions. They would necessarily lead excessively long ignition delay.

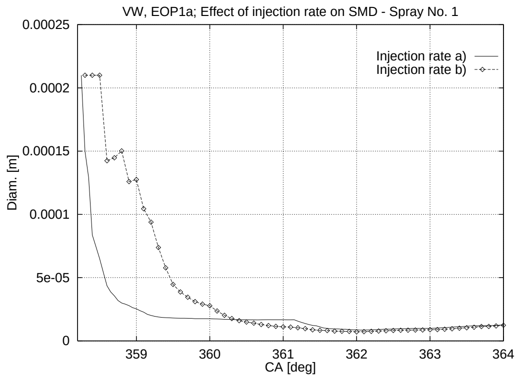

Figure 6.102: Effects of different injection rates on the spray Sauter mean diameter.

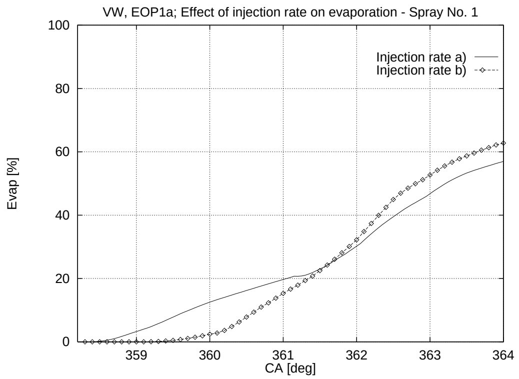

Figure 6.103: Effects of different injection rates on the spray evaporation.

Gas-spray evolution

In this section a series of plots showing development of gas flow and spray is presented. There are two sorts of plots; one shows spatial distribution of gas fields and spray, and another gives informations about global spray characteristics.

The gas fields are presented at the two cross-section planes; one parallel to the piston crown (called here a horizontal plane) and another parallel to the cylinder axis and passing through the axis of the injector hole No. 1 (a vertical plane). At the plots these planes are denoted by solid lines and accompanied by a corresponding label. The following three characteristic time steps are chosen; 8.5^o CA before the start of injection, 1.1^o CA after the end of injection, and at 380^o CA.

The gas velocity at the three time steps are given in Figs.6.104, 6.105 and 6.106. In Fig.6.104 the maximum gas velocities are in the squish region where the gas flows towards the piston bowl. A weak swirl flow can be noticed in the horizontal cross-section. At 1.1^o CA after the end of injection, Fig.6.105, five jet-like streams can be noticed in the horizontal plane, caused by the five sprays; the maximum gas velocity is about 50 m/s. As the piston moves downwards, gas from the piston bowl flows towards the squish region, Fig.6.106, in opposite direction than during compression stroke, Fig.6.104.

The fuel vapour mass fraction and gas temperature at two time steps are shown in Figs.6.107, 6.108, 6.109 and 6.110. The local extremes of these quantities are found close to the injection axes. This is particularly noticeable at the horizontal cross-sections in Figs.6.107 and 6.109. The patterns of the fuel vapour mass fraction and gas temperature contours at the corresponding time steps show a distinct similarity; compare Figs.6.107 and 6.109, and Figs.6.108 and 6.110. This is because in the regions with the higher fuel vapour mass fraction more heat is needed to evaporate the fuel, and this heat taken from the gas lowers its temperature.

Two different views on sprays at one time step (361.0^o CA) are shown in Fig.6.111, and the spray development vs. time is given in Fig.6.112. Since the sprays follow their injection directions, Fig.6.112, it can be concluded that the gas swirl velocity component is too weak to deflect them. As a measure of this deflection the local radial coordinate of the spray centre of mass, Fig.6.100, and its time

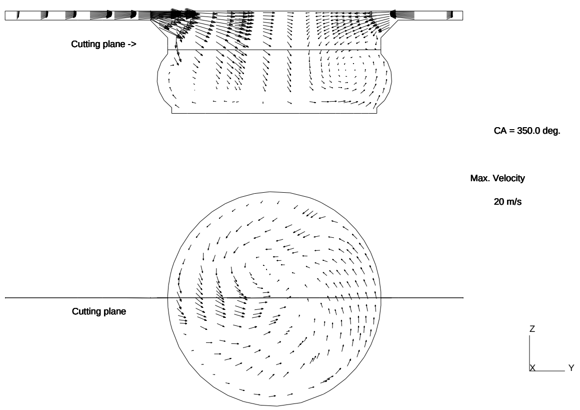

Figure 6.104: Gas velocity at 350.0^o CA.

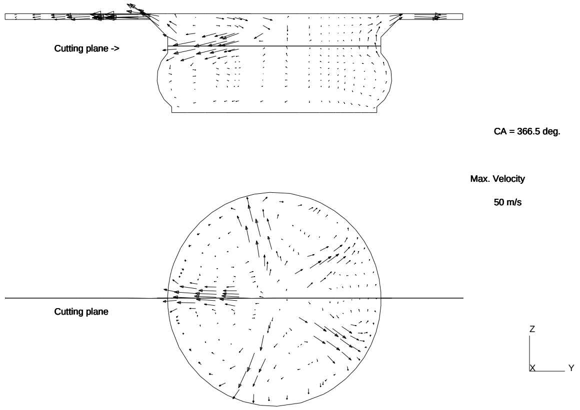

Figure 6.105: Gas velocity at 366.5^o CA.

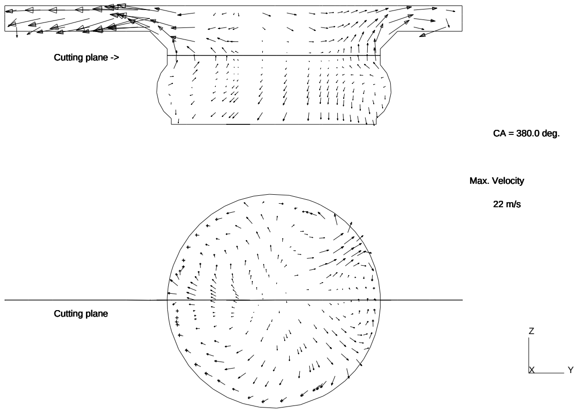

Figure 6.106: Gas velocity at 380.0^o CA.

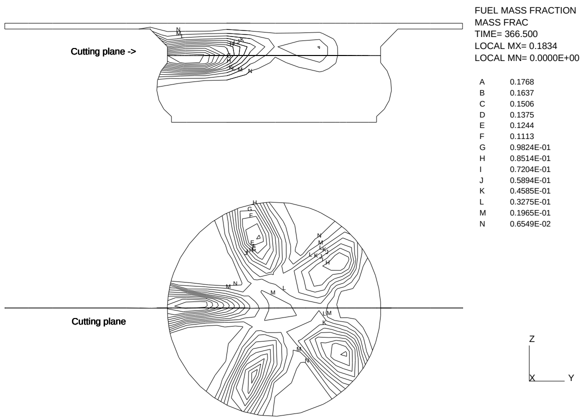

Figure 6.107: Fuel vapour mass fraction distribution at 366.5^o CA.

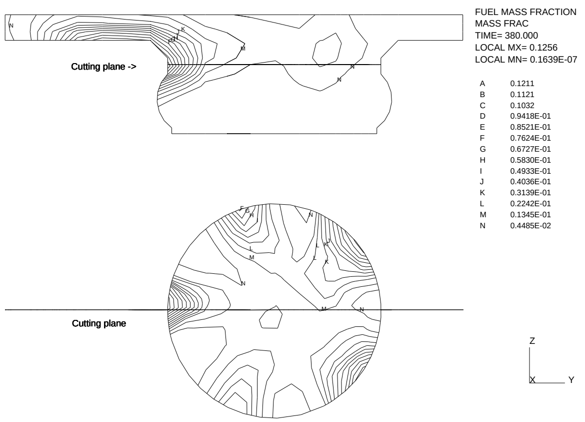

Figure 6.108: Fuel vapour mass fraction distribution at 380.0^o CA.

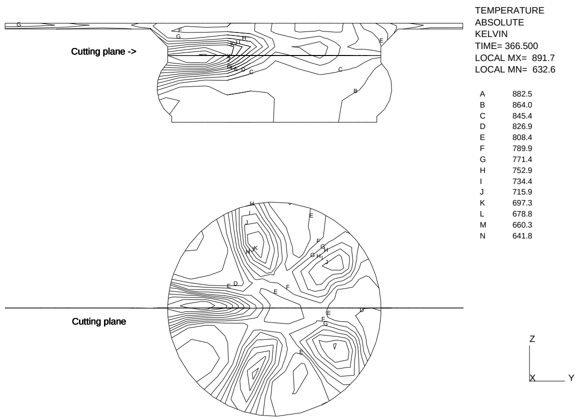

Figure 6.109: Gas temperature distribution at 366.5^o CA.

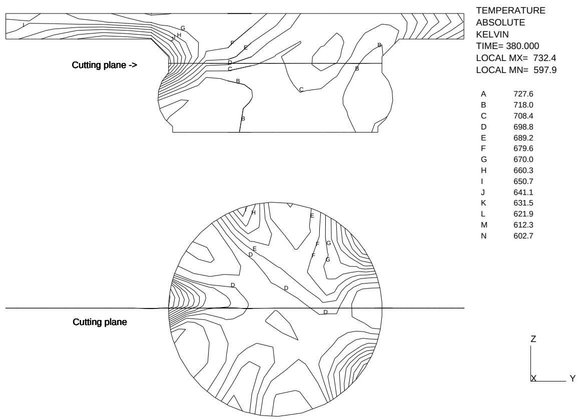

Figure 6.110: Gas temperature distribution at 380.0^o CA.

variation for each spray is given in Fig.6.114 may be examined. The plots of spray at 366.5 and 380.0^o CA, Fig.6.112, reveal that the sprays hit a wall of the piston bowl. As a result of this, some new droplets are created due to splashing, which can be seen as an increase in the number of computational parcels after the injection is finished, Fig.6.113.

The cumulative evaporation, spray Sauter mean diameter and the axial distance of the spray centre of mass from the injector, for each spray, are shown in Figs.6.113 and 6.114. All the curves are very close to each other, apart from the curves representing spray No.1 in the plots of evaporation and axial spray centre distance. This can be attributed to the influence of the non-uniform mesh density in the near-injector region, which is the finest in the direction of the spray No.1.

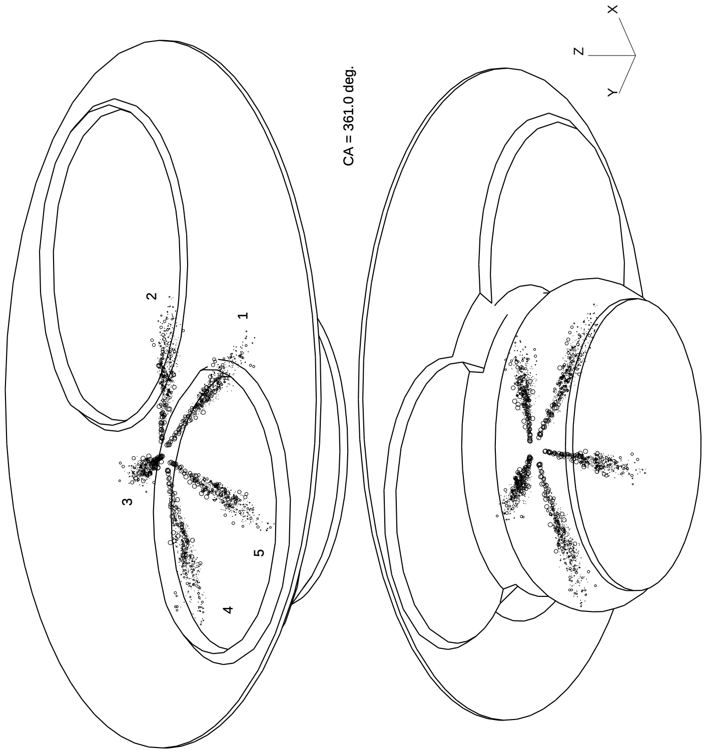

Figure 6.111: Perspective views on sprays at 361.0 ^{o} CA.

B

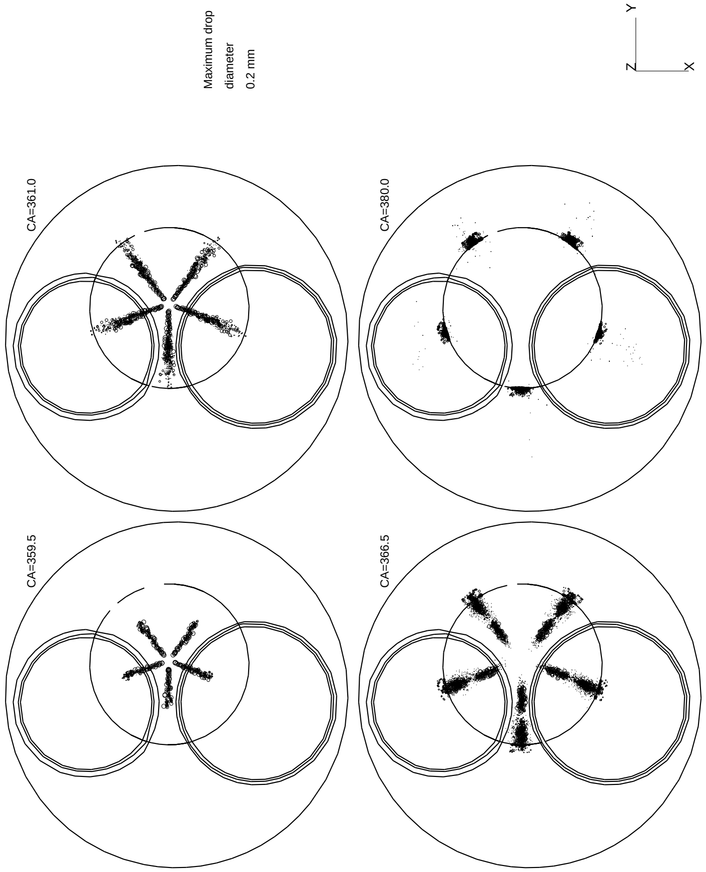

Figure 6.112: Spray development.

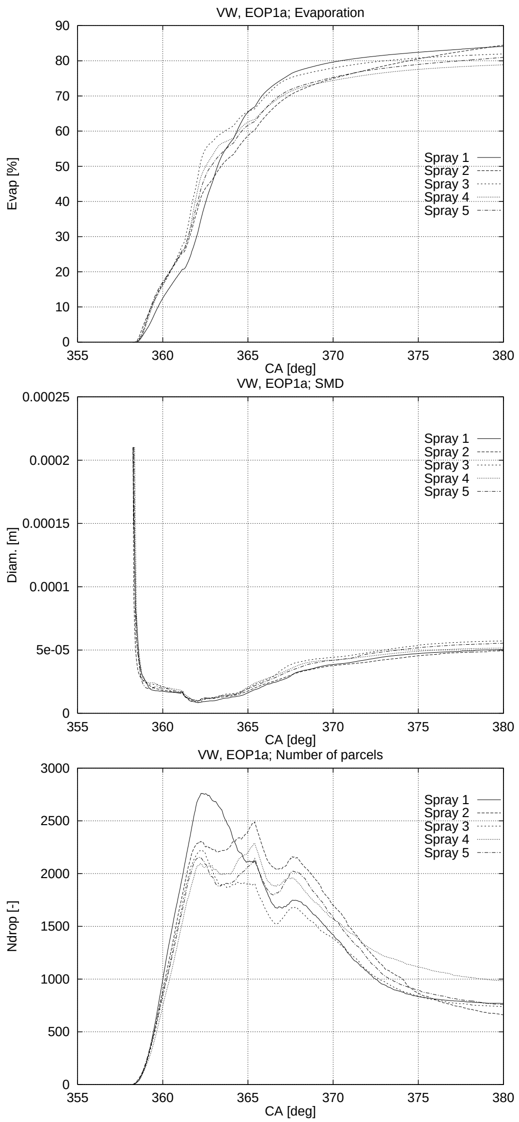

Figure 6.113: Spray evaporation, Sauter mean diameter, and number of parcels vs. time.

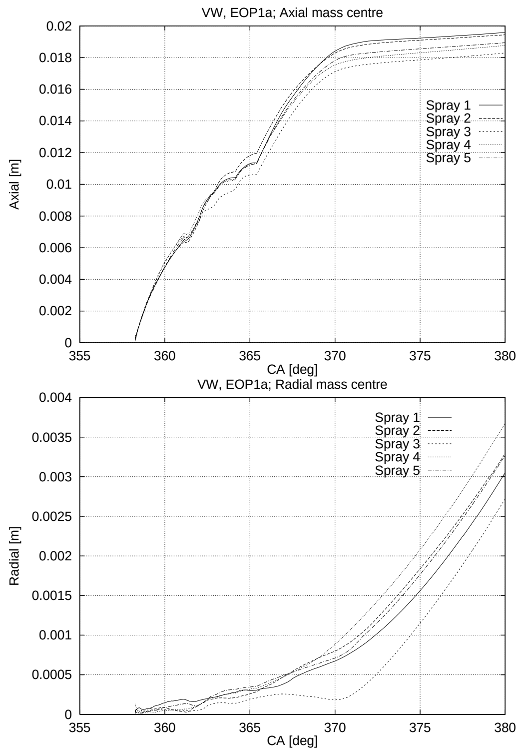

Figure 6.114: Local axial (a_m) and radial (r_m) coordinates of spray centre of mass vs. time; see Fig.6.100.

Comparison with measurements

In Fig.6.115 a comparison of the cylinder pressure prediction with the measurements is presented. As can be seen from the figure, there is a big discrepancy between three measurements with a maximum difference of about 15 *bar*. The prediction falls between the two closer measurements, between which the maximum pressure difference is less than 5 *bar*, and as a such can be assessed as acceptable[14]. More details about the problem of the large difference between pressure measurements and its consequences on the computational simulation ca be found in [79].

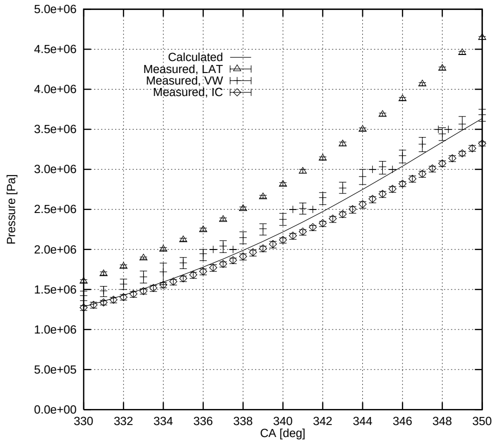

Figure 6.115: Pressure in the cylinder; comparison with the measurements.

The fact that the average measured ignition delay was 6.7^o CA (364.9^o CA), [95], allows us to use the spray measurements for comparison. In [95] the spray tip penetration for the five sprays are evaluated as an ensemble average over 61 cycles from the photographs made by the high-speed laser shadophotography. The comparison of the spray penetration is given in Figs.6.116 and 6.117. It can be

[14]The measurements were accomplished at the Lehrstul für Angewandte Thermodynamik, Aachen, Volkswagen AG, Wolfsburg and Imperial College, London. A full investigation of the pressure measurement problem was done by B.N. Adamson and his contribution and assistance are gratefully acknowledged.

seen that the calculated penetrations are well within the range of the considerably scattered measurements.

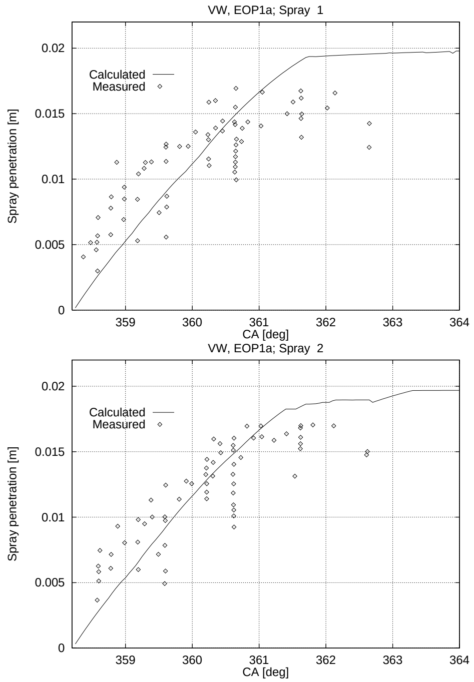

Figure 6.116: Comparison of the spray penetration based on the leading droplet criterion.

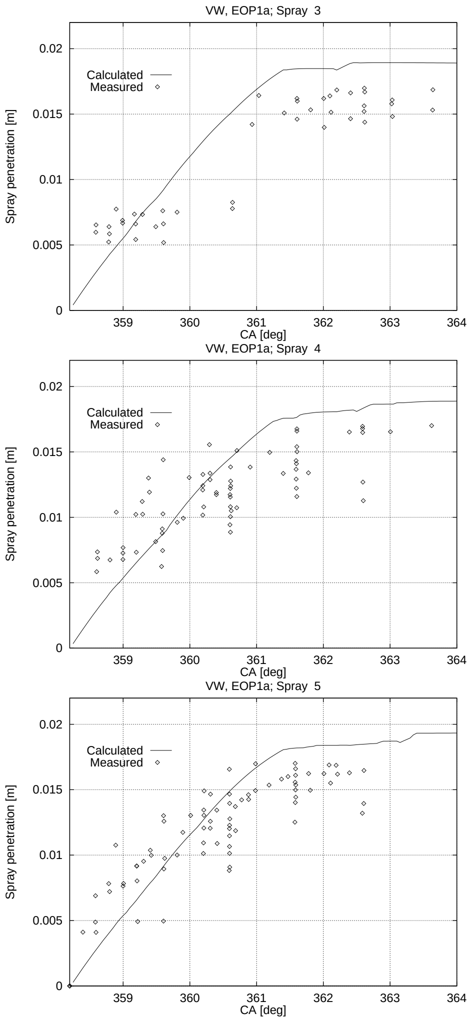

Figure 6.117: Comparison of the spray penetration based on the leading droplet criterion.

6.6 Closure

In this chapter the results of the sensitivity and validation studies have been presented. Three different sets of measurements have been used for comparison, namely, the measurements on the Aachen pressure chamber and two direct injection experimental diesel engines, the IFP and VW engines. The closure will summarize the main findings.

The results of the Aachen pressure chamber has been given in §(6). The influence of the mesh density on the predictions has been investigated in §(6.3.2). The effects of different correlations for the drop drag coefficient, and the effects of the two breakup submodels and turbulence modulation on the gas-spray behaviour have been presented in §(6.3.3). Among all these combinations one labelled as Variant 1 shows the best agreement with the measurements.

It was found that the mesh density strongly affects spray penetration; in general, the spray penetration on coarse meshes is smaller than on the fine. The two correlations for the drop drag coefficient used in the study produce very small differences in the predictions of spray penetration, evaporation ratio and Sauter mean diameter. The two tested breakup models, Reitz-Diwakar and Pilch-Erdman, produce very different spray penetrations due to the big differences in the predicted sizes of droplets; the 'Pilch-Erdman' Sauter mean diameter is almost twice as big as that predicted by the Reitz-Diwakar model. The predictions of the latter agree better with the measurements. The inclusion of turbulence modulation in the mathematical model reduces the turbulence viscosity and radial spreading of the spray, slightly increases the Sauter mean diameter and significantly enhances the penetrations. The predictions without turbulence modulation agree better with the measurements. The local gas velocity, fuel mass fraction and turbulence intensity are rather poorly predicted, especially near the injector.

The predictions of the two atomisation models have been given in §(6.3.4). The comparison with the measurements has been done for the spray penetration and for the fuel vapour mass fraction at several locations in the chamber; other spray properties which were not or cannot be measured, have been used in the sensitivity studies. The MPI predictions of the spray penetrations agree better with the measurements, while both the models overpredict the local fuel vapour mass fraction. Comparison of the models reveals that the MPI model predicts significantly smaller Sauter mean diameter than the Huh model. The spray semi-cone angle, which is the input parameter of the MPI model, slightly affects the spray predictions.

The same computational mesh used for the pressure chamber calculations, but with different initial and injection regimes, has been used to illustrate outcomes of the MPI spray-wall impingement model, §(6.3.5).

The results for the IFP engine have been presented in §(6.4). The influences of the mesh density on the gas-spray predictions have been investigated on four different computational meshes in §(6.4.3). The two atomisation models have been used in calculations, and their results have been compared with the measurements in §(6.4.5). Both models significantly underpredict the fuel vapour penetration. The reasons for this could not be identified, and a possible explanation has been offered.

Finally, in §(6.5) the results for the five-hole-injector VW engine have been given. The initial and boundary conditions and details related to the valve flow have been presented in §(6.5.2). The computations have been performed with the MPI atomisation model in two injection regimes, one obtained from measurements and other assumed. In §(6.5.5) the effects of the injection regimes on the spray predictions have been extensively analysed. At the end of the section various spray parameters for each of the five sprays, together with the penetration comparison with the measurements, have been presented. The obtained predictions of the spray tip penetration are well within the range of rather scattered measurements.

The following, and at the same time the last chapter, will deal with conclusions and suggestions for the future work.

Chapter 7

Conclusions and suggestions for future work

The previous chapter has demonstrated that the present multi-dimensional mathematical model and solution procedure, in combination with the experimental results, can offer valuable information, not only in the features of particular spray submodels considered in the study, but also in the gas-spray evolution in the experimental apparatus and diesel engines. In particular, it has exposed the significance of the computational parameters employed in simulations, as well as the importance of the initial and boundary conditions on the gas and spray sides on the quality of predictions.

This is the last chapter of the present study, and it is divided into two sections. The first summarises the conclusions acquired from this work and the second makes some suggestions for the future work.

7.1 Conclusions

The detailed results of the present study have been extensively assessed and discussed in the previous chapter. Therefore, the following items just summarise the most important conclusions.

- Two atomisation models compared in the present study produce similar predictions of spray penetration. The predictions of the fuel vapour penetration are in reasonably good agreement with the measurements in the Aachen pressure chamber. Both models overpredict the liquid core penetration, but allowing for the difficulty in its numerical interpretation, the results can be assessed as acceptable. The MPI model predicts sprays with significantly smaller droplets than the Huh model. This results in higher prediction of the spray evaporation rate than in the case of the Huh model.

The agreement between the predictions and measurements for the fuel vapour penetration in the case of the IFP engine is, however, disappointing. The cause of the disagreements could not be identified without doubts.

- The predictions of the local field quantities such as the fuel vapour mass fraction and gas velocity vs. time, particularly in the near-injector region, significantly disagree with measurements. In the early stage of injection both atomisation models tend to overpredict the local fuel vapour mass fraction. The gas velocity is underpredicted at the locations closer to the injector, while the predictions farther from it are somewhat better.

- The density of the computational meshes strongly affects spray predictions. On the coarser meshes the predictions of the fuel vapour and liquid core penetrations, as well as the spray evaporation are smaller than on the finer meshes, and when compared with measurements, the predictions show larger discrepancies. The predictions tend to be most sensitive to the mesh density in the direction normal to the spray axis.

- The two correlations tested for the droplet drag coefficient cause insignificant differences in spray predictions.

- The predictions of the Reitz-Diwakar and Pilch-Erdman breakup models show substantial differences. The latter model produces a spray with greater droplets, and the predictions of spray penetration disagree more with measurements than those predicted by the Reitz-Diwakar model.

- The model of the turbulence modulation does not cause as big discrepancies in the prediction of the mean droplet size and spray evaporation, as in the prediction of the vapour and liquid core penetrations. The turbulence intensity in the gas and the spray radial spreading predicted by the model are reduced. In terms of validation, the model devoid of the turbulence modulation contributions shows better agreement with measurements.

- The importance of having complete knowledge of initial and boundary conditions on gas-spray predictions is shown on the IFP experimental engine case, §(6.4). The substantial underprediction of the fuel vapour penetration, which after various parameters changes and mesh refinement did not essentially improve predictions, points to the inadequate specification of the gas initial and boundary conditions and uncertain fuel injection rate data as possible causes of the discrepancies.

- The knowledge and adequate specification of the fuel injection rates is found to be extremely important for good spray predictions, as shown in the VW engine case, §(6.5), where the calculations with the two different injection specifications produce very different spray penetration, droplet sizes and spray evaporation.

- The model of the spray-wall impingement is included in the overall gas-spray description. It recognises different regimes (splashing, fragmentation, and sticking on the wall) and does not allow for possible formation of a liquid film. The effects of roughness and curvature of the target surface, as well as heat transfer between the wall and the droplets are neglected.

7.2 Suggestions for future work

Before we proceed with the recommendations for the future work, the important role of measurements on diesel sprays in spray modelling and validation has to be emphasized. Since many of spray submodels to large extent rely on the accuracy and availability of these measurements, only more accurate and extensive experimental data will reduce the uncertainty of a number of coefficients in the spray model, and/or will give a new evidence in some of the spray processes. To achieve this aim, close collaboration between two groups of researchers, experimentalists and modellers, is of a paramount importance.

Since the author of the present study is far from being an expert in the experimental methods, the suggestions which follow are mainly directed towards researchers in the field of modelling and numerics. The tasks which are, arguably, of the most priority are as follows:

- Validate the accuracy of the present spray model, and combinations of its submodels, against a more complete experimental data for a far greater range of operating conditions. Attention should be paid to further improvement in modelling of nozzle flow and fuel atomisation, as the most important processes which determine the initial conditions of drops.

- To implement adaptive mesh refinement in the spray-affected region in the light of the strong dependency of spray predictions on the mesh density, and, in combustion calculations, to extend the refinement to the region of high field gradients. This will also simplify the time-consuming task of mesh generation, and will further exploit flexibility of the unstructured mesh environment, already used in this work.

- With respect to turbulence modelling, introduction of the Reynolds stress model should improve the accuracy of predictions of flow evolution in the cylinder, especially in terms of swirl motion which is crucial for spray predictions. (It is particularly important in the cases where the merged geometries of cylinders and manifolds are used in order to avoid specification of boundary conditions at the valve curtains, rarely known to the required details.) It will also solve the known disadvantage of k-ϵ model, the one of assumed isotropy of a turbulence length scales, and will offer a new approach to the random-walk technique employed in the droplet trajectory calculation in the present study.

- To further investigate other influences on the individual drop motion, primarily effects of non-spherical shape of droplet and presence of neighbouring droplets on the drop drag coefficient, and their implications on the spray predictions.

- The spray-impingement model should include formation of liquid films at walls, and must be subjected to extensive validation against a wide spectrum of measurements. These experimental data ought to include conditions encountered in real engines with respect to gas temperature and density, and wall conditions such as temperature, shape and roughness.

This study should be regarded as a step towards the simulation of all the processes in diesel engines, including combustion, and building up a comprehensive computational tool for their prediction. Its aim was to include and investigate effects of alternative spray models, and to assess the quality of predictions. In this respect, it is the hope of the author, that the study will be of benefit to modellers and experimentalists, and also to engine designers in their applications.

Appendix A

A.1 Density-weighted ensemble averaging

Any instantaneous field, $\hat{\phi}$, can be decomposed into the Reynolds mean, $\overline{\phi}$, defined by Eq.(2.9), and fluctuation, ϕ', as follows:

$$\hat{\phi} = \overline{\phi} + \phi' \tag{A.1}$$

According to the above definition, the following relations can be deduced:

$$\begin{aligned} \overline{\phi'} &= 0 \\ \overline{\hat{\phi}\hat{\psi}} &= \overline{\phi}\,\overline{\psi} + \overline{\phi'\psi'} \end{aligned} \tag{A.2}$$

where ψ denotes another fluctuating field variable.

The same field $\hat{\phi}$ can be resolved into the Favre mean, $\tilde{\phi}$, defined by Eq.(2.12), and corresponding fluctuation ϕ'', as:

$$\hat{\phi} = \tilde{\phi} + \phi'' \tag{A.3}$$

From the aforementioned definitions, the following useful relations can be derived:

$$\begin{aligned} \overline{\hat{\rho}\phi''} &= 0 \\ \overline{\hat{\rho}\hat{\phi}\hat{\psi}} &= \overline{\rho}\tilde{\phi}\tilde{\psi} + \overline{\hat{\rho}\phi''\psi''} \\ \tilde{\overline{\phi}} = \overline{\phi} \quad &, \quad \overline{\tilde{\phi}} = \tilde{\phi} \end{aligned} \tag{A.4}$$

Applying the above definitions, the following relations which link the Reynolds and Favre mean values can be obtained:

$$\begin{aligned} \overline{\phi} &= \tilde{\phi} - \frac{1}{\overline{\rho}}\overline{\rho'\,\phi'} \\ \tilde{\phi} &= \overline{\phi} - \overline{\phi''} \end{aligned} \tag{A.5}$$

A.2 Gas conservation equations

A.2.1 Mass conservation equation

The instantaneous mass conservation equation reads:

$$\frac{d}{dt}\int_V \hat{\rho}_m \hat{\vartheta}\, dV + \int_S d\mathcal{S}\cdot \hat{\rho}_m \hat{\mathbf{u}}_r \hat{\vartheta} = \int_V \hat{s}^d\, dV \tag{A.6}$$

Averaging the integrand of the particular terms of this equations gives:

- rate-of-change term:

$$\overline{\hat{\rho}_m \hat{\vartheta}} = \overline{\rho} \tag{A.7}$$

- convection term:

$$\begin{aligned} \overline{\hat{\rho}_m \hat{\mathbf{u}}_r \hat{\vartheta}} &= \overline{\hat{\rho}\,(\tilde{\mathbf{u}}_r + \mathbf{u}'')} \\ &= \overline{\rho}\,\tilde{\mathbf{u}}_r + \overline{\hat{\rho}\mathbf{u}''} \\ &= \overline{\rho}\,\tilde{\mathbf{u}}_r \end{aligned} \tag{A.8}$$

  because $\overline{\hat{\rho}\mathbf{u}''}$ is equal to zero according to Eq.(A.4).

- source term:

$$\overline{\hat{s}^d} = \overline{s}^d \tag{A.9}$$

Hence, the final form of the averaged equation reads:

$$\frac{d}{dt}\int_V \overline{\rho}\, dV + \int_S d\mathcal{S}\cdot \overline{\rho}\,\tilde{\mathbf{u}}_r = \int_V \overline{s}^d\, dV \tag{A.10}$$

A.2.2 Momentum conservation equation

The instantaneous momentum conservation equation reads:

$$\begin{aligned} \frac{d}{dt}\int_V \hat{\rho}_m \hat{\vartheta}\hat{\mathbf{u}}\, dV + \int_S d\mathcal{S}\cdot \hat{\rho}_m \hat{\vartheta}\hat{\mathbf{u}}_r\hat{\mathbf{u}} &= -\int_V \hat{\vartheta}\nabla\hat{p}\, dV + \\ &+ \int_S d\mathcal{S}\cdot\hat{\vartheta}\hat{\mathbf{T}}_m + \int_V \hat{\mathbf{s}}^d_{\mathbf{u}}\, dV \end{aligned} \tag{A.11}$$

where the instantaneous shear stress and rate-of-strain (deformation) tensors are given respectively by:

$$\hat{\mathbf{T}}_m = \hat{\rho}_m\,(\,2\,\nu_m\hat{\mathbf{D}} - \frac{2}{3}\,\nu_m\nabla\cdot\hat{\mathbf{u}}) \tag{A.12}$$

$$\hat{\mathbf{D}} = \frac{1}{2}[\nabla\hat{\mathbf{u}} + (\nabla\hat{\mathbf{u}})^T] \tag{A.13}$$

Note here that the molecular kinematic viscosity is assumed constant, i.e. its fluctuation is equal to zero.

The density-weighted average of the integrand of the each terms reads:

- rate-of-change term:

$$\begin{aligned} \overline{\hat{\rho}_m\hat{\vartheta}\hat{\mathbf{u}}} &= \overline{\hat{\rho}(\tilde{\mathbf{u}} + \mathbf{u}'')} \\ &= \overline{\rho}\,\tilde{\mathbf{u}} \end{aligned} \tag{A.14}$$

- convection term:

$$\begin{aligned} \overline{\hat{\rho}_m\hat{\vartheta}\hat{\mathbf{u}}_r\hat{\mathbf{u}}} &= \overline{\hat{\rho}(\tilde{\mathbf{u}}_r + \mathbf{u}''_r)(\tilde{\mathbf{u}} + \mathbf{u}'')} \\ &= \overline{\rho}\tilde{\mathbf{u}}_r\tilde{\mathbf{u}} + \overline{\hat{\rho}\mathbf{u}''\mathbf{u}''} \end{aligned} \tag{A.15}$$

  because $\overline{\hat{\rho}\mathbf{u}''_r\tilde{\mathbf{u}}} = 0$, and $\overline{\hat{\rho}\tilde{\mathbf{u}}_r\mathbf{u}''} = 0$ according to Eq.(A.4). The last term in Eq.(A.15) represents the Reynolds stress tensor, $\mathbf{T}_t$, .i.e. :

$$\mathbf{T}_t = -\overline{\hat{\rho}\mathbf{u}''\mathbf{u}''} \tag{A.16}$$

- 'pressure' term:

$$\begin{aligned} \overline{\hat{\vartheta}\nabla\hat{p}} &= \overline{(\overline{\vartheta} + \vartheta')\nabla(\overline{p} + p')} \\ &= \overline{\vartheta}\nabla\overline{p} + \overline{\vartheta'\nabla p'} \end{aligned} \tag{A.17}$$

Since it was decided, for want of a better practice, that all correlations with ϑ' will be neglected (see §(2.2.3) and §(2.2.6)), the last term in Eq.(A.17) becomes zero. Hence, the final expression reads:

$$\overline{\hat{\vartheta}\nabla\hat{p}} = \overline{\vartheta}\nabla\overline{p} \tag{A.18}$$

- molecular shear stress term:

$$\begin{aligned}\overline{\hat{\vartheta}\hat{\mathbf{T}}_m} &= \overline{\hat{\vartheta}\hat{\rho}_m\ (\ 2\nu_m\hat{\mathbf{D}} - \frac{2}{3}\nu_m\nabla\cdot\hat{\mathbf{u}}\ \mathbf{I}\ )} \\ &= \overline{\rho}\ (\ 2\ \nu_m\tilde{\mathbf{D}} - \frac{2}{3}\nu_m\nabla\cdot\tilde{\mathbf{u}}\ \mathbf{I}\ ) \\ &= \mathbf{T}_m \end{aligned} \tag{A.19}$$

where the deformation tensor, $\tilde{\mathbf{D}}$ is given by:

$$\tilde{\mathbf{D}} = \frac{1}{2}[\nabla\tilde{\mathbf{u}} + (\nabla\tilde{\mathbf{u}})^T] \tag{A.20}$$

- source term:

$$\overline{\hat{\mathbf{s}}^d_{\mathbf{u}}} = \overline{\mathbf{s}}^d_{\mathbf{u}} \tag{A.21}$$

With the above expressions, the averaged momentum equation is:

$$\begin{aligned}\frac{d}{dt}\int_V \overline{\rho}\tilde{\mathbf{u}}\ dV + \int_S d\mathcal{S}\cdot\overline{\rho}\tilde{\mathbf{u}}_r\tilde{\mathbf{u}} &= -\int_V \overline{\vartheta}\nabla\overline{p}\ dV + \\ &+ \int_S d\mathcal{S}\cdot(\mathbf{T}_m + \mathbf{T}_t) + \int_V \overline{\mathbf{s}}^d_{\mathbf{u}}\ dV \end{aligned} \tag{A.22}$$

A.2.3 Energy conservation equation

The instantaneous energy conservation equation reads:

$$\begin{aligned}\frac{d}{dt}\int_V \hat{\rho}\hat{e}\ dV + \int_S d\mathcal{S}\cdot\hat{\rho}\hat{\mathbf{u}}_r\hat{e} &= \int_S d\mathcal{S}\cdot\hat{\rho}\Gamma_e\nabla\hat{e} \\ &+ \int_V \Big(-\ \hat{\vartheta}\hat{p}\nabla\cdot\hat{\mathbf{u}} + \hat{s}_e + \hat{s}^d_e\Big)\ dV \end{aligned} \tag{A.23}$$

Note that in this equation the absence of body forces is assumed, and the work of the shear stresses ($\hat{\mathbf{T}}_m : \nabla\hat{\mathbf{u}}$) is neglected on the ground that their contribution

to the gas internal energy is small, [24]. After averaging, the energy conservation equation takes the following form:

$$\begin{aligned}\frac{d}{dt}\int_V \overline{\rho}\tilde{e}\ dV + \int_S d\mathcal{S}\cdot\overline{\rho}\tilde{\mathbf{u}}_r\tilde{e} = \int_S d\mathcal{S}\cdot\overline{\rho}\Gamma_{e,eff}\nabla\tilde{e} + \\ + \int_V \Big(-\ \overline{\vartheta}\overline{p}\nabla\cdot\tilde{\mathbf{u}} + \overline{s}_e + \overline{s}^d_e\Big)\ dV \end{aligned} \tag{A.24}$$

where $\Gamma_{e,eff}$ is the effective diffusivity defined as:

$$\Gamma_{e,eff} = \Gamma_e + \Gamma_{e,t} \tag{A.25}$$

The turbulence diffusivity $\Gamma_{e,t}$ links the turbulent flux $\overline{\hat{\rho}e''\mathbf{u}''}$ with ∇e as:

$$-\ \overline{\hat{\rho}e''\mathbf{u}''} = \overline{\rho}\ \Gamma_{e,t}\nabla\tilde{e} \tag{A.26}$$

The term $\overline{\hat{\rho}e''\mathbf{u}''}$ appears as a result of the averaging of convective term.

A.2.4 Turbulence model

Derivation of the k-equation

The derivation of the conservation equation for the turbulence kinetic energy presented here follows the procedure given in [6]. It starts with the derivation of the transport equation for Reynolds stresses, and then by contraction of this equation, the k-equation is obtained. However, derivation here takes into account the presence of the spray.

The derivation starts with the following two expressions:

$$\hat{\rho}\frac{Du''_iu''_j}{Dt} = u''_j\hat{\rho}\frac{Du''_i}{Dt} + u''_i\hat{\rho}\frac{Du''_j}{Dt} \tag{A.27}$$

$$\begin{aligned}\frac{Du''_i}{Dt} &= \frac{D\hat{u}_i}{Dt} - \frac{D\tilde{u}_i}{Dt} \\ &= \frac{D\hat{u}_i}{Dt} - \left(\frac{\partial\tilde{u}_i}{\partial t} + \tilde{u}_k\frac{\partial\tilde{u}_i}{\partial x_k} + u''_k\frac{\partial\tilde{u}_i}{\partial x_k}\right)\end{aligned} \tag{A.28}$$

where D/Dt denotes the material derivative[1]. The substitution of Eq.(A.28) multi-

[1] The operator of material derivative (also called a substantial or total derivative) is defined as, [209]:

$$\frac{D}{Dt} = \frac{\partial}{\partial t} + \hat{u}_k\frac{\partial}{\partial x_k}$$

where the repeated index k means summation.

plied by $\hat\rho$ into Eq.(A.27) gives:

$$\begin{aligned}\hat\rho\frac{Du''_iu''_j}{Dt} &= u''_j\hat\rho\frac{D\hat u_i}{Dt} - \left(u''_j\hat\rho\frac{\partial\tilde u_i}{\partial t} + u''_j\hat\rho\tilde u_k\frac{\partial\tilde u_i}{\partial x_k} + u''_j\hat\rho u''_k\frac{\partial\tilde u_i}{\partial x_k}\right) + \\ &+ u''_i\hat\rho\frac{D\hat u_j}{Dt} - \left(u''_i\hat\rho\frac{\partial\tilde u_j}{\partial t} + u''_i\hat\rho\tilde u_k\frac{\partial\tilde u_j}{\partial x_k} + u''_i\hat\rho u''_k\frac{\partial\tilde u_j}{\partial x_k}\right)\end{aligned} \tag{A.29}$$

In the above equation, the terms $\hat\rho D\hat u_i/Dt$ and $\hat\rho D\hat u_j/Dt$ can be written from the instantaneous gas momentum conservation equation A.11, given here in the following differential form:

$$\hat\rho\frac{D\hat u_i}{Dt} + \hat u_i\hat s^d = -\hat\vartheta\frac{\partial\hat p}{\partial x_k}\delta_{ki} + \frac{\partial\hat\vartheta(\hat T_m)_{ki}}{\partial x_k} + (\hat s^d_{u_i})_i \tag{A.30}$$

where $\hat s^d$ and $(\hat s^d_{u_i})_i$ are respectively the local evaporation rate and the rate of momentum exchange between the droplets and gas (see Eqs.(2.44) and (2.39)).

The LHS of Eq.(A.29) may be replaced by:

$$\begin{aligned}\hat\rho\frac{Du''_iu''_j}{Dt} &= \frac{\partial\hat\rho u''_iu''_j}{\partial t} + \frac{\partial\hat\rho\hat u_ku''_iu''_j}{\partial x_k} - u''_iu''_j\left(\frac{\partial\hat\rho}{\partial t} + \frac{\partial\hat\rho\hat u_k}{\partial x_k}\right) \\ &= \frac{\partial\hat\rho u''_iu''_j}{\partial t} + \frac{\partial\hat\rho\tilde u_ku''_iu''_j}{\partial x_k} + \frac{\partial\hat\rho u''_ku''_iu''_j}{\partial x_k} - u''_iu''_j\hat s^d\end{aligned} \tag{A.31}$$

Substituting Eqs.(A.30) and (A.31) into Eq.(A.29) gives:

$$\begin{aligned}\frac{\partial\hat\rho u''_iu''_j}{\partial t} + \frac{\partial\hat\rho\tilde u_ku''_iu''_j}{\partial x_k} + \frac{\partial\hat\rho u''_ku''_iu''_j}{\partial x_k} &= u''_j\left(-\hat\vartheta\frac{\partial\hat p}{\partial x_k}\delta_{ki} + \frac{\partial\,\hat\vartheta(\hat T_m)_{ki}}{\partial x_k}\right) - \\ - \left(u''_j\hat\rho\frac{\partial\tilde u_i}{\partial t} + u''_j\hat\rho\tilde u_k\frac{\partial\tilde u_i}{\partial x_k} + u''_j\hat\rho u''_k\frac{\partial\tilde u_i}{\partial x_k}\right) &+ u''_i\left(-\hat\vartheta\frac{\partial\hat p}{\partial x_k}\delta_{kj} + \frac{\partial\,\hat\vartheta(\hat T_m)_{kj}}{\partial x_k}\right) - \\ - \left(u''_i\hat\rho\frac{\partial\tilde u_j}{\partial t} + u''_i\hat\rho\tilde u_k\frac{\partial\tilde u_j}{\partial x_k} + u''_i\hat\rho u''_k\frac{\partial\tilde u_j}{\partial x_k}\right) &+ \\ + u''_j(\hat s^d_{u_i})_i + u''_i(\hat s^d_{u_j})_j - u''_j\hat u_i\hat s^d &- u''_i\hat u_j\hat s^d + u''_iu''_j\hat s^d\end{aligned} \tag{A.32}$$

Averaging of the above equation and taking into account that

$$\overline{u''_j\hat\rho}\frac{\partial\tilde u_i}{\partial t} = \overline{u''_j\hat\rho}\tilde u_k\frac{\partial\tilde u_i}{\partial x_k} = \overline{u''_i\hat\rho}\frac{\partial\tilde u_j}{\partial t} = \overline{u''_i\hat\rho}\tilde u_k\frac{\partial\tilde u_j}{\partial x_k} = 0 \tag{A.33}$$

because $\overline{u''_i\hat\rho}$ and $\overline{u''_j\hat\rho}$ vanish by definition (Eq.(A.4)), yields:

$$\begin{aligned}\frac{\partial\overline{\hat\rho u''_iu''_j}}{\partial t} + \frac{\partial\overline{\hat\rho\tilde u_ku''_iu''_j}}{\partial x_k} + \frac{\partial\overline{\hat\rho u''_ku''_iu''_j}}{\partial x_k} &= \overline{u''_j\left(-\hat\vartheta\frac{\partial\hat p}{\partial x_k}\delta_{ki} + \frac{\partial\,\hat\vartheta(\hat T_m)_{ki}}{\partial x_k}\right)} - \\ -\overline{u''_j\hat\rho u''_k}\frac{\partial\tilde u_i}{\partial x_k} + \overline{u''_i\left(-\hat\vartheta\frac{\partial\hat p}{\partial x_k}\delta_{kj} + \frac{\partial\,\hat\vartheta(\hat T_m)_{kj}}{\partial x_k}\right)} &- \overline{u''_i\hat\rho u''_k}\frac{\partial\tilde u_j}{\partial x_k} + \\ +\overline{u''_j(\hat s^d_{u_i})_i} + \overline{u''_i(\hat s^d_{u_j})_j} - \overline{u''_j\hat u_i\hat s^d} &- \overline{u''_i\hat u_j\hat s^d} + \overline{u''_iu''_j\hat s^d}\end{aligned} \tag{A.34}$$

Resolving the pressure and shear stress tensor into their mean and fluctuating components ($\hat p = \overline{p} + p'$ and $(\hat T_m)_{ki} = (\overline{T}_m)_{ki} + (T'_m)_{ki}$) and after some rearrangement, the following expression for the transport of Reynolds stresses is obtained:

$$\begin{aligned}\frac{\partial\overline{\hat\rho u''_iu''_j}}{\partial t} + \frac{\partial\overline{\hat\rho\tilde u_ku''_iu''_j}}{\partial x_k} &= -\left(\overline{u''_j\hat\rho u''_k}\frac{\partial\tilde u_i}{\partial x_k} + \overline{u''_i\hat\rho u''_k}\frac{\partial\tilde u_j}{\partial x_k}\right) - \frac{\partial\overline{\hat\rho u''_ku''_iu''_j}}{\partial x_k} - \\ -\left(\overline{u''_j\hat\vartheta}\frac{\partial\overline{p}}{\partial x_k}\delta_{ki} + \overline{u''_i\hat\vartheta}\frac{\partial\overline{p}}{\partial x_k}\delta_{kj}\right) &- \left(\overline{\hat\vartheta\frac{\partial u''_jp'}{\partial x_k}}\delta_{ki} + \overline{\hat\vartheta\frac{\partial u''_ip'}{\partial x_k}}\delta_{kj}\right) + \\ +\left(\overline{p'\hat\vartheta\frac{\partial u''_j}{\partial x_k}}\delta_{ki} + \overline{p'\hat\vartheta\frac{\partial u''_i}{\partial x_k}}\delta_{kj}\right) &+ \\ +\frac{\partial\overline{u''_j\,\hat\vartheta(\hat T_m)_{ki}}}{\partial x_k} + \frac{\partial\overline{u''_i\,\hat\vartheta(\hat T_m)_{kj}}}{\partial x_k} &- \left(\overline{\hat\vartheta(\hat T_m)_{ki}\frac{\partial u''_j}{\partial x_k}} + \overline{\hat\vartheta(\hat T_m)_{kj}\frac{\partial u''_i}{\partial x_k}}\right) + \\ +\overline{u''_j(\hat s^d_{u_i})_i} + \overline{u''_i(\hat s^d_{u_j})_j} - \overline{u''_j\hat u_i\hat s^d} &- \overline{u''_i\hat u_j\hat s^d} + \overline{u''_iu''_j\hat s^d}\end{aligned} \tag{A.35}$$

In high Reynolds number flows, the terms containing the mean shear stresses and the terms which represent their viscous diffusion, $\partial\overline{u''_j\hat\vartheta(\overline{T}_m)_{ki}}/\partial x_k$ can be neglected on the ground that these terms are small, Johns [113], so the above equations then reads:

$$\begin{aligned}\frac{\partial\overline{\hat\rho u''_iu''_j}}{\partial t} + \frac{\partial\overline{\hat\rho\tilde u_ku''_iu''_j}}{\partial x_k} &= -\left(\overline{u''_j\hat\rho u''_k}\frac{\partial\tilde u_i}{\partial x_k} + \overline{u''_i\hat\rho u''_k}\frac{\partial\tilde u_j}{\partial x_k}\right) - \frac{\partial\overline{\hat\rho u''_ku''_iu''_j}}{\partial x_k} - \\ -\left(\overline{u''_j\hat\vartheta}\frac{\partial\overline{p}}{\partial x_k}\delta_{ki} + \overline{u''_i\hat\vartheta}\frac{\partial\overline{p}}{\partial x_k}\delta_{kj}\right) &- \left(\overline{\hat\vartheta\frac{\partial u''_jp'}{\partial x_k}}\delta_{ki} + \overline{\hat\vartheta\frac{\partial u''_ip'}{\partial x_k}}\delta_{kj}\right) + \\ +\left(\overline{p'\hat\vartheta\frac{\partial u''_j}{\partial x_k}}\delta_{ki} + \overline{p'\hat\vartheta\frac{\partial u''_i}{\partial x_k}}\delta_{kj}\right) &+ \\ +\frac{\partial\overline{u''_j\,\hat\vartheta(T'_m)_{ki}}}{\partial x_k} + \frac{\partial\overline{u''_i\,\hat\vartheta(T'_m)_{kj}}}{\partial x_k} &- \left(\overline{\hat\vartheta(T'_m)_{ki}\frac{\partial u''_j}{\partial x_k}} + \overline{\hat\vartheta(T'_m)_{kj}\frac{\partial u''_i}{\partial x_k}}\right) +\end{aligned}$$

$$+\overline{u_j''(\hat{s}^d_{u_i})_i} + \overline{u_i''(\hat{s}^d_{u_j})_j} - \overline{u_j''\hat{u}_i\hat{s}^d} - \overline{u_i''\hat{u}_j\hat{s}^d} + \overline{u_j''u_i''\hat{s}^d} \tag{A.36}$$

The transport equation for the turbulence kinetic energy is obtained by contraction of Eq.(A.36), i.e. by setting $j = i$, and then division by 2:

$$\begin{array}{ccccc}
\dfrac{\partial\overline{\rho}\tilde{k}}{\partial t} & +\dfrac{\partial\overline{\rho}\tilde{u}_k\tilde{k}}{\partial x_k} & = -\overline{u_i''\hat{\rho}u_k''}\dfrac{\partial\tilde{u}_i}{\partial x_k} & -\frac{1}{2}\,\dfrac{\partial\overline{\hat{\rho}u_k''u_i''u_i''}}{\partial x_k}- \\
I & II & III & IV \\
& -\overline{u_i''\hat{\vartheta}}\dfrac{\partial\overline{p}}{\partial x_k}\delta_{ki} & -\overline{\hat{\vartheta}\dfrac{\partial u_i''p'}{\partial x_k}\delta_{ki}} & +\overline{p'\hat{\vartheta}\dfrac{\partial u_i''}{\partial x_k}\delta_{ki}}+ \\
& V & VI & VII \\
& +\overline{\dfrac{\partial u_i''\,\hat{\vartheta}(T_m')_{ki}}{\partial x_k}} & -\overline{\hat{\vartheta}(T_m')_{ki}\dfrac{\partial u_i''}{\partial x_k}}+ & \\
& VIII & IX & \\
& +\overline{u_i''(\hat{s}^d_{u_i})_i} & -\overline{u_i''\hat{u}_i\hat{s}^d} + \frac{1}{2}\,\overline{u_i''u_i''\hat{s}^d} & \\
& X & XI &
\end{array} \tag{A.37}$$

where the turbulence energy $\tilde{k}$ is defined as:

$$\begin{aligned}
\tilde{k} &= \frac{1}{\overline{\rho}}\,\overline{\hat{\rho}u_i''u_i''} \\
&= \frac{1}{\overline{\rho}}\,\overline{\hat{\rho}\mathbf{u}''\cdot\mathbf{u}''}
\end{aligned} \tag{A.38}$$

The terms in Eq.(A.37) represent: I and II - local rate of change and convection of k, III - rate of generation of $u_i''\hat{\rho}u_k''$ by the mean rates of strain, IV - turbulent diffusion, V - effect of the correlation between velocity and density fluctuation ($\overline{u_i''} = -\overline{\rho' u_i'}/\overline{\rho}$), VI - diffusion due to the pressure gradient, VII - pressure-strain fluctuation correlation, $VIII$ - viscous diffusion, IX - viscous dissipation, X - rate of work exchanged between turbulent eddies and droplets due to the drag force, and XI - effects of the droplet evaporation.

Inspection of the above equation shows a number of unknown terms on the RHS which need modelling, and differences when Eq.(A.37) is compared with its single-phase counterpart. These differences are in the appearance of the void fraction ϑ in all terms apart from X and XI, and additional spray-related terms X and XI. We assume here that the same approach used for the modelling of particular terms in

the k-equation in the case of single-phase flow, can be adopted for the modelling of their counterparts in the two-phase case. That means that the particular terms are modelled as follows ([6]):

- Terms IV, VI, and $VIII$ are modelled by the following one term:

$$-\frac{1}{2}\frac{\partial\overline{\hat{\rho}u_k''u_i''u_i''}}{\partial x_k} - \overline{\hat{\vartheta}\frac{\partial u_i''p'}{\partial x_k}\delta_{ki}} + \overline{\frac{\partial u_i''\,\hat{\vartheta}(T_m')_{ki}}{\partial x_k}} = \frac{\partial}{\partial x_k}\left(\frac{\overline{\rho}\,\nu_t}{\sigma_k}\frac{\partial\tilde{k}}{\partial x_k}\right) \tag{A.39}$$

  where ν_t is the turbulent kinematic viscosity (in high Reynolds number flows $\nu_t \approx \nu_{eff}$, because ν_t is then two to three order of magnitude larger than the molecular viscosity, [24]), and σ_k is the Prandtl-Schmidt number for k.

- Term III, which represent the generation rate of k:

$$-\overline{u_i''\hat{\rho}u_k''}\frac{\partial\tilde{u}_i}{\partial x_k} = \mathbf{T}_t : \nabla\tilde{\mathbf{u}} = G \tag{A.40}$$

  where $\mathbf{T}_t$ is the Reynolds stress tensor, see §(A.2.2) and Eq.(A.16).

The terms V and VII are neglected, assuming that they are in non-reacting flows of less importance, [60], while the term IX, the dissipation rate of k, is expressed in term of a newly introduced variable ϵ (governed by its own transport equation) defined as:

$$\overline{\hat{\vartheta}(T_m')_{ki}\frac{\partial u_i''}{\partial x_k}} = \overline{\rho}\,\tilde{\epsilon} \tag{A.41}$$

With the above modelling terms and assumptions, the final form of Eq.(A.37) reads:

$$\frac{\partial\overline{\rho}\tilde{k}}{\partial t} + \frac{\partial\overline{\rho}\tilde{u}_k\tilde{k}}{\partial x_k} = \frac{\partial}{\partial x_k}\left(\overline{\rho}\,\frac{\nu_t}{\sigma_k}\frac{\partial\tilde{k}}{\partial x_k}\right) + G - \overline{\rho}\,\tilde{\epsilon} + \overline{s}^d_k \tag{A.42}$$

or in a integro-differential form:

$$\frac{d}{dt}\int_V \overline{\rho}\tilde{k}\,dV + \int_S d\mathcal{S}\cdot\overline{\rho}\tilde{\mathbf{u}}_r\tilde{k} = \int_S d\mathcal{S}\cdot\overline{\rho}\frac{\nu_t}{\sigma_k}\nabla\tilde{k} + \int_V \left(G - \overline{\rho}\tilde{\epsilon} + \overline{s}^d_k\right)\,dV \tag{A.43}$$

where the two spray-related terms, X and XI, are denoted by $\overline{s}^d_k$.

The term $\overline{s}^d_k$ can be directly calculated from:

$$\begin{aligned}
\overline{s}^d_k &= \overline{u_i''(\hat{s}^d_{u_i})_i} - \overline{u_i''\hat{u}_i\hat{s}^d} + \frac{1}{2}\,\overline{u_i''u_i''\hat{s}^d} \\
&= \overline{\mathbf{u}''\cdot\hat{\mathbf{s}}^d_{\mathbf{u}}} - \overline{\mathbf{u}''\cdot\hat{\mathbf{u}}\,\hat{s}^d} + \frac{1}{2}\,\overline{\mathbf{u}''\cdot\mathbf{u}''\,\hat{s}^d}
\end{aligned} \tag{A.44}$$

When $\hat{\mathbf{s}}^d_{\mathbf{u}}$ and $\hat{s}^d$ are expressed in terms of the parcel momentum and mass changes (see §(3.4) and (3.5)), and when the ensemble averaging is resolved according to Eq.(B.3), the above equation yields:

$$\overline{s}^d_k = - \lim_{\substack{\Delta t \to 0 \\ \delta V \to 0}} \frac{1}{\Delta t\, \delta V} \int_{\delta V} \sum_{p=1}^{p=N_p} \int_t^{t+\Delta t} \left[\frac{1}{\tau_{\mathbf{u}}} (\mathbf{u}_p - \hat{\mathbf{u}}) - (\hat{\mathbf{u}} - \frac{1}{2}\mathbf{u}'')\frac{1}{\tau} \right] \delta(\mathbf{x} - \mathbf{x}_p)\, m_p \cdot \mathbf{u}''\, dt dV \tag{A.45}$$

The discretised version of Eq.(A.45) is, (see Eq.(B.4)):

$$\overline{s}^d_k = - \frac{1}{\Delta t\, \delta V} \int_{\delta V} \sum_{p=1}^{p=N_p} \sum_{i=1}^{i=N_s} \delta(\mathbf{x} - \mathbf{x}^i_p) \left\{ (m_p \mathbf{u}_p)^i - (m_p \mathbf{u}_p)^{i-1} - [\hat{\mathbf{u}}^i - \frac{1}{2}(\mathbf{u}'')^i]\,(m^i_p - m^{i-1}_p) \right\} \cdot (\mathbf{u}'')^i\, \Delta t'\, dV \tag{A.46}$$

where the superscripts $i-1$ and i denote the values at the subsequent times, and $\Delta t'$ is the subcycling time step; the summation is performed over all parcels and over all N_s subcycling time steps (for details see §(4.5.1)).

Derivation of the ϵ-equation

Derivation of the transport equation for ϵ in the case of compressible flows is difficult and complex. El Tahry [60] derived the exact ϵ-equation in therm of unweighted averaged quantities, and obtained 66 terms. After applying an order of magnitude analysis, the number of terms in the case of non-reacting flows was reduced to 10, of which 8 require modelling.

Although studies of the exact transport equation can gain a lot of information about importance of the particular terms in the equation, in density-variable flows an alternative approach is usually adopted[2]. In it, a more convenient definition of ϵ is used (valid strictly only in high Reynolds number flows), and assumption is made that the ϵ-equation for the constant density flow can be used for the density-variable flows with the substitution of the conventionally (non-weighted) averaged

[2]Some argue that, since the modelling of particular terms in this equation relies mainly on a dimensional and order on magnitude analysis, intuition and analogy, there is a little point in mathematically strict derivation of this equation, Jones [113].

quantities with their density-weighted counterparts, [6]. This approach is therefore used in this study, keeping account in the course of derivation of the ϵ-equation of the spray-related terms in the gas momentum equation, Eq.(A.30).

The starting ϵ-equation, the one valid strictly for incompressible flows, is based on the following assumptions, [121]:

- fluctuation of the molecular kinematic viscosity can be neglected,
- adoption of the continuity equation for incompressible flows, i.e. assuming that $\partial \hat{u}_k / \partial x_k \approx 0$,
- in high Reynolds number flows turbulence tends to be isotropic, therefore the cross-correlation terms $\overline{(\partial u''_k/\partial x_i)(\partial u''_i/\partial x_k)} \approx 0$; with these assumptions, the definition of ϵ reduces to:

$$\epsilon = \frac{\nu_m}{\overline{\rho}} \overline{\hat{\rho} \frac{\partial u''_i}{\partial x_k} \frac{\partial u''_i}{\partial x_k}} \tag{A.47}$$

With the above assumptions, the transport equation for ϵ can be formally obtained by taking the derivative of the momentum conservation equation with respect to x_j, multiplying by $2\nu_m \partial u''_i / \partial x_j$, and averaging.

The same procedure applied to spray-related terms $\hat{u}_i \hat{s}^d$ and $(\hat{s}^d_{u_i})_i$ in Eq.(A.30), yields:

$$\overline{s}^d_\epsilon = 2\, \nu_m \overline{\frac{\partial u''_i}{\partial x_j} \frac{\partial}{\partial x_j} \left[(\hat{s}^d_{u_i})_i - \hat{u}_i \hat{s}^d \right]} \tag{A.48}$$

where $\overline{s}^d_\epsilon$ is the additional source term which represents the spray contribution to the ϵ-equation.

When the conventionally averaged quantities in the ϵ-equation for the incompressible flow, see for example [89] or [217], are replaced with their density-weighted counterparts, and the above term $\overline{s}^d_\epsilon$ is added to the source terms, the following expression is obtained:

$$\underbrace{\frac{\partial \overline{\rho}\tilde{\epsilon}}{\partial t}}_{I} + \underbrace{\frac{\partial \overline{\rho}\tilde{u}_i\tilde{\epsilon}}{\partial x_k}}_{II} = \underbrace{- \frac{\partial}{\partial x_k} \left(\nu_m \overline{\rho}\, \overline{\hat{\vartheta}\, u''_k \frac{\partial u''_i}{\partial x_j} \frac{\partial u''_i}{\partial x_j}} \right)}_{III} \underbrace{- 2 \frac{\partial}{\partial x_k} \left(\nu_m \overline{\hat{\vartheta}\, \frac{\partial p'}{\partial x_i} \frac{\partial u''_k}{\partial x_i}} \right)}_{IV} + \underbrace{\frac{\partial}{\partial x_k} \left(\nu_m\, \overline{\rho} \frac{\partial \tilde{\epsilon}}{\partial x_k} \right)}_{V} \underbrace{- 2\nu_m \overline{\rho} \frac{\partial \tilde{u}_i}{\partial x_k} \left(\overline{\hat{\vartheta} \frac{\partial u''_i}{\partial x_j} \frac{\partial u''_k}{\partial x_j}} + \overline{\hat{\vartheta} \frac{\partial u''_j}{\partial x_i} \frac{\partial u''_j}{\partial x_k}} \right)}_{VI} -$$

$$-2\,\nu_m\overline{\rho}\,\overline{\hat{\vartheta}u_k''\frac{\partial u_i''}{\partial x_j}}\frac{\partial^2\tilde{u}_i}{\partial x_j\partial x_k} \quad -2\,\nu_m\overline{\rho}\,\overline{\hat{\vartheta}\frac{\partial u_i''}{\partial x_k}\frac{\partial u_i''}{\partial x_j}\frac{\partial u_k''}{\partial x_j}}-$$
$$VII \qquad\qquad VIII$$
$$-\,2\,\overline{\left(\nu_m\,\hat{\vartheta}\frac{\partial^2 u_i''}{\partial x_k\partial x_i}\right)^2} \;+\; \overline{s}_\epsilon^d \tag{A.49}$$
$$IX \qquad\qquad X$$

where the terms represent the following: I and II - local rate of change of ϵ, III, IV and V - rate of supply of ϵ by diffusion from the velocity, pressure and viscous contributions, VI and VII - rate of creation of ϵ by vortex stretching by the mean rate of strain and the mean motion, respectively, $VIII$ - rate of generation by vortex stretching by the turbulence, IX - rate of destruction of ϵ by the viscous action, and X - contribution from the spray-turbulence interaction.

Inspection of Eq.(A.49) reveals a number of unknown correlations in the RHS of equation, which therefore need modelling. The first three terms on the RHS, III , IV and V, are modelled as a one diffusion term, i.e.:

$$-\frac{\partial}{\partial x_k}\left(\nu_m\overline{\rho}\,\overline{\hat{\vartheta}\,u_k''\frac{\partial u_i''}{\partial x_j}\frac{\partial u_i''}{\partial x_j}}\right)-2\frac{\partial}{\partial x_k}\left(\nu_m\overline{\hat{\vartheta}\,\frac{\partial p'}{\partial x_i}\frac{\partial u_k''}{\partial x_i}}\right)+$$
$$+\frac{\partial}{\partial x_k}\left(\nu_m\,\overline{\rho}\frac{\partial\tilde{\epsilon}}{\partial x_k}\right)=\frac{\partial}{\partial x_k}\left(\overline{\rho}\frac{\nu_t}{\sigma_\epsilon}\frac{\partial\tilde{\epsilon}}{\partial x_k}\right) \tag{A.50}$$

where σ_ϵ is the empirical coefficient (the Prandtl/Schmidt number for ϵ), assumed constant.

The remaining RHS terms of Eq.(A.49), apart from a term X, are modelled as, [6]:

$$-2\nu_m\overline{\rho}\frac{\partial\tilde{u}_i}{\partial x_k}\left(\overline{\hat{\vartheta}\frac{\partial u_i''}{\partial x_j}\frac{\partial u_k''}{\partial x_j}}+\overline{\hat{\vartheta}\frac{\partial u_j''}{\partial x_i}\frac{\partial u_j''}{\partial x_k}}\right)-$$
$$-2\,\nu_m\overline{\rho}\,\overline{\hat{\vartheta}u_k''\frac{\partial u_i''}{\partial x_j}}\frac{\partial^2\tilde{u}_i}{\partial x_j\partial x_k}-2\,\nu_m\overline{\rho}\,\overline{\hat{\vartheta}\frac{\partial u_i''}{\partial x_k}\frac{\partial u_i''}{\partial x_j}\frac{\partial u_k''}{\partial x_j}}-2\,\overline{\left(\nu_m\,\hat{\vartheta}\frac{\partial^2 u_i''}{\partial x_k\partial x_i}\right)^2}=$$
$$=C_{\epsilon1}\frac{\tilde{\epsilon}}{\tilde{k}}G-C_{\epsilon2}\frac{\tilde{\epsilon}^2}{\tilde{k}}\overline{\rho}+C_{\epsilon3}\overline{\rho}\tilde{\epsilon}\frac{\partial\tilde{u}_k}{\partial x_k}+C_{\epsilon4}\frac{\tilde{\epsilon}}{\tilde{k}}\overline{\rho}\nu_t\left(\frac{\partial\tilde{u}_k}{\partial x_k}\right)^2+C_{\epsilon5}\frac{\overline{\rho}\tilde{\epsilon}}{\overline{\mu}_m}\frac{\partial\overline{\mu}_m}{\partial t} \tag{A.51}$$

where $C_{\epsilon1},\ldots C_{\epsilon5}$ are the empirical coefficients whose values vary from author to author [7]. It was shown in [8] that the predictions of non-reactive flows with the above equation are almost insensitive to the exclusion of $C_{\epsilon4}$ and $C_{\epsilon5}$, so they are not included in this study, i.e. $C_{\epsilon4}=C_{\epsilon5}=0$.

The spray-related term X is modelled in a similar manner to the source term in Eq.(A.51) which originates from the turbulence energy production, G. It is made proportional to the spray contribution in the k-equation, $\overline{s}_k^d$, and inversely proportional to turbulence time scale $\tilde{k}/\tilde{\epsilon}$, i.e.,

$$\overline{s}_\epsilon^d=C_{\epsilon4}\,\frac{\tilde{\epsilon}}{\tilde{k}}\,\overline{s}_k^d \tag{A.52}$$

where $C_{\epsilon4}$ is the new coefficient (not related to the previously mentioned coefficient), whose value has been chosen by Mostafa and Mongia [146] to match experimental data of the particle-laden jet measured by Shuen et al. [189].

The final form of the transport equation for ϵ thus reads:

$$\frac{\partial\overline{\rho}\tilde{\epsilon}}{\partial t}+\frac{\partial\overline{\rho}\tilde{u}_i\tilde{\epsilon}}{\partial x_k} \;=\; \frac{\partial}{\partial x_k}\left(\overline{\rho}\frac{\nu_t}{\sigma_\epsilon}\frac{\partial\tilde{\epsilon}}{\partial x_k}\right)+$$
$$+C_{\epsilon1}\frac{\tilde{\epsilon}}{\tilde{k}}G-C_{\epsilon2}\frac{\tilde{\epsilon}^2}{\tilde{k}}\overline{\rho}+C_{\epsilon3}\overline{\rho}\tilde{\epsilon}\frac{\partial\tilde{u}_k}{\partial x_k}+\overline{s}_\epsilon^d \tag{A.53}$$

or in a integro-differential form:

$$\frac{d}{dt}\int_V\overline{\rho}\tilde{\epsilon}\,dV+\int_S d\mathcal{S}\cdot\overline{\rho}\tilde{\mathbf{u}}_r\tilde{\epsilon}=\int_S d\mathcal{S}\cdot\overline{\rho}\frac{\nu_t}{\sigma_\epsilon}\nabla\tilde{\epsilon}$$
$$+\int_V\left(C_{\epsilon1}G\frac{\tilde{\epsilon}}{\tilde{k}}-C_{\epsilon2}\overline{\rho}\,\frac{\tilde{\epsilon}^2}{\tilde{k}}+C_{\epsilon3}\overline{\rho}\,\tilde{\epsilon}\nabla\cdot\tilde{\mathbf{u}}+\overline{s}_\epsilon^d\right)dV \tag{A.54}$$

The coefficients of the model are given in Table 2.2.

Appendix B

B.1 Ensemble-averaging of the general spray source term

Suppose that $\widehat{\frac{d}{dt}f_p^\phi}$ represents the instantaneous exchange rate of ϕ between the parcel p and the surrounding gas. Then, the total instantaneous exchange rate from all parcels at a location $\mathbf{x}$ and time t is:

$$\hat{s}_\phi^d(\mathbf{x},t) = -\sum_{p=1}^{N_p}\left[\delta(\mathbf{x}-\mathbf{x}_p)\,\widehat{\frac{d}{dt}f_p^\phi}\right]_t \tag{B.1}$$

where $\mathbf{x}_p = \mathbf{x}_p(t)$ represents the trajectory of the parcel p.

According to the definition of the ensemble averaging, the ensemble-averaged exchange rate is as follows:

$$\overline{s}_\phi^d(\mathbf{x},t) = -\lim_{N\to\infty}\frac{1}{N}\sum_{i=1}^{N}\sum_{p=1}^{N_p(i)}\left[\delta(\mathbf{x}-\mathbf{x}_p)\,\widehat{\frac{d}{dt}f_p^\phi}\right]_{t+i\tau_C} \tag{B.2}$$

where τ_C is an engine cycle time period and N the number of identically performed experiments.

Calculation of $\overline{s}_\phi^d(\mathbf{x},t)$ by Eq.(B.2) would require a large number of samples with the randomised gas properties, $(N \to \infty)$, which is clearly impractical and time consuming. Therefore, since the ensemble-averaged quantities are expected to be approximately constant over the small time interval Δt and within the small control volume δV, it is assumed that $\overline{s}_\phi^d(\mathbf{x})$ can be calculated as a mean value over Δt and δV when they both tend to zero, by the following expression:

$$\overline{s}_\phi^d(\mathbf{x},t) = -\lim_{\substack{\Delta t\to 0\\ \delta V\to 0}}\frac{1}{\Delta t\,\delta V}\int_{\delta V}\left(\sum_{p=1}^{N_p}\int_t^{t+\Delta t}\left[\delta(\mathbf{x}-\mathbf{x}_p)\,\widehat{\frac{d}{dt}f_p^\phi}\right]_t dt\right)dV \tag{B.3}$$

When the above equation is discretised and the temporal integration over Δt is replaced by the sum over a finite number of subcycling time steps N_s, the equation reads:

$$\begin{aligned}\overline{s}^d_\phi(\mathbf{x},t) &\approx -\frac{1}{\delta V}\frac{1}{\Delta t}\int_{\delta V}\left(\sum_{p=1}^{N_p}\sum_{i=1}^{N_s}\left[\delta(\mathbf{x}-\mathbf{x}_p)\,\widehat{\frac{d}{dt}f_p^\phi}\right]^i\Delta t'\right)dV\\ &\approx -\frac{1}{\delta V}\frac{1}{\Delta t}\int_{\delta V}\left(\sum_{p=1}^{N_p}\sum_{i=1}^{N_s}\delta(\mathbf{x}-\mathbf{x}_p^i)\left[(\hat{f}_p^\phi)^i-(\hat{f}_p^\phi)^{i-1}\right]\right)dV \qquad \text{(B.4)}\end{aligned}$$

where the superscripts $i-1$ and i denote the values at the subsequent times, and $\Delta t'$ is the subcycling time step; $N_s\Delta t' = \Delta t$.

More details about the averaging of the spray terms can be found in Dukowicz [58].

Appendix C

C.1 The normal diffusion

The diffusion flux vector at the face f between the neighbouring cells P and N is interpolated according to Eq.(4.4) as:

$$(\rho\,\Gamma_\phi\nabla\phi)_f = \lambda_f^P\,(\rho\,\Gamma_\phi\nabla\phi)_P + (1-\lambda_f^P)\,(\rho\,\Gamma_\phi\nabla\phi)_N \qquad \text{(C.1)}$$

and approximated by:

$$(\rho\,\Gamma_\phi\nabla\phi)_f \approx \lambda_f^P\,(\rho\,\Gamma_\phi)_P(\nabla\phi)_P + (1-\lambda_f^P)\,(\rho\,\Gamma_\phi)_N(\nabla\phi)_N \qquad \text{(C.2)}$$

Substitution of Eq.(4.8) for the gradient in cell into the above equation, yields:

$$\begin{aligned}(\rho\,\Gamma_\phi\nabla\phi)_f &\approx \lambda_f^P\left(\frac{\rho\,\Gamma_\phi}{V}\right)_P\sum_{\{l\}_P}\mathcal{S}_l^P\,(1-\lambda_l^P)(\phi_N-\phi_P) +\\ &+ (1-\lambda_f^P)\left(\frac{\rho\,\Gamma_\phi}{V}\right)_N\sum_{\{l\}_N}\mathcal{S}_l^N\,(1-\lambda_l^N)(\phi_{NN}-\phi_N) \qquad \text{(C.3)}\end{aligned}$$

According to Eq.(4.20), the diffusion flux vector $(\rho\,\Gamma_\phi\nabla\phi)_f$ is resolved into the normal and cross diffusion components, $\mathbf{d}_f^{nor}$ and $\mathbf{d}_f^c$, as:

$$(\rho\,\Gamma_\phi\nabla\phi)_f = \mathbf{d}_f^{nor}(\phi) + \mathbf{d}_f^c(\phi) \qquad \text{(C.4)}$$

As defined in §(4.2.2), the normal diffusion takes into account only the contributions from the $+f$ and $-f$ directions, it follows from Eqs.(C.3) and (C.4) that:

$$\begin{aligned}\mathbf{d}_f^{nor}(\phi) &= \lambda_f^P\left(\frac{\rho\,\Gamma_\phi}{V}\right)_P\\ &\quad\left[\mathcal{S}_f^P\,(1-\lambda_f^P)(\phi_N-\phi_P) + \mathcal{S}_{-f}^P\,(1-\lambda_{-f}^P)(\phi_{N(-f)}-\phi_P)\right] +\\ &+ (1-\lambda_f^P)\left(\frac{\rho\,\Gamma_\phi}{V}\right)_N\\ &\quad\left[\mathcal{S}_f^N\,(1-\lambda_f^N)(\phi_{NN}-\phi_N) + \mathcal{S}_{-f}^N\,(1-\lambda_{-f}^N)(\phi_{NN(-f)}-\phi_N)\right] \qquad \text{(C.5)}\end{aligned}$$

In order to express $\mathbf{d}_f^{nor}(\phi)$ in terms of the values at cells P and N, a linear variation of ϕ over cells is assumed. This leads to the following relations:

$$\begin{aligned}(1-\lambda_{-f}^{P})(\phi_{N(-f)}-\phi_P) &= -(1-\lambda_f^P)(\phi_N-\phi_P)\\ (1-\lambda_f^N)(\phi_{NN}-\phi_N) &= -(1-\lambda_{-f}^N)(\phi_{NN(-f)}-\phi_N)\end{aligned} \tag{C.6}$$

Substitution of the above expressions into Eq.(C.5) taking into account that

$$1-\lambda_{-f}^N = \lambda_f^P$$

and

$$\phi_{NN(-f)} = \phi_P$$

(see Fig.4.2), yields:

$$\begin{aligned}\mathbf{d}_f^{nor}(\phi) = {} & \lambda_f^P\,(1-\lambda_f^P)\,(\phi_N-\phi_P)\\ & \left[\left(\frac{\rho\,\Gamma_\phi}{V}\right)_P(\mathcal{S}_f^P-\mathcal{S}_{-f}^P)+\left(\frac{\rho\,\Gamma_\phi}{V}\right)_N(\mathcal{S}_f^N-\mathcal{S}_{-f}^N)\right]\end{aligned} \tag{C.7}$$

Appendix D

D.1 Cylinder averaged thermodynamic

The first task of the bulk adjustment calculation is to estimate changes in the bulk properties (and their new values), which are, in general case, caused by:

1. compression/expansion due to the piston motion,
2. inlet and outlet valve flow, and
3. heat exchange through the wall of the cylinder.

Note that the effect of heat release due to the combustion is not included.

The second task is to determine global (uniform) increments of pressure and density with which the local values of these quantities will be corrected.

The derivation given below follows [24] and [219].

D.1.1 Cylinder presure

The change of the total enthalpy in the cylinder, dH, during the time period, dt, can be expressed by:

$$dH = dE + d(p_{cyl}V_{cyl}) \tag{D.1}$$

where E is the total internal energy, and p_{cyl} and V_{cyl} are the average (cylinder) pressure and cylinder volume, respectively. The change in the total internal energy of the gas, according to the first law of thermodynamics, is given by:

$$dE = \underbrace{-\,p_{cyl}dV_{cyl}}_{I}\ \underbrace{-\,e_v\dot{m}_v dt}_{II}\ \underbrace{+\,\dot{Q}_b dt}_{III} \tag{D.2}$$

The three terms on the r.h.s of Eq.(D.2) are contributions due to the change in cylinder volume (I), valve flow (II), where e_v and $\dot{m}_v$ are the specific internal energy and mass flow rate of the valve flow (negative $\dot{m}_v$ means inflow), and heat transfer (III), where $\dot{Q}_b$ is the total heat transfer rate.

Assuming that the gas obeys the perfect gas law, i.e. $p_{cyl} V_{cyl} = m_{cyl} RT$, and that $H = m_{cyl}\, c_{cyl} T$, the enthalpy change, dH, can also be expressed as:

$$dH = dm_{cyl} c_p T + \frac{c_p}{R}\left[d(p_{cyl} V_{cyl}) - \frac{p_{cyl} V_{cyl}}{m_{cyl}} dm_{cyl}\right] \tag{D.3}$$

where $dm_{cyl} = -\dot{m}_v dt$ stands for the change of the mass in the cylinder due to the valve flow.

Combining Eqs.(D.1), (D.2) and (D.3), the following relation for the pressure change is extracted:

$$\left(\frac{c_p}{R} - 1\right) V_{cyl}\, dp_{cyl} = -\frac{c_p}{R}\, dV_{cyl}\, p_{cyl} - e_v\, \dot{m}_v\, dt + \dot{Q}_b\, dt \tag{D.4}$$

Discretisation of this equation with the following substitutions:

$$\begin{aligned} dp_{cyl} &\rightarrow (p_{cyl} - p^o_{cyl}) \\ dt &\rightarrow \Delta t \\ V_{cyl} &\rightarrow \overline{V}_{cyl} = (V^o_{cyl} + V_{cyl})/2, \end{aligned}$$

yields:

$$p_{cyl} = \frac{\left[\left(\frac{c_p}{R}\right)_{cyl} - 1\right] \overline{V}_{cyl}\, p^o_{cyl} + [\dot{Q}_b - e_v\, \dot{m}_v]\Delta t}{\left[\left(\frac{c_p}{R}\right)_{cyl} - 1\right] \overline{V}_{cyl} + \left(\frac{c_p}{R}\right)_{cyl} (V_{cyl} - V^o_{cyl})} \tag{D.5}$$

where the superscript ^{o} denotes the old time values. The term $\left(\frac{c_p}{R}\right)_{cyl}$ is the volume averaged quantity, defined by:

$$\left(\frac{c_p}{R}\right)_{cyl} = \frac{1}{V_{cyl}} \sum_i^{N_c} V_i \frac{c_p(T_i)}{R_i} \tag{D.6}$$

where the summation in this expression is performed over all the cells in the domain (N_c).

D.1.2 Cylinder density

The average (cylinder) density, defined as $\rho_{cyl} = m_{cyl}/V_{cyl}$, is calculated directly from the mass conservation equation:

$$d(\rho_{cyl} V_{cyl}) = -\dot{m}_v dt \tag{D.7}$$

From this equation, after discretisation, the following expression for ρ_{cyl} is obtained:

$$\rho_{cyl} = \frac{\left(\rho^o_{cyl} V^o_{cyl} - \dot{m}_v \Delta t\right)}{V_{cyl}} \tag{D.8}$$

D.1.3 Pressure and density increments

Since the average values of the pressure and density are changed, as explained above, the local (cell) values are modified by the (spatially uniform) corrections, denoted by the superscript '$^+$', given by:

$$p^+ = -\frac{1}{\vartheta_{cyl} V_{cyl}} \sum_{i=1}^{N_c} (p')^o_i \vartheta_i V_i \tag{D.9}$$

$$\rho^+ = \rho_{cyl} - \frac{1}{V_{cyl}} \sum_{i=1}^{N_c} \rho^o_i V_i \tag{D.10}$$

The formula for the pressure correction (p^+) is obtained from the overall balance of the product pV, i.e.:

$$\begin{aligned} \sum_{i=1}^{N_c} [p_{cyl} + (p')^o_i + p^+] \vartheta_i V_i &= p_{cyl} \sum_{i=1}^{N_c} \vartheta_i V_i \;\Rightarrow \\ \sum_{i=1}^{N_c} (p')^o_i \vartheta_i V_i + p^+ \sum_{i=1}^{N_c} \vartheta_i V_i &= 0 \end{aligned} \tag{D.11}$$

where p' is the relative pressure, and ϑ_{cyl} stands for the average (cylinder) void fraction, defined as:

$$\vartheta_{cyl} = \frac{1}{\sum_{i=1}^{N_c} V_i} \sum_{i=1}^{N_c} \vartheta_i V_i = \frac{1}{V_{cyl}} \sum_{i=1}^{N_c} \vartheta_i V_i \tag{D.12}$$

The following relation for the overall mass balance in a cylinder is the base of Eq.(D.10):

$$\begin{aligned} \sum_{i=1}^{N_c} (\rho^o_i + \rho^+) \vartheta_i V_i &= \rho_{cyl} \sum_{i=1}^{N_c} \vartheta_i V_i \;\Rightarrow \\ \sum_{i=1}^{N_c} \rho^o_i \vartheta_i V_i + \rho^+ \vartheta_{cyl} V_{cyl} &= \rho_{cyl} \vartheta_{cyl} V_{cyl} \end{aligned} \tag{D.13}$$

D.2 The pressure equation

In incompressible and low Mach number flows, it is preferable to create an extra equation for pressure rather than attempt to evaluate the density from the continuity equation and then calculate pressure from the equation of state. (Moreover, in incompressible flows there is no link between pressure and density). There are many methods which follow this preferred route, notably the MAC method of Harlow and Welch [92], the SIMPLE method of Patankar and Spalding [169], the SIMPLER method of Patankar [166], and the PISO procedure of Issa [110]. Here the last-named is used.

The pressure equation is derived from the discretised continuity and momentum conservation equations as described below.

From the discretised gas momentum conservation equation, Eq.(4.61), the velocity in a cell P can be extracted as:

$$\mathbf{u}_P = \frac{1}{\mathcal{A}_P^{\mathbf{u}}}\left[\sum_N \mathcal{A}_N^{\mathbf{u}}\mathbf{u}_N + \mathbf{b}_P^{\mathbf{u}} + (\mathbf{S}_{\mathcal{U}}^{\mathbf{u},d})_P - (V\vartheta\mathbf{N}p)_P\right] \tag{D.14}$$

$$= \mathbf{H}_P - \frac{1}{\mathcal{A}_P^{\mathbf{u}}}(V\vartheta\mathbf{N}p)_P \tag{D.15}$$

where $\mathbf{H}_P$ is:

$$\mathbf{H}_P = \frac{1}{\mathcal{A}_P^{\mathbf{u}}}\left[\sum_N \mathcal{A}_N^{\mathbf{u}}\mathbf{u}_N + \mathbf{b}_P^{\mathbf{u}} + (\mathbf{S}_{\mathcal{U}}^{\mathbf{u},d})_P\right] \tag{D.16}$$

In order to avoid possible oscillations which can arise if a simple spatial interpolation for the velocity at the cell face is used for determination of the mass flux, [184], a special interpolation procedure, suggested by Prakash [172], Rhie [182] and Rhie and Chow [183] is employed. It is based on the interpolation of the discretised momentum equation, such that the total mass flux $\sum_{\{f\}_P}\mathcal{C}_f$ through the surface of cell P is evaluated as follows:

$$\sum_{\{f\}_P}\mathcal{C}_f = \sum_{\{f\}_P}\mathcal{S}_f\cdot\rho_f\left[\mathbf{H}-\mathbf{u}_b\right]_f - \sum_{\{f\}_P}\mathcal{S}_f\cdot\left(\frac{1}{\mathcal{A}^{\mathbf{u}}}V\vartheta\rho\mathbf{N}p\right)_f \tag{D.17}$$

where $\mathcal{A}^{\mathbf{u}}$ denotes the central coefficient in the momentum equation; the way how the term $\sum_{\{f\}_P}\mathcal{S}_f\cdot\left(\frac{1}{\mathcal{A}^{\mathbf{u}}}V\vartheta\rho\mathbf{N}p\right)_f$ is resolved is given later on by Eq.(D.21).

If the local density ρ is expressed via the gas equation of state as:

$$\rho = \vartheta\,\frac{p}{RT} = \vartheta\,\frac{p_{ref}+p'}{RT} \tag{D.18}$$

where p_{ref} is the average (spatially uniform) pressure in the cylinder, and p' stands for the relative pressure, and then substituted, together with the expression for the mass flux, Eq.(D.17), into the mass conservation equation, (2.39),

$$\frac{(\rho V)_P-(\rho V)_P^o}{\Delta t} + \sum_{\{f\}_P}\mathcal{C}_f = (S^d)_P \tag{D.19}$$

the result is the following pressure equation:

$$\frac{1}{\Delta t}\left(\frac{V\vartheta p'}{RT}\right)_P - \sum_{\{f\}_P}\mathcal{S}_f\cdot\left(\frac{1}{\mathcal{A}^{\mathbf{u}}}V\vartheta\rho\mathbf{N}p'\right)_f = -\sum_{\{f\}_P}\mathcal{S}_f\cdot\rho_f\left[\mathbf{H}-\mathbf{u}_b\right]_f + (S^d)_P - \frac{1}{\Delta t}\left(\frac{V\vartheta p_{ref}}{RT}\right)_P + \frac{(\rho V)_P^o}{\Delta t} \tag{D.20}$$

In the above equation, p in Eq.(D.17) is resolved into p' and p_{ref}, and account has been taken that $\mathbf{N}p_{ref} = \mathbf{0}$.

The term $\sum_{\{f\}_P}\mathcal{S}_f\cdot\left(\frac{1}{\mathcal{A}^{\mathbf{u}}}V\vartheta\rho\mathbf{N}p'\right)_f$ in Eq.(D.20) is resolved with $\Gamma_\phi = V\vartheta/\mathcal{A}^{\mathbf{u}}$ into the orthogonal and non-orthogonal parts according to Eqs.(4.26) and (4.27) for the former, and Eg.(4.28) for the latter (see §(4.3.2) for details), as:

$$\sum_{\{f\}_P}\mathcal{S}_f\cdot\left(\frac{1}{\mathcal{A}^{\mathbf{u}}}V\vartheta\rho\mathbf{N}p'\right)_f = \sum_{\{f\}_P}\mathcal{D}_f^p(p'_N-p'_P) + \sum_{\{f\}_P}D_f^{p,c} \tag{D.21}$$

where the non-orthogonal part $\sum_{\{f\}_P}D_f^{p,c}$ is used in the iterative process, i.e. it is evaluated using the currently available values of p'. Therefore, the final form of the discretised pressure equation is:

$$\mathcal{A}_P^p(p')_P = \sum_N \mathcal{A}_N^p(p')_N + b_P^p \quad,\ P=1,\ldots N_c \tag{D.22}$$

$$\mathcal{A}_P^p = \sum_N \mathcal{A}_N^p + \frac{1}{\Delta t}\left(\frac{V\vartheta}{RT}\right)_P \tag{D.23}$$

$$\mathcal{A}_N^p = \mathcal{D}_f^p \tag{D.24}$$

$$b_P^p = -\sum_{\{f\}_P}\rho_f\left[\mathbf{H}-\mathbf{u}_b\right]_f\cdot\mathcal{S}_f + (S^d)_P - \frac{1}{\Delta t}\left(\frac{V\vartheta p_{ref}}{RT}\right)_P + \frac{(\rho V)_P^o}{\Delta t} + \sum_{\{f\}_P}D_f^{p,c} \tag{D.25}$$

It can be seen that the above is a Poisson type equation where the source term represents the mass imbalance due to the imperfect velocity prediction.

The zero-gradient boundary condition is applied to this equation, which is achieved by setting the corresponding $\mathcal{A}_N^p$ coefficient to zero. However, the mass fluxes at the inflow/outflow boundaries, which make a part of the total source term of the equation, are taken into account via the $\mathcal{S}_f \cdot \rho_f \, [\, \mathbf{H} - \mathbf{u}_b \,]_f$ term at these boundaries.

The pressure equation is solved by the CG solver in the iterative loop with subsequent updating of the non-orthogonal term. In matrix form this procedure can be written as:

$$\mathbf{A}^p (\underline{p}')^{j+1} = \underline{b}^p + \mathbf{L}(\underline{p}')^j \ , \quad j = 1, \ldots \tag{D.26}$$

where the non-orthogonal term $(\sum_{\{f\}_P} D_f^{p,c})$ is separated from the rest of the source term and represented by $\mathbf{L}(\underline{p}')^j$.

Appendix E

E.1 Aachen pressure chamber - Injection data

This appendix includes injection data for the Aachen pressure chamber obtained from the Institut für Thermodynamik, Aachen on a disk[1]. Some of the data are reported in [118].

The main data of injection system are as follows:

In-line injector pump:	Bosch Type PES 4 MW 80
Plunger diameter:	8 mm
Pressure valve:	70 bar
Max. camshaft speed:	2400 rpm
Prestroke:	3.5 mm
Injection pipe:	Length - 310 mm; Diameter - 1.5 mm
Nozzle:	1 hole;$D_{inj} = 0.2mm$, $L = 0.8mm$
Opening pressure:	250 bar

The nozzle discharge coefficient, C_d versus needle lift, l_n was measured under the constant pressure difference of 100 bar with a diesel fuel, Table E.1.

The pressure in the injection pipe is measured with a piezoelectric transducer, 10 mm above the nozzle holder inlet; the needle lift is measured with a BOSCH needle lift sensor placed in the nozzle holder. Their measured data for operating points OP1 and OP4, and OP3 are shown in Figs. E.1 and E.2, respectively. The

[1] The measurement are carried out as a part of the IDEA project.

fuel injection rates for both injection regimes are calculated from the above data by RWTH; the data are given in Tables E.2 and E.3.

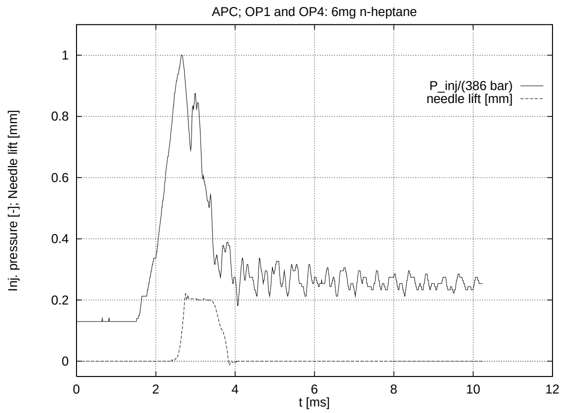

Figure E.1: APC; Injection pressure (normalised by the peak pressure) and needle lift vs. time for OP1 and OP4.

l_n [mm]	0.0	0.022	0.055	0.111	0.166	0.221
C_d [-]	0.0	0.59	0.64	0.65	0.66	0.66

Table E.1: Discharge coefficient vs. needle lift.

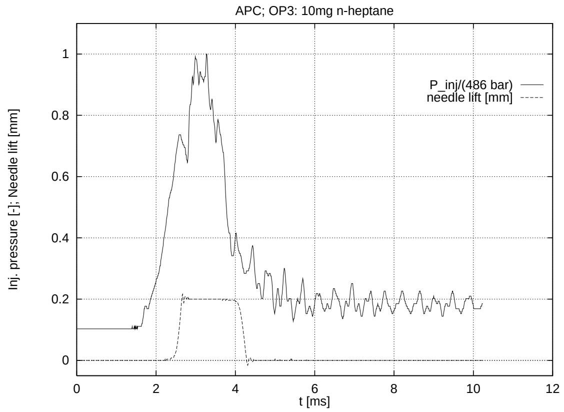

Figure E.2: APC; Injection pressure (normalised by the peak pressure) and needle lift vs. time for OP3.

t [ms]	$\dot{Q}$ $[mm^3/s]$	t [ms]	$\dot{Q}$ $[mm^3/s]$	t [ms]	$\dot{Q}$ $[mm^3/s]$
0.0100	0.0000	0.4600	8.7710	0.9100	4.9390
0.0200	2.2710	0.4700	8.7560	0.9200	4.8310
0.0300	3.7830	0.4800	8.8360	0.9300	4.8600
0.0400	5.8120	0.4900	8.9150	0.9400	4.9240
0.0500	7.9730	0.5000	8.9560	0.9500	5.0440
0.0600	8.8190	0.5100	8.9290	0.9600	5.1190
0.0700	9.0460	0.5200	8.8480	0.9700	5.1920
0.0800	9.2780	0.5300	8.7170	0.9800	5.2440
0.0900	9.5400	0.5400	8.6090	0.9900	5.1190
0.1000	9.6090	0.5500	8.4990	1.0000	4.9180
0.1100	9.5710	0.5600	8.3490	1.0100	4.7730
0.1200	9.5630	0.5700	8.1420	1.0200	4.6750
0.1300	9.5770	0.5800	7.9470	1.0300	4.6390
0.1400	9.5400	0.5900	7.7290	1.0400	4.5970
0.1500	9.5080	0.6000	7.5240	1.0500	4.4590
0.1600	9.4520	0.6100	7.3180	1.0600	4.3880
0.1700	9.3970	0.6200	7.2580	1.0700	4.3830
0.1800	9.3290	0.6300	7.3420	1.0800	4.4180
0.1900	9.2000	0.6400	7.3720	1.0900	4.5820
0.2000	9.1160	0.6500	7.3190	1.1000	4.8220
0.2100	9.0630	0.6600	7.2560	1.1100	5.0770
0.2200	8.9290	0.6700	7.2110	1.1200	5.2510
0.2300	8.8420	0.6800	7.1250	1.1300	5.3880
0.2400	8.7520	0.6900	7.0820	1.1400	5.4250
0.2500	8.6230	0.7000	7.0700	1.1500	5.3500
0.2600	8.4950	0.7100	7.0150	1.1600	5.2630
0.2700	8.3680	0.7200	6.9360	1.1700	5.2290
0.2800	8.2490	0.7300	6.8700	1.1800	5.2230
0.2900	8.1640	0.7400	6.8350	1.1900	5.1940
0.3000	8.0850	0.7500	6.7900	1.2000	5.1660
0.3100	7.9900	0.7600	6.7420	1.2100	5.2080
0.3200	7.9740	0.7700	6.6510	1.2200	5.1700
0.3300	8.0710	0.7800	6.6050	1.2300	5.0950
0.3400	8.2460	0.7900	6.6310	1.2400	4.6480
0.3500	8.5410	0.8000	6.7480	1.2500	3.2160
0.3600	8.7900	0.8100	6.8830	1.2600	1.1610
0.3700	8.8600	0.8200	6.9150	1.2700	0.0260
0.3800	8.8410	0.8300	6.8320		
0.3900	8.7910	0.8400	6.6200		
0.4000	8.8450	0.8500	6.3040		
0.4100	8.9670	0.8600	5.9780		
0.4200	9.0690	0.8700	5.7420		
0.4300	9.1030	0.8800	5.5320		
0.4400	9.0650	0.8900	5.2890		
0.4500	8.9090	0.9000	5.1090		

Table E.2: APC; Injection rate for OP1 and OP4; Q=6mg.

t [ms]	$\dot{Q}$ $[mm^3/s]$	t [ms]	$\dot{Q}$ $[mm^3/s]$	t [ms]	$\dot{Q}$ $[mm^3/s]$	t [ms]	$\dot{Q}$ $[mm^3/s]$
0.0100	0.0000	0.4600	10.0370	0.9100	9.4780	1.3600	6.4710
0.0200	1.3530	0.4700	9.9910	0.9200	9.5430	1.3700	6.4620
0.0300	2.9260	0.4800	10.0280	0.9300	9.6210	1.3800	6.4620
0.0400	4.8600	0.4900	10.1360	0.9400	9.6590	1.3900	6.4320
0.0500	6.6640	0.5000	10.2760	0.9500	9.6470	1.4000	6.3030
0.0600	7.8560	0.5100	10.3930	0.9600	9.5620	1.4100	6.0810
0.0700	8.1110	0.5200	10.4470	0.9700	9.4170	1.4200	5.8640
0.0800	8.3390	0.5300	10.4560	0.9800	9.2780	1.4300	5.7160
0.0900	8.5730	0.5400	10.4560	0.9900	9.1850	1.4400	5.6510
0.1000	8.6920	0.5500	10.4480	1.0000	9.1230	1.4500	5.6400
0.1100	8.7610	0.5600	10.3990	1.0100	9.0480	1.4600	5.6400
0.1200	8.8040	0.5700	10.3120	1.0200	8.9230	1.4700	5.6400
0.1300	8.8370	0.5800	10.2340	1.0300	8.7830	1.4800	5.6400
0.1400	8.8610	0.5900	10.1700	1.0400	8.7270	1.4900	5.6730
0.1500	8.8580	0.6000	10.0900	1.0500	8.8050	1.5000	5.7810
0.1600	8.8240	0.6100	10.0130	1.0600	8.9580	1.5100	5.9400
0.1700	8.8060	0.6200	10.0130	1.0700	9.1030	1.5200	6.1050
0.1800	8.7940	0.6300	10.1110	1.0800	9.1980	1.5300	6.2510
0.1900	8.7670	0.6400	10.2060	1.0900	9.2390	1.5400	6.3450
0.2000	8.7370	0.6500	10.2180	1.1000	9.2350	1.5500	6.3650
0.2100	8.7110	0.6600	10.1880	1.1100	9.2020	1.5600	6.3050
0.2200	8.6950	0.6700	10.1610	1.1200	9.1410	1.5700	6.1960
0.2300	8.6900	0.6800	10.1270	1.1300	9.0620	1.5800	6.0890
0.2400	8.6920	0.6900	10.0900	1.1400	8.9900	1.5900	5.9840
0.2500	8.6690	0.7000	10.0720	1.1500	8.9420	1.6000	5.8790
0.2600	8.6060	0.7100	10.0690	1.1600	8.9000	1.6100	5.8190
0.2700	8.5340	0.7200	10.0690	1.1700	8.8470	1.6200	5.8060
0.2800	8.4840	0.7300	10.0690	1.1800	8.7910	1.6300	5.8030
0.2900	8.4400	0.7400	10.0780	1.1900	8.7350	1.6400	5.7840
0.3000	8.3740	0.7500	10.0900	1.2000	8.6770	1.6500	5.7430
0.3100	8.2990	0.7600	10.0840	1.2100	8.6200	1.6600	5.6960
0.3200	8.2690	0.7700	10.1090	1.2200	8.5730	1.6700	5.6470
0.3300	8.3210	0.7800	10.2270	1.2300	8.5070	1.6800	5.5810
0.3400	8.4510	0.7900	10.3990	1.2400	8.3890	1.6900	5.4730
0.3500	8.6810	0.8000	10.5330	1.2500	8.2430	1.7000	5.3510
0.3600	9.0160	0.8100	10.5620	1.2600	8.0790	1.7100	5.2240
0.3700	9.3290	0.8200	10.4730	1.2700	7.8840	1.7200	5.0940
0.3800	9.5030	0.8300	10.3080	1.2800	7.6510	1.7300	5.0170
0.3900	9.5560	0.8400	10.1160	1.2900	7.4170	1.7400	4.9910
0.4000	9.5620	0.8500	9.9370	1.3000	7.2310	1.7500	4.9100
0.4100	9.5820	0.8600	9.7990	1.3100	7.0560	1.7600	4.7490
0.4200	9.6650	0.8700	9.6910	1.3200	6.8650	1.7700	4.4680
0.4300	9.8240	0.8800	9.5880	1.3300	6.7200	1.7800	3.5360
0.4400	10.0000	0.8900	9.5030	1.3400	6.6180	1.7900	1.8640
0.4500	10.0810	0.9000	9.4640	1.3500	6.5230	1.8000	0.5580

Table E.3: APC; Injection rate for OP3; Q=10mg.

Bibliography

[1] Abbas, A. S., Koussa, S. S., and Lockwood, F. C. Prediction of the particle laden gas flows. In *18th Symposium (Int) on Combustion* (1981), The Combustion Institute, pp. 1427–1438.

[2] Abramzon, B., and Sirignano, W. A. Droplet vaporization model for spray combustion calculations. *Int. J. Heat Mass Transfer 32* (1989), 1605–1618.

[3] Achenbach, E. Vortex shedding from spheres. *J. Fluid Mech. 62* (1974), 209–221.

[4] Aggarwal, S. A. Modeling of a dilute vaporizing multicomponent fuel spray. *Int. J. Heat Mass Transfer 30* (1987), 1949–1961.

[5] Ahamdi-Befrui, B., Wiesler, B., and Winklhofer, E. The propagation of fuel sprays in a research diesel engine - A joint numerical and experimental analysis. *SAE*, 910181 (1991).

[6] Ahmadi-Befrui, B. *Analysis of flow evolution in the cylinder of motored reciprocating engines.* PhD thesis, Imperial College, University of London, 1985.

[7] Ahmadi-Befrui, B. Assessment of Variants of the $k - \epsilon$ Turbulence Model for Engine Flow Applications. In *Energy-Sources Technology Conference, 87-FE-11* (1987), The American Society of Mechanical Engineers.

[8] Ahmadi-Befrui, B., Gosman, A. D., and Watkins, A. P. Prediction of in-cylinder flow and turbulence with three versions of k-ϵ turbulence model and comparison with data. Internal report, Imperial College, Mechanical Engineering Department, 1985.

[9] Al Tawell, A. M., and Landau, J. Turbulence modulation in two-phase jets. *Int. J. Multiphase Flow 3* (1977), 341–351.

[10] AMERICAN PETROLEUM INSTITUTE. *Technical data book - Petroleum refining*, 1981.

[11] AMSDEN, A. A., RAMSHAW, J. D., O'ROURKE, P. J., AND DUKOVICZ, J. K. Kiva: a computer program for two- and three-dimensional fluid flows with chemical reactions and fuel sprays. Report LA 10245-MS, Los Alamos National Laboratory, 1985.

[12] ARCOUMANIS, C. Private communication. (Imperial College), Pressure measurements, 1993.

[13] ARCOUMANIS, C., AND JEONG, K. Steady flow characterisation of the Volkswagen 1.9l Diesel cylinder head. Technical report submitted to Volkswagen AG, Imperial College of Science, Technology and Medicine, date unknown.

[14] ARCOUMANIS, C., AND WHITELAW, J. H. Fluid mechanics of internal combustion engines - a review. *I Mech E 201*, C1 (1987).

[15] ARGYRIS, J., AND KELSEY, S. Energy theorems and structural analysis. *Aircraft Eng.* (Oct 1954 - May 1955).

[16] BÄCKER,H., AND WIARTALLA, A. Pressure chamber measurement data. Additional report, LAT,RWTH Aachen, December, 1992.

[17] BAI, C. Private communication. Imperial College, 1994.

[18] BAI, C., AND GOSMAN, A. D. Development of methodology for spray impingement simulation. *SAE-950283* (1995).

[19] BAKER, A. J. *Finite element computational fluid mechanics.* Hemisphere / McGraw-Hill, New York, 1983.

[20] BARITAUD, T. A. Private communication. (Institut Français du Pétrole, Rueil-Malmaison France), 1993.

[21] BARITAUD, T. A. Experimantal study of vaporization, self-ignition and combustion of a diesel spray. *IDEA/JRC Subprogrma A4- Contract JOUE 0008-D (AM), Final Report* (February, 1993).

[22] BARITAUD, T. A., HEINZE, T. A., DUMAS, J. P., AND LE COZ, J. F. Experimental study of vaporization, self-ignition and combustion of a diesel spray. Annual Report 6, Institut Français du Pétrole, Rueil-Malmaison France, April, 1992.

[23] BARITAUD, T. A., HEINZE, T. A., DUMAS, J. P., AND LE COZ, J. F. Experimental study of vaporization, self-ignition and combustion of a diesel spray. Annual Report 8, Institut Français du Pétrole, Rueil-Malmaison France, January, 1993.

[24] BEGLERIS, P. *Three-dimensional flow predictions in motored diesel engines.* PhD thesis, Imperial College, University of London, 1986.

[25] BERLAD, A., AND HIBBARD, R. Effect of radiant energy on vaporization and combustion of liquid fuels. *NACA*, RME-52109 (1952).

[26] BERLEMONT, A., GOUESBET, G., AND GRANCHER, M. Lagrangian simulation of heat and mass transfers in turbulent two phase flows. In *International Conference on Multiphase Flows* (1991), vol. 2, Tsukuba, pp. 79–82.

[27] BESHAY, K. R. *Computer Modelling of Diesel Spray Dispersion and Evaporation.* PhD thesis, Imperial College, University of London, 1985.

[28] BESHAY, K. R., GOSMAN, A. D., AND WATKINS, A. P. Assessments of multidimensional diesel spray predictions. *SAE Paper No.861570* (1986).

[29] BIRD, R. B. STEWART, E. W., AND LIGHTFOOT, E. N. *Transport phenomena.* J. Willey, 1960.

[30] BLUMBERG, P. N., LAVOIE, G. A., AND TABACZYNSKY, R. J. Phenomenological models for reciprocating internal combustion engines. *Prog. Energy Combust. Sci. 5* (1979), 123–167.

[31] BORMAN, G. L., AND JOHNSON, J. H. Unsteady vaporization histories and trajectories of fuel drops injected into swirling air. *SAE*, 598C (1962).

[32] BOUSSINESQ, J. Théorie de l'écoulement tourbillant. *Mem. par. div. Sav., Paris 23* (1877).

[33] BRACCO, F. V. Application of steady state spray equations to combustion modelling. *AIAA Journal 12* (1976), 1534–1540.

[34] BRACCO, F. V. In *Recent advances in gas dynamics*, C. C., Ed. Plenum Publishing Corp., 1983.

[35] BRACCO, F. V. Modeling of engine sprays. *SAE Paper No.850394* (1985).

[36] Brazier-Smith, P. R., Jennings, S. G., and Latham, J. The interaction of falling water drop; coalescence. *Prog. Roy. Soc. , London*, A326 (1972), 393–408.

[37] Butler, T., Cloutman, L., Dukovicz, J. K., and Ramshaw, J. D. Conchas: an arbitrary lagrangian-eulerian computer program for multicomponent chemically reactive fluid flow at all speeds. Report LA 8929-MS, Los Alamos National Laboratory, 1979.

[38] Chao, B. T. Turbulent transport behaviour of small particles in dilute suspensions. *Ostereichisches Ingenieur-Archiv. 18* (1964), 1.

[39] Chaves, H., Hentschel, W., Obermeier, F., Schindler, K. P., and Weiss, D. Fuel spray in diesel engines; Part II: Spray propagation and wall interaction. In *3rd International Conference - Inovation and Reliability in Automotive Design and Testing* (1992), ATA and DMTI, pp. 761–772.

[40] Chen, C. P., and Wood, P. E. A turbulence closure model for dilute gas-particle flows. *Can. J. Chem. Eng. 63* (1985), 349–360.

[41] Cheroudi, B., Chen, S. H., Bracco, F. V., and Onuma, Y. On the intact core of full-cone sprays. *SAE-850126* (1985).

[42] Chung, T. *Finite element analysis in fluid dynamics.* McGraw-Hill, New York, 1978.

[43] Clamen, A., and Gauvin, W. H. Effects of turbulence on the drag coefficients of spheres in a supercritical flow regimes. *American Institute of Chemical Engineers, Journal 15*, 2 (1969), 184–189.

[44] Clift, A. K., Grace, J. R., and Weber, M. E. *Bubbles, Drops and Particles.* Academic Press, 1978.

[45] Clough, R. The finite element in plane stress analysis. In *Proceedings* 2^{nd} *ASCE conf. on Electronic Computation, Pittsburg* (1960), .

[46] Collins, P. *Prediction of turbulent flow of inelastic shear-thinning fluids in ducts and mixing vessels.* PhD thesis, Imperial College, University of London, 1990.

[47] Courant, R., Friedrichs, K. O., and Lewy, H. Uber die partiellen differenzgleichungen der matematishen Physik. *Matematishe Annalen 100* (1928), 32–74.

[48] Crank, J., and Nicolson, P. A pratical method for numerical evaluation of solutions of prartial differencial equations of the heat-conduction type. *Proc. Cambridge Philos. Soc. 43* (1947), 50–67.

[49] Crowe, C. T. A computational model for the gas-droplet flow-field in the vicinity of an atomiser. In *11th JANAF Symposium* (1974), no. 74-23, The Combustion Institute.

[50] Crowe, C. T. Review - numerical models for dilute gas-particle flows. *ASME Journal of Fluids Engineering 104* (1982), 297–303.

[51] Crowe, C. T., Sharma, M. P., and Stock, D. E. The particle-source-in-cell (PSI-Cell) model for gas-droplet flows. *ASME Journal of Fluids Engineering* (1977), 325–332.

[52] Dandy, D. S., and Dwyer, H. A. A sphere in a shear flow at finite Reynolds number. *J. Fluid Mech. 216* (1990), 381–410.

[53] Daubert, T. E., and Danner, R. P. *Data compilation tables of properties of pure compounds.* Design Institute for Physical Property Data, American Institute of Chemical Engineers, 1985.

[54] Demirdzic, I. Progress report on indirect addressing method. Tech. Rep. Internal report, Imperial College, London, 1985.

[55] Demirdzic, I. A., and Peric, M. Space conservation law in finite volume calculations of fluid flow. *International journal for numerical methods in fluids 8* (1988), 1037–1050.

[56] Diwakar, R., Anderson, J. D., Griffin, M. D., and Jones, E. Inviscid solutions of the flowfield in an internal combustion engine. *AIAA Journal 14*, 12 (1976), 1667.

[57] Dopazo, C. On conditional averages for intermittent turbulent flows. *J. Fluid Mech. 81* (1977), 433–438.

[58] Dukowicz, J. K. A particle-fluid numerical model for liquid sprays. *Journal of Computational Physics 35* (1980), 229–253.

[59] Eisenklam, P., Arunachalam, S. A., and Weston, J. A. Evaporation rates and drag resistance of burning drops. In *11th Symposium (Int) on Combustion* (1967), The Combustion Institute, pp. 715–728.

[60] El Tahry, S. H. *k-ε* equations for compressible reciprocating engine flows. *AIAA Journal of Energy 7* (1983), 345–353.

[61] El Wakill, M. M., Uyehara, O. A., and Myers, P. S. Theoretical investigation of the heating up period of injected fuel droplets vaporizing in air. *NACA*, TN 3179 (1954).

[62] Elghobashi, S. E., and Abou-Arab, T. W. A two-equation turbulence model for two-phase flows. *Physics of Fluids 26* (1983), 931–938.

[63] Elghobashi, S. E., Abou-Arab, T. W., and Mostafa, A. Prediction of the particle-laden jet with a two-equation turbulence model. *Int. J. Multiphase Flow 10* (1984), 697–710.

[64] Elghobashi, S. E., and Truesdell, G. C. On the two-way interaction between homogeneous turbulence and dispersed solid particles.I: Turbulence modification. *Physics of Fluids 5* (1993), 1790–1801.

[65] Engel, O. G. Water drop collisions with solid surfaces. *National Bureau of Standards, Journal of Research 54* (1955), 281–298.

[66] Engel, O. G. Crater depth in fluid impacts. *J. Appl. Phys. 37* (1966), 1798–1808.

[67] Faeth, G. M. Current status of droplet and liquid combustion. *Prog. Energy Combust. Sci. 3* (1977), 191–224.

[68] Faeth, G. M. Evaporation and combustion of sprays. *Prog. Energy Combust. Sci. 9* (1983), 1–76.

[69] Faeth, G. M. Mixing, transport and combustion in sprays. *Prog. Energy Combust. Sci. 13* (1987), 293–345.

[70] Faeth, G. M. Structure and atomization properties of dense turbulent sprays. In *23th Symposium (Int) on Combustion* (1990), The Combustion Institute, pp. 1345–1352.

[71] Favre, A. Equations des gaz turbulents compressibles. *J. de Mécanique 4* (1965), 361.

[72] Fletcher, R. Conjugate gradient methods for infinite systems. In *Proc. Dundee Conference on Numerical Analysis* (1976), G. A. Watson, Ed., Springer-Verlag.

[73] Fraser, R. A., and Bracco, F. V. Cycle-resolved LDV integral length scale measurements in an IC engine. *SAE-880381* (1988).

[74] Fraser, R. A., and Bracco, F. V. Cycle-resolved LDV integral length scale measurements investigating clearence height scaling, isotropy, and homogeneity in an IC engine. *SAE-890615* (1989).

[75] Goldschmidt, V., and Eskinazi, S. Two-phase turbulent flow in a plane jet. *J. Appl. Mech. 33* (1966), 735–747.

[76] Gore, R. A., and Crowe, C. T. Brief communication; Effect of Particle Size on Modulating Turbulent Intensity. *Int. J. Multiphase Flow 15*, 2 (1989), 279–285.

[77] Gore, R. A., and Crowe, C. T. Modulation of turbulence by a dispersed phase. *ASME Journal of Fluids Engineering 113* (1991), 304–307.

[78] Gosman, A. D. Flow processes in cylinders. In *Thermodynamics and gas dynamics of internal combustion engines*, J. Horlock and D. Winterborn, Eds., vol. 2. Oxford University Press, 1985.

[79] Gosman, A. D. Development and validation of a computer code for diesel combustion. IDEA Subprogramme E1; Final Report, Imperial College, London, 1994.

[80] Gosman, A. D., Huh, K., and Zhang, Q. Development and evaluation of a three-dimensional fuel spray model for reciprocating engines. Tech. Rep. Internal report, Imperial College, London, Progress Report for Joint Research Committee of European Automobile Manufacturers, May, 1989.

[81] Gosman, A. D., and Ideriah, H. J. K. TEACH-T: A general computer program for two-dimensional, turbulent, recirculating flows. Internal report, Imperial College, Mechanical Engineering Department, 1976.

[82] Gosman, A. D., and Ideriah, H. J. K. Teach-2E: a general computer program for two-dimensional, turbulent, recirculating flows. Internal report, Imperial College, Mechanical Engineering Department, 1983.

[83] Gosman, A. D., and Ioannides, E. Aspects of computer simulation of liquid fuelled combustors. *AIAA Journal of Energy 7*, 6 (1983), 482–490.

[84] Gosman, A. D., Ioannides, E., Lever, D. A., and Cliffe, K. A. A comparison of continuum and discrete droplet finite-difference models used in the calculation of spray combustion in swirling turbulen flows. Report TP 865, AERE Harwell, 1980.

[85] Gosman, A. D., and Johns, R. A computer analysis of fuel-air mixing in direct-injection engines. *SAE-800091* (1980).

[86] Gosman, A. D., Kralj, C., Marooney, C. J., and Theodossopoulos, P. Development strategies for diesel combustion simulation using the SPEED code. *I Mech E*, C448/035 (1992).

[87] Gosman, A. D., Pun, W. N., Runchal, A. K., Spalding, D., and Wolfshtein, M. *Heat and mass transfer in recirculating flows.* Academic Press, 1969.

[88] Gosman, A. D. Marooney, C. J. Development and validation of computer models of in-cylinder flow and combustion in diesel and sprak-ignition engines. *I Mech E*, C399/169 (1989).

[89] Hanjalić, K. *Two-Dimensional Asymmetric Flow in Ducts.* PhD thesis, Imperial College, University of London, 1970.

[90] Harlow, F. H., and Amsden, A. A. Numerical calculation of multiphase fluid flow. *Journal of Computational Physics 17* (1975), 19–52.

[91] Harlow, F. H., and Nakayama, P. Transport of turbulence energy decay rate. Report LA 3854, Los Alamos National Laboratory, 1968.

[92] Harlow, F. H., and Welch, J. E. Numerical calculation of time-dependent viscous incompressible flow of fluid with a free surface. *Physics of Fluids 12* (1965), 2182.

[93] Haselman, L. C., and Westbrook, C. K. A theoretical model for two-phase fuel injection in stratified charge engines. *SAE-780138* (1978).

[94] Hentschel, W., Hesse, A., and Schindler, K. Experimental investigation of spray formation and combustion in an actual Diesel engine. In *2nd Workshop of the IDEA Programme* (February 1989).

[95] Hentschel, W., and Schindler, K. P. Experimental investigation of spray formation and combustion in a real diesel engine. In *Periodic Report for the period 01.01.1991 - 30.06.1991* (1991), IDEA, Subprogramme C4.

[96] Hentschel, W., and Schindler, K. P. Experimental investigation of spray formation and combustion in a real diesel engine. In *Periodic Report for the period 01.07.1991 - 31.12.1991* (1992), IDEA, Subprogramme C4.

[97] Hestenes, M. R., and Stiefel, E. L. Method of conjugate gradients for solving linear systems. *National Bureau of Standards, Journal of Research 29* (1952), 409–436.

[98] Hestroni, G. Particles-Turbulence interaction. *Int. J. Multiphase Flow 15*, 5 (1989), 735–746.

[99] Hestroni, G., and Sokolov, M. Distribution of mass, velocity and intensity of turbulence in a two-phase jet. *J. Appl. Mech. 93* (1971), 315–327.

[100] Heywood, J. B. *Internal combustion engine fundamentals.* McGraw-Hill Kogakusha Ltd., 1989.

[101] Hinze, J. In *Progress in Heat and Mass transfer*, vol. 6. Pergamon Press, N.Y., 1972, p. 433.

[102] Hinze, J. O. *Turbulence*, 2 ed. McGraw-Hill, 1975.

[103] Hirsch, C. *Numerical computation of internal and external flows.* John Willey & Sons, 1991.

[104] Hobbs, P. V., and Alkezweeny, A. J. Spalshing of water drop. *Science*, 155 (1967), 1112–1114.

[105] Hobbs, P. V., and Osheroff, T. Spalshing of drops on shallow liquids. *Science*, 158 (1967), 1184–1186.

[106] Hsiang, L. P., and Faeth, G. M. Near-limit drop deformation and secondary breakup. *Int. J. Multiphase Flow 18* (1992), 635–652.

[107] Hubbard, G. L., Denny, V. E., and Mills, A. F. Droplet evaporation: effects of transients and variable properties. *Int. J. Heat Mass Transfer 18* (1975), 1003–1008.

[108] Huh, K. Y., and Gosman, A. D. A phenomenological model of diesel spray atomization. In *International Conference on Multiphase Flows* (1991), vol. 2, Tsukuba, pp. 515–518.

[109] Ingebo, R. D. Heat transfer rates and drag coefficients for ethanol drops in a rocket motor. In *8th Symposium (Int) on Combustion* (1962), The Combustion Institute, pp. 1104–1113.

[110] Issa, R. I. Solution of the implicitly discretized fluid flow equation by operator splitting. *Journal of Computational Physics 62* (1986), 40–65.

[111] Jayaratne, O., and Mason, B. The coalescence and bouncing of water drops at an air/water interface. In *Proc. R. Soc. London*, vol. A 280. 1964, pp. 545–565.

[112] Jayatillaka, C. L. V. The influence of Prandtl number and surface roughness on the resistance of the laminar sublayer to momentum and heat transfer. In *Progress in Heat and Mass transfer*, U. Grigull and E. Hahre, Eds., vol. 1. Pergamon Press, N.Y., 1969.

[113] Jones, W. P. Models for turbulent flows with variable density and combustion. In *Lecture Series* (1979), von Karman Institute for Fluid Dynamics.

[114] Jones, W. P., and Launder, B. E. The prediction of laminarization with a 2-equation model of turbulence. *Int. J. Heat Mass Transfer 15* (1972), 301–314.

[115] Jones, W. P., and Launder, B. E. The prediction of low-Reynolds-number phenomena with a 2-equation model of turbulence. *Int. J. Heat Mass Transfer 16* (1973), 1119–1130.

[116] Kershaw, D. S. The incomplete Cholesky conjugate gradient method for the iterative solution of linear equations. *Journal of Computational Physics 26* (1978), 43–65.

[117] Khalil, E. E., and Whitelaw, J. H. Aerodynamic and thermodynamic characteristics of kerosene-spray flames. In *16th Symposium (Int) on Combustion* (1976), The Combustion Institute, pp. 569–576.

[118] Koss, H. J., Brüggemann,D. and Wiartalla,A. and Bäcker,H., and Bruer, A. Results from fuel/air ratio measurements in an n-heptane injection spray. IDEA Subprogramme A2, revised additional report, RWTH Aachen, December, 1992.

[119] Krzeczkowski, S. A. Measurement of liquid droplet disintegration mechanisms. *Int. J. Multiphase Flow 6* (1980), 227–239.

[120] Langmuir, I. The production of rain by a chain reaction in cumulus clouds at temperatures above freezing. *Journal of Meteorology 5* (1948), 175–192.

[121] Launder, B. E. Second moment closure: methodology and practice. In *Turbulence models and their applications*, B. E. Launder, W. C. Reynolds, and W. Rodi, Eds. Editions Eyrolles, Paris, 1984.

[122] Launder, B. E., and Spalding, D. B. *Mathematical models of turbulence.* Academic Press, London, 1972.

[123] Launder, B. E., and Spalding, D. B. The numerical computation of turbulent flows. *Computer methods in applied mechanics and engineering 3* (1974), 269–289.

[124] Law, C. K. Recent advances in droplet vaporization and combustion. *Prog. Energy Combust. Sci. 8* (1982), 169–199.

[125] Lefebvre, A. H. *Prog. Energy Combust. Sci. 6* (1980), 233.

[126] Lefebvre, A. H. Atomization performance of gas turbine gas injectors. In *Proceedings of Central States Meeting* (1986), The Combustion Institut.

[127] Lefebvre, A. H. *Atomization and sprays.* Hemisphere Publishing Corporation, 1989.

[128] Levin, Z. *Splashing of water drops: A study of the hydrodynamics and charge separation.* PhD thesis, University of Washington, Seattle, 1970.

[129] Levin, Z., and Hobbs, P. V. Splashing of water drops on solid and wetted surfaces: Hydrodynamics and charge separation. *Phil. Trans. Roy. Soc. London*, A269 (1971), 555–585.

[130] Libby, P. A. On the prediction of intermittent turbulent flows. *J. Fluid Mech. 68* (1975), 273–295.

[131] Liu, D. Y., Anders, K., and Frohn, A. Drag coefficients of single droplets moving in an infinite droplet chain on the axis of a tube. *Int. J. Multiphase Flow 14* (1988), 217–232.

[132] MacCormac, R. W., and Paullay, A. J. Computational efficiency achieved by time splitting of the finite difference operators. *AIAA Paper*, 72-154 (1972).

[133] MacDonald, P. W. The computation of transonic flow through two-dimensional gas turbine cascade. *ASME Paper*, 71-GT-89 (1971).

[134] Mao, C.-P., Wakamtsu, Y., and Faeth, G. M. Simplified model of high pressure combustion. In *18th Symposium (Int) on Combustion* (1981), The Combustion Institute, pp. 337–347.

[135] Matsui, Y., and Sugihara, K. Sources of hydrocarbon emissions from a small direct injection diesel engine. *JSAE Review 7* (1986), 4–11.

[136] McCarty, M. J., and Molloy, N. A. Review of stability of liquid jets and the influence of nozzle design. *Chem. Engng. J. 7* (1974), 1–20.

[137] Megaridis, C. M., and Sirignano, W. A. Numerical modeling of a vaporizing multicomponent droplet. In *23rd Symposium (Int) on Combustion* (1990), The Combustion Institute, pp. 1413–1421.

[138] Mei, R. An approximate expression for the shear lift force on a spherical particle at the finite Reynolds number. *Int. J. Multiphase Flow 18* (1992), 145–147.

[139] Meier, G. Study of pressure fluctuations, flow separation and cavitation in the nozzle and thier influence on spray formation. IDEA Subprogram A1, Periodic Report iii, Max-Planck-Institut für Strömungsforschung, Göttingen, 1990.

[140] Meier, G. Study of pressure fluctuations, flow separation and cavitation in the nozzle and thier influence on spray formation. IDEA Subprogram A1, Periodic Report i, Max-Planck-Institut für Strömungsforschung, Göttingen, August, 1989.

[141] Meier, G. Study of pressure fluctuations, flow separation and cavitation in the nozzle and thier influence on spray formation. IDEA Subprogram A1, Periodic Report ii, Max-Planck-Institut für Strömungsforschung, Göttingen, July, 1990.

[142] Meijerink, J. A. Guidelines for the usage of incomplete decompositions in solving sets of linear equations as they occur in practical problems. *Journal of Computational Physics 44* (1981), 134–155.

[143] Moler, T., and Mansour, N. Modeling of turbulence in rapidly compressed flows. *SAE Paper*, 820040 (1982).

[144] Monaghan, M. L. The diesel passenger car in a green world. *Ricardo Consulting Engineers Ltd. DP 90/0390* (1990).

[145] Mostafa, A. A., and Mongia, H. C. On the modeling of turbulent evaporating sprays: Eulerian versus Lagrangian approach. *Int. J. Heat Mass Transfer 30* (1987), 2583–2593.

[146] Mostafa, A. A., and Mongia, H. C. On the interaction of particles and turbulent fluid flow. *Int. J. Heat Mass Transfer 31* (1988), 2063–2075.

[147] Myškis, A. D. *Introductory Mathematics for Engineers - Lectures in Higher Mathematics*. MIR Publisher, Moskow, 1975.

[148] Naber, J. D., and Reitz, R. D. Modeling of engines spray/wall impingement. *SAE Paper No.880107* (1988).

[149] Newman, J. A., and Brzustowski, T. Behavior of a liquid jet near the thermodynamic critical region. *AIAA Journal 9* (1971), 1595–1602.

[150] Nicholls, J. Stream and droplet breakup by shock waves. NASA SP-194, 1972.

[151] Obermeier, F. Study of pressure fluctuations, flow separation and cavitation in the nozzle and their influence on spray formation. IDEA Subprogram A1, Periodic Report iv, Max-Planck-Institut für Strömungsforschung, Göttingen, 1990.

[152] Obermeier, F. Deposition and re-evaporation of fuel at the wall of a diesel combustion chamber. IDEA Subprogramme A1, Periodic Report iv, Max-Planck-Institut für Strömungsforschung, Göttingen, 1991.

[153] Obermeier, F. Deposition and re-evaporation of fuel at the wall of a diesel combustion chamber. IDEA Subprogramme A1, Periodic Report v, Max-Planck-Institut für Strömungsforschung, Göttingen, 1991.

[154] Obermeier, F. Deposition and re-evaporation of fuel at the wall of a diesel combustion chamber. IDEA Subprogramme A1, Periodic Report vi, Max-Planck-Institut für Strömungsforschung, Göttingen, 1992.

[155] Obermeier, F. Deposition and re-evaporation of fuel at the wall of a diesel combustion chamber. IDEA Subprogramme A1, Periodic Report vii, Max-Planck-Institut für Strömungsforschung, Göttingen, 1992.

[156] Obermeier, F. Deposition and re-evaporation of fuel at the wall of a diesel combustion chamber. IDEA Subprogramme A3, Periodic Report viii, Max-Planck-Institut für Strömungsforschung, Göttingen, January, 1993.

[157] Obermeier, F. Study of pressure fluctuations, flow separation and cavitation in the nozzle and thier influence on spray formation. IDEA Subprogramme A1, Periodic Report viii, Max-Planck-Institut für Strömungsforschung, Göttingen, January, 1993.

[158] Obermeier, F. Modelling of atomisation. Additional report, Max-Planck-Institut für Strömungsforschung, Göttingen, March 1993.

[159] Obermeier, F. Modelling of nozzle-flow. Additional report, Max-Planck-Institut für Strömungsforschung, Göttingen, March 1993.

[160] Obermeier, F., and Chaves, H. Study of pressure fluctuations flows, separation and cavitation in the nozzle and their influence on spray formation. 9^{th} *Workshop of the IDEA Programme; Subprogram A3* (October, 1992).

[161] O'Connor, L. Computational fluid dynamics; Giving a boost to engine design. *Mechanical Engineering, ASME* (1992), 44–50.

[162] O'Rourke, P. J. *Collective drop effects on vaporizing liquid sprays.* PhD thesis, University of Princeton, 1981.

[163] O'Rourke, P. J., and Bracco, F. V. Modeling of drop interaction in thick sprays and comparison with experiment. *I Mech E*, C404/80 (1980).

[164] O'Rourke, R. J., and Amsden, A. A. The TAB method for numerical calculations of spray droplet breakup. *SAE-872089* (1987).

[165] Patankar, S. V. *Numerical heat transfer and fluid flow.* McGraw Hill, New York, 1980.

[166] Patankar, S. V. A calculation procedure for two-dimensional elliptic situations. *Numerical Heat Transfer 4* (1981), 409–425.

[167] Patankar, S. V., and Baliga, B. R. A new finite-difference scheme for parabolic differential equations. *Numerical Heat Transfer 1* (1978), 27–37.

[168] Patankar, S. V., and Spalding, D. B. *Heat and mass transfer in boundary layers.* Morgan Grampian, London, 1967.

[169] Patankar, S. V., and Spalding, D. B. A calculation procedure for heat, mass and momentum transfer in three-dimensional parabolic flows. *Int. J. Heat Mass Transfer 15* (1972), 1787–1806.

[170] Pei, D., and Haywars, G. Local heat transfer rates from two adjacent spheres in turbulent flow. *Int. J. Heat Mass Transfer 26* (1983), 1547–1556.

[171] Pilch, M., and Erdman, C. A. Use of breakup time data and velocity history data to predict the maximum size of stable fragments for acceleration-induced breakup of a liquid drop. *Int. J. Multiphase Flow 13* (1987), 741–757.

[172] Prakash, C. *A finite element method for predicting flow through ducts with arbitrary cross sections.* PhD thesis, University of Minnesota, 1981.

[173] Ranz, W., and Marshall, W. R. J. Evaporation from drops, part i. *Chemical Engineering Progress 48* (1952), 141–146.

[174] Rayleigh, L. In *Proc. Lond. Math. Soc.*, vol. X. 1879, p. 4.

[175] Reid, J. K. On the method of conjugate gradients for the solution of large sparse system of linear equations'. In *Large sparce sets of linear equations*, J. K. Reid, Ed. Academic Press, New York, 1971.

[176] Reitz, R. D. Modelling atomization processes in high-pressure vaporizing sprays. *Atomization and Spray Technology 3* (1987), 309–337.

[177] Reitz, R. D., and Bracco, F. V. Mechanisms of atomization of a liquid jet. *Physics of Fluids 25* (1982), 1730.

[178] Reitz, R. D., and Diwakar, R. Effect of drop breakup on fuel sprays. *SAE Tech. paper series*, 860469 (1986).

[179] Reitz, R. D., and Diwakar, R. Structure of high-pressure fuel sprays. *SAE Tech. paper series*, 870598 (1987).

[180] Renksizbulut, M., and Yuen, M. C. Numerical study of droplet evaporation in a high-temperature stream. *ASME Journal of Heat Transfer 105* (1983), 389–397.

[181] Reynolds, W. C. The potential and limitations of direct and large eddy simulation. In *Whither Turbulence: turbulence at the crossroads*, J. L. Lumley, Ed., no. 357, Lecture notes in Physics. Springer-Verlag, Berlin, 1990.

[182] Rhie, C. M. *A numerical study of the flow past an isolated airfoil with separation.* PhD thesis, University of Illinois, Urbana-Champaign, 1981.

[183] Rhie, C. M., and Chow, W. L. Numerical study of the turbulent flow past an airfoil with edge separation. *AIAA Journal 21* (1983), 1525–1532.

[184] Rubin, S. J. e. a. Numerical studies of incompressible viscous flow in a driven cavity. Tech. Rep. NASA SP-378, 1975.

[185] Schmidt, T., Esser-Schmittmann, W., Roosen, P., Hassel, E., Xu, H., Reuter, U., and Scheid, E. Pressure chamber experiments for fuel spray model development. Final Report Contract No. EN3E-0102-D, Institut für Thermodynamic, RWTH Aachen, October, 1988.

[186] Schweimer, G. Notes on the peak compression pressure in the IDEA engine. Private communication, FAX, June 1993.

[187] Shearer, A. J., and Faeth, G. M. Combustion of liquid spray at high pressures. Tech. Rep. CR-135210, NASA, 1977.

[188] Shuen, J.-S., Chen, L.-D., and Faeth, G. M. Evaluation of a stochastic model of particle dispersion in a turbulent round jet. *The American Institute of Chemical Engineers 29*, 1 (1983), 167–170.

[189] Shuen, J. S., Solomon, A. S. P., Zhang, Q. F., and Faeth, G. M. A theoretical and experimental study of turbulent particle-laden jets. Report CR-168293, NASA, 1983.

[190] Sirignano, W. A. *Prog. Energy Combust. Sci. 9* (1983), 291.

[191] Soo, S. L. *Multiphase fluid dynamics.* Science Pr., Beijing, 1990.

[192] Spalding, D. B. A novel finite-difference formulation for differential expressions involving both first and second derivatives. *Int. J. Num. Meth. Eng. 4* (1972), 551–559.

[193] SPEED-DC. *User's Manual; Version 2.7.* Comuptational Dynamics, Limited, 1992.

[194] STAR-CD. *Manuals; Version 2.2.* Comuptational Dynamics, Limited, 1993.

[195] Stow, C. D., and Stainer, R. D. The physical products of a splashing water drop. *Journal of Meteorological Society of Japan 55* (1977), 518–531.

[196] Strauss, T. Notes on the injector data. Private communication, FAX, August 1992.

[197] Strauss, T. Notes on the valve lift tables. Private communication, FAX, August 1992.

[198] Strauss, T. Notes on the wall temperatures. Private communication, FAX, August 1992.

[199] Syed, S. A., and Bracco, F. V. Further comparison of computed and measured divided-chamber engine combustion. *SAE Paper*, 790247 (1979).

[200] Tabrizi, B. S. *Three-Dimensional Diesel Spray Predictions in Combustion Chamber Flows.* PhD thesis, Imperial College, University of London, 1991.

[201] Taylor, A. M. K. P. *Instrumentation for flows with combustion.* Academic Press, Lonodn, 1993.

[202] Taylor, G. I. Generation of ripples by wind blowing over a viscous fluid. In *Scientific papers of Sir G. I. Taylor*, G. Batchelor, Ed., vol. 3. Cambridge Press, 1963, pp. 244–254.

[203] Tennekes, H., and Lumley, J. L. *A first course in turbulence*, vol. 1. MIT Press, Cambridge, Massachusetss, 1977.

[204] Theodoropoulos, T. *Prediction of Three-Dimensional Engine Flow on Unstructured Meshes.* PhD thesis, Imperial College, University of London, 1990.

[205] Thring, M. W., and Newby, M. P. Combustion length of enclosed turbulent jet flames. In *4th Symposium (Int) on Combustion* (1953), The Williams & and Wilkins Company, Baltimore, pp. 789–796.

[206] Torobin, L. B., and Gauvin, W. H. The drag coefficients of single spheres moving in steady and accelerated motion in a turbulent fluid. *American Institute of Chemical Engineers, Journal 7*, 4 (1961), 615–619.

[207] Townsend, A. A. *The structure of turbulent shear flow.* Cambridge University Press, New York, 1956.

[208] Travis, J. R., Harlow, F. H., and Amsden, A. A. Numerical calculation of two-phase flows. *Nuclear science and engineering 61* (1976), 1–10.

[209] Truesdell, C. *A first course in rational continuum mechanics*, vol. 1. Academic Press, 1977.

[210] Tsui, Y. Y. *Calculation of Three-Dimensional Flow in motored Engine.* PhD thesis, Imperial College, University of London, 1987.

[211] Tsuji, Y., and Morikawa, Y. LDV measurements of an air-solid two-phase flow in a horizontal pipe. *J. Fluid Mech. 120* (1982), 385–409.

[212] Tsuji, Y., Morikawa, Y., and Shiomi, H. LDV measurements of an air-solid two-phase flow in a vertical pipe. *J. Fluid Mech. 139* (1984), 417–434.

[213] Tsuji, Y., Morikawa, Y., and Terashima, K. Fluid-dynamic interaction between two spheres. *Int. J. Multiphase Flow 8* (1982), 71–82.

[214] Turner, M., Clough, R., Martin, H., and Topp, L. Stiffness and deflection analysis of complex structures. *Journal of Aeronautical Society 23* (1956), 805–823.

[215] Wallis, G. B. *One dimensional two phase flows.* McGraw Hill, 1969.

[216] Watcher, L. H. J., and Westrling, N. A. J. The heat transfer from a hot wall to impinging water drops in the spheroidal state. *Chem. Eng. Sc. 21* (1966), 1047–1056.

[217] Watkins, A. P. *Flow and heat transfer in piston/cylinder assemblies.* PhD thesis, Imperial College, University of London, 1977.

[218] Watkins, A. P., and Wang, D. M. A new model for diesel spray impaction on walls and comparison with experiments. In *International Symposium COMODIA 90* (1990), pp. 243–248.

[219] Weller, H. Private communication. Imperial College, 1994.

[220] White, F. *Fluid mechanics.* McGraw-Hill, 1979.

[221] Wierzba, A., and Takayama, K. The state of the art of the experimental investigation of the liquid drop atomization in high speed gas flow. In *14th Conference on liquid atomisation and spray systems* (1986), Japan Institute of fuel, Tokyo, pp. 133–146.

[222] Wierzba, A., and Takayama, K. Experimental investigation of the aerodynamic breakup of liquid drops. *AIAA Journal 26*, 11 (1988), 1329–1335.

[223] Williams, A. *Combustion of sprays of liquid fuels.* Elek Science, London, 1976.

[224] Williams, F. A. *Combustion theory.* Addison-Wesley Publishing Co. Inc. London, 1965.

[225] Yuen, M. C., and Chen, L. W. On drag of evaporating liquid droplets. *Combustion Science and Technology 14* (1976), 147–154.

[226] Yuu, S., Yasukouchi, N., Hirosawa, Y., and Jotaki, T. Particle turbulent diffusion in a dust laden round jet. *American Institute of Chemical Engineers, Journal 24* (1978), 509.

[227] Zhang, Q. Private communication, 1992.

[228] Zhang, Q. PhD thesis, Imperial College, University of London, 1994. In preparation.

[229] Zienkiewicz, O., and Cheung, Y. Finite elements in the solution of field problems. *The Engineer 220*, 5722 (1965), 507–510.

[230] Ziman, H. *Computer prediction of chemically reacting flows in stirred tanks.* PhD thesis, Imperial College, University of London, 1990.